Mouse Models of Vascular Diseases

Masataka Sata
Editor

Springer

Mouse Models of Vascular Diseases

Masataka Sata
Editor

Mouse Models of Vascular Diseases

Springer

Editor
Masataka Sata
Tokushima University
Tokushima, Japan

ISBN 978-4-431-55811-8 ISBN 978-4-431-55813-2 (eBook)
DOI 10.1007/978-4-431-55813-2

Library of Congress Control Number: 2016931990

Printed on acid-free paper

This Springer imprint is published by SpringerNature
The registered company is Springer Japan KK.

Preface

There are many patients who are suffering from various types of vascular diseases. Atherosclerosis results in luminal narrowing and insufficient blood perfusion, leading to organ damage such as myocardial infarction, cerebral infarction, and amputation of lower extremities. Atherosclerotic diseases are a leading cause of death in industrialized countries. Obstructive atherosclerotic diseases are treated by percutaneous catheter intervention or bypass surgery, which requires subsequent re-vascularization procedures due to re-stenosis of the target lesion or a bypass graft in many cases. Aortic aneurysm and cerebral aneurysm may cause sudden death by unanticipated rupture. Graft vasculopathy—diffuse intimal hyperplasia in arteries of the transplanted organs—causes grant failure. Moreover, coronary aneurysm is the major sequel of Kawasaki's disease, a mucocutaneous lymph node syndrome in children. Unfortunately, exact pathogenesis of most of the vascular diseases remains to be clarified. Subsequently, there are no established methods to diagnose and prevent those vascular diseases accurately.

Genetically modified mice are a very powerful tool for studying the pathogenesis of various diseases, including immunology, oncology, the central nervous system, autoimmune disease, and congenital diseases. Genetically modified mice also provide good tools to track the origin and the fate of the cells that play a key role in the disease process. However, mice had always been thought to be too small to be used for research in the field of vascular diseases. Most of the models of vascular diseases, which have been used for larger animals, could not be applied to mice.

I have been working as an interventional cardiologist. I treated many patients with coronary artery diseases by performing percutaneous coronary intervention (PCI). However, re-stenosis at the site of PCI limited the long-term prognosis of the treatment in many patients. Therefore, I started research on gene therapy to prevent post-PCI re-stenosis. However, no gene therapy has been shown to be effective enough to be used in clinical practice. When I became an independent researcher in Japan in 1999, I realized that we should clarify the exact pathogenesis of re-stenosis using genetically modified mice. I had a hard time developing a mouse model of post-angioplasty re-stenosis. After many efforts and failures, I finally succeeded in

establishing a mouse model of vascular injury that induces rapid onset of medial cell apoptosis followed by reproducible neointimal hyperplasia like a rat model of balloon-induced arterial injury. With this useful model, I published numerous papers by taking advantage of genetically modified mice to investigate the cell cycle, apoptosis, and origin of neointimal cells. I welcomed all visitors who wanted to learn the method to my laboratory. Moreover, I sent a videotape or CD of the tutorial videos of the procedure. Now, the tutorial videos (Ver. 1 and Ver. 2) can be viewed on the Internet. The method has been adopted successfully in many laboratories in the world and used to elucidate the pathogenesis of post-PCI re-stenosis. The methodological paper published in the *Journal of Molecular and Cellular Cardiology* in 2000 has been cited in 229 papers.

Besides my wire-mediated endovascular injury, other mouse models of vascular diseases have been reported and have substantially contributed to basic research on cardiovascular and metabolic disorders. However, like my wire-mediated vascular injury model, those models are technically very difficult to reproduce in other laboratories, even when researchers carefully read the literature in which the model has been used to analyze genetically modified mice. Many investigators in the vascular disease area have wanted a detailed methodological source to learn how to treat mice to get reproducible vascular lesions in mice.

Under these conditions, I had a chance to edit a book with Springer. I had no hesitation to edit a methodological sourcebook on mouse models of vascular diseases. Covering various areas, each chapter is written by a pioneering researcher who has developed an original vascular disease model. Notoriously difficult to reproduce, each model is described in detail and numerous photographs are provided, with links to videos. There are detailed descriptions about the knacks and pitfalls for each procedure. I hope that this book can be used as a bible in many laboratories that are working on cardiovascular diseases. Finally, I acknowledge all authors for their generosity in providing detailed descriptions of the methods that they had spent tremendous efforts and time to establish.

Tokushima, Japan Masataka Sata

Contents

Part I
Re-stenosis Models After Angioplasty

Chapter 1
Wire-Mediated Endovascular Injury that Induces Rapid Onset of Medial Cell Apoptosis Followed by Reproducible Neointimal Hyperplasia

Masataka Sata, Kimie Tanaka, and Daiju Fukuda

Abstract Genetically modified mice serve as a powerful tool to determine the role of specific molecules in a wide variety of biological phenomena including vascular remodeling. Several models of arterial injury have been proposed to analyze transgenic/knockout mice. About 15 years ago, we have developed a new mouse model of vascular injury that resembles balloon angioplasty. A straight spring wire is inserted into the femoral artery via arterioctomy in a small muscular branch. The wire is left in place for 1 min to denude and dilate the artery. After the wire is removed, the muscular branch is tied off and the blood flow of the femoral artery is restored. The lumen is enlarged with rapid onset of medial cell apoptosis as determined by TUNEL staining and transmission electron microscopy. While the circumference of the external elastic lamina remained enlarged, the lumen is gradually narrowed by neointimal hyperplasia composed of smooth muscle cells. At 4 weeks, a concentric and homogeneous neointimal lesion could be formed reproducibly in the region where the wire had been inserted. Similar exuberant hyperplasia could be induced in all strains examined (C57BL/6 J, C3H/HeJ, BALB/c, and 129/SVj). This model has been adopted in many laboratories all over the world to study the molecular mechanism of post-angioplasty restenosis at the genetic level.

Keywords Restenosis • Angioplasty • Mouse • Smooth muscle cell apoptosis

---

The online version of this chapter (doi:10.1007/978-4-431-55813-2_1) contains supplementary material, which is available to authorized users.

M. Sata (✉) • D. Fukuda
Department of Cardiovascular Medicine, Institute of Biomedical Sciences, Tokushima University Graduate School, 3-18-15 Kuramoto-cho, Tokushima-city, Tokushima 770-8503, Japan
e-mail: masataka.sata@tokushima-u.ac.jp

K. Tanaka
Division for Health Service Promotion, The University of Tokyo, Tokyo, Japan

M. Sata (ed.), *Mouse Models of Vascular Diseases*,
DOI 10.1007/978-4-431-55813-2_1

1.1 Introduction

Percutaneous coronary intervention (PCI) has been widely adopted for the treatment of coronary atherosclerosis. However, a significant number of these procedures fail due to post-angioplasty restenosis. Although the increasing use of new devices, particularly drug-eluting stents, for dilatation of stenosed arteries has lowered the incidence of acute complications, restenosis still limits the long-term outcome of percutaneous interventions [1, 2]. Thus, much effort has been devoted to both understanding the molecular pathways regulating vessel wall responses to acute injury and developing strategies to prevent post-angioplasty restenosis.

Recent advances in gene-manipulating techniques have produced various genetically modified mice to determine the role of specific molecules in vascular remodeling [3]. There are established mouse models for hypercholesterolemia-induced atherosclerosis [4, 5], transplant-induced arteriosclerosis [6], and angiogenesis [7]. However, mouse arteries, unlike those of larger animals such as pigs [8], rabbits [9], and rats [10], are too small for transluminal injury with a balloon. Alternatively, several models of vascular injury [11–16] have been shown to produce neointimal hyperplasia and are used to evaluate the susceptibility of transgenic/knockout mice to post-angioplasty restenosis.

In contrast to other models, in which arteries are injured from adventitia, we developed a new mouse model of vascular injury that resembles balloon angioplasty [17–19]. Dilatation of the mouse femoral artery by intraluminal insertion of a large wire resulted in rapid onset of medial cell apoptosis followed by reproducible neointimal hyperplasia. After we published the original methodological paper [17], this model has been wildly adopted in many laboratories to analyze genetically modified mice in studies on the pathophysiology of post-angioplasty restenosis. More than 200 studies have published using this model by us [19–26] and others [27–34]. In this chapter, we describe how the procedures can be performed in detail. Moreover, electrical version of this book provides tutorial videos 1.1 and 1.2 that could be viewed on the Internet.

1.2 Methods

1.2.1 Surgical Procedures

1. Adult mice weighing between 25 and 35 g are kept in microisolator cages on a 12-h day/night cycle and fed regular chow. For all surgical procedures, the mice are anesthetized by intraperitoneal injection of 50 mg/kg Nembutal (Abbott Laboratories, North Chicago, IL) diluted in 0.9 % sodium chloride solution. All procedures involving experimental animals are performed in accordance with protocols approved by local institutional guidelines for animal care and complied with the *"Guide for the Care and Use of Laboratory Animals"* (NIH publication No. 86–23, revised 1985).

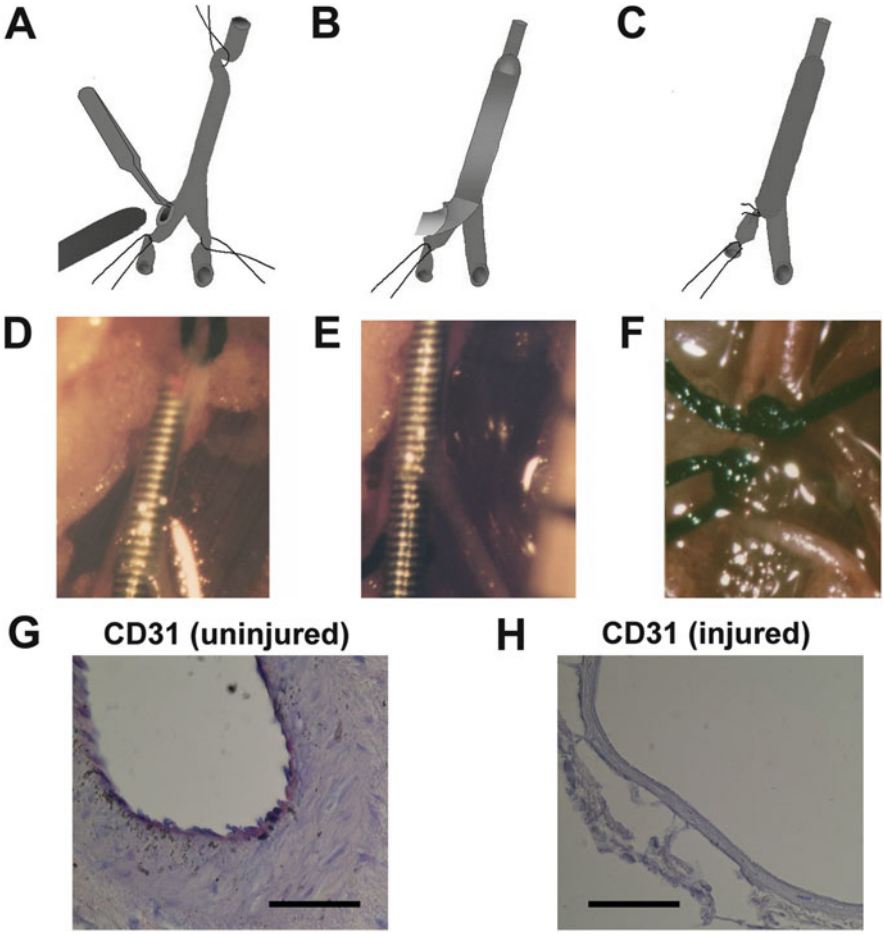

Fig. 1.1 The endovascular injury of the murine femoral artery
Either the left or right femoral artery was exposed by blunted dissection and looped proximally and distally with a 6-0 silk suture for temporary vascular control during the procedure. A small branch was isolated and ligated distally. Transverse arterioctomy was performed in the muscular branch (**a**). Microsurgery forceps were used to extend the arterioctomy through which a 0.015 in. straight wire was inserted for more than 5 mm into the femoral artery toward the iliac artery (**b**, **d**). The wire was left in place for 1 min to denude and dilate the artery (**e**). After removal of the wire, the proximal portion of the arterial branch was tied off. Blood flow of the femoral artery was restored (**c**, **f**). Anti-CD31 immunostaining revealed that the endothelium was completely denuded (**g**, **h**). Bar, 50 μm (Reproduced from Ref. [17] with permission)

2. Surgery is carried out using a dissecting microscope (SMZ-800, Nikon, Tokyo). Transluminal mechanical injury of the femoral arteries is induced basically according to a method developed for rodent carotid arteries [19, 23] with various modifications (Fig. 1.1).

3. Either the left or right femoral artery is exposed by blunted dissection. The accompanying femoral nerve is carefully separated, but the femoral vein is not isolated from the artery.
4. The femoral artery and vein are looped together proximally and distally with 6-0 silk suture (Natsume Co., Tokyo) for temporary vascular control during the procedure.
5. A small branch between the rectus femoris and vastus medialis muscles is isolated and looped proximally and ligated distally with 6-0 silk sutures.
6. Veins and connective tissues around the artery are carefully removed with microsurgery forceps (No. 11253–20, Dumont S.A., Switzerland).
7. The exposed muscular branch artery is dilated by topical application of one drop of 1 % lidocaine hydrochloride for 1 min.
8. Transverse arterioctomy is performed in the muscular branch with Vannas style iris spring scissors (No. 15000–00, Fine Science Tools, Inc., Foster City, CA).
9. Microsurgery forceps (No. 11253–25, Dumont S.A., Switzerland) are used to extend the arterioctomy through which a straight spring wire (0.38 mm in diameter, No. C-SF-15-15, COOK, Bloomington, IN) is carefully inserted into the femoral artery for more than 5 mm toward the iliac artery.
10. The wire is left in place for 1 min to denude and dilate the artery.
11. Then, the wire is removed, and the silk suture looped at the proximal portion of the muscular branch artery is secured.
12. Blood flow in the femoral artery is restored by releasing the sutures placed in the proximal and distal femoral portions.
13. The skin incision is closed with a 5-0 silk suture (Natsume Co., Japan).
14. The mice are euthanized by intraperitoneal administration of an overdose of Nembutal at the time points indicated.
15. At death, the mice are perfused at a constant pressure (80 mmHg) via the left ventricle with 0.9 % NaCl solution followed by perfusion fixation with freshly depolymerized 4 % paraformaldehyde in PBS (pH 7.4). The femoral artery is carefully excised, postfixed in 4 % paraformaldehyde overnight at 4 °C, and embedded in paraffin.

1.2.2 Morphometric Analysis

Cross sections (5 μm) are deparaffinized, stained with hematoxylin and eosin, and mounted with MOUNT QUICK mounting media (DAIDO, Tokyo). The image is digitized by a digital camera on a PROVIS AX80 microscope (Olympus, Tokyo). Digitalized images were analyzed using software (Image J, NIH). The lumen, internal elastic lamina, and external elastic lamina were defined. The intimal (tissue between the lumen and internal elastic lamia) and medial (tissue between the internal elastic lamina and external elastic lamina) areas were measured, and neointima/media ratio was calculated. All data are expressed as mean ± SEM.

1.2.3 TUNEL Staining

The 4 % paraformaldehyde-fixed paraffin-embedded sections (5 μm) are deparaffinized and rehydrated. The tissue is permeabilized with 20 mg/ml proteinase K for 30 min. Terminal deoxynucleotidyl transferase enzyme and dUTP conjugated to a fluorescein cocktail are added to the tissue sections according to the manufacturer's specifications (Roche Molecular Biochemicals, in situ death detection kit). Nuclei are counterstained with Hoechst 33258 (Sigma, St. Louis, MO) and mounted with VECTASHIELD mounting media (Vector Laboratories, Inc., Burlingame, CA). Specimens are examined and photographed on a PROVIS AX80 microscope (Olympus, Tokyo) equipped with an epifluorescence optical lens. Pictures are recorded on a CCD camera.

1.2.4 Transmission Electron Microscopy

The femoral artery is excised at 2 h after the injury and fixed in 2.5 % glutaraldehyde, 4 % paraformaldehyde, and 0.1 mol/L sodium cacodylate. Sections are postfixed in 1 % osmium tetroxide, dehydrated, stained en bloc with 3 % uranyl acetate and Sato lead stain, and embedded in epoxy resin (Epon 812). Thin sections are examined with a Hitachi H-7000 electron microscope.

1.2.5 Scanning Electron Microscopy

The injured arteries are opened longitudinally, washed, and fixed in 2 % paraformaldehyde and 2.5 % glutaraldehyde in PBS. The tissue is postfixed in 2 % OsO4 in PBS for 2 h, followed by 1 h in 1 % thiocarbohydrazide and finally again in 2 % aqueous OsO4 for 2 h, all at room temperature. The tissue is next dehydrated in ethanol, critical point dried with CO_2, and sputter coated with a 20–30 nm layer of platinum palladium (E-1010, Hitachi). The sample is then examined with a scanning electron microscope (S-3500 N, Hitachi).

1.2.6 Immunohistochemistry

Paraffin-embedded sections (5 μm thick) are deparaffinized and blocked with 5 % goat serum and 0.01 % Triton-X in PBS for 1 h at room temperature. Distributions of endothelial cells, T lymphocytes, polymorphonuclear cells, and macrophages are revealed by anti-mouse CD31 rat monoclonal antibody (clone MEC13.3, Pharmingen, San Diego, CA), anti-CD3 rabbit polyclonal antibody (Sigma,

St. Luis, MO), anti-mouse CD11b rat monoclonal antibody (clone M1/70, Serotec, Oxford, England), and anti-mouse F4/80 rat monoclonal antibody (clone A3-1, Serotec, Oxford, England), respectively, followed by the avidin-biotin complex technique and Vector Red substrate (Vector Laboratories, Burlingame, CA). Smooth muscle cells can be identified by immunostaining with an alkaline phosphatase-conjugated monoclonal antibody to α-smooth muscle actin (clone 1A4, Sigma). Sections were counterstained with hematoxylin.

1.3 Typical Histological Changes of the Injured Artery

1.3.1 A Wire Can Be Inserted into the Mouse Femoral Artery

A straight spring wire (0.38 mm in diameter) is readily inserted into the femoral artery via an arterioctomy in a small muscular branch between the rectus femoris and vastus intermedius muscles, following the protocol described in Methods (Fig. 1.1, the tutorial videos 1.1 and 1.2). The success rate of the wire insertion is more than 95 % for all mice examined at age of 6 weeks or older. The wire is left in place for one minute to denude and dilate the artery (wire/artery diameter ratio $= 2.0 \pm 0.1$). The muscular branch is ligated, and blood flow of the femoral artery is restored. I observed neither extravasation of the wire nor rupture of the femoral artery. All mice can survive the surgery.

1.3.2 Mouse Femoral Artery Is Mechanically Distended by Intraluminal Insertion of a Large Wire

The wire insertion caused overexpansion of the artery. The media was markedly thinned and the lumen remained enlarged even after the wire was removed (Fig. 1.1g, h, Table 1.1). Anti-CD31 immunostaining revealed that the endothelium was completely denuded (Fig. 1.1g, h). We occasionally (about 6 %) observed acute thrombosis in the injured arteries. The occluded arteries were not used for the analysis.

1.3.3 The Artery Remained Dilated with Rapid Onset of Medial Cell Apoptosis

The TUNEL procedure stains nuclei that contain nicked DNA, a characteristic exhibited by cells in the early stages of apoptotic cell death. Immunofluorescent TUNEL analysis was performed on sections from uninjured and injured mouse

Table 1.1 Morphometric changes in the injured artery

Time point	uninjured	1D	3D	1 W	2 W	3 W	4 W	8 W
EEL (mm)	0.59 ± 0.02	0.91 ± 0.08	1.16 ± 0.08	0.81 ± 0.12	1.37 ± 0.20	1.11 ± 0.07	0.84 ± 0.06	0.98 ± 0.15
I/M ratio	0	0	0	0.31 ± 0.17	1.25 ± 0.27	1.51 ± 0.36	1.97 ± 0.32	1.69 ± 0.37

Reproduced from Ref. [17] with permission
Femoral arteries of C57BL/6 J mice were injured, perfusion fixed, and harvested at the time points indicated ($n = 5$ for each group). Morphometric analysis was performed on the digitized cross-sectional images of the arteries.
EEL circumference of the external elastic lamina, *I/M ratio* ratio of intima area/media area

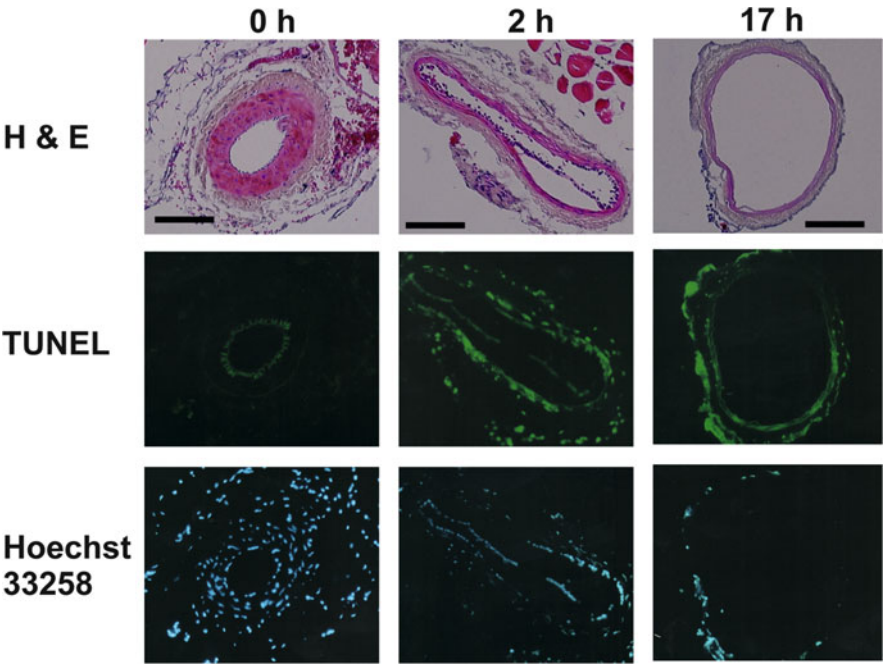

Fig. 1.2 The injury induces dilatation of the artery with rapid onset of apoptosis of smooth muscle cells
The injured artery was perfusion fixed with 4 % paraformaldehyde and excised carefully at the time points indicated. Paraffin-embedded cross sections (5 μm) were stained with hematoxylin and eosin (H & E), TUNEL, and Hoechst 33258. Bar indicates 100 μm (Reproduced from Ref. [17] with permission)

femoral arteries. Uninjured arteries had no detectable TUNEL-positive nuclei. However, a large number of TUNEL-positive nuclei were detected in the layers of the media at two hours after injury (Fig. 1.2). At 8 h after injury, a higher level of TUNEL-positive nuclei was detected. At 17 h, the cellularity of the media appeared to decline dramatically and a few TUNEL-positive cells were detected in the media.

1.3.4 Electron Microscopic Observation of the Injured Artery

Ultrastructure was also examined by transmission and scanning electron microscopes. In uninjured arteries, the endothelium lined at the luminal side of the internal elastic lamina (Fig. 1.3a, b). At two hours after injury, the artery remained dilated with a thin media containing very few cells. Fibrin deposition and platelet accumulation were observed on the denuded luminal side (Fig. 1.3a–c). At 6 days, leukocytes including monocytes and lymphocytes homed at the luminal side (Fig. 1.3d). At 14 days, neointimal hyperplasia of SMC-like cells was observed

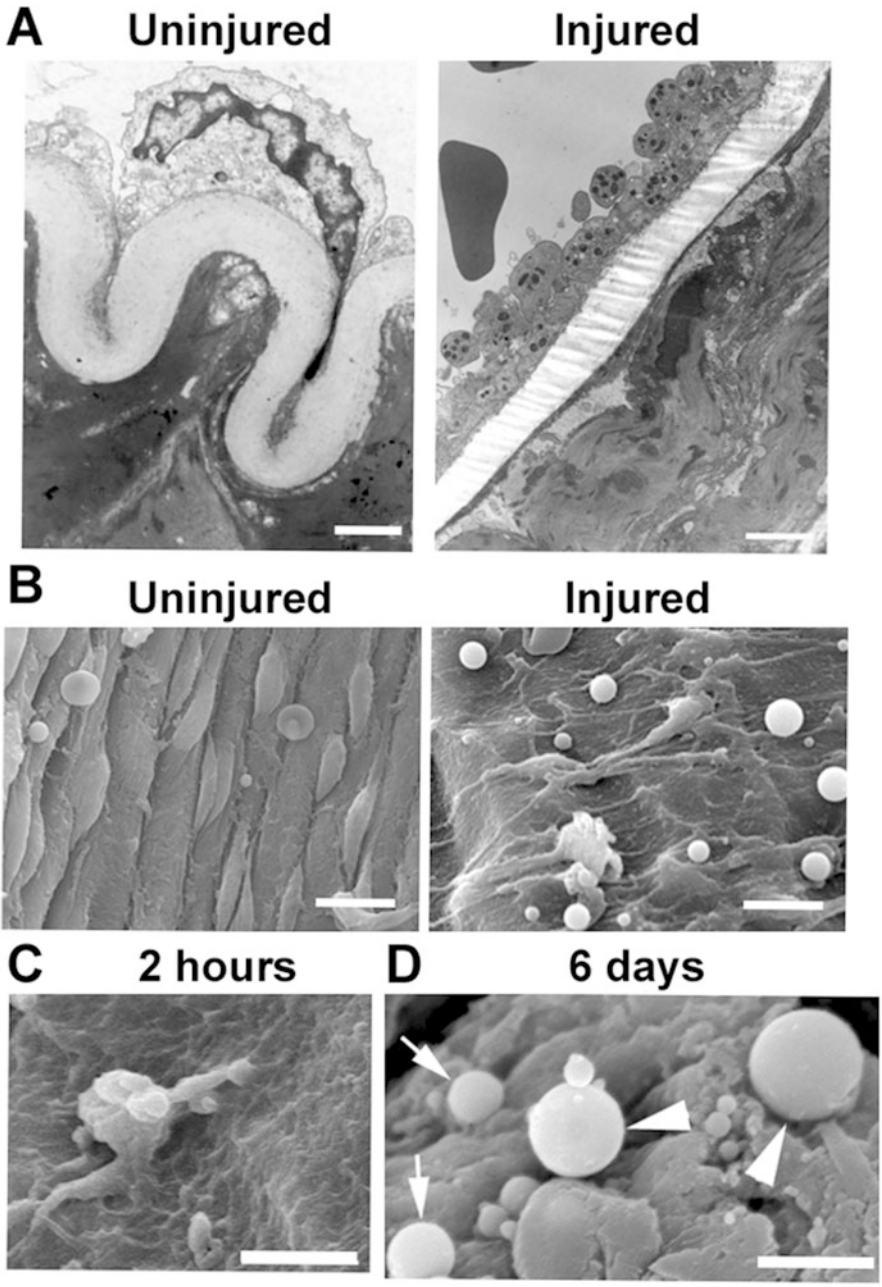

Fig. 1.3 Electron microscopic observation of femoral artery after wire-mediated endovascular injury

(**a**) At 2 h after surgery, the injured and uninjured arteries were perfusion fixed with 2.5 % glutaraldehyde and 2 % paraformaldehyde in PBS. The arteries were postfixed in 1 % osmium tetroxide and embedded in epoxy resin (Epon 812). Thin sections were stained with 3 % uranyl acetate and examined under a transmission electron microscope (H-7000, Hitachi, Tokyo). Bar,

(data not shown). Scanning electron microscope demonstrated that luminal side was partially re-endothelialized. As far as we examined, it was not observed that smooth muscle cells were migrating from the media into the luminal side across the internal elastic lamina.

1.3.5 The Enlarged Lumen Was Narrowed by Neointimal Hyperplasia Composed of Smooth Muscle Cells

The lumen of the injured artery remained dilated as determined by the circumference of the external elastic lamina (Table 1.1). Cellular constituents of the arterial wall were evaluated by immunohistochemistry. At one week, small neointima was found on the luminal side of the injured artery (Fig. 1.4a). Most of the neointimal cells expressed CD45, a marker for hematopoietic cells, but not α-SMA (Fig. 1.4b). At three weeks, large neointima had grown on the luminal side. A few CD45-positive cells were detected, particularly in the luminal side of the neointima. There were some α-SMA-positive cells (Fig. 1.4b). At six weeks, CD45-positive cells were seldom detected in neointima or in media, whereas the neointima was predominantly composed of α-SMA-positive cells. Cellular constituents of the arterial wall after wire-mediated injury were also examined by RT-PCR using RNA obtained from total homogenate of the vessel wall (Fig. 1.4c). Marked downregulation of α-smooth muscle actin (α-SMA) expression was observed at one week. α-SMA expression gradually increased at two weeks and reached to that of uninjured artery at 4 and 6 weeks.

1.3.6 The Injury Can Induce Reproducible Neointimal Hyperplasia that Is Composed of Smooth Muscle Cells

The neointimal hyperplasia continued to grow up to 3 or 4 weeks after which lesion formation did not advance further. The lesion was concentric and very homogenous in the region where the wire was inserted (Fig. 1.5a). An immunohistochemical

---

Fig. 1.3 (continued) 2 μm. (**b–d**) Mice were sacrificed at 2 h and 6 days after injury. The excised arteries were opened longitudinally and fixed in 2 % paraformaldehyde and 2.5 % glutaraldehyde in PBS. The tissue was postfixed in 2 % OsO_4, dehydrated in ethanol, critical point dried with CO_2, and sputter coated with a 20–30 nm layer of platinum palladium (E-1010, Hitachi). (**b**) The luminal side of uninjured and injured arteries was examined at 2 h with a scanning electron microscope (S-3500 N, Hitachi). Bar, 2 μm. (**c**) Platelets adhering to the luminal surface of the injured artery at 2 h. Bar, 6 μm. (**d**) Monocytes or granulocytes (*arrowheads*) were homing on the luminal side at 6 days after injury. Lymphocytes also adhered on the injured artery (*arrows*). Bar, 6 μm (Reproduced from Ref. [47] with permission)

Table 1.2 Representative studies in which this endovascular injury was used

Author	Year	Journal	Theme	Genetically modified mice
Sata et al. [18]	2001	Arterioscler Thromb Vasc Biol.	Apoptosis	lpr (Fas deficient), gld (FasL deficient)
Sata et al. [19]	2002	Nat Med.	Origin of neointimal cells	GFP-Tg, ROSA26
Sata et al. [20]	2002	Arterioscler Thromb Vasc Biol.	Drug effect	p21-KO
Konishi et al. [33]	2002	Circulation	Platelet activation	FcRgamm-KO
Matsuda et al. [32]	2002	J Biol Chem.	Adipocytokine	Adiponectin-KO
Sata et al. [21]	2003	Arterioscler Thromb Vasc Biol.	Cell cycle	p53-KO
Tanaka et al. [22]	2003	Circ Res.	Origin of neointimal cells	GFP-Tg, ROSA26
Shoji et al. [47]	2004	Cardiovasc Pathol.	Origin of neointimal cells	GFP-Tg, ROSA26
Wang et al. [31]	2004	Circulation	Drug effect	eYFP-Tg
Sahara et al. [48]	2005	Stem Cells.	Origin of neointimal cells	GFP-Tg
Fukuda et al. [24]	2005	Circulation	Drug effect	LacZ, GFP-Tg
Komatsu et al. [29]	2005	Nat Med	Small GTPase	R-Ras KO
Konishi et al. [28]	2007	J Am Coll Cardiol.	Nitric oxide synthase	Dimethylarginine dimethylaminohydrolase-Tg
Aihara et al. [27]	2007	J Clin Invest.	Coagulation	Heparin cofactor II-KO
Tanaka et al. [23]	2008	Faseb J.	Origin of neointimal cells.	GFP-Tg
Hirata et al. [30]	2013	Atherosclerosis	HMGB-1	TLR9-KO

KO knockout mouse, *Tg* transgenic mouse

study of α-smooth muscle actin revealed that the neointima was exclusively composed of smooth muscle cells (Fig. 1.5b). The luminal side of the intima was almost completely re-endothelialized at 4 weeks as determined by anti-mouse CD31 staining. No capillary formation was detected in the intima, excluding the possibility that neointimal formation results from recanalized thrombosis. Macrophages were detected in the adventitia, occasionally also in the intima. No polymorphonuclear cells were detected in the intima (data not shown).

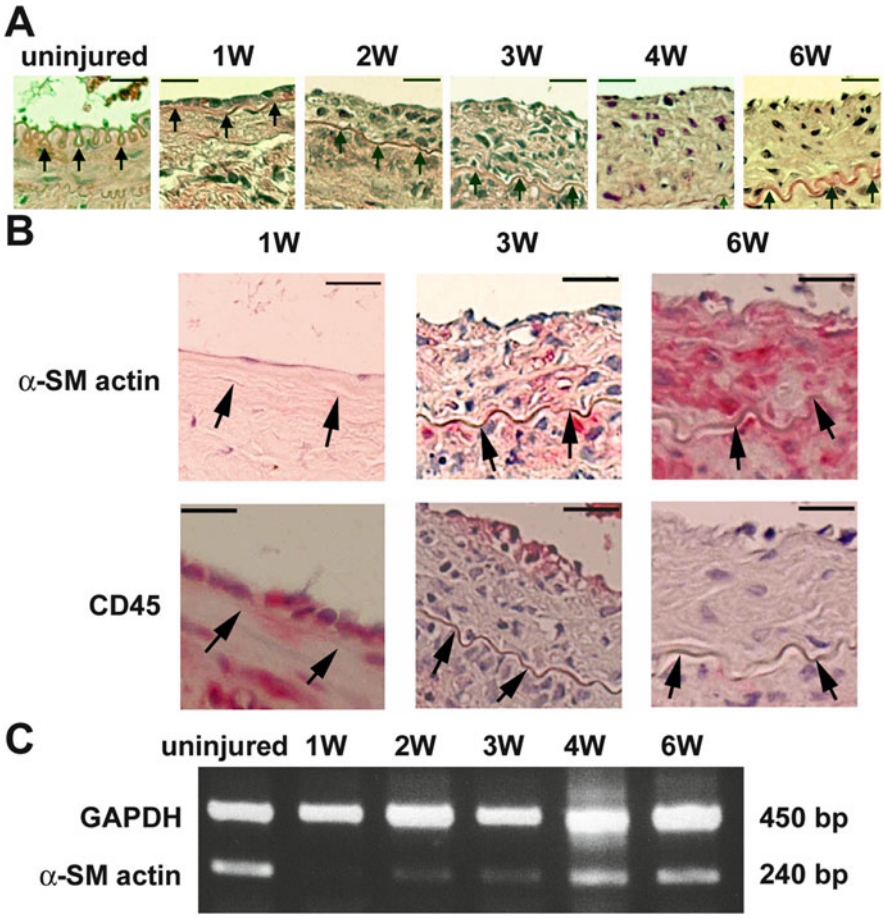

Fig. 1.4 Temporal and spatial characterization of cellular constituents during neointima hyperplasia development

A large wire was inserted into the femoral artery of adult male wild-type mice. After injury, blood flow was restored and the injured arteries were harvested at the time points indicated. (**a**) Injured arteries were embedded in paraffin and stained with hematoxylin and eosin. Arrows indicate internal elastic lamina. Bar, 20 μm. (**b**) Cross sections were stained for α-smooth muscle actin (α-SMA) or CD45.using the avidin-biotin complex technique and VECTOR RED substrate. Arrows indicate internal elastic lamina. Bar, 20 μm. (**c**) Total RNA was prepared from the femoral artery with the use of RNazol reagent. RT-PCR was performed (Reproduced from Ref. [47] with permission)

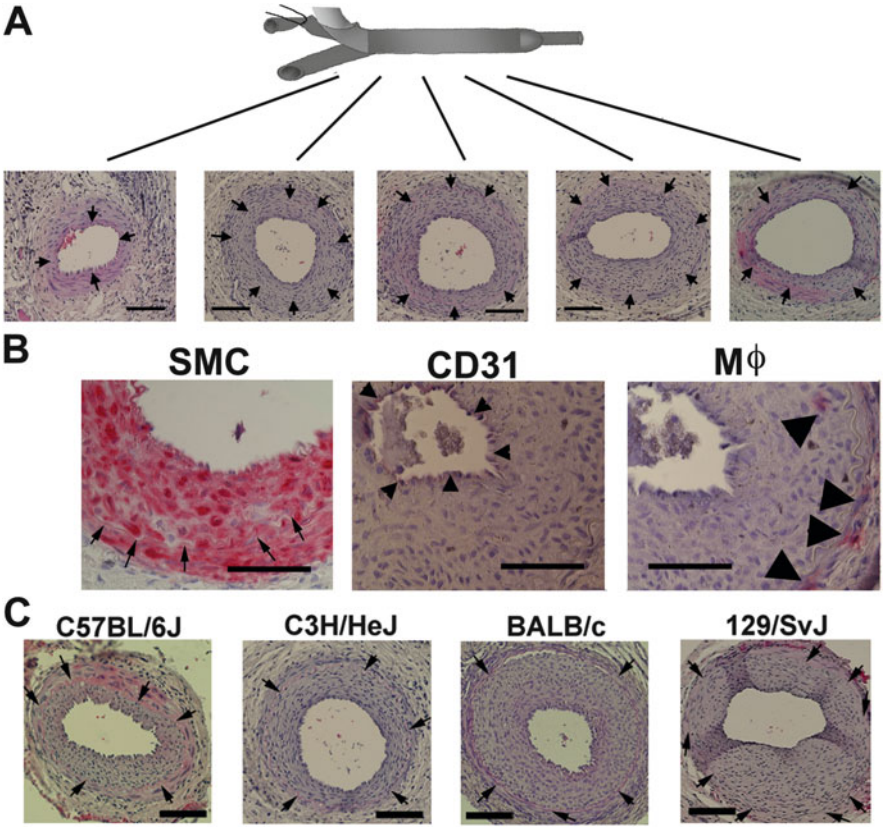

Fig. 1.5 Characterization of the neointimal hyperplasia
(**a**) Three-dimensional characterization of the neointima. The injured femoral artery of the C57BL/6 mouse was perfusion fixed at 4 weeks after the injury. Paraffin-embedded femoral artery was sectioned every 500 μm as indicated. Sections were deparaffinized and stained with hematoxylin and eosin. The lesion formation was homogenous in the region where the wire expanded the artery. Bar, 100 μm. Arrows indicate internal elastic lamina. (**b**) The paraffin-embedded cross sections were stained for smooth muscle cells (SMC, α-smooth muscle actin), endothelial cells (CD31), and macrophages (MΦ, F4/80) using the avidin-biotin complex technique and VECTOR RED as substrate. Sections were counterstained with hematoxylin. The neointima was exclusively composed of smooth muscle cells. Arrows indicate internal elastic lamina. The luminal side was almost completely re-endothelialized (*small arrow heads*). Macrophages were detected in the adventitia, occasionally also in the neointima (*large arrows*), but not in the intima or in the media. Bar 50 μm. (**c**) The femoral artery of the inbred mice was injured by the wire and harvested at 4 weeks. The wire injury produced similar exuberant neointimal formation in all inbred mice. Bar, 100 μm. *Arrows* indicate internal elastic lamina (Reproduced from Ref. [17] with permission)

1.3.7 The Injury Can Induce Neointimal Hyperplasia in All Strains Examined

Although another model of mechanical injury is reported to be significantly influenced by the genetic background of the mouse, as C57Bl/6 mice appear to be less responsive than mice with a mixed genetic background of C57Bl/6 and 129 [35], our method induced reproducible neointimal hyperplasia in all inbred mice with different backgrounds ($n = 5$ for each group, intima/media ratio: C57BL6/J, 2.0 ± 0.4; BALB/c, 2.0 ± 0.3; C3H/HeJ, 2.3 ± 0.3; 129/SvJ, 2.6 ± 0.3) (Fig. 1.5c).

1.4 Discussion

In this chapter, we described an endovascular dilatation injury model of the mouse artery. Mechanical expansion of the femoral artery resulted in rapid onset of apoptosis of medial smooth muscle cells and enlargement of the artery. The dilated lumen was gradually narrowed by neointimal hyperplasia exclusively composed of smooth muscle cells.

Although much effort has been devoted to utilize genetically modified mice for a better understanding of the mechanism of post-PCI restenosis [3], there is no balloon which can be inserted into minute mouse arteries. Alternatively, several models of vascular injury have been reported to produce significant neointimal hyperplasia [35], and perivascular approaches have often been used to avoid technical difficulties of transluminal injury [11–13, 15, 16].

Carmeliet et al. reported that in their initial experience, the genetic background of the mouse significantly influenced lesion formation by this method since C57BL/6 mice appeared to be less responsive than mice with a mixed genetic background of C57BL/6 and 129/SV [35]. Mendelsohn and his colleagues also reported that this injury resulted in only thickening of the media in inbred mice with a C57BL/6 background [36–38]. Thus, the relatively small proliferative response and the technical challenge to achieve complete denudation limited the use of this model.

It was reported that dilatation and denudation of mouse carotid artery by insertion of a polyethylene tube (PE10, tube/artery ratio $= 1.2 \pm 0.09$) resulted in neointimal formation in mice with a mixed background of C57BL/6 and CBA [39]. We made effort to reproduce the results using the same method. We were also able to achieve neointimal formation in the carotid artery (M. Sata, unpublished observation). However, we found that the lesion produced by this tube insertion was less extensive and less reproducible than those induced by our method, at least in inbred mice (BALB/c, C57BL/6 J, and C3H/HeJ). Moreover, in our hands, the procedure was associated with frequent extravasation of the tube and a high incidence of postsurgery mortality (M. Sata, unpublished observation).

While we were developing this model, it was reported that insertion of a 0.010 in. wire (0.254 mm in diameter) into the femoral artery can cause endothelial

denudation, rapid accumulation of neutrophils, and neointimal hyperplasia [40]. In this report, the authors performed an arteriotomy in the femoral artery distal to the epigastric branch. Subsequently, the femoral artery was ligated proximal to the arteriotomy site, interrupting blood flow to the distal femoral artery. Thus, the blood flow of the injured artery was only partially restored by blood supply to the epigastric branch. Therefore, it seems plausible that neointimal hyperplasia results only from restriction of the blood flow as reported for vascular remodeling of uninjured carotid artery after ligation of the distal portion [12]. On the other hand, in our model, we tied off the small muscular branch where the arterioctomy was performed and observed no decrease in blood flow to the hind limb as determined by laser Doppler perfusion imaging [7] (Moor Instruments Limited, Devon, England). Thus, we could exclude the effect of flow restriction on neointimal formation produced by our model.

One great advantage of our model comes from evidence of the rapid onset of medial smooth muscle cell apoptosis as reported for balloon injuries in other animals [41–43]. This model will enable us to analyze various mice in which apoptosis-regulating genes are modified to clarify the role of apoptosis in post-angioplasty restenosis [44–46].

Insertion of the guide wire into the femoral artery appears to be technically challenging. However, the muscular branch described here is large enough for arterioctomy, and the straight wire can be inserted easily following the procedure described here in detail. Most experienced animal researchers, particularly those who are familiar with balloon injury of the rat carotid artery [10], should be able to produce this model routinely after several rounds of practice. Actually, since we published the original methodological paper in 2000 [17], this model has been successfully adopted in many laboratories to analyze genetically modified mice in studies on the pathophysiology of post-PCI restenosis, leading to more than 200 publications by us [19–26] and others [27–34] (Table 1.2). We hope that this model will be used in more and more laboratories to find therapeutic strategy for post-PCI restenosis.

In conclusion, we described our mouse model of vascular injury that could induce rapid onset of apoptosis and smooth muscle cell hyperplasia in response to transluminal mechanical injury in the mouse artery. This model should be wildly used for a genetic understanding of the molecular pathways of post-PCI restenosis.

Acknowledgements This work was partially supported by JSPS Kakenhi Grants (Number 24659392, 22390159, 25670390, and 25293184 to M. Sata), MEXT KAKENHI Grant Number 21117007 (M. Sata). We are grateful to E. Uematsu, Y. Saga (Tokushima Univ.), H. Kato, Y. Sugawara, Y. Maejima, M. Kinoshita, T. Hasegawa, I. Shirakawa, M. Washida, Y. Kaneda, H. Yashiro, and F. Adachi (Tokyo Univ.) for their expert technical assistance. I also thank Mr. Satoru Fukuda for his help in the electron microscopic study.

References

1. Minha S, Pichard AD, Waksman R. In-stent restenosis of drug-eluting stents. Future Cardiol. 2013;9(5):721–31. doi:10.2217/fca.13.45.
2. Nakatani S, Onuma Y, Ishibashi Y, Muramatsu T, Iqbal J, Zhang YJ, et al. Early (before 6 months), late (6–12 months) and very late (after 12 months) angiographic scaffold restenosis in the ABSORB Cohort B trial. EuroIntervention. 2014;10:1288–98. doi:10.4244/EIJV10I11A218.
3. Faraci FM, Sigmund CD. Vascular biology in genetically altered mice. Smaller vessels, bigger insight. Circ Res. 1999;85:1214–25.
4. Ishibashi S, Brown MS, Goldstein JL, Gerard RD, Hammer RE, Herz J. Hypercholesterolemia in low density lipoprotein receptor knockout mice and its reversal by adenovirus-mediated gene delivery. J Clin Invest. 1993;92(2):883–93.
5. Plump AS, Smith JD, Hayek T, Aalto-Setala K, Walsh A, Verstuyft JG, et al. Severe hypercholesterolemia and atherosclerosis in apolipoprotein E-deficient mice created by homologous recombination in ES cells. Cell. 1992;71(2):343–53.
6. Nagano H, Mitchell RN, Taylor MK, Hasegawa S, Tilney NL, Libby P. Interferon-gamma deficiency prevents coronary arteriosclerosis but not myocardial rejection in transplanted mouse hearts. J Clin Invest. 1997;100:550–7.
7. Couffinhal T, Silver M, Zheng LP, Kearney M, Witzenbichler B, Isner JM. Mouse model of angiogenesis. Am J Pathol. 1998;152(6):1667–79.
8. Ohno T, Gordon D, San H, Pompili VJ, Imperiale MJ, Nabel GJ, et al. Gene therapy for vascular smooth muscle cell proliferation after arterial injury. Science. 1994;265:781–4.
9. Maillard L, Van Belle E, Smith RC, Le Roux A, Denéfle P, Steg G, et al. Percutaneous delivery of the gax gene inhibits vessel stenosis in a rabbit model of balloon angioplasty. Cardiovasc Res. 1997;35:536–46.
10. Clowes AW, Reidy MA, Clowes MM. Kinetics of cellular proliferation after arterial injury. I. Smooth muscle growth in the absence of endothelium. Lab Invest. 1983;49(3):327–33.
11. Carmeliet P, Moons L, Stassen J-M, Mol MD, Bouche A, van den Oord JJ, et al. Vascular wound healing and neointima formation induced by perivascular electric injury in mice. Am J Pathol. 1997;150:761–76.
12. Kumar A, Lindner V. Remodeling with neointima formation in the mouse carotid artery after cessation of blood flow. Arterioscler Thromb Vasc Biol. 1997;17:2238–44.
13. Moroi M, Zhang L, Yasuda T, Virmani R, Gold HK, Fishman MC, et al. Interaction of genetic deficiency of endothelial nitric oxide, gender, and pregnancy in vascular response to injury in mice. J Clin Invest. 1998;101:1225–32.
14. Lindner V, Fingerle J, Reidy MA. Mouse model of arterial injury. Circ Res. 1993;73:792–6.
15. Umemura K, Watanabe S, Kondo K, Hashimoto H, Nakashima M. Inhibitory effect of prostaglandin E1 on intimal thickening following photochemically induced endothelial injury in the rat femoral artery. Atherosclerosis. 1997;130:11–6.
16. Simon DI, Chen Z, Seifert P, Edelman ER, Ballantyne CM, Rogers C. Decreased neointimal formation in *MAC-1*−/− mice reveals a role for inflammation in vascular repair after angioplasty. J Clin Invest. 2000;105:293–300.
17. Sata M, Maejima Y, Adachi F, Fukino K, Saiura A, Sugiura S, et al. A mouse model of vascular injury that induces rapid onset of medial cell apoptosis followed by reproducible neointimal hyperplasia. J Mol Cell Cardiol. 2000;32:2097–104.
18. Sata M, Sugiura S, Yoshizumi M, Ouchi Y, Hirata Y, Nagai R. Acute and chronic smooth muscle cell apoptosis after mechanical vascular injury can occur independently of the Fas-death pathway. Arterioscler Thromb Vasc Biol. 2001;21(11):1733–7.
19. Sata M, Saiura A, Kunisato A, Tojo A, Okada S, Tokuhisa T, et al. Hematopoietic stem cells differentiate into vascular cells that participate in the pathogenesis of atherosclerosis. Nat Med. 2002;8(4):403–9.

20. Sata M, Takahashi A, Tanaka K, Washida M, Ishizaka N, Ako J, et al. Mouse genetic evidence that tranilast reduces smooth muscle cell hyperplasia via a p21(WAF1)-dependent pathway. Arterioscler Thromb Vasc Biol. 2002;22(8):1305–9.
21. Sata M, Tanaka K, Ishizaka N, Hirata Y, Nagai R. Absence of p53 leads to accelerated neointimal hyperplasia after vascular injury. Arterioscler Thromb Vasc Biol. 2003;23 (9):1548–52.
22. Tanaka K, Sata M, Hirata Y, Nagai R. Diverse contribution of bone marrow cells to neointimal hyperplasia after mechanical vascular injuries. Circ Res. 2003;93:783–90.
23. Tanaka K, Sata M, Natori T, Kim-Kaneyama JR, Nose K, Shibanuma M, et al. Circulating progenitor cells contribute to neointimal formation in nonirradiated chimeric mice. Faseb J. 2008;22(2):428–36.
24. Fukuda D, Sata M, Tanaka K, Nagai R. Potent inhibitory effect of sirolimus on circulating vascular progenitor cells. Circulation. 2005;111(7):926–31.
25. Takaoka M, Nagata D, Kihara S, Shimomura I, Kimura Y, Tabata Y, et al. Periadventitial adipose tissue plays a critical role in vascular remodeling. Circ Res. 2009;105(9):906–11.
26. Takaoka M, Suzuki H, Shioda S, Sekikawa K, Saito Y, Nagai R, et al. Endovascular injury induces rapid phenotypic changes in perivascular adipose tissue. Arterioscler Thromb Vasc Biol. 2010;30(8):1576–82.
27. Aihara K, Azuma H, Akaike M, Ikeda Y, Sata M, Takamori N, et al. Strain-dependent embryonic lethality and exaggerated vascular remodeling in heparin cofactor II-deficient mice. J Clin Invest. 2007;117(6):1514–26. doi:10.1172/JCI27095.
28. Konishi H, Sydow K, Cooke JP. Dimethylarginine dimethylaminohydrolase promotes endothelial repair after vascular injury. J Am Coll Cardiol. 2007;49(10):1099–105. doi:10.1016/j.jacc.2006.10.068.
29. Komatsu M, Ruoslahti E. R-Ras is a global regulator of vascular regeneration that suppresses intimal hyperplasia and tumor angiogenesis. Nat Med. 2005;11(12):1346–50. doi:10.1038/nm1324.
30. Hirata Y, Kurobe H, Higashida M, Fukuda D, Shimabukuro M, Tanaka K, et al. HMGB1 plays a critical role in vascular inflammation and lesion formation via toll-like receptor 9. Atherosclerosis. 2013;231(2):227–33. doi:10.1016/j.atherosclerosis.2013.09.010.
31. Wang CH, Ciliberti N, Li SH, Szmitko PE, Weisel RD, Fedak PW, et al. Rosiglitazone facilitates angiogenic progenitor cell differentiation toward endothelial lineage: a new paradigm in glitazone pleiotropy. Circulation. 2004;109(11):1392–400. doi:10.1161/01.CIR.0000123231.49594.21.
32. Matsuda M, Shimomura I, Sata M, Arita Y, Nishida M, Maeda N, et al. Role of adiponectin in preventing vascular stenosis. The missing link of adipo-vascular axis. J Biol Chem. 2002;277 (40):37487–91. doi:10.1074/jbc.M206083200.
33. Konishi H, Katoh Y, Takaya N, Kashiwakura Y, Itoh S, Ra C, et al. Platelets activated by collagen through immunoreceptor tyrosine-based activation motif play pivotal role in initiation and generation of neointimal hyperplasia after vascular injury. Circulation. 2002;105 (8):912–6.
34. Takaoka M, Uemura S, Kawata H, Imagawa K, Takeda Y, Nakatani K, et al. Inflammatory response to acute myocardial infarction augments neointimal hyperplasia after vascular injury in a remote artery. Arterioscler Thromb Vasc Biol. 2006;26(9):2083–9.
35. Carmeliet P, Moons L, Collen D. Mouse models of angiogenesis, arterial stenosis, atherosclerosis and hemostasis. Cardiovasc Res. 1998;39:8–33.
36. Karas RH, Hodgin JB, Kwoun M, Krege JH, Aronovitz M, Mackey W, et al. Estrogen inhibits the vascular injury response in estrogen receptor β-deficient female mice. Proc Natl Acad Sci U S A. 1999;96:15133–6.
37. Iafrati MD, Karas RH, Aronovitz M, Kim S, Sullivan TRJ, Lubahn DB, et al. Estrogen inhibits the vascular injury response in estrogen receptor alpha-deficient mice. Nat Med. 1997;3:545–8.

38. Sullivan TR, Karas RH, Aronovitz M, Faller GT, Ziar JP, Smith JJ, et al. Estrogen inhibits the response-to-injury in a mouse carotid artery model. J Clin Invest. 1995;96:2482–8.
39. Harada K, Komuro I, Sugaya T, Murakami K, Yazaki Y. Vascular injury causes neointimal formation in angiotensin II type 1a receptor knockout mice. Circ Res. 1999;84(2):179–85.
40. Roque M, Fallon JT, Badimon JJ, Zhang WX, Taubman MB, Reis ED. Mouse model of femoral artery denudation injury associated with the rapid accumulation of adhesion molecules on the luminal surface and recruitment of neutrophils. Arterioscler Thromb Vasc Biol. 2000;20:335–42.
41. Pollman MJ, Hall JL, Gibbons GH. Determinants of vascular smooth muscle cell apoptosis after balloon angioplasty injury. Circ Res. 1999;84:113–21.
42. Perlman H, Maillard L, Krasinski K, Walsh K. Evidence for the rapid onset of apoptosis in medial smooth muscle cells after balloon injury. Circulation. 1997;95(4):981–7.
43. Rivard A, Luo Z, Perlman H, Fabre J, Nguyen T, Walsh K. Early cell loss following angioplasty results in a disproportionate decrease in gene transfer to the vessel wall. Hum Gene Ther. 1999;10:711–21.
44. Han DKM, Haudenschild CC, Hong MK, Tinkle BT, Leon MB, Liau G. Evidence for apoptosis in human atherogenesis and in a rat vascular injury model. Am J Pathol. 1995;147:267–77.
45. Isner JM, Kearney M, Bortman S, Passeri J. Apoptosis in human atherosclerosis and restenosis. Circulation. 1995;91:2703–11.
46. Walsh K, Isner JM. Apoptosis in inflammatory-fibroproliferative disorders of the vessel wall. Cardiovasc Res. 2000;45:756–65.
47. Shoji M, Sata M, Fukuda D, Tanaka K, Sato T, Iso Y, et al. Temporal and spatial characterization of cellular constituents during neointimal hyperplasia after vascular injury: Potential contribution of bone-marrow-derived progenitors to arterial remodeling. Cardiovasc Pathol. 2004;13(6):306–12.
48. Sahara M, Sata M, Matsuzaki Y, Tanaka K, Morita T, Hirata Y, et al. Comparison of various bone marrow fractions in the ability to participate in vascular remodeling after mechanical injury. Stem Cells. 2005;23(7):874–8.

Chapter 2
Cuff-Induced Neointimal Formation in Mouse Models

Tetsuya Kubota and Naoto Kubota

Abstract Ischemic heart failure caused by atherosclerosis is a major cause of death worldwide. Although remarkable technological advances have been made in the treatment of coronary heart disease, there is as yet no treatment that can sufficiently suppress the progression of atherosclerosis, including neointimal thickening. Therefore, a precise understanding of the mechanism of neointimal hyperplasia will provide the development of new technologies. Both ApoE-KO and LDLR-KO mice have been employed to generate other relevant mouse models of cardiovascular disease through breeding strategies. Although these mice are effective tools for the investigation of atherosclerosis, development of a progressive atherosclerotic lesion takes a long time, resulting in increase of both the costs and the space needed for the research. Thus, it is necessary to develop simpler tools that would allow easy evaluation of atherosclerosis in mouse models. In this review, we discuss our experience in generating mouse models of cuff-induced injury of the femoral artery and attempt to provide a better understanding of cuff-induced neointimal formation.

Keywords Cuff placement • Mice • Polyethylene tube

T. Kubota
Laboratory for Metabolic Homeostasis, RIKEN Center for Integrative Medical Science, Yokohama, Kanagawa 230-0045, Japan

Department of Diabetes and Metabolic Diseases, Graduate School of Medicine, University of Tokyo, 7-3-1 Hongo, Bunkyo-ku, Tokyo 113-8655, Japan

Clinical Nutrition Program, National Institute of Health and Nutrition, Tokyo 162-8636, Japan

N. Kubota, M.D., Ph.D. (✉)
Laboratory for Metabolic Homeostasis, RIKEN Center for Integrative Medical Science, Yokohama, Kanagawa 230-0045, Japan

Department of Diabetes and Metabolic Diseases, Graduate School of Medicine, University of Tokyo, 7-3-1 Hongo, Bunkyo-ku, Tokyo 113-8655, Japan

Clinical Nutrition Program, National Institute of Health and Nutrition, Tokyo 162-8636, Japan

Department of Clinical Nutrition Therapy, University of Tokyo, Tokyo 113-8655, Japan
e-mail: nkubota-tky@umin.ac.jp

M. Sata (ed.), *Mouse Models of Vascular Diseases*,
DOI 10.1007/978-4-431-55813-2_2

2.1 Introduction

Epidemiological studies reveal that coronary heart diseases caused by atherosclerosis, including myocardial infarction and other forms of ischemic heart disease, are major causes of death worldwide [1]. If coronary blood flow is impaired by the development of atherosclerosis, interventions such as balloon angioplasty and endovascular stent placement are employed to overcome the vascular occlusion. These interventions can produce mechanical damage to the vasculature, including endothelial cells, smooth muscle cells (SMCs), and the adventitia [2–4]. Destruction of the endothelial cell layer is observed in the early phase after these interventions, with the formation of a thin thrombus layer covering the vascular surface [5]. Within several weeks, the vascular endothelial cells completely cover the neointima. Endothelial injury causes recruitment and adherence of circulating leucocytes, which results in the progression of neointimal formation [6]. The extent of neointimal formation has been reported to be correlated with the number of macrophages in the neointima [7]. Macrophages and neutrophils enhance the inflammatory response through the release of growth factors such as fibroblast growth factor (FGF), transforming growth factor-beta (TGF-β), platelet-derived growth factor (PDGF), and vascular endothelial growth factor (VEGF) [5]. Human studies have shown the existence of a correlation between chronic inflammation after stent placement and intimal thickening [7]. The release of the aforementioned growth factors and cytokines by the injured endothelium and infiltrating inflammatory cells leads to SMC migration and proliferation, which is preceded by transition of the SMCs from a contractile to a synthetic phenotype with excessive extracellular matrix (ECM) deposition in the intima [8, 9]. Although remarkable technological advances have been made in the treatment of coronary heart disease, none of the available treatments up to date can sufficiently suppress atherosclerosis or entirely prevent restenosis after angioplasty [10–12]. Although in-stent restenosis can be alleviated by the use of drug-eluting stents, a number of cases treated with drug-eluting stents are still reported to develop restenosis [13, 14]. There also remains the question of the safety of drug-eluting stents, including in relation to the higher frequency of occurrence of thrombotic events observed with the use of drug-eluting stents as compared to bare-metal stents [15, 16]. Moreover, cases with neointimal hyperplasia occurring after bypass surgery or allograft cardiac transplantation cannot be treated with drug-eluting stents [17, 18]. Thus, a more precise understanding of the mechanism of neointimal hyperplasia will provide the development of new technologies. In this review, we discuss our experience in generating mouse models of cuff-induced injury of the femoral artery and attempt to provide a better understanding of cuff-induced neointimal formation.

2.2 Rabbit Models of Cuff-Induced Injury

Many previous studies have reported rabbit models of cuff-induced injury. Two types of materials have been used for the generation of these rabbit models, a polyethylene tube and a silastic tube. In 1969, Mizukawa et al. have reported neointimal formation induced by the insertion of a polyethylene tube in the rabbit carotid artery [19]. Histological analysis revealed that the neointima was composed of SMCs, but had no other characteristics of atherosclerosis, e.g., foam cells [20–22]. Importantly, the polyethylene tube produced only mild, not severe, injury of the endothelial cells. Hirosumi et al. carried out an in-depth investigation of the morphometric changes induced in an artery by the insertion of a polyethylene tube by scanning electron microscopy and light microscopy (1.5 cm long PE-280; inner diameter, 2.15 mm; outer diameter, 3.25 mm; Becton, Dickinson and Company) [23]. At 30 min after cuff placement, small endothelial defects and adherence of a small number of platelets were observed in the subendothelium. At 2 h, a number of leukocytes were recruited to this cuff-injured area. The endothelial defects increased for 24 h, and leukocytic infiltration of the internal elastic lamina and endothelial cells was observed. After the 3rd day, regeneration of spindle-shaped endothelial cells occurred and covered the exposed subendothelium. However, the leukocytic infiltration persisted. The internal elastic laminae were irregular, swollen, and wavy. The SMCs under these laminae were markedly deformed and edematous. Although the endothelial cells became flat after 1 week, gaps were often observed at the cell junctions. Light microscopy revealed regression of the edematous media and SMC-like intimal cell proliferation. After 2 weeks, the endothelial cells completely covered the subendothelium, and the gaps between the cells acquired normal tightness. Leukocytes were no longer seen at the endothelial surface. On the other hand, Booth et al. were the first to use a biologically inert soft and flexible Silastic cuff, 2.1 cm length with an internal volume of 0.3 cm^3 in the carotid artery of a New Zealand White male rabbit [24]. Neointimal formation consisted largely of SMC-like cells, similar to the case in the polyethylene cuff-induced injury. No foam cells were detected in any of the sections obtained from the carotid arteries of the New Zealand White rabbits at 7 days after the placement of the Silastic cuff. Moreover, an intact endothelial layer was observed after 7 days. The endothelial cells remained in contact with each other, and no denudation or exposure of the subendothelium was seen at 24 h after placement of the silastic cuff [25]. Kockx et al. revealed that silicone cuff-induced neointimal formation can be distinguished into three phases [26]. The first phase begins within 2 h, with polymorphonuclear leukocyte (PMN) infiltration from the luminal surface toward the intima and the inner media. In the second phase, which starts within 12 h, the replication rate of the SMCs in the media increases by about 20-fold as compared with that in unmanipulated arteries. The third phase, beginning from day 3, is characterized by the appearance of subendothelial SMCs that are immunoreactive for α-SM actin (α-SMA). Although the neointima formed in response to both injury caused by a polyethylene and that caused by a silastic cuff consists of SMCs,

the injury caused by the polyethylene cuff was associated with injury of the endothelial cells, whereas that caused by the silastic cuff was devoid of injury to the endothelium.

2.3 Mouse Models of Cuff-Induced Injury

Mouse models have been used popularly as experimental animal models due to their well-defined genetic background and the possibility of manipulating the mouse genome. Mouse models are useful for evaluating the roles of specific molecules in vascular remodeling, such as in the case of post-percutaneous coronary intervention (PCI) restenosis. Apolipoprotein (Apo) E-knockout (KO) mice have been used extensively because they develop spontaneous atherosclerosis [27, 28]. Furthermore, the atherosclerotic lesions in this mouse model closely resemble the atherosclerotic lesions, both stable and unstable, in humans. Low-density lipoprotein (LDL) R-KO mice also serve as good models to evaluate human atherosclerotic lesions [29]. However, unlike the ApoE-KO mice, the LDLR-KO mice do not develop spontaneous atherosclerosis [28]. Both ApoE-KO and LDLR-KO mice have also been utilized to generate other relevant mouse models of cardiovascular disease through a variety of breeding strategies. Although these mice are effective tools for the investigation of atherosclerosis, development of a progressive atherosclerotic lesion takes a long time, resulting in an increase of both the costs and the space for the research. Mouse arteries, unlike the arteries of larger animals, are too small for transluminal injury to be induced with a balloon. Thus, it is necessary to develop tools for easier evaluation of atherosclerosis in mouse models.

Three methods for the induction of neointimal formation in mice have been mainly reported [10]. In the arterial ligation model, blood flow through the common carotid artery is disrupted by ligation near the distal bifurcation [30]. The decrease in the blood flow resulting from the dramatic reduction of the vessel diameter results in the formation of an extensive SMC-rich neointima within 2–4 weeks. This model has the advantage of reproducibility due to the ease of use of the method for inducing neointimal hyperplasia. Lindner and colleagues were the first to report mechanically induced endothelial denudation model, which involves passage of a flexible guidewire three times in the carotid artery [31]. This procedure completely removes the endothelial cell layer, which results in the recruitment of platelets to the denuded surface and activation of the medial SMCs. Neointimal hyperplasia is typically observed within 2 weeks after the injury. This procedure is the most similar to angioplasty. However, this procedure is a relatively challenging procedure, which leads to difficulty in achieving reproducible results. Subsequently, Sata et al. modified the wire injury method to develop a more convenient and reproducible results [32]. Since the wire injury model shows complete denudation of the endothelial cell layer, it may not be suitable for investigation of the involvement of endothelial cell-specific molecules in the development of atherosclerosis. Use of a

polyethylene cuff also causes damage to the endothelial cell layer as described above, but it produces milder injury as compared to wire injury. The endothelium itself is not directly injured by a polyethylene cuff. In fact, endothelial cells have reported to remain relatively intact after perivascular cuff placement [33]. Moroi et al. first adapted an external vascular cuff model used in rabbits to mice deleted with endothelial cell-specific eNOS gene [34]. Since the virus-mediated vector and drug can be injected easily between the cuff and the vessel, this cuff-induced injury model is also excellent for the observation of changes in the adventitia associated with arteriosclerosis [35]. Thus, the use of mouse models of cuff-induced injury has increased in recent years.

2.4 Method for Creation of Cuff-Induced Injury in the Femoral Artery

Dr. Moroi kindly taught us the procedure for the cuff placement [34]. Before the operation, the cuff (Intramedic Polyethylene Tubing (PE-50, inner diameter = 0.58 mm), Becton Dickinson) needs to be prepared. Polyethylene tube was cut for each length 2 mm and cut in longitudinal direction. We tied polyethylene tube directly to 8–0 nylon suture with needle (Bear Medic Corporation) in two places on both side and made stringlike. The mice were anesthetized by an intraperitoneal (IP) injection of sodium pentobarbital at the dose of 40–50 mg/kg. Then, the mice were fixed in the supine position and their skin was shaved from the inguinal region to the medial aspect of the thigh above the knee and disinfected with 70 % ethanol. The skin was next lifted with tweezers under stereomicroscopic observation, and an incision about 7–10 mm length was placed in the inguinal region. The subcutaneous connective tissue was carefully removed to expose both the femoral artery and the femoral vein. The femoral artery is separated from the femoral vein by blunt dissection with micro tweezers. A stringlike nylon suture with polyethylene tube is sent under a separating femoral artery. The break of the polyethylene tube is expanded by pulling stringlike nylon suture of polyethylene tube. The polyethylene tube is placed around the femoral artery. Finally, the surrounding tissue is straightened and the skin is sutured (Fig. 2.1). A sham operation is performed without polyethylene tube placement in the other femoral artery, as control. The mice are anesthetized by IP injection of pentobarbital 14 days after the operation and fix in the supine position. After laparotomy, the diaphragm is incised to expose the heart. Ice-cold 4 % paraformaldehyde is injected into the systemic circulation via the cardiac apex at a pressure of 100 cm H_2O, followed by incision of the right auricular appendage. Both the cuffed-femoral artery and the sham-operated artery of the opposite sides are removed and immersed in OCT compound. For the immunohistochemical staining, 5- to 6-μm-thick sections are prepared from each sample. Paraffin sections are more suitable for the measurement of intimal thickness than frozen sections. Femoral artery samples embedded in

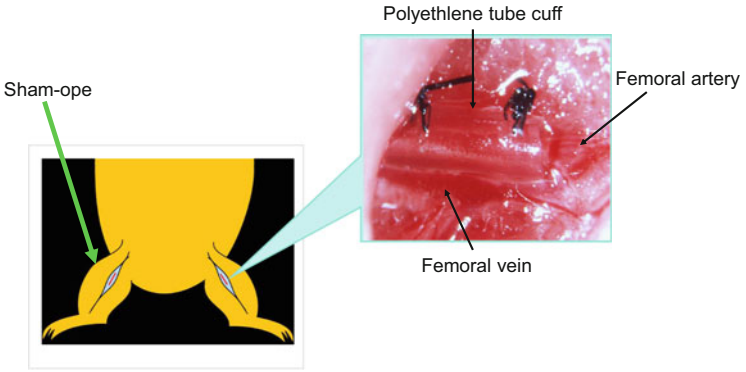

Fig. 2.1 Cuff placement for the femoral artery

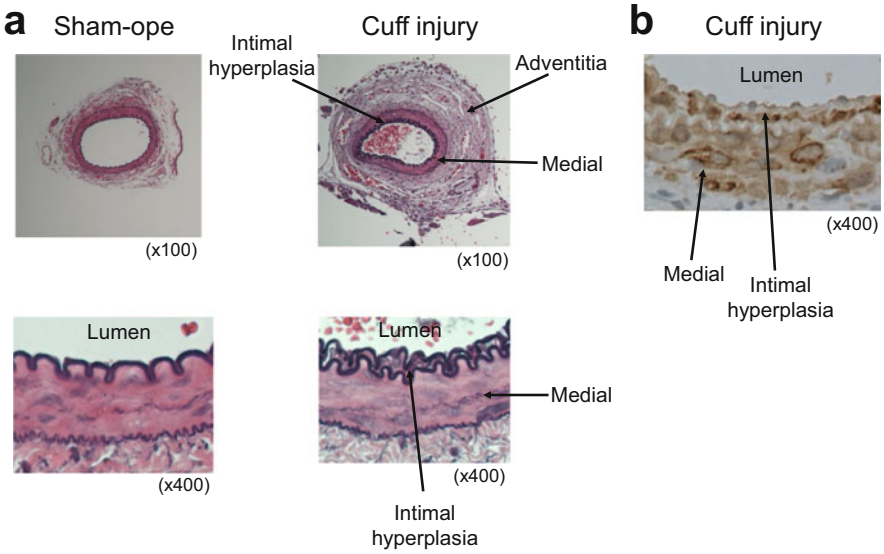

Fig. 2.2 Representative arteries after sham-operated or cuff placement (**a**) and alpha smooth muscle actin staining for cuff-injured artery in C57B6 mice (**b**)

paraffin were cut from one edge to the other edge of the cuffed portion. The areas of the lumen, intima, and media were measured in 10 cross sections using the image analyzer. Images are digitized and captured with a CCD camera connected to a personal computer (Fig. 2.2a). Measurements are performed at a magnification of $\times$200 using the Scion Image analysis software. For each artery, the luminal area, area inside the internal elastic lamina, and the area encircled by the external elastic lamina are measured. The medial area is calculated as the area encircled by the external elastic lamina area inside the internal elastic lamina, and the intimal area is calculated as the area inside the internal elastic lamina-luminal area. To calculate

the medial thickness for each vessel cross section, the linear distance between the internal elastic lamina and external elastic lamina is measured independently in 10 places, separated by 90° each and then averaged. The ratio of the intimal to the medial area and the percent luminal stenosis are calculated based on these measurements [10, 34].

2.5 Etiology of Cuff-Induced Neointimal Formation

Since cuff-induced neointimal formation showed positive staining with an α-SMC antibody (Fig. 2.2b), the neointima appears to be almost entirely composed of SMCs. Neointimal formation induced by cuff placement can be considered as a consequence of migration and/or proliferation of the SMCs induced by some factors such as PDGF-BB or inflammatory cytokines (Fig. 2.3). Although the exact mechanisms underlying the neointimal formation in cuff-induced injury models are still uncertain, I would like to refer to reports from the literature of studies carried out using genetically manipulated mouse models to discuss the mechanisms of neointimal formation (Table 2.1).

2.5.1 Factors Directly Inducing SMC Proliferation and Migration

Cuff replacement around the femoral artery induced neointimal hyperplasia, which was exclusively composed of SMCs, as mentioned above. Platelet-derived growth factor (PDGF)-BB, which is mainly secreted from platelets, is one of the most

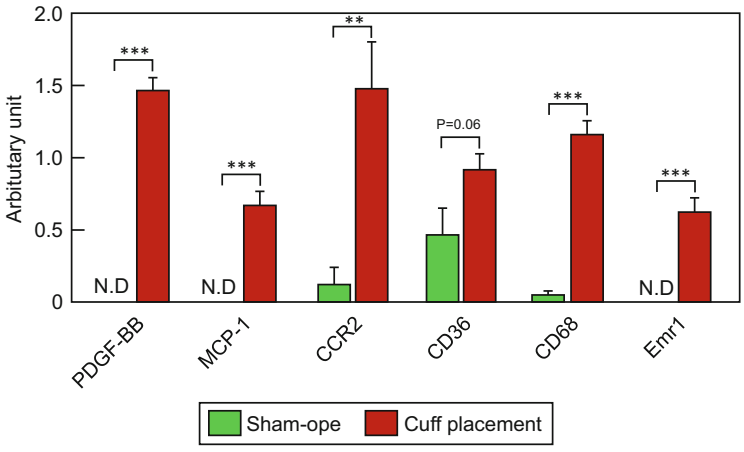

Fig. 2.3 Comparison of the gene profiles between sham-operated artery and cuff-injured artery

Table 2.1 Representative cuff placement in genetically manipulated mouse models

Gene	Location	Neointimal formation	References	
LR11-KO	Carotid artery	Reduced	Arterioscler Thromb Vasc Biol	2007 [38]
Rag-1-KO	Carotid artery	Increased	Arterioscler Thromb Vasc Biol	2002 [45]
CD4-KO	Carotid artery	Reduced	J Am Heart Assoc	2013 [50]
eNOS-KO	Femoral artery	Increased	J Clin Invest	1998 [34]
iNOS-KO	Carotid artery	Reduced	Circ Res	1999 [59]
sEH/ApoE double-KO	Femoral	Reduced	Arterioscler Thromb Vasc Biol	2010 [61]
sEH/ApoE double-KO				
Tlr4-KO	Femoral	Reduced	Circulation	2002 [64]
Tlr2-KO	Femoral	Reduced	Cardiovasc Res	2005 [65]
CatK-KO	Carotid	Reduced	Hypertension	2014 [66]
AT1 receptor-KO	Femoral	Reduced	Circulation	2002 [74]
AT2 receptor-KO	Femoral	Increased	Circulation	2002 [74]
Mas-KO	Femoral	Increased	Hypertension	2014 [78]
Cu/ZnSOD-KO	Femoral	Unchanged	Journal of atherosclerosis and thrombosis	2011 [81]
HAS2Tg (SMC-specific)	Femoral	Increased	PLoS One	2013 [39]
IRS1-KO	Femoral	Increased	Circulation	2003 [85]
IRS2-KO	Femoral	Increased	Circulation	2003 [85]

potent factors inducing migration and proliferation of the SMCs after balloon angioplasty. The expression levels of PDGF-BB mRNA in the cuffed artery were significantly increased as compared to those in the sham-operated artery (Fig. 2.3). An antagonist of the PDGF-BB receptor was shown to suppress the proliferation of vascular SMCs after balloon-induced injury in a rat model [36]. PDGF-BB induces vascular SMC proliferation via, at least in part, regulation of the cell cycle. Schwaiberger et al. demonstrated that local treatment with a cyclin-dependent kinase inhibitor inhibited cuff-induced neointimal formation, accompanied by reduction of the phosphorylation level of signal transducer and activator of

transcription 3 (STAT3), but not of Akt, ERK1/2, or p38MAPK activation [35]. These data suggest that PDGF-BB-STAT3 signaling is involved in cuff-induced neointimal formation.

In addition to PDGF-BB-STAT3 signaling, PDGF-BB has been reported to augment the migration of SMCs through the LR11, a member of the LDL receptor family/urokinase-type plasminogen activator receptor (uPAR) pathway [37]. Ohwaki et al. found that balloon-injured intimal SMCs showed strong expression of LR11 in rat arteries. High-fat diet-fed LR11-KO mice showed a decrease of cuff-induced neointimal formation [38]. In in vitro experiments, the secreted soluble form of LR11 (soILR11) promoted the migration of THP-1 induced by PDGF-BB, an effect that was completely canceled by the anti-uPAR antibody [38]. These data suggest that PDGF-BB induced by cuff-induced injury is one of strongest regulators of neointimal formation.

The ECM has been reported to be a key player in arterial remodeling after vascular injury [4]. Hyaluronan 2 (HAS2), which is a primary component of the ECM, is expressed in neointimal lesions in humans with atherosclerosis and at sites of wire-induced injury of the arteries in mice. Mice overexpressing the murine HAS2 gene specifically in the vascular SMCs (cHAS2/CreSM22a mice) showed markedly enhanced cuff-induced neointimal formation, with augmentation of SMC migration and proliferation, and production of inflammatory cytokines and ROS [39]. Consistent with these data, in a wire-induced injury model, a HA synthesis inhibitor markedly suppressed neointimal formation. The ECM induced by arterial cuff-induced injury promotes migration of SMCs into the intima, leading to neointimal formation.

2.5.2 Roles of BM-Derived Cells in Cuff-Induced Neointimal Formation

The roles of bone marrow (BM)-derived cells in the pathogenesis of atherosclerosis have been extensively studied [40]. Fluorescence in situ hybridization (FISH) analysis has revealed that female-derived BM cells transplanted into male mice were detected in the neointima of male mice (Fig. 2.4). Following BMT from green fluorescent protein (GFP)-transgenic mice to ApoE-KO mice, GFP-positive cells were confirmed in the vascular neointima (4–10 %) and media (5–32 %) in the latter mice. Following bone marrow transplantation (BMT) from LacZ mice to wild-type (WT) mice, a number of LacZ-positive macrophages were found in the neointima (25.7 %), media (7.3 %), and adventitia (73.7 %) of the arteries of the WT mice at 4 weeks after cuff placement [33]. It was worthy of note that more marked infiltration of the adventitia by macrophages was observed after injury induced by cuff placement than after wire injury or ligation injury.

Xu et al. transplanted the BM of GFP-transgenic mice into LDLR-KO mice to identify the cell lineage in the lesion [41]. Two weeks after cuff placement

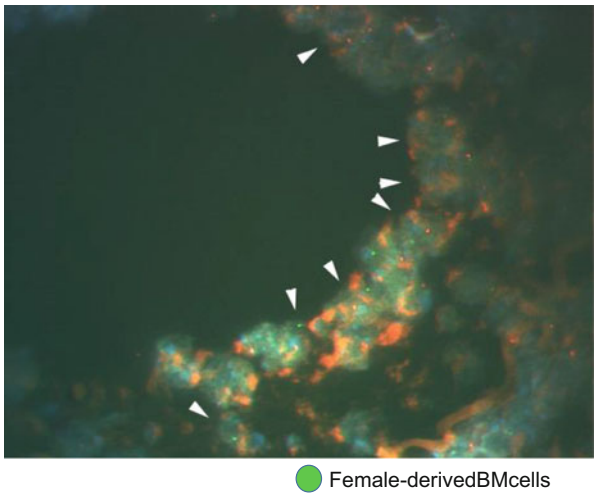

Fig. 2.4 Fluorescence in situ hybridization (FISH) of cuff-injured artery in male mice transplanted female-derived BM cells

following a high-fat diet for 4 weeks, atherosclerotic lesions developing in the intima predominantly consisted of a massive accumulation of foam cells with a number of α-SMA- and GFP-positive cells. In addition to macrophages, adventitial small vessels also showed positive staining for both the endothelium-specific marker CD31 and GFP in mice transplanted with BM obtained from GFP-transgenic mice [41]. Most of the macrophages are GFP-positive, and some of the SMCs and ECs are also GFP-positive. In a cuff-induced vascular injury model, BM-derived cells are recruited to the adventitia and differentiate into macrophages, SMCs, and endothelial cells. Treatment with a blocker of M-CSF, which guides differentiation into macrophages, caused a prominent decrease of macrophages, and inhibition of the PDGF receptor suppressed the recruitment of SMCs to the adventitia after cuff placement [42]. These data suggest that the adventitia plays a pivotal role in neointimal formation induced by cuff placement. Scott et al. demonstrated that the adventitia is important in the first wave of growth after angioplasty following occurrence of neointimal hyperplasia [43].

2.5.3 Roles of T Cells and B Cells in Cuff-Induced Neointimal Formation

The importance of T and B lymphocytes in the process of restenosis after PCI has been pointed out [44]. Rag-1-KO mice, which lack mature B and T cells, have been demonstrated to show increased thickness of cuff-induced neointima in the carotid artery. Reconstitution of the Rag-1-KO mice with B cells from WT mice reduced the neointimal formation. Moreover, both IgG and IgM were detected in the cuff-injured carotid arteries of reconstituted Rag-1-KO mice with B cells [45]. These data suggest that an increase of immunoglobulin by activation of B cells exerts a

protective action against intimal thickening. The neointimal area and intima/media ratio were significantly reduced in mice treated with immunoglobulin administered intraperitoneally for 5 consecutive days starting 1 day prior to cuff placement. On the other hand, immunoglobulin could not suppress cuff-induced neointimal formation, when the treatment was commenced 3 days after cuff placement [46]. When pooled mouse IgG or IgM was given to Rag-1-KO mice by intravenous injection, a significant reduction of intimal thickening was observed as compared with that in the untreated Rag-1-KO mice. Immunoglobulin treatments modify the serum complement C3 profile, and the amount of complement C3 was decreased in the injured arteries. Depletion of complement C3 in the Rag-1-KO mice significantly decreased the degree of intimal thickening [47]. These data suggest that IgG, IgM, and complement C3 are involved in the modulation of the neointimal hyperplasia response to cuff-induced injury.

Moreover, treatment with immunoglobulin significantly enhanced the secretion of interleukin (IL)-10, suggesting activation of T cells by immunoglobulin [46]. Rag-1-KO mice reconstituted with T cells from WT mice showed a reduction of neointimal formation after cuff placement [48]. Dimayuga et al. carried out a detailed examination of the T-cell fraction. Splenic $CD8^+CD25^+$ T cells and $CD8^+CD28^+$ T cells, but not $CD4^+CD25^+$ and $CD4^+CD28^+$ T cells, were also significantly increased after arterial injury in the WT mice. Rag-1-KO mice given $CD8^+$ T cells showed a significant decrease of neointimal formation as compared to Rag-1-KO mice not given the cells. On the other hand, transfer of $CD4^+$ T cells was not associated with inhibition of the neointimal formation [49]. Neointimal formation induced by cuff placement was significantly reduced in CD4-KO mice as compared with that in the WT mice, because of the higher percentage of $CD8^+$ T cells. Moreover, adoptive transfer of $CD8^+CD28^{hi}$ T cells into recipient Rag-1-KO mice significantly reduced neointimal formation as compared to that of $CD8^+CD28^+$ T cells [50]. Although both $CD8^+$ T cells and $CD4^+$ T cells are activated in response to arterial injury, $CD8^+$ T cells, which constitute at least a fraction of the $CD8^+CD28^{hi}$, are mainly involved in the inhibition of cuff-induced neointimal formation.

2.5.4 Roles of eNOS and iNOS in Cuff-Induced Neointimal Formation

Nitric oxide (NO) is an important vascular regulatory factor that is generated by the enzyme nitric oxide synthase (NOS) [51]. Three different isoforms of NOS are recognized: among these is endothelial NOS (eNOS), which is constitutively expressed mainly in the vascular endothelial cells [52]. eNOS can be an important factor modulating vascular endothelial function and is activated by acetylcholine (ACh) and insulin. eNOS-KO mice exhibit impaired ACh-induced vascular relaxation [53]. The second isoform is inducible NOS (iNOS), which cannot be detected

in normal tissue, but is expressed in several cell types, including macrophages and vascular SMCs, after cytokine stimulation [54], and the third isoform is neuronal NOS (nNOS), which is constitutively expressed mainly in the nervous tissues and skeletal muscle type II.

eNOS-KO mice exhibit increased neointimal formation following cuff placement [34]. Consistent with these data, the neointimal formation induced by ligation is also significantly more pronounced in the eNOS-KO mice than in the WT mice [55]. Since antiplatelet and antihypertensive treatments cannot attenuate the progression of neointimal formation, the neointimal hyperplasia observed in eNOS-KO mice is produced by the direct action of eNOS and not mediated by thrombus formation or high blood pressure [33]. When adenovirus-mediated human endothelial constitutive NOS cDNA (AdCMVceNOS) was transduced into the rat carotid artery after balloon injury, the intima/media ratio decreased significantly because of inhibition of SMC proliferation [56]. These data suggest that NO mediated by eNOS inhibits neointimal hyperplasia induced by vascular injury.

iNOS has been shown to be expressed in the SMCs after cuff-induced vascular injury in rabbits [57, 58], and iNOS-KO mice showed a significant reduction of neointimal thickening induced by cuff placement [59]. Unlike eNOS-deficient mice, iNOS-KO mice showed no reduction of the neointimal hyperplasia associated with mechanically induced endothelial denudation. Both the medial area and medial thickness were increased in the iNOS-KO mice after mechanically induced endothelial denudation [60]. Consistent with these data, Yogo et al. demonstrated that vascular remodeling, but not neointimal hyperplasia, after carotid artery ligation was increased in the iNOS-KO mice [55]. The differences in the procedure used to induce vascular injury may be related to the degree of neointimal hyperplasia and vascular remodeling in the iNOS-KO mice. Cuff placement evokes significant participation of inflammatory cells, including macrophages, in the adventitia as compared to the ligation model, as mentioned above. Increase of inflammation in the adventitia may be associated with increased iNOS expression levels, which may promote neointimal formation induced by cuff placement. Mechanically induced endothelial denudation and ligation may mainly induce migration of the SMCs from the media to the intima, resulting in increased neointimal hyperplasia.

Similar results were also observed in soluble epoxide hydrolase (sEH)/ApoE double-KO mice and inhibition of sEH by 12-(3-adamantan-1-yl-ureido) dodecanoic acid, which suppress metabolism of epoxyeicosatrienoic acids (EETs). sEH/ApoE double-KO mice or mice with inhibition of sEH showed significant reduction of the neointimal formation in the femoral artery cuff model, but not in the carotid artery ligation model. The expressions of proinflammatory genes were significantly reduced in the femoral arteries of the sEH/ApoE double-KO mice [61].

2.5.5 *Roles of Inflammatory Cytokines in Cuff-Induced Neointimal Formation*

Inflammation is considered as an important factor in human atherogenesis [8]. An inflammatory response to vascular injury, mediated by proinflammatory cytokines, influences the progression of neointimal formation and development of atherosclerotic lesions.

It has been demonstrated that the expressions of toll-like receptors (Tlrs) 2 and 4 are markedly enhanced in human atherosclerotic plaques and vascular adventitia [62]. Tlr4 serves as the receptor for bacterial lipopolysaccharides (LPS) and also recognizes cellular fibronectin, heat shock protein 60, and endogenous peptides that are produced in response to tissue injury [63]. In the adventitia, not all Tlr4-positive cells are colocalized with macrophages. Although application of LPS between the cuff and artery augmented the neointimal formation induced by cuff-induced injury in the WT mice, no such finding was observed in the Tlr4-KO mice [64]. Application of Pam3Cys-SK4, a synthetic Tlr2 ligand, significantly enhanced the neointimal formation induced by cuff placement in the femoral arteries of the WT mice. No such increase of the neointimal formation was observed in the Tlr2-KO mice. In ApoE-KO mice, application of Pam3Cys-SK4 led to a significant increase in the formation of atherosclerotic plaques [65]. Tlr2 stimulation produced significant induction of inflammatory cytokines in human adventitial fibroblasts in vitro. Treatment with cathepsin K (CatK), which is one of the most potent of mammalian collagenases, increased the mRNA levels of inflammatory cytokines, including Tlr2 and Tlr4. CatK-KO mice showed significantly reduced neointimal formation following cuff placement and ligation, accompanied by a decrease in the expression levels of Tlr2 and Tlr4 mRNA [66]. These findings provide evidence for a link between inflammatory cytokines in the adventitia and intimal lesion formation.

Although Tlr2/4 are expressed on the cell surface, Tlr7/9 are expressed on the endosomes. Tlr7/9 were detected at sites of post-interventional remodeling and accelerated atherosclerosis [67]. In hypercholesterolemic apolipoprotein E*3-Leiden mice, femoral artery cuff placement led to a strong increase of the Tlr7/9 expressions [68]. Blockade of Tlr7/9 with a dual antagonist reduced neointimal thickening and foam cell accumulation; the intima/media ratio was reduced by 64.5 % and luminal stenosis by 62.8 %. Application of the Tlr7/9 dual antagonist also reduced arterial wall inflammation, with reduced macrophage infiltration and altered serum IL-10 levels. Stimulation of cultured macrophages with Tlr7/9 ligands enhanced TNFα expression, which was decreased by coadministration of the Tlr7/9 antagonist. Furthermore, the antagonist abolished the Tlr7/9-enhanced LDL uptake. The antagonist also reduced oxidized LDL-induced foam cell formation, most likely not via decreased influx, but via increased efflux induced by increased IL-10 levels.

2.5.6 Role of RAS in Cuff-Induced Neointimal Formation

The renin-angiotensin-aldosterone system (RAAS) has various physiological actions such as vasoconstriction and is known to be involved in the development of hypertension and atherosclerosis [69, 70]. Specifically, modulation of the local RAAS may play a key role, just like that of the systemic RAS, in the development of cardiovascular diseases. Angiotensin (Ang) II is a peptide that exerts potent vasoconstrictive action via the AT1 receptor-MAPK pathway. Although human renin (hRN)/human angiotensinogen (hANG)-transgenic (Tg) mice showed increased blood pressure and medial thickening even in the absence of cuff placement, the hRN/hANG-Tg mice showed even more pronounced inflammatory vascular remodeling after cuff placement. Treatment with an AT1 blocker inhibited cuff-induced neointimal formation associated with reduced inflammation, but independently of the blood pressure change [71]. When the direct renin inhibitor aliskiren was administered to C57BL/6 mice via an osmotic pump, it inhibited cuff-induced vascular remodeling. The number of adherent leukocytes was increased in the cuff-injured mice not treated with aliskiren, where it was significantly reduced in the aliskiren-treated mice without any change of the blood pressure. Aliskiren decreased the adhesion of THP-1 cells to TNFα-stimulated human umbilical vein endothelial cells [72]. These data indicate that RAS activation augments neointimal hyperplasia induced by cuff placement via increased release of inflammatory cytokines.

Moreover, the ACE expression level increased in a time-dependent manner after cuff placement and was observed in the medial and neointimal layers and the adventitia of the cuffed arteries in FVB/N mice. The intima/media ratio after cuff placement was significantly decreased by ACE inhibitor treatment [73]. Ang II appears to be one of the factors exacerbating cuff-induced neointimal formation. In fact, AT1 receptor-KO mice showed decreased neointimal formation following cuff placement, accompanied by an increase of apoptotic cells among the SMCs [74]. Consistent with these data, the AT1-selective receptor blocker olmesartan suppressed cuff-induced neointimal formation via reducing ERK phosphorylation [75]. On the other hand, neointimal formation induced by cuff placement was increased in AT2 receptor-KO mice. The expressions of bcl-2 and bcl-xL mRNA, which are regulators of apoptosis, were enhanced in the AT2 receptor-KO mice showing enhanced neointimal formation [74].

Recently, in addition to the Ang II-AT1 receptor pathway, Ang-(1-7), which is synthesized from Ang I and Ang II mainly via ACE2 activity, has been reported to play a crucial role in vascular remodeling via Mas receptor activation [76, 77]. Mas-KO mice showed markedly increased neointimal formation after cuff placement, independently of the AT1 receptor. Treatment with Ang-(1-7) also suppressed neointimal formation, associated with suppression of vascular SMC proliferation, release of inflammatory cytokines and superoxide anion production in the injured artery. On the other hand, these inhibitory effects of Ang-(1-7) were less marked in the Mas-KO [78]. Interestingly, treatment with an

AT1 receptor blocker inhibited neointimal formation induced by cuff placement, accompanied by a decrease in the expression levels of ACE2 and Mas mRNA and an increase in the expression of AT2 receptor mRNA. AT2 receptor-KO mice showed no reduction of the neointimal formation by treatment with Ang-(1-7). These results suggest that in addition to the activities of the ACE2/Ang-(1-7)/Mas axis, blockade of the AT1 receptor could enhance the activities of the ACE2/Ang-(1-7)/AT2 receptor axis and thereby inhibit neointimal formation induced by cuff placement.

2.5.7 Role of ROS in Cuff-Induced Neointimal Formation

Atherosclerosis is associated with increased production of reactive oxygen species (ROS) in the vessel [79]. The superoxide dismutases (SODs) are enzymes that catalyze the dismutation of superoxide anions to hydrogen peroxide; three isoenzymes of the SODs have been identified, namely, manganese SOD (MnSOD), which is localized in the mitochondria; copper/zinc SOD (Cu/ZnSOD), which is localized in the cytosol; and extracellular SOD (EC-SOD). The antioxidant enzyme Cu/ZnSOD metabolizes superoxide anions (O2-) in the vascular endothelial cells [80].

Although there was no difference in the degree of cuff-induced neointimal formation between the Cu/ZnSOD-KO and WT mice, the former showed a significant decrease in the intima/media ratio after cuff placement [81]. This increased medial SMCs in the Cu/ZnSOD-KO mice showed positive staining for SMemb/MHC-B, which is a useful molecular marker of embryonic-type SMCs. Moreover, the expression levels of TNFα, ICAM1, VCAM1, and iNOS in the media were higher in the Cu/ZnSOD-KO mice than in the WT mice, suggesting that Cu/ZnSOD-KO mice showed enhanced inflammation, expression of adhesion molecules, and altered structure of the media post-injury.

When an adenovirus vector expressing EC-SOD (AxCAEC-SOD) was injected between the cuff and the adventitia of the femoral arteries in rat models, neointimal formation was significantly reduced in the AxCAEC-SOD-transfected arteries [82]. Furthermore, proliferation of SMCs in the neointima and media was inhibited by EC-SOD treatment. Augmented iNOS expression, apoptosis, collagen content, and ROS generation in the vascular wall were also reduced by EC-SOD treatment. The amount of generation of ROS may have influence on the degree of medial thickening as well as neointimal formation induced by cuff placement.

2.5.8 *Role of Insulin Signaling in Cuff-Induced Neointimal Formation*

Insulin resistance has been reported to be associated with atherosclerosis; however, the underlying mechanism is still unknown [83]. Insulin resistance is caused by impaired insulin signaling induced by some factors. Insulin activates insulin receptor substrates (IRS) 1 and 2, which are expressed ubiquitously in various tissues, including the endothelial cells and SMCs, through the insulin receptor and the downstream signaling [84]. Both IRS1- and IRS2-KO mice show features of the metabolic syndrome, including insulin resistance, dyslipidemia, and hypertension. Although both genotypes of mice show a similar degree of insulin resistance, the IRS2-KO mice show more pronounced cuff-induced neointimal formation than the IRS1-KO mice, which in turn show more pronounced cuff-induced neointimal formation than the WT mice. IRS2 expression, but not IRS1 expression, is detected in the blood vessels [85]. Insulin resistance in the blood vessels is considered to exacerbate cuff-induced neointimal formation.

On the other hand, mice with phosphatase and tensin homology deleted on chromosome 10 (PTEN), which is an antagonist of phosphatidylinositol 3-kinase (PI3K), exhibited significant reduction of neointimal formation when adenovirus-mediated human PTEN (AdPTEN) type 1 was injected between the cuff and the adventitia. AdPTEN reduced SMC proliferation and release of inflammatory cytokines [86]. Since insulin activates PI3K via the IRS, the overexpression of PTEN in response to cuff-induced injury appears to be a seemingly contradictory finding to that observed in the IRS-KO mice. However, as PI3K has known to be activated by some factors independently of insulin signaling, activated PI3K may enhance neointimal hyperplasia induced by cuff placement under some conditions.

2.6 Conclusion

Cuff placement causes mild endothelial cell damage, SMC proliferation and migration, and inflammation of the adventitia. This is a convenient and reproducible tool and is relatively less expensive and time-consuming. This tool is effective for analyzing the mechanism of vascular remodeling using mice, including genetically engineered mice. Further experiments to identify the precise mechanisms of neointimal hyperplasia by using this tool will provide the development of new technologies in the future.

References

1. GBD 2013 Mortality and Causes of Death Collaborators. Global, regional, and national age-sex specific all-cause and cause-specific mortality for 240 causes of death, 1990–2013: a systematic analysis for the Global Burden of Disease Study 2013. Lancet. 2015;385 (9963):117–71. doi:10.1016/s0140-6736(14)61682-2
2. Mitra AK, Agrawal DK. In stent restenosis: bane of the stent era. J Clin Pathol. 2006;59 (3):232–9. doi:10.1136/jcp.2005.025742.
3. Otsuka F, Finn AV, Yazdani SK, Nakano M, Kolodgie FD, Virmani R. The importance of the endothelium in atherothrombosis and coronary stenting. Nat Rev Cardiol. 2012;9(8):439–53. doi:10.1038/nrcardio.2012.64.
4. Goel SA, Guo LW, Liu B, Kent KC. Mechanisms of post-intervention arterial remodelling. Cardiovasc Res. 2012;96(3):363–71. doi:10.1093/cvr/cvs276.
5. Chaabane C, Otsuka F, Virmani R, Bochaton-Piallat ML. Biological responses in stented arteries. Cardiovasc Res. 2013;99(2):353–63. doi:10.1093/cvr/cvt115.
6. Grewe PH, Deneke T, Machraoui A, Barmeyer J, Muller KM. Acute and chronic tissue response to coronary stent implantation: pathologic findings in human specimen. J Am Coll Cardiol. 2000;35(1):157–63.
7. Burke AP, Kolodgie FD, Farb A, Weber D, Virmani R. Morphological predictors of arterial remodeling in coronary atherosclerosis. Circulation. 2002;105(3):297–303.
8. Ross R. Atherosclerosis – an inflammatory disease. N Engl J Med. 1999;340(2):115–26. doi:10.1056/nejm199901143400207.
9. Campbell JH, Campbell GR. Smooth muscle phenotypic modulation – a personal experience. Arterioscler Thromb Vasc Biol. 2012;32(8):1784–9. doi:10.1161/atvbaha.111.243212.
10. Hui DY. Intimal hyperplasia in murine models. Curr Drug Targets. 2008;9(3):251–60.
11. Virmani R, Farb A. Pathology of in-stent restenosis. Curr Opin Lipidol. 1999;10(6):499–506.
12. Lowe HC, Oesterle SN, Khachigian LM. Coronary in-stent restenosis: current status and future strategies. J Am Coll Cardiol. 2002;39(2):183–93.
13. Moses JW, Leon MB, Popma JJ, Fitzgerald PJ, Holmes DR, O'Shaughnessy C, et al. Sirolimus-eluting stents versus standard stents in patients with stenosis in a native coronary artery. N Engl J Med. 2003;349(14):1315–23. doi:10.1056/NEJMoa035071.
14. Stone GW, Ellis SG, Cox DA, Hermiller J, O'Shaughnessy C, Mann JT, et al. A polymer-based, paclitaxel-eluting stent in patients with coronary artery disease. N Engl J Med. 2004;350(3):221–31. doi:10.1056/NEJMoa032441.
15. Stone GW, Moses JW, Ellis SG, Schofer J, Dawkins KD, Morice MC, et al. Safety and efficacy of sirolimus- and paclitaxel-eluting coronary stents. N Engl J Med. 2007;356(10):998–1008. doi:10.1056/NEJMoa067193.
16. Joner M, Finn AV, Farb A, Mont EK, Kolodgie FD, Ladich E, et al. Pathology of drug-eluting stents in humans: delayed healing and late thrombotic risk. J Am Coll Cardiol. 2006;48 (1):193–202. doi:10.1016/j.jacc.2006.03.042.
17. Mehra MR, Ventura HO, Stapleton DD, Smart FW. The prognostic significance of intimal proliferation in cardiac allograft vasculopathy: a paradigm shift. J Heart Lung Transplant. 1995;14(6 Pt 2):S207–11.
18. Roy-Chaudhury P, Kelly BS, Miller MA, Reaves A, Armstrong J, Nanayakkara N, et al. Venous neointimal hyperplasia in polytetrafluoroethylene dialysis grafts. Kidney Int. 2001;59(6):2325–34. doi:10.1046/j.1523-1755.2001.00750.x.
19. Mizukawa H. Experimental studies on the morphogenesis of arteriosclerosis. Kitakanto Med J. 1969;19:175.
20. Huth F, Kojimahara M, Franken T, Rhedin P, Rosenbauer KA. Aortic alterations in rabbits following sheathing with silastic and polyethylene tubes. Curr Top Pathol. 1975;60:1–32.
21. Gebrane J, Roland J, Orcel L. Experimental diffuse intimal thickening of the femoral arteries in the rabbit. Virchows Arch A Pathol Anat Histol. 1982;396(1):41–59.

22. Kitamura T. An electron microscopic study on the early change of intimal thickening in arteriosclerosis. J Juzen Med Soc. 1982;91:876.
23. Hirosumi J, Nomoto A, Ohkubo Y, Sekiguchi C, Mutoh S, Yamaguchi I, et al. Inflammatory responses in cuff-induced atherosclerosis in rabbits. Atherosclerosis. 1987;64(2–3):243–54.
24. Booth RF, Martin JF, Honey AC, Hassall DG, Beesley JE, Moncada S. Rapid development of atherosclerotic lesions in the rabbit carotid artery induced by perivascular manipulation. Atherosclerosis. 1989;76(2–3):257–68.
25. Kockx MM, De Meyer GR, Andries LJ, Bult H, Jacob WA, Herman AG. The endothelium during cuff-induced neointima formation in the rabbit carotid artery. Arterioscler Thromb. 1993;13(12):1874–84.
26. Kockx MM, De Meyer GR, Jacob WA, Bult H, Herman AG. Triphasic sequence of neointimal formation in the cuffed carotid artery of the rabbit. Arterioscler Thromb. 1992;12 (12):1447–57.
27. Zhang SH, Reddick RL, Piedrahita JA, Maeda N. Spontaneous hypercholesterolemia and arterial lesions in mice lacking apolipoprotein E. Science. 1992;258(5081):468–71.
28. Kapourchali FR, Surendiran G, Chen L, Uitz E, Bahadori B, Moghadasian MH. Animal models of atherosclerosis. World J Clin Cases. 2014;2(5):126–32. doi:10.12998/wjcc.v2.i5.126.
29. Sanan DA, Newland DL, Tao R, Marcovina S, Wang J, Mooser V, et al. Low density lipoprotein receptor-negative mice expressing human apolipoprotein B-100 develop complex atherosclerotic lesions on a chow diet: no accentuation by apolipoprotein(a). Proc Natl Acad Sci U S A. 1998;95(8):4544–9.
30. Kumar A, Lindner V. Remodeling with neointima formation in the mouse carotid artery after cessation of blood flow. Arterioscler Thromb Vasc Biol. 1997;17(10):2238–44.
31. Lindner V, Fingerle J, Reidy MA. Mouse model of arterial injury. Circ Res. 1993;73(5):792–6.
32. Sata M, Maejima Y, Adachi F, Fukino K, Saiura A, Sugiura S, et al. A mouse model of vascular injury that induces rapid onset of medial cell apoptosis followed by reproducible neointimal hyperplasia. J Mol Cell Cardiol. 2000;32(11):2097–104. doi:10.1006/jmcc.2000.1238.
33. Tanaka K, Sata M, Hirata Y, Nagai R. Diverse contribution of bone marrow cells to neointimal hyperplasia after mechanical vascular injuries. Circ Res. 2003;93(8):783–90. doi:10.1161/01.RES.0000096651.13001.B4.
34. Moroi M, Zhang L, Yasuda T, Virmani R, Gold HK, Fishman MC, et al. Interaction of genetic deficiency of endothelial nitric oxide, gender, and pregnancy in vascular response to injury in mice. J Clin Invest. 1998;101(6):1225–32. doi:10.1172/jci1293.
35. Schwaiberger AV, Heiss EH, Cabaravdic M, Oberan T, Zaujec J, Schachner D, et al. Indirubin-3′-monoxime blocks vascular smooth muscle cell proliferation by inhibition of signal transducer and activator of transcription 3 signaling and reduces neointima formation in vivo. Arterioscler Thromb Vasc Biol. 2010;30(12):2475–81. doi:10.1161/ATVBAHA.110.212654.
36. Deguchi J, Namba T, Hamada H, Nakaoka T, Abe J, Sato O, et al. Targeting endogenous platelet-derived growth factor B-chain by adenovirus-mediated gene transfer potently inhibits in vivo smooth muscle proliferation after arterial injury. Gene Ther. 1999;6(6):956–65. doi:10.1038/sj.gt.3300918.
37. Jiang M, Bujo H, Ohwaki K, Unoki H, Yamazaki H, Kanaki T, et al. Ang II-stimulated migration of vascular smooth muscle cells is dependent on LR11 in mice. J Clin Invest. 2008;118(8):2733–46. doi:10.1172/JCI32381.
38. Ohwaki K, Bujo H, Jiang M, Yamazaki H, Schneider WJ, Saito Y. A secreted soluble form of LR11, specifically expressed in intimal smooth muscle cells, accelerates formation of lipid-laden macrophages. Arterioscler Thromb Vasc Biol. 2007;27(5):1050–6. doi:10.1161/ATVBAHA.106.137091.
39. Kashima Y, Takahashi M, Shiba Y, Itano N, Izawa A, Koyama J, et al. Crucial role of hyaluronan in neointimal formation after vascular injury. PLoS One. 2013;8(3):e58760. doi:10.1371/journal.pone.0058760.

40. Sata M, Saiura A, Kunisato A, Tojo A, Okada S, Tokuhisa T, et al. Hematopoietic stem cells differentiate into vascular cells that participate in the pathogenesis of atherosclerosis. Nat Med. 2002;8(4):403–9. doi:10.1038/nm0402-403.
41. Xu Y, Arai H, Murayama T, Kita T, Yokode M. Hypercholesterolemia contributes to the development of atherosclerosis and vascular remodeling by recruiting bone marrow-derived cells in cuff-induced vascular injury. Biochem Biophys Res Commun. 2007;363(3):782–7. doi:10.1016/j.bbrc.2007.09.029.
42. Xu Y, Arai H, Zhuge X, Sano H, Murayama T, Yoshimoto M, et al. Role of bone marrow-derived progenitor cells in cuff-induced vascular injury in mice. Arterioscler Thromb Vasc Biol. 2004;24(3):477–82. doi:10.1161/01.ATV.0000118016.94368.35.
43. Scott NA, Cipolla GD, Ross CE, Dunn B, Martin FH, Simonet L, et al. Identification of a potential role for the adventitia in vascular lesion formation after balloon overstretch injury of porcine coronary arteries. Circulation. 1996;93(12):2178–87.
44. Brunetti ND, Pepe M, Munno I, Tiecco F, Quagliara D, De Gennaro L, et al. Th2-dependent cytokine release in patients treated with coronary angioplasty. Coron Artery Dis. 2008;19 (3):133–7. doi:10.1097/MCA.0b013e3282f3fbcb.
45. Dimayuga P, Cercek B, Oguchi S, Fredrikson GN, Yano J, Shah PK, et al. Inhibitory effect on arterial injury-induced neointimal formation by adoptive B-cell transfer in Rag-1 knockout mice. Arterioscler Thromb Vasc Biol. 2002;22(4):644–9.
46. Keren G, Keren P, Barshack I, Pri-Chen S, George J. The effect of intravenous immunoglobulins on intimal thickening in a mouse model of arterial injury. Atherosclerosis. 2001;159 (1):77–83.
47. Dimayuga PC, Cesena FH, Chyu KY, Yano J, Amorn A, Fishbein MC, et al. Natural antibodies and complement modulate intimal thickening after arterial injury. Am J Physiol Regul Integr Comp Physiol. 2009;297(5):R1593–600. doi:10.1152/ajpregu.00114.2009.
48. Dimayuga PC, Li H, Chyu KY, Fredrikson GN, Nilsson J, Fishbein MC, et al. T cell modulation of intimal thickening after vascular injury: the bimodal role of IFN-gamma in immune deficiency. Arterioscler Thromb Vasc Biol. 2005;25(12):2528–34. doi:10.1161/01.ATV.0000190606.41121.00.
49. Dimayuga PC, Chyu KY, Kirzner J, Yano J, Zhao X, Zhou J, et al. Enhanced neointima formation following arterial injury in immune deficient Rag-1−/− mice is attenuated by adoptive transfer of CD8 T cells. PLoS One. 2011;6(5):e20214. doi:10.1371/journal.pone.0020214.
50. Dimayuga PC, Chyu KY, Lio WM, Zhao X, Yano J, Zhou J, et al. Reduced neointima formation after arterial injury in CD4−/− mice is mediated by CD8+CD28hi T cells. J Am Heart Assoc. 2013;2(3):e000155. doi:10.1161/JAHA.113.000155.
51. Harrison DG. Cellular and molecular mechanisms of endothelial cell dysfunction. J Clin Invest. 1997;100(9):2153–7. doi:10.1172/jci119751.
52. Shimokawa H. Primary endothelial dysfunction: atherosclerosis. J Mol Cell Cardiol. 1999;31 (1):23–37. doi:10.1006/jmcc.1998.0841.
53. Huang PL, Huang Z, Mashimo H, Bloch KD, Moskowitz MA, Bevan JA, et al. Hypertension in mice lacking the gene for endothelial nitric oxide synthase. Nature. 1995;377(6546):239–42. doi:10.1038/377239a0.
54. Forstermann U, Schmidt HH, Pollock JS, Sheng H, Mitchell JA, Warner TD, et al. Isoforms of nitric oxide synthase. Characterization and purification from different cell types. Biochem Pharmacol. 1991;42(10):1849–57.
55. Yogo K, Shimokawa H, Funakoshi H, Kandabashi T, Miyata K, Okamoto S, et al. Different vasculoprotective roles of NO synthase isoforms in vascular lesion formation in mice. Arterioscler Thromb Vasc Biol. 2000;20(11):E96–100.
56. Janssens S, Flaherty D, Nong Z, Varenne O, van Pelt N, Haustermans C, et al. Human endothelial nitric oxide synthase gene transfer inhibits vascular smooth muscle cell proliferation and neointima formation after balloon injury in rats. Circulation. 1998;97(13):1274–81.

57. Hansson GK, Geng YJ, Holm J, Hardhammar P, Wennmalm A, Jennische E. Arterial smooth muscle cells express nitric oxide synthase in response to endothelial injury. J Exp Med. 1994;180(2):733–8.
58. Arthur JF, Yin ZL, Young HM, Dusting GJ. Induction of nitric oxide synthase in the neointima induced by a periarterial collar in rabbits. Arterioscler Thromb Vasc Biol. 1997;17(4):737–40.
59. Chyu KY, Dimayuga P, Zhu J, Nilsson J, Kaul S, Shah PK, et al. Decreased neointimal thickening after arterial wall injury in inducible nitric oxide synthase knockout mice. Circ Res. 1999;85(12):1192–8.
60. Moore ZW, Hui DY. Apolipoprotein E inhibition of vascular hyperplasia and neointima formation requires inducible nitric oxide synthase. J Lipid Res. 2005;46(10):2083–90. doi:10.1194/jlr.M500177-JLR200.
61. Revermann M, Schloss M, Barbosa-Sicard E, Mieth A, Liebner S, Morisseau C, et al. Soluble epoxide hydrolase deficiency attenuates neointima formation in the femoral cuff model of hyperlipidemic mice. Arterioscler Thromb Vasc Biol. 2010;30(5):909–14. doi:10.1161/ATVBAHA.110.204099.
62. Edfeldt K, Swedenborg J, Hansson GK, Yan ZQ. Expression of toll-like receptors in human atherosclerotic lesions: a possible pathway for plaque activation. Circulation. 2002;105(10):1158–61.
63. Chow JC, Young DW, Golenbock DT, Christ WJ, Gusovsky F. Toll-like receptor-4 mediates lipopolysaccharide-induced signal transduction. J Biol Chem. 1999;274(16):10689–92.
64. Vink A. In vivo evidence for a role of toll-like receptor 4 in the development of intimal lesions. Circulation. 2002;106(15):1985–90. doi:10.1161/01.cir.0000032146.75113.ee.
65. Schoneveld AH, Oude Nijhuis MM, van Middelaar B, Laman JD, de Kleijn DP, Pasterkamp G. Toll-like receptor 2 stimulation induces intimal hyperplasia and atherosclerotic lesion development. Cardiovasc Res. 2005;66(1):162–9. doi:10.1016/j.cardiores.2004.12.016.
66. Hu L, Cheng XW, Song H, Inoue A, Jiang H, Li X, et al. Cathepsin K activity controls injury-related vascular repair in mice. Hypertension. 2014;63(3):607–15. doi:10.1161/HYPERTENSIONAHA.113.02141.
67. Pryshchep O, Ma-Krupa W, Younge BR, Goronzy JJ, Weyand CM. Vessel-specific Toll-like receptor profiles in human medium and large arteries. Circulation. 2008;118(12):1276–84. doi:10.1161/circulationaha.108.789172.
68. Karper JC, Ewing MM, Habets KL, de Vries MR, Peters EA, van Oeveren-Rietdijk AM, et al. Blocking toll-like receptors 7 and 9 reduces postinterventional remodeling via reduced macrophage activation, foam cell formation, and migration. Arterioscler Thromb Vasc Biol. 2012;32(8):e72–80. doi:10.1161/ATVBAHA.112.249391.
69. Daugherty A, Manning MW, Cassis LA. Angiotensin II promotes atherosclerotic lesions and aneurysms in apolipoprotein E-deficient mice. J Clin Invest. 2000;105(11):1605–12. doi:10.1172/jci7818.
70. Weiss D, Kools JJ, Taylor WR. Angiotensin II-induced hypertension accelerates the development of atherosclerosis in apoE-deficient mice. Circulation. 2001;103(3):448–54.
71. Inaba S, Iwai M, Furuno M, Kanno H, Senba I, Okayama H, et al. Temporary treatment with AT1 receptor blocker, valsartan, from early stage of hypertension prevented vascular remodeling. Am J Hypertens. 2011;24(5):550–6. doi:10.1038/ajh.2011.6.
72. Ino J, Kojima C, Osaka M, Nitta K, Yoshida M. Dynamic observation of mechanically-injured mouse femoral artery reveals an antiinflammatory effect of renin inhibitor. Arterioscler Thromb Vasc Biol. 2009;29(11):1858–63. doi:10.1161/ATVBAHA.108.182519.
73. Akishita M, Shirakami G, Iwai M, Wu L, Aoki M, Zhang L, et al. Angiotensin converting enzyme inhibitor restrains inflammation-induced vascular injury in mice. J Hypertens. 2001;19(6):1083–8.
74. Suzuki J, Iwai M, Nakagami H, Wu L, Chen R, Sugaya T, et al. Role of angiotensin II-regulated apoptosis through distinct AT1 and AT2 receptors in neointimal formation. Circulation. 2002;106(7):847–53. doi:10.1161/01.cir.0000024103.04821.86.

75. Liu HW, Iwai M, Takeda-Matsubara Y, Wu L, Li JM, Okumura M, et al. Effect of estrogen and AT1 receptor blocker on neointima formation. Hypertension. 2002;40(4):451–7. doi:10.1161/01.hyp.0000033466.05496.89.
76. Passos-Silva DG, Verano-Braga T, Santos RA. Angiotensin-(1–7): beyond the cardio-renal actions. Clin Sci (Lond). 2013;124(7):443–56. doi:10.1042/cs20120461.
77. Iwai M, Nakaoka H, Senba I, Kanno H, Moritani T, Horiuchi M. Possible involvement of angiotensin-converting enzyme 2 and Mas activation in inhibitory effects of angiotensin II Type 1 receptor blockade on vascular remodeling. Hypertension. 2012;60(1):137–44. doi:10.1161/hypertensionaha.112.191452.
78. Ohshima K, Mogi M, Nakaoka H, Iwanami J, Min LJ, Kanno H, et al. Possible role of angiotensin-converting enzyme 2 and activation of angiotensin II type 2 receptor by angiotensin-(1–7) in improvement of vascular remodeling by angiotensin II type 1 receptor blockade. Hypertension. 2014;63(3):e53–9. doi:10.1161/HYPERTENSIONAHA.113.02426.
79. Stocker R, Keaney Jr JF. Role of oxidative modifications in atherosclerosis. Physiol Rev. 2004;84(4):1381–478. doi:10.1152/physrev.00047.2003.
80. Fukai T, Galis ZS, Meng XP, Parthasarathy S, Harrison DG. Vascular expression of extracellular superoxide dismutase in atherosclerosis. J Clin Invest. 1998;101(10):2101–11. doi:10.1172/jci2105.
81. Ishigami N, Isoda K, Adachi T, Niida T, Kujiraoka T, Hakuno D, et al. Deficiency of CuZn superoxide dismutase promotes inflammation and alters medial structure following vascular injury. J Atheroscler Thromb. 2011;18(11):1009–17.
82. Ozumi K, Tasaki H, Takatsu H, Nakata S, Morishita T, Koide S, et al. Extracellular superoxide dismutase overexpression reduces cuff-induced arterial neointimal formation. Atherosclerosis. 2005;181(1):55–62. doi:10.1016/j.atherosclerosis.2005.01.051.
83. Howard G, O'Leary DH, Zaccaro D, Haffner S, Rewers M, Hamman R, et al. Insulin sensitivity and atherosclerosis. The Insulin Resistance Atherosclerosis Study (IRAS) Investigators. Circulation. 1996;93(10):1809–17.
84. Kadowaki T, Kubota N, Ueki K, Yamauchi T. SnapShot: physiology of insulin signaling. Cell. 2012;148(4):834-e1. doi:10.1016/j.cell.2012.02.004.
85. Kubota T, Kubota N, Moroi M, Terauchi Y, Kobayashi T, Kamata K, et al. Lack of insulin receptor substrate-2 causes progressive neointima formation in response to vessel injury. Circulation. 2003;107(24):3073–80. doi:10.1161/01.cir.0000070937.52035.25.
86. Koide S, Okazaki M, Tamura M, Ozumi K, Takatsu H, Kamezaki F, et al. PTEN reduces cuff-induced neointima formation and proinflammatory cytokines. Am J Physiol Heart Circ Physiol. 2007;292(6):H2824–31. doi:10.1152/ajpheart.01221.2006.

Chapter 3
Ligation of the Mouse Common Carotid Artery

Sarah M. Peterson, Lucy Liaw, and Volkhard Lindner

Abstract Arterial injury leads to vascular remodeling, with contributions from endothelial cells, smooth muscle cells, inflammatory cells, and potentially other circulating cells. The resultant intimal lesion formation, also described as neointima or intimal hyperplasia, is a major cause of morbidity and mortality in cardiovascular disease as it contributes to the restriction of oxygenated blood flow to organs critical to survival. The ability to perform reproducible arterial injury in the mouse has opened up vascular remodeling studies with genetically modified mice. Complete ligation of the common carotid artery of the mouse is a highly feasible, reproducible injury model that initiates a vascular response involving primarily vascular smooth muscle cells. Typically, in this flow cessation model, the ligated carotid artery undergoes proliferation and migration of medial smooth muscle cells, forming a significant neointima with associated constrictive remodeling. The contralateral carotid artery undergoes outward remodeling, increasing circumference in response to changes in blood flow. Gene expression changes occur in both the ligated and contralateral artery, and a stable lesion is formed within 3–4 weeks after ligation. The extent of lesion response in this model depends on the genetic background of the mice. This injury model has features of maintaining an intact endothelium, and generally low levels of mechanical injury, without a major inflammatory response. For these reasons, mouse carotid artery ligation has been widely used for elucidation of the factors controlling vascular smooth muscle cell behavior in response to injury. Proteins and microRNAs known to affect the remodeling response in this model are summarized.

Keywords Vascular remodeling • Neointimal lesion • Intimal hyperplasia • Carotid injury • MicroRNA

S.M. Peterson • L. Liaw • V. Lindner (✉)
Center for Molecular Medicine, Maine Medical Center Research Institute, 81 Research Drive, Scarborough, ME 04074, USA

Graduate School of Biomedical Science and Engineering, University of Maine, Orono, ME 04469, USA
e-mail: lindnv@mmc.org

M. Sata (ed.), *Mouse Models of Vascular Diseases*,
DOI 10.1007/978-4-431-55813-2_3

3.1 Introduction

Prior to the advances in the manipulation of the mouse genome, arterial injury and repair processes were typically studied in larger species such as rats and rabbits [1, 2]. These models have provided valuable insight into the mechanisms of neointima formation and endothelial regeneration of denuded arteries. The availability of genetic mouse models provided the opportunity to identify the contribution of specific factors to the development of cardiovascular diseases. To capitalize on the genetic mouse models, suitable vascular injury protocols needed to be developed in the mouse. Embolectomy catheters suitable for denudation of mouse arteries were never developed, and this situation led us to the development of alternative murine arterial injury models in the early 1990s. Analogous to the denuding injury of the rat carotid artery, we developed a mouse carotid artery injury model using a guide wire tip [3]. Several models that present variations on this wire denudation model have since been reported by others [4, 5]. The technical challenges stemming from achieving complete denudation with wire denudation models and uncontrolled thrombus formation are likely factors contributing to significant inter-operator variability in denuding injury models. This prompted us to develop the technically very simple model of mouse carotid artery ligation [6]. As this flow cessation model is relatively easy to perform, it has the advantage of being relatively free from operator-induced variables. This ligation model was primarily designed to induce smooth muscle dedifferentiation and proliferation with neointima formation in a reproducible manner. The vascular response to complete carotid artery ligation is shown in Fig. 3.1a–e. Components of the vascular response may include (1) expansion of the endothelial cell-containing intima in a normal artery into a multilayered lesion (Fig. 3.1a–c); (2) reduction in lumen area due to constrictive remodeling (described below), due to neointimal formation (Fig. 3.1b, ligated artery), or due to a combination of both processes; 3) compensatory outward remodeling, which is increased circumference of the contralateral artery (Fig. 3.1e, contralateral artery) associated with increased flow; and 4) constrictive remodeling (Fig. 3.1f), characterized by decreased circumference of the injured artery in response to decreased flow, which is also a significant component of human vascular disease.

In this injury model, medial vascular smooth muscle cells dedifferentiate, proliferate, and migrate across the internal elastic lamina to comprise the majority of neointimal cells present in the lesion [7]. We performed lineage tracing studies that follow the fate of fully differentiated medial vascular smooth muscle cells expressing smooth muscle myosin heavy chain (SM MHC) [7] to estimate the proportion of neointimal cells derived from differentiated SM MHC-positive cells. We crossed ROSA26 Cre reporter mice [8] with conditional, inducible SM MHC-*Cre*ER^{T2} mice [9] and performed tamoxifen induction in 10–14-week-old male mice ending 18 days prior to subsequent carotid ligation. The lesions were allowed to progress for 14 days, harvested by perfusion fixation as described below, rinsed with a Nonidet P-40-based detergent rinse, and stained with X-gal solution.

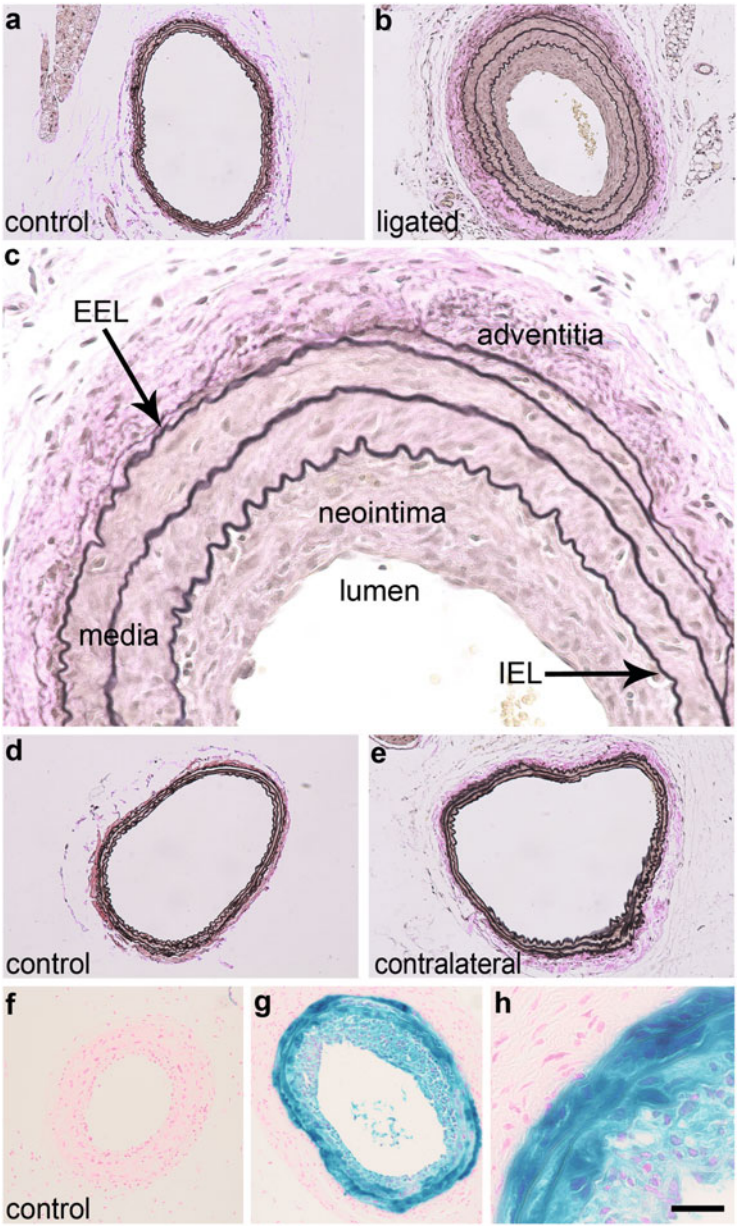

Fig. 3.1 Vascular response to complete carotid artery ligation. (**a–b)** Representative cross sections of the left common carotid artery at postoperative day 14 following sham ligation (*a*, *control*) or carotid artery ligation (*b*, *ligated*). (**c)** Lesion composition at high magnification (*lumen*, *neointima*, *media*, *adventitia*), with arrows identifying the external elastic lamina (*EEL*) and the internal elastic lamina (*IEL*). (**d–e**) Representative contralateral right common carotid artery following sham ligation (*d*, *control*) or left carotid artery ligation (*e*, *contralateral*), with

We found that the majority of the neointimal and medial vascular smooth muscle cells were positive for beta-galactosidase activity, indicating that the majority of neointimal cells were derived of medial vascular smooth muscle cell origin (Fig. 3.1f–h).

This review covers the materials needed (see Sect. 3.2), the ligation model (see Sect. 3.3), and a discussion of key points related to the model and the factors that contribute to the remodeling response in this model (see Sect. 3.4).

3.2 Materials

All procedures are performed in compliance with institutional and federal regulations and in accordance with *The Guide for the Care and Use of Laboratory Animals* by the National Academy of Sciences [10]. A veterinarian should be consulted prior to initiating this injury model. This is a survival surgery that is optimally performed under aseptic conditions. For the anesthesia, ketamine (50 mg/ml) and xylazine (20 mg/ml) are mixed with 0.17 ml of xylazine added per 1 ml of ketamine. The addition of atropine is optional. To anesthetize a mouse weighing approximately 25 g, 50–70 μl of this mixture are injected intraperitoneally with an insulin syringe (0.5 ml, Becton Dickinson). To prevent drying of the cornea during anesthesia, an ophthalmic ointment should be applied (e.g., Lacri-Lube®, Allergan). There are many suppliers of surgical instruments that carry the same or similar tools as those described, and specific descriptions are provided here only as a convenience. Materials needed for this surgical model are summarized in Table 3.1.

Fig. 3.1 (continued) evidence of outward remodeling (*e*). (**f–h**) Representative cross sections of ligated vessels from a Rosa26 Cre reporter line [8] crossed with a conditional, inducible smooth muscle myosin heavy chain (SM MHC)-CreER^{T2} line [9]. The reporter was activated prior to injury to constitutively express LacZ in fully differentiated vascular smooth muscle cells expressing the SM MHC marker [7]. After injury, tissues from vehicle-treated mice (*f*, *control*) and tamoxifen-induced mice (*g–h*) were assayed for β-galactosidase activity, yielding strong staining in the media and neointima, showing that the neointima is predominantly derived from differentiated medial vascular smooth muscle cells. Constrictive remodeling (*f*) also occurs in human vascular disease and is characterized by decreased circumference of the injured artery in response to decreased flow. Tissue collected by perfusion fixation followed by paraffin embedding and Verhoeff's staining (*a–e*) or by perfusion fixation followed by staining for β-galactosidase activity, post fixation, and counterstaining with nuclear fast red (*f–h*). Scale bar indicates 100 μm (*a*, *b*, *d–g*) or 25 μm (*c*, *h*)

Table 3.1 Materials needed for the carotid artery ligation model

Materials for the ligation procedure	Materials for the collection procedure	Materials used for both ligation and collection
Surgery platform, small rubber bands, and tape	Catheter (i.v.), 24-gauge or a 10 mL syringe with a 24–26-gauge needle for fixative perfusion	Dissecting microscope with adequate lighting
Small hair clipper	Fixative (glutaraldehyde, 4 % paraformaldehyde, or other fixative as desired)	Scalpel
Betadine solution and 70 % ethanol for skin disinfection	An absorbent underpad for the dissecting surface	Gauze (2 × 2 in.)
Cotton applicators	Rat tooth forceps	Jeweler's forceps, straight, 4″
6-0 silk suture	Phosphate-buffered saline (PBS) for rinsing the carotids	Microforceps
Bulldog clamp, Johns Hopkins, 1″ straight	Tissue processing/embedding cassettes	Microdissecting forceps with curved tip
Bulldog clamp, DeBakey, curved 5″	Lens paper for wrapping and immobilizing carotids arteries during tissue processing	Scissors, McPherson-Vannas, straight
Michel wound clip applying forceps 5″	Carboy with liquid nitrogen	Scissors, additional assorted sizes as desired
Michel wound clips, 7.5 mm	Dry ice for transfer of flash-frozen specimens	Hemostat, 3″, curved

3.3 Ligation Model of the Mouse Common Carotid Artery

This model is described in the 1997 publication by Kumar and Lindner [6]. Application of this model to a variety of inbred mouse strains has indicated that the remodeling responses vary depending on genetic background [11]. The surgical procedure is easy to perform and can be completed in less than 5 min from start to finish. This makes this model suitable for studies where large numbers of mice need to be examined.

3.3.1 Surgical Procedure

Following the induction of anesthesia, the mouse is placed in dorsal recumbency on the surgery platform, and rubber bands are used to secure the hind legs to the screws mounted on the side of the platform. Another rubber band is used to hold down the head by the upper incisors. A piece of tape is used to keep the front legs clear from the operating field. The skin along the ventral side of the neck is shaved followed by

the application of Betadine and ethanol disinfectant. A midline incision is made along the ventral side of the neck (1.5 cm in length). We routinely perform procedures on the left carotid artery because it has no side branches. The left salivary gland is moved laterally by blunt dissection and held away from the carotid bifurcation by the DeBakey clamp. The pretracheal strap muscles are pushed medially, while blunt dissection of the distal common carotid artery is performed with the microdissecting forceps with curved tips. These forceps are ideally suited to separate the connective tissue from the vessel and place the ligature. The common carotid artery is tied off by placing the ligature just proximal of the carotid bifurcation, with care taken not to disrupt or ligate the vagus nerve. For sham ligation, which may be performed as a surgical control, the common carotid artery is isolated but not ligated. Next, the skin edges are approximated and everted, and the incision is closed with wound clips. The recovery of the mouse on a heating pad is monitored, and postsurgical analgesics and care are administered in accordance with regulations and institutional operating procedures.

3.3.1.1 Surgical Complications

This procedure is generally well tolerated due to redundant blood supply to the brain via the circle of Willis. However, occasionally mice may undergo stroke and/or death following this procedure, especially in cases where there is altered cerebrovascular anatomy with impaired ability to compensate for local flow cessation [12]. Postoperative care should be provided in accordance with institutional and federal guidelines, and appropriate postoperative care may include euthanasia in the case of stroke or impairment. Evidence of nerve damage or stroke may include circling behavior, balance impairment, motor deficits, or spontaneous death. In the absence of other underlying factors, the complications of stroke or death are uncommon. Infection is rare in the carotid artery ligation model although precautions should still be taken to perform the surgery with aseptic technique.

The primary complication associated with this surgery is clotting of the carotid artery, and this can be managed as described in the quantification section.

3.3.2 Perfusion Fixation

For morphometric analyses, perfusion fixation should ideally be performed under physiological pressure with a glutaraldehyde-based fixative, because this abolishes any elastic recoil when the vessel is no longer under pressure. Perfusion fixation via a catheter (24 gauge) placed into the left ventricle is a preferred approach, although a syringe and needle can also be used. If desired, a very small incision can be cut into the left common carotid artery in situ just proximal of the ligature for optimal perfusion prior to fixation. As an alternative to glutaraldehyde, perfusion fixation

with 4 % paraformaldehyde can be performed. This is frequently utilized if required for subsequent tissue analysis such as immunostaining.

3.3.3 Tissue Collection and Processing

Careful attention to setup prior to carotid artery harvesting yields the best results for perfusion fixation and collection of carotid arteries for flash freezing.

Procedure for Carotid Artery Collection Anesthetize the mouse, and confirm anesthesia by loss of toe-pinch withdrawal. Lay the mouse in dorsal recumbency, and spray the neck and chest with 70 % ethanol, which mats the fur and minimizes release of loose fur during subsequent steps. Pinch the skin upward with rat tooth forceps, and cut to remove the skin over the thorax and upper abdomen. Locate the xiphoid process and make lateral cuts from the xiphoid process down the sides of the abdominal cavity. Grasping the xiphoid process upward, carefully poke the scissors into the thorax just lateral to the sternum and cut out the body of the sternum leaving the manubrium intact. Next, cut out the ventral portion of the left ribs to expose the heart. Perform the perfusion fixation step as desired (see Sect. 3.3.2). The whiskers, extremities, and tail will begin to twitch during the perfusion fixation, and the liver will turn from dark red to mottled and light brown. The use of an absorbent underpad over the dissecting surface aids in quick cleanup from this portion of the procedure. After perfusion fixation, the mouse is moved to the dissecting scope platform, in dorsal recumbency with the head proximal to the collector, and the remainder of the skin over the neck is removed. The salivary glands are then pinched upward and cut out, keeping the scissor tips up and dabbing the pooling blood with gauze. Lifting each forepaw in turn allows the clavicle and pectoralis muscles to be cut away from the sternal manubrium in a single cut. Next the sternocleidomastoid muscles are cut away. Then the scissor tips are inserted just below the suprasternal notch, and the manubrium is bisected and then removed by cutting away a portion of the upper ribs on each side to expose the heart. The pretracheal strap muscles are then retracted superiorly, exposing the trachea, followed by sequential removal of the trachea and the underlying esophagus. The carotids are then exposed and cleared. The pericardial fat overlying the base of the heart is pulled upward and snipped, keeping the scissor tips upward to avoid damage to the aortic arch. Using straight forceps, the heart is then flipped and retracted superiorly, allowing a single snip to cut across the ascending aortic arch at the base of the heart. The ascending aortic arch is then grasped with the forceps, and the aortic arch and carotids are removed en bloc, snipping away excess tissue and blotting released blood with gauze. The specimen is freed by snipping at the level of the carotid bifurcation, which will include the suture on the ligated side. The carotids are then rinsed in the PBS and placed in 4 % paraformaldehyde overnight. The following day, the specimens are rinsed in PBS, laid out and wrapped in a single layer of lens paper moistened with 70 % ethanol, and placed in a tissue

processing cassette in 70 % ethanol in preparation for tissue processing. The lens paper wrapping allows the carotids and aorta to be placed in anatomical orientation and immobilized during tissue processing. The specimen can then be paraffin embedded on end, with the ligated side on the left, and cross-sectioned at 5 μm, with 5 sections per slide across the 2 mm proximal to the ligature.

Flash-Freezing Protocol Alternatively, carotids can be harvested and flash frozen for downstream applications of DNA, RNA, or protein analysis. For flash freezing, the perfusion step is performed with PBS rather than fixative, and an effort is made to harvest the carotids as quickly as possible. In the interest of time, the carotids can be separately cut out directly from the aortic arch (left carotid) or from the subclavian artery branch point (right carotid) in situ without first removing the heart. The carotids are then wrapped in small foil packets and dropped into liquid nitrogen, followed by transfer to dry ice for transport to storage at −80 °C.

3.3.4 Morphometric Analysis of Arteries

3.3.4.1 Location

The importance of location in morphometric analysis of vascular lesion formation is well established [6, 13, 14]. Strain differences in neointimal lesion formation should also be considered [11]. In general, the severity of the lesion tends to decrease with distance from the ligature, with the most severe lesion occurring within the first 500 μm of the ligature in wild-type mice [14, 15]. Multiple valid models of quantification have been used, from intermittent sections along the length of the injured artery [13], to sections across a 500 μm–3 mm segment proximal to the ligation [16], to sections at the set distances 2.5, 4.5, and 6.5 mm from the ligation [17], to sections from a single point 3 mm from the ligation [18]. Alternatively, some groups have chosen to obtain measurements from the apex of the lesion as determined by serial sections at 150 μm intervals across the entire length of the artery [19]. Considerations in choosing an appropriate quantification scheme may include whether there is an expected increase or decrease in lesion size in comparison to control, overall cost, and desired number of slides generated and whether the intervening sections are retained for additional analysis.

A quantification scheme that we typically use for lesion analysis includes measurements at the six set distances of 200 μm, 350 μm, 500 μm, 1 mm, 1.5 mm, and 2 mm from the ligature. The rationale is that three measurements are taken 150 μm apart in the proximal 500 μm where the lesion is largest and three measurements are taken at 500 μm apart over the adjacent segment where the lesion tends to start tapering off [14]. The 200, 350, and 500 μm approaches have been previously described in the literature [20], and the additional 1, 1.5, and 2 mm sections ensure capture across a broader section of the lesion. The six measurements can then be used to generate an average lesion size per mouse. The averages

can then be compared by student's t-test, assuming normal distribution of the data, or by analysis of variance (ANOVA), in the case where study design involves comparison of more than two groups. While we have investigated the use of more sophisticated statistical modeling [14] (and Liaw Lab, unpublished data), we find that averaging data for each metric over the six distances is a straightforward and user-friendly method of quantification. Alternatively, depending on the study design, morphometric analysis can be performed at a set distance of 1.5 or 2 mm from the ligature. The advantage of this approach is that it results in less missing data than with models that include the 1 mm proximal to the ligature, the region most prone to clot.

3.3.4.2 Morphometry

The method of fixation and the type of fixative can have a major impact on the morphometric analysis of sectioned vessels. It is important that the vessels be perfusion fixed at physiological pressure. However, intravascular pressure at the time of perfusion is difficult to assess, and with the use of relatively small caliber perfusion catheters, a large drop in pressure is likely to occur along the length of the catheter itself. In addition, if fixatives are used that do not contain glutaraldehyde, the vessel will retain some of its elastic properties which will cause the vessel to contract or shrink upon excision. As a consequence, elastic lamellae will appear wrinkled and wavy, and this can be particularly evident in normal vessels that lack a neointima. The morphometric analysis of sections is facilitated if a histological stain is chosen that highlights the elastic lamellae such as Verhoeff's stain. This stain makes it particularly easy to trace the internal and external elastic laminae (IEL and EEL) and thus adds to increased accuracy of the measurements. An artery that has undergone constrictive arterial remodeling will display wavy elastic lamellae even if the vessels were harvested following optimal perfusion fixation. With the in situ morphology preserved, glutaraldehyde-based fixatives are ideal when morphometric analyses have a high priority. However, the need to perform immunohistochemistry on vessel sections may require formalin fixation or fresh-frozen tissue.

We typically perform the morphometric analysis by tracing out the lumen circumference, the IEL circumference, and the EEL circumference using a graphics pad, such as the Intuos 4® professional pen tablet by Wacom, in National Institutes of Health ImageJ software [21]. A photo of a stage micrometer at the desired magnification can be used to set the linear conversion rate of number of pixels per mm. This allows determination of the areas within the luminal and elastic laminae perimeter tracings. Tracing of the IEL and EEL should include bisection of the sinusoidal pattern in the case of a wavy line to most accurately capture the circumference and area measurements. The luminal area can be measured directly. The area of the neointima can be determined by subtracting the luminal area from the area bound by the IEL. The medial area is determined by subtracting the area

bound by the IEL from the area bound by the EEL. If desired, the tracings can be done by a trained blinded independent observer. Inter-rater reliability tends to be high as long as there are clear guidelines, such as excluding sections where clot is present as the presence of clot can interfere with the determination of the extent of the neointima present (Liaw lab, unpublished data). In this model, the most common outcome measures presented are lumen area, neointimal area, and neointimal/medial (N/M or intimal/medial) ratio, which is determined by dividing the neointimal area by the medial area. N/M ratio is a companion measure of neointimal lesion formation that takes into account changes that may be occurring in the media. Alternatively, some groups prefer to report neointimal lesion formation by measures of intimal thickness and medial thickness [22]. In this scenario, intimal thickness may be measured at the widest point. As neointimal lesion formation is not always concentric or symmetric, we prefer area measurements to thickness measurements. As an additional alternative, numbers of cells in the neointimal and medial layers can be counted and reported. If desired, some groups also present quantification measures for the adventitia [23]. In this case, care should be taken during collection to keep the adventitial layer completely intact.

Morphometric measurements are performed on the ligated side as well as on the unligated side, as the increase in blood flow experienced on the contralateral side can result in outward remodeling of the vessel. For this reason, a sham ligated artery, where the left common carotid artery is isolated but not ligated, is a preferable control vessel for comparison than the contralateral vessel from a ligated animal.

3.3.4.3 Exclusions from Morphometric Analysis

In most cases, the ligated vessels do not show signs of complete thrombotic occlusion with the exception of the 1 mm segment proximal to the ligature. Sections where clot is present are noted but excluded from the morphometric analysis. The percentage of excluded sections can be included in the statistical analysis to rule out statistically different percentages of excluded sections between groups. In rare instances where clotting occurs along a longer segment of the vessel (>2 mm proximal to the ligature), it is usually quite obvious at the time of vessel harvest, and these vessels are excluded from the analysis. Again, these vessels are noted but in our experience do not tend to correlate preferentially with control or experimental groups (Liaw Lab, unpublished data) or with a more or less experienced surgeon.

3.4 Discussion

Features of the vascular response to carotid artery ligation may include a combination of lumen narrowing by neointimal lesion formation and by constrictive remodeling, with relative contributions dependent on factors such as the

experimental model used and the genetic background of the mice. Strain-dependent data are available for assistance in choosing an appropriate mouse model for the desired experiment [11]. One major advantage of the ligation model over other models is that it is less likely to be influenced by variables related to surgical technique because it is easy to perform. This fact has made it a very popular model for studying vascular smooth muscle cell dedifferentiation, proliferation, migration, and redifferentiation in vivo [13, 24–38]. In addition, the quick duration of the ligation procedure makes it one of the most suitable models for high-throughput screening.

The type of question to be answered by the experiment will determine when the arteries will be harvested for analysis. In the ligation model, an extensive neointimal lesion will form within 2 weeks. The composition of the neointima, however, will continue to change over the course of several more weeks usually with an increase in extracellular matrix and a decrease in cellularity. Vascular smooth muscle cell proliferation is therefore preferably examined at earlier time points (less than 2 weeks after ligation) and neointimal lesion size preferably at later times (at or after 2 weeks). Typical collection days chosen for this model include an early collection time point (3–7 days), 14 days, and 28 days, although other time points may be used as desired.

In contrast with other denuding arterial injury models, a major inflammatory response is not typical of this model as there is preservation of the endothelium and generally low levels of mechanical injury. Carotid artery ligation would not therefore be an appropriate model for study of the inflammatory response associated with intimal lesion formation unless combined with other atherosclerosis mouse models that might be expected to contribute to the inflammatory response.

Review of the carotid artery ligation literature includes many mediators of the neointimal response, and these have been summarized in Table 3.2. These mediators include the broad categories of adhesion molecules; growth factors, cytokine, and hormone signaling; cytoskeletal; blood pathways/enzymes/blood pressure; reactive oxygen/oxidative stress; secreted proteins/enzymes; cell cycle related; transcriptional regulators; extracellular matrix related/proteases; transmembrane or membrane-anchored signaling molecules; intracellular enzymes; and microRNAs (miRNA). Of particular interest, the contribution of miRNA in neointima formation is a highly dynamic and emerging field. miRNA are small ~18–22 nucleotide noncoding RNA sequences that regulate gene expression. Carotid artery ligation studies focusing on miRNA regulation of intimal hyperplasia are expanding in number, and there is abundant in vitro and in vivo evidence for the role of miRNA in neointimal lesion formation. While the role of miRNA in other models of neointimal lesion formation is outside the scope of this chapter, there are several excellent reviews available on this topic [39–46]. Of note, the use of the carotid artery ligation model in combination with other atherosclerosis mouse models, such as the ApoE null with high-fat feeding or LDL null models, is also beyond the scope of this focused review and thus is not included in Table 3.2.

Table 3.2 Genes involved in the remodeling response after complete ligation of the mouse common carotid artery

Gene target	Description	Phenotype
Adhesion molecules		
P-selectin	Null mouse model	Decreased intimal/medial area ratio at 4 weeks, no inflammatory infiltration [13]
Growth factors, cytokine, and hormone signaling		
FGF-2	Blocking monoclonal antibody	Increased lumen size and vessel diameter at 4 weeks, outward remodeling of contralateral artery [47]
TNF-alpha	Null mouse model	Decreased intimal lesion at 4 weeks [48]
p75(NTR)	Null mouse model	Increased intimal lesion and decreased apoptosis at 2 and 4 weeks [34]
Endothelin (B) receptor	Null mouse model	Increased intimal area, intimal/medial area ratio, and stenosis at 2 weeks [29]
Fas ligand	FasL-*gld* mice; point mutation	Increased intimal lesion formation at 4 weeks [30]
PDGFRbeta	Chimeric mice with PDGFRbeta null cells	At 4 weeks after injury, increased proportion of PDGFRbeta null cells in media and decreased proportion in intima, showing deficiency in migration into intima [49]
MEKK1	Null mouse model	Decreased intimal area at 4 weeks [50]
Akt	Transgenic active Akt1 driven by a VE-cadherin promoter or a minimal SM22α promoter lacking the G/C-rich repressor region	Decreased intimal area and intimal/medial area ratio [51]; transgenic expression in smooth muscle cells inhibits apoptosis after ligation [52]
IL1beta, IL1R1	Null mouse models	Loss of either led to reduced intimal/medial area ratios [53]
Cthrc1	Transgenic mice with constitutive Cthrc1 expression	Decreased intimal area and intimal smooth muscle cell proliferation at 2 weeks [54]
S1P receptor2	Null mouse model	Increased smooth muscle cell replication, yielding large intimal lesions at 4 weeks [55]
Lysophosphatidic acid receptor	LPA1-null mouse model; LPA1/LPA2 double-null mouse model	LPA1-null mouse had increased intimal area, intimal/medial area ratio, and increased vessel area; LPA1/LPA2 double-null mice had decreased intimal area and intimal/medial area ratio [56]

(continued)

Table 3.2 (continued)

Gene target	Description	Phenotype
Soluble guanylate cyclase	Null mouse model	Selectively in males, sGCα1 nulls have decreased intimal medial area ratio and decreased stenosis [57]
Protein kinase Cδ	Null mouse model	Loss of PKCδ led to increased intimal/medial area ratio and small luminal area at 4 weeks, associated with decreased apoptosis [58]
Erythropoietin	i.p. protein injections 3x/week	Epo treatment increased intimal area and intimal/medial area ratio at 4 weeks [59]
Apelin	Null mouse model	Reduced intimal area and intimal/medial area ratio at 4 weeks [60]
Wnt4	Null mouse model	Decreased lesion area and proliferation at 3 weeks [61]
uPAR	Null mouse model	Decreased medial thickness and intimal/medial area ratio at 4 weeks [62]
ASK1	Null mouse model	Decreased intimal area and intimal/medial area ratio at 3 weeks [63]
Platelet factor 4	Null mouse model	Decreased total vessel area at 3 weeks [64]
Cortistatin	i.p. injections of protein every 2 days after ligation; null mouse model	Decreased intimal area with decreased cell proliferation at 4 weeks; null mouse had increased intimal/medial area ratio at 3 weeks [65]
Histidine carboxylase, histidine receptor	HDC-null mouse; H1R-null mouse	Decreased intimal/medial area ratio at 3 weeks [66]; H1R-null mouse had decreased intimal/medial area ratio at 2 and 3 weeks [67]
IL-19	Null mouse model	Increased intimal lesion formation at 4 weeks [68]
Cytoskeletal		
Vimentin	Null mouse model	Decreased vessel diameter and medial area at 4 weeks [37]
ROCK1	ROCK1+/− mice	Decreased intimal area and intimal/medial area ratio at 4 weeks [69]
Blood pathways/enzymes/blood pressure		
Kallikrein	Adenoviral transduction of human form i.v.	Decreased neointimal lesion formation at 2 weeks, dependent on kinin B(2) receptor [70]
uPA, α2AP, factor VIII	Null mouse models	uPA null had higher luminal stenosis, and FVIII null had lower luminal stenosis at 1, 2 weeks; α2AP null had lower luminal stenosis at 1 week [25]; uPA null had no intimal lesion at 4 weeks [71]

(continued)

Table 3.2 (continued)

Gene target	Description	Phenotype
Tissue factor pathway inhibitor	Intravascular adenoviral delivery of TFPI; TFPI heterozygous mouse	Adenoviral TFPI decreased intimal lesion and increased lumen area at 4 weeks [72]; TFPI heterozygous mice had increased intimal area at 2 weeks [36]
Haptoglobin	Null mouse model	Null females had increased intimal hyperplasia only at 8 days, no differences at 20 days [73]
Vitronectin, PAI-1	Null mouse models	Loss of either vitronectin or PAI-1 decreased intimal area and intimal/medial area ratio [74]; loss of PAI-1 or vitronectin generated larger intimal lesion and more smooth muscle proliferation [35]
Tissue ACE	Null mouse model	Suppressed medial thickening and less outward remodeling [75]
C-reactive protein	Human CRP transgenic mouse model	Increased intimal area at 4 weeks [76]
Thrombomodulin	Recombinant protein i.v.	Decreased intimal lesion and total vessel area in mice receiving thrombomodulin at 4 weeks [77]
Endothelin1	Conditional null driven by Tie2-Cre	Decreased intimal area and intimal/medial area ratio at 4 weeks with decreased cell proliferation [78]
Plasminogen/angiostatin	Plasminogen kringle 1–5 for 4 weeks after injury; angiostatin	Both angiostatin and kringle 1–5 suppressed intimal area and intimal/medial area ratio at 4 weeks [79]
Reactive oxygen/oxidative stress		
Nitric oxide synthase	eNOS or iNOS null mice; eNOS transgenic mice (preproendothelin-1 promoter); NOS2 (iNOS) null mice	Increased intima at 4 weeks in eNOS null; more constrictive remodeling in iNOS null [17, 27]; iNOS null males had decreased intimal area at 4 weeks; females only showed this effect if ovariectomized [80]; loss of NOS2 (iNOS) increased intimal lesion area and intimal/medial area ratio at 4 weeks [81]; decreased intimal and medical areas at 4 weeks in eNOS transgenics [16]; null nNOS or eNOS increased intimal/medial area ratio, while null iNOS did not, and the triple null mice had further increased intimal/medial area ratio [82]

(continued)

Table 3.2 (continued)

Gene target	Description	Phenotype
Cyclophilin A	Null mouse model and conditional transgenic mouse model activated by SM22α-Cre	On null background, decreased intimal and medial areas, and decreased intimal/medial area ratio; transgenic overexpression led to increased intimal and medial areas, and increased intimal/medial area ratio at 2 weeks [83]
Sequestosome1	Null mouse model	Increased intimal area and stenotic ratio (percent intima within the total IEL area) [84]
Secreted proteins/enzymes		
Uteroglobin	Adventitial adenoviral delivery of uteroglobin	Uteroglobin decreased intima/media area ratio at 30 days [85]
Endothelial lipase	Null and transgenic overexpressing mouse models	Null had decreased and transgenic had increased intimal area and intimal/medial area ratio at 2 and 4 weeks [86]
Cell cycle related		
p130	Null mouse model	Increased intimal lesion and overall vessel wall area [33]
Skp2	Null mouse model	Reduced intimal area at 4 weeks [87]
BubR1	Hypomorph mouse (20 % of normal)	Decreased intimal area and intimal/medial area ratio at 4 weeks [88]
Transcriptional regulators		
Steroid receptor coactivator-3	Null mouse model	Increased intimal area and intimal/medial area ratio at 4 weeks [89]
TR3	Transgenic expressing dominant-negative TR3 or full-length TR3 (SM22α promoter)	Dominant-negative TR3 led to increased intimal lesion formation; transgenic expression of full-length TR3 inhibited intimal lesion formation [90]
NF-κB	p105 null mouse model or adeno-associated viral transduction of IκBα into tunica media 2 weeks prior to injury; p50 null mouse model	Loss of p105 decreased intimal area at 2 weeks [91] and 4 weeks [92]; introduction of IκBα decreased intimal area at 2 weeks [91]; loss of p50 led to increased outward remodeling (EEL area) in the contralateral artery [93]
Klf4	$Klf4^{loxP}$ allele activated by ERT-CRE or Tie2-Cre	Increased intimal and medial areas at 1, 2, and 3 weeks associated with increased proliferation [94]; increased intimal and decreased luminal area in Tie2-Cre activated null mouse at 3 weeks [95]
YAP	Conditional heterozygous mouse model driven by SM22α-Cre	Reduction in intimal area and intimal/medial area ratio at 3 weeks [96]

(continued)

Table 3.2 (continued)

Gene target	Description	Phenotype
NOR-1	Transgenic mice driven by SM22α promoter	Increased intimal/medial area ratio and % stenosis at 3 weeks [97]
DJ-1/park7	Null mouse model	Increased intimal/medial area ratio at 3 weeks [98]
FHL2	Null mouse model	Accelerated intimal lesion formation with increased intimal/medial area ratio at 1, 2, and 4 weeks, associated with higher proliferation rates [99]
Myocardin	Heterozygous-null mouse model	Heterozygous loss of myocardin increased neointimal area, neointimal cell number, and medial area but not medial cell number at 2 weeks [100]
Extracellular matrix related/proteases		
Osteopontin	Null mouse model	Decreased inflammation at 4 days, smaller intimal lesions with greater constrictive remodeling at 2 weeks, which normalized by 4 weeks [101]
MMP2	Null mouse model	Decreased intimal area and intimal/medial area ratio at 2 and 4 weeks [31]
MMP3	Null mouse model	Decreased intimal lesion area at 4 weeks; associated with loss of MMP9 activation [102]
MMP9	Null mouse model	Slight decrease in lumen diameter of contralateral unligated artery at 3 and 6 weeks [103]
Beta3 integrin	Null mouse model	Reduced intimal area and intimal smooth muscle number 1, 2, and 3 weeks and 3 months after injury [104]
Fibulin-5	Null mouse model	Enhanced intimal/medial area ratio, decreased medial thickness and reduced vessel extensibility [105]
PAPP-A	Null mouse model; transgenic mice driven by SM22α promoter (G/C-rich mutant)	Null had lack of IGFBP-4 activity and reduced intimal area at 4 weeks [106]; transgenic had decreased intimal area at 5 and 10 days with early suppression of proliferation, no difference by 15 days [107]
TSP1	Null mouse model	Decreased intimal size and increased medial area at 4 weeks [108]
Fibulin-2, fibulin-5	Null mouse models, double null	Double null mice had increased outward remodeling, with decreased thickness of the media and increased intimal/medial area ratio with a propensity for thrombus formation [109]

(continued)

Table 3.2 (continued)

Gene target	Description	Phenotype
Cathepsin K	Null mouse model	Decreased intimal and intimal/medial area ratio at 4 weeks [110]
Transglutaminase 2	Null mouse model	Decreased intimal area and intimal/medial area ratio at 2 and 4 weeks [111, 112]
Transmembrane or membrane-anchored signaling molecules		
Tetraspanin CD9	Neutralizing CD9 antibody or human CD9 adenovirus given intraluminally	Small decrease in intimal/medial area ratios with antibody at 2 and 4 weeks; small increase in intimal/medial area ratio at 2 weeks with adenoviral CD9 transduction [113]
Notch1	Notch1+/− and conditional het activated by SM MHC-Cre; perivascular siRNA in pluronic gel after injury	Notch1+/− and smooth muscle heterozygous have similar phenotype of decreased intimal area and intimal/medial area ratio at 4 weeks [114]; siRNA decreased intimal lesion and intimal/medial area ratio at 2 weeks associated with decreased proliferation [115]
Jagged1	Conditional Jag1 heterozygous mouse model controlled by Tie2-Cre	Enhanced intimal area and intimal/medial area ratio at 4 weeks [116]
MAML1 (Notch signaling)	Dominant-negative MAML1 controlled by SM22-Cre	No survival after carotid artery ligation due to defects in the cerebral collateral circulation within the circle of Willis [12]
CD40	Null mouse model	Decreased intimal area and intimal/medial area ratio at 3 weeks with loss of CD40 in vessel wall or in bone marrow-transplanted cells with high-cholesterol diet [117]; reduced intimal area [118]
RAGE	Null mouse model	Decreased intimal area and intimal/medial area ratio at 3 weeks [119]
Vanin1	Null mouse model	Decreased intimal area and intimal/medial area ratio at 3 weeks with decreased proliferation [120]
Necl-5	Null mouse model	Decreased intimal/medial area ratio at 4 weeks associated with decreased proliferation [121]
ENPP1	Null mouse model	Decreased intimal area and intimal/medial area ratio at 2 and 3 weeks [122]
Intracellular enzymes		
Ephx2	Null mouse model	Decreased intimal area and intimal/medial area ratio at 6 weeks [123]

(continued)

Table 3.2 (continued)

Gene target	Description	Phenotype
PTEN	Conditional null mouse model controlled by SM22α-Cre, as heterozygotes	Reduction of PTEN (+/−) globally or mediated by SM22α-Cre has increased intimal areas and increased intimal/medial area ratios at 2 weeks [124]
CaMKIIδ	Null mouse model	Decreased intimal lesion formation at 2 weeks associated with decreased cell proliferation [125]
SIRT1	Transgenic mice expressing human SIRT1 under SM22α promoter	Decreased intimal/medial area ratio at 4 weeks associated with decreased proliferation [126]
Cystathionine gamma-lyase	Null mouse model	Increased intimal area and intimal/medial area ratio at 4 weeks [127]
VIA phospholipase A2 (iPLA2β)	Null mouse model and transgenic mouse model with smooth muscle cell expression (SM MHC promoter)	Null mice had decreased intimal area and intimal/medial area ratio at 4 weeks; transgenic mice increased intimal area and intimal/medial area ratio at 4 weeks [128]
miRNA		
miR-126	Null mouse model	Decreased intimal lesion formation at 4 weeks [129]
miR-143/145	Null mouse model	Decreased intimal thickness, medial thickness, and intimal/medial area ratio at 4 weeks [22]
miR-155	Null mouse model	Decreased intimal area and intimal/medial area ratio at 3 weeks [130]
miR-663	Adventitial adenoviral delivery of miR-663	Decreased intimal area and intimal/medial area ratio at 2 weeks [131]

Drug or small molecule treatments as pathway antagonists or agonists are not included. Studies with this injury model used in combination in atherosclerosis models (i.e., ApoE null with high-fat feeding, LDL null background) are also not included

In summary, the carotid artery ligation model has been an invaluable tool for elucidating the role of specific gene contributions to the complex vascular remodeling response.

Acknowledgments The Histopathology Core Facility is supported by P20GM103465 (D. Wojchowski, PI) and P30GM103392 (R. Friesel, PI). Additional funding is provided by the American Heart Association Predoctoral Fellowship 14PRE17820000, 1/1/14–12/31/15 (S. Peterson, PI), and R01 HL070865 (L. Liaw, PI). We would like to thank Anne Harrington and Jacqueline Turner for their excellent technical assistance. We acknowledge Dr. Stefan Offermann's generous gift of the SM MHC-*Cre*ER^{T2} mice via the Dr. Joseph M. Miano laboratory at the University of Rochester Medical Center.

References

1. Baumgartner HR. The role of blood flow in platelet adhesion, fibrin deposition, and formation of mural thrombi. Microvasc Res. 1973;5(2):167–79. 0026-2862(73)90069-1 [pii].
2. Reidy MA, Schwartz SM. Endothelial regeneration. III. Time course of intimal changes after small defined injury to rat aortic endothelium. Lab Invest. 1981;44(4):301–8.
3. Lindner V, Fingerle J, Reidy MA. Mouse model of arterial injury. Circ Res. 1993;73 (5):792–6.
4. Roque M, Fallon JT, Badimon JJ, Zhang WX, Taubman MB, Reis ED. Mouse model of femoral artery denudation injury associated with the rapid accumulation of adhesion molecules on the luminal surface and recruitment of neutrophils. Arterioscler Thromb Vasc Biol. 2000;20(2):335–42.
5. Zhou M, Sutliff RL, Paul RJ, Lorenz JN, Hoying JB, Haudenschild CC, et al. Fibroblast growth factor 2 control of vascular tone. Nat Med. 1998;4(2):201–7.
6. Kumar A, Lindner V. Remodeling with neointima formation in the mouse carotid artery after cessation of blood flow. Arterioscler Thromb Vasc Biol. 1997;17(10):2238–44.
7. Nguyen AT, Gomez D, Bell RD, Campbell JH, Clowes AW, Gabbiani G, et al. Smooth muscle cell plasticity: fact or fiction? Circ Res. 2013;112(1):17–22. doi:10.1161/CIRCRESAHA.112.281048.
8. Soriano P. Generalized lacZ expression with the ROSA26 Cre reporter strain. Nat Genet. 1999;21(1):70–1. doi:10.1038/5007.
9. Wirth A, Benyo Z, Lukasova M, Leutgeb B, Wettschureck N, Gorbey S, et al. G12-G13-LARG-mediated signaling in vascular smooth muscle is required for salt-induced hypertension. Nat Med. 2008;14(1):64–8. doi:10.1038/nm1666.
10. CUGCULA. Guide for the care and use of laboratory animals. 8th ed. The National Academies Collection: Reports funded by National Institutes of Health. Washington (DC); 2011.
11. Harmon KJ, Couper LL, Lindner V. Strain-dependent vascular remodeling phenotypes in inbred mice. Am J Pathol. 2000;156(5):1741–8.
12. Proweller A, Wright AC, Horng D, Cheng L, Lu MM, Lepore JJ et al. Notch signaling in vascular smooth muscle cells is required to pattern the cerebral vasculature. Proc Natl Acad Sci U S A. 2007;104(41):16275–80. doi:10.1073/pnas.0707950104
13. Kumar A, Hoover JL, Simmons CA, Lindner V, Shebuski RJ. Remodeling and neointimal formation in the carotid artery of normal and P-selectin-deficient mice [see comments]. Circulation. 1997;96(12):4333–42.
14. Myers DL, Liaw L. Improved analysis of the vascular response to arterial ligation using a multivariate approach. Am J Pathol. 2004;164(1):43–8.
15. Holt AW, Tulis DA. Experimental rat and mouse carotid artery surgery: injury & remodeling studies. ISRN Minim Invasive Surg. 2013;2013. doi:10.1155/2013/167407.
16. Kawashima S, Yamashita T, Ozaki M, Ohashi Y, Azumi H, Inoue N, et al. Endothelial NO synthase overexpression inhibits lesion formation in mouse model of vascular remodeling. Arterioscler Thromb Vasc Biol. 2001;21(2):201–7.
17. Zhang LN, Wilson DW, da Cunha V, Sullivan ME, Vergona R, Rutledge JC, et al. Endothelial NO synthase deficiency promotes smooth muscle progenitor cells in association with upregulation of stromal cell-derived factor-1alpha in a mouse model of carotid artery ligation. Arterioscler Thromb Vasc Biol. 2006;26(4):765–72. doi:10.1161/01.ATV.0000207319.28254.8c.
18. da Cunha V, Martin-McNulty B, Vincelette J, Zhang L, Rutledge JC, Wilson DW, et al. Interaction between mild hypercholesterolemia, HDL-cholesterol levels, and angiotensin II in intimal hyperplasia in mice. J Lipid Res. 2006;47(3):476–83. doi:10.1194/jlr.M500341-JLR200.
19. Ivan E, Khatri JJ, Johnson C, Magid R, Godin D, Nandi S, et al. Expansive arterial remodeling is associated with increased neointimal macrophage foam cell content: the murine model of macrophage-rich carotid artery lesions. Circulation. 2002;105(22):2686–91.

20. Hage FG, Oparil S, Xing D, Chen YF, McCrory MA, Szalai AJ. C-reactive protein-mediated vascular injury requires complement. Arterioscler Thromb Vasc Biol. 2010;30(6):1189–95. doi:10.1161/ATVBAHA.110.205377.
21. Schneider CA, Rasband WS, Eliceiri KW. NIH image to imagej: 25 years of image analysis. Nat Methods. 2012;9(7):671–5.
22. Xin M, Small EM, Sutherland LB, Qi X, McAnally J, Plato CF et al. MicroRNAs miR-143 and miR-145 modulate cytoskeletal dynamics and responsiveness of smooth muscle cells to injury. Genes Dev. 2009;23(18):2166–78. doi:10.1101/gad.1842409. gad.1842409 [pii]
23. Godin D, Ivan E, Johnson C, Magid R, Galis ZS. Remodeling of carotid artery is associated with increased expression of matrix metalloproteinases in mouse blood flow cessation model. Circulation. 2000;102(23):2861–6.
24. Galis ZS, Johnson C, Godin D, Magid R, Shipley JM, Senior RM, et al. Targeted disruption of the matrix metalloproteinase-9 gene impairs smooth muscle cell migration and geometrical arterial remodeling. Circ Res. 2002;91(9):852–9.
25. Kawasaki T, Dewerchin M, Lijnen HR, Vreys I, Vermylen J, Hoylaerts MF. Mouse carotid artery ligation induces platelet-leukocyte-dependent luminal fibrin, required for neointima development. Circ Res. 2001;88(2):159–66.
26. Morishita T, Tsutsui M, Shimokawa H, Horiuchi M, Tanimoto A, Suda O, et al. Vasculoprotective roles of neuronal nitric oxide synthase. FASEB J. 2002;16 (14):1994–6.
27. Yogo K, Shimokawa H, Funakoshi H, Kandabashi T, Miyata K, Okamoto S, et al. Different vasculoprotective roles of NO synthase isoforms in vascular lesion formation in mice. Arterioscler Thromb Vasc Biol. 2000;20(11):E96–100.
28. Hollestelle SC, De Vries MR, Van Keulen JK, Schoneveld AH, Vink A, Strijder CF, et al. Toll-like receptor 4 is involved in outward arterial remodeling. Circulation. 2004;109 (3):393–8.
29. Murakoshi N, Miyauchi T, Kakinuma Y, Ohuchi T, Goto K, Yanagisawa M, et al. Vascular endothelin-B receptor system in vivo plays a favorable inhibitory role in vascular remodeling after injury revealed by endothelin-B receptor-knockout mice. Circulation. 2002;106 (15):1991–8.
30. Sata M, Walsh K. Fas ligand-deficient mice display enhanced leukocyte infiltration and intima hyperplasia in flow-restricted vessels. J Mol Cell Cardiol. 2000;32(8):1395–400. doi:10.1006/jmcc.2000.1176.
31. Kuzuya M, Kanda S, Sasaki T, Tamaya-Mori N, Cheng XW, Itoh T, et al. Deficiency of gelatinase a suppresses smooth muscle cell invasion and development of experimental intimal hyperplasia. Circulation. 2003;108(11):1375–81. doi:10.1161/01.CIR.0000086463.15540.3C.
32. Acevedo L, Yu J, Erdjument-Bromage H, Miao RQ, Kim JE, Fulton D, et al. A new role for Nogo as a regulator of vascular remodeling. Nat Med. 2004;10(4):382–8.
33. Sindermann JR, Smith J, Kobbert C, Plenz G, Skaletz-Rorowski A, Solomon JL, et al. Direct evidence for the importance of p130 in injury response and arterial remodeling following carotid artery ligation. Cardiovasc Res. 2002;54(3):676–83.
34. Kraemer R. Reduced apoptosis and increased lesion development in the flow-restricted carotid artery of p75(NTR)-null mutant mice. Circ Res. 2002;91(6):494–500.
35. de Waard V, Arkenbout EK, Carmeliet P, Lindner V, Pannekoek H. Plasminogen activator inhibitor 1 and vitronectin protect against stenosis in a murine carotid artery ligation model. Arterioscler Thromb Vasc Biol. 2002;22(12):1978–83.
36. Singh R, Pan S, Mueske CS, Witt TA, Kleppe LS, Peterson TE, et al. Tissue factor pathway inhibitor deficiency enhances neointimal proliferation and formation in a murine model of vascular remodelling. Thromb Haemost. 2003;89(4):747–51. doi:10.1267/THRO03040747.
37. Schiffers PM, Henrion D, Boulanger CM, Colucci-Guyon E, Langa-Vuves F, van Essen H, et al. Altered flow-induced arterial remodeling in vimentin-deficient mice. Arterioscler Thromb Vasc Biol. 2000;20(3):611–6.

38. Rectenwald JE, Minter RM, Moldawer LL, Abouhamze Z, La Face D, Hutchins E, et al. Interleukin-10 fails to modulate low shear stress-induced neointimal hyperplasia. J Surg Res. 2002;102(2):110–8.
39. Wei Y, Schober A, Weber C. Pathogenic arterial remodeling: the good and bad of microRNAs. Am J Physiol Heart Circ Physiol. 2013;304(8):H1050–9. doi:10.1152/ajpheart.00267.2012.
40. Albinsson S, Sward K. Targeting smooth muscle microRNAs for therapeutic benefit in vascular disease. Pharmacol Res. 2013;75:28–36. doi:10.1016/j.phrs.2013.04.003.
41. O'Sullivan JF, Neylon A, McGorrian C, Blake GJ. MicroRNA Expression in Coronary Artery Disease. MicroRNA. 2014;2(3):205–11.
42. Jakob P, Landmesser U. Role of microRNAs in stem/progenitor cells and cardiovascular repair. Cardiovasc Res. 2012;93(4):614–22. doi:10.1093/cvr/cvr311.
43. Jamaluddin MS, Weakley SM, Zhang L, Kougias P, Lin PH, Yao Q, et al. miRNAs: roles and clinical applications in vascular disease. Expert Rev Mol Diagn. 2011;11(1):79–89. doi:10.1586/erm.10.103.
44. Bonauer A, Boon RA, Dimmeler S. Vascular microRNAs. Curr Drug Targets. 2010;11(8):943–9.
45. Song Z, Li G. Role of specific microRNAs in regulation of vascular smooth muscle cell differentiation and the response to injury. J Cardiovasc Transl Res. 2010;3(3):246–50. doi:10.1007/s12265-010-9163-0.
46. Lacolley P, Regnault V, Nicoletti A, Li Z, Michel JB. The vascular smooth muscle cell in arterial pathology: a cell that can take on multiple roles. Cardiovasc Res. 2012;95(2):194–204. doi:10.1093/cvr/cvs135.
47. Bryant SR, Bjercke RJ, Erichsen DA, Rege A, Lindner V. Vascular remodeling in response to altered blood flow is mediated by fibroblast growth factor-2. Circ Res. 1999;84(3):323–8.
48. Rectenwald JE, Moldawer LL, Huber TS, Seeger JM, Ozaki CK. Direct evidence for cytokine involvement in neointimal hyperplasia. Circulation. 2000;102(14):1697–702.
49. Buetow BS, Tappan KA, Crosby JR, Seifert RA, Bowen-Pope DF. Chimera analysis supports a predominant role of PDGFRbeta in promoting smooth-muscle cell chemotaxis after arterial injury. Am J Pathol. 2003;163(3):979–84.
50. Li Y, Minamino T, Tsukamoto O, Yujiri T, Shintani Y, Okada K, et al. Ablation of MEK kinase 1 suppresses intimal hyperplasia by impairing smooth muscle cell migration and urokinase plasminogen activator expression in a mouse blood-flow cessation model. Circulation. 2005;111(13):1672–8. doi:10.1161/01.CIR.0000160350.20810.0F.
51. Mukai Y, Rikitake Y, Shiojima I, Wolfrum S, Satoh M, Takeshita K, et al. Decreased vascular lesion formation in mice with inducible endothelial-specific expression of protein kinase Akt. J Clin Invest. 2006;116(2):334–43. doi:10.1172/JCI26223.
52. Tucka J et al. (2014) Akt1 regulates vascular smooth muscle cell apoptosis through FoxO3a and Apaf1 and protects against arterial remodeling and atherosclerosis. Arterioscler Thromb Vasc Biol. PMID: 25234814, doi: 10.1161/ATVBAHA.114.304284.
53. Chamberlain J, Evans D, King A, Dewberry R, Dower S, Crossman D, et al. Interleukin-1beta and signaling of interleukin-1 in vascular wall and circulating cells modulates the extent of neointima formation in mice. Am J Pathol. 2006;168(4):1396–403.
54. LeClair RJ, Durmus T, Wang Q, Pyagay P, Terzic A, Lindner V. Cthrc1 is a novel inhibitor of transforming growth factor-beta signaling and neointimal lesion formation. Circ Res. 2007;100(6):826–33.
55. Shimizu T, Nakazawa T, Cho A, Dastvan F, Shilling D, Daum G, et al. Sphingosine 1-phosphate receptor 2 negatively regulates neointimal formation in mouse arteries. Circ Res. 2007;101(10):995–1000. doi:10.1161/CIRCRESAHA.107.159228.
56. Panchatcharam M, Miriyala S, Yang F, Rojas M, End C, Vallant C, et al. Lysophosphatidic acid receptors 1 and 2 play roles in regulation of vascular injury responses but not blood pressure. Circ Res. 2008;103(6):662–70. doi:10.1161/CIRCRESAHA.108.180778.
57. Vermeersch P, Buys E, Sips P, Pokreisz P, Marsboom G, Gillijns H, et al. Gender-specific modulation of the response to arterial injury by soluble guanylate cyclase alpha1. Open Cardiovasc Med J. 2009;3:98–104. doi:10.2174/1874192400903010098.

58. Yamanouchi D, Kato K, Ryer EJ, Zhang F, Liu B. Protein kinase C delta mediates arterial injury responses through regulation of vascular smooth muscle cell apoptosis. Cardiovasc Res. 2010;85(3):434–43. doi:10.1093/cvr/cvp328.
59. Janmaat ML, Heerkens JL, de Bruin AM, Klous A, de Waard V, de Vries CJ. Erythropoietin accelerates smooth muscle cell-rich vascular lesion formation in mice through endothelial cell activation involving enhanced PDGF-BB release. Blood. 2010;115(7):1453–60. doi:10.1182/blood-2009-07-230870.
60. Kojima Y, Kundu RK, Cox CM, Leeper NJ, Anderson JA, Chun HJ, et al. Upregulation of the apelin-APJ pathway promotes neointima formation in the carotid ligation model in mouse. Cardiovasc Res. 2010;87(1):156–65. doi:10.1093/cvr/cvq052.
61. Tsaousi A, Williams H, Lyon CA, Taylor V, Swain A, Johnson JL, et al. Wnt4/beta-catenin signaling induces VSMC proliferation and is associated with intimal thickening. Circ Res. 2011;108(4):427–36. doi:10.1161/CIRCRESAHA.110.233999.
62. Kiyan Y, Limbourg A, Kiyan R, Tkachuk S, Limbourg FP, Ovsianikov A, et al. Urokinase receptor associates with myocardin to control vascular smooth muscle cells phenotype in vascular disease. Arterioscler Thromb Vasc Biol. 2012;32(1):110–22. doi:10.1161/ATVBAHA.111.234369.
63. Tasaki T, Yamada S, Guo X, Tanimoto A, Wang KY, Nabeshima A, et al. Apoptosis signal-regulating kinase 1 deficiency attenuates vascular injury-induced neointimal hyperplasia by suppressing apoptosis in smooth muscle cells. Am J Pathol. 2013;182(2):597–609. doi:10.1016/j.ajpath.2012.10.008.
64. Shi G, Field DJ, Long X, Mickelsen D, Ko KA, Ture S, et al. Platelet factor 4 mediates vascular smooth muscle cell injury responses. Blood. 2013;121(21):4417–27. doi:10.1182/blood-2012-09-454710.
65. Duran-Prado M, Morell M, Delgado-Maroto V, Castano JP, Aneiros-Fernandez J, de Lecea L, et al. Cortistatin inhibits migration and proliferation of human vascular smooth muscle cells and decreases neointimal formation on carotid artery ligation. Circ Res. 2013;112(11):1444–55. doi:10.1161/CIRCRESAHA.112.300695.
66. Sasaguri Y, Wang KY, Tanimoto A, Tsutsui M, Ueno H, Murata Y, et al. Role of histamine produced by bone marrow-derived vascular cells in pathogenesis of atherosclerosis. Circ Res. 2005;96(9):974–81. doi:10.1161/01.RES.0000166325.00383.ed.
67. Yamada S, Wang KY, Tanimoto A, Guo X, Nabeshima A, Watanabe T, et al. Histamine receptors expressed in circulating progenitor cells have reciprocal actions in ligation-induced arteriosclerosis. Pathol Int. 2013;63(9):435–47. doi:10.1111/pin.12091.
68. Ellison S, Gabunia K, Richards JM, Kelemen SE, England RN, Rudic D, et al. IL-19 reduces ligation-mediated neointimal hyperplasia by reducing vascular smooth muscle cell activation. Am J Pathol. 2014;184(7):2134–43. doi:10.1016/j.ajpath.2014.04.001.
69. Noma K, Rikitake Y, Oyama N, Yan G, Alcaide P, Liu PY, et al. ROCK1 mediates leukocyte recruitment and neointima formation following vascular injury. J Clin Invest. 2008;118(5):1632–44. doi:10.1172/JCI29226.
70. Emanueli C, Salis MB, Chao J, Chao L, Agata J, Lin KF, et al. Adenovirus-mediated human tissue kallikrein gene delivery inhibits neointima formation induced by interruption of blood flow in mice. Arterioscler Thromb Vasc Biol. 2000;20(6):1459–66.
71. Martin-McNulty B, Zhang L, da Cunha V, Vincelette J, Rutledge JC, Vergona R, et al. Urokinase-type plasminogen activator deficiency (uPA-KO) prevented carotid artery ligation-induced vascular remodeling in mice. Transl Res. 2007;149(2):70–5. doi:10.1016/j.trsl.2006.09.002.
72. Singh R, Pan S, Mueske CS, Witt T, Kleppe LS, Peterson TE, et al. Role for tissue factor pathway in murine model of vascular remodeling. Circ Res. 2001;89(1):71–6.
73. de Kleijn DP, Smeets MB, Kemmeren PP, Lim SK, Van Middelaar BJ, Velema E, et al. Acute-phase protein haptoglobin is a cell migration factor involved in arterial restructuring. FASEB J. 2002;16(9):1123–5. doi:10.1096/fj.02-0019fje.

74. Peng L, Bhatia N, Parker AC, Zhu Y, Fay WP. Endogenous vitronectin and plasminogen activator inhibitor-1 promote neointima formation in murine carotid arteries. Arterioscler Thromb Vasc Biol. 2002;22(6):934–9.
75. Hilgers RH, Schiffers PM, Aartsen WM, Fazzi GE, Smits JF, De Mey JG. Tissue angiotensin-converting enzyme in imposed and physiological flow-related arterial remodeling in mice. Arterioscler Thromb Vasc Biol. 2004;24(5):892–7. doi:10.1161/01.ATV.0000126374.60073.3d.
76. Wang D, Oparil S, Chen YF, McCrory MA, Skibinski GA, Feng W, et al. Estrogen treatment abrogates neointima formation in human C-reactive protein transgenic mice. Arterioscler Thromb Vasc Biol. 2005;25(10):2094–9. doi:10.1161/01.ATV.0000179602.85797.3f.
77. Li YH, Liu SL, Shi GY, Tseng GH, Liu PY, Wu HL. Thrombomodulin plays an important role in arterial remodeling and neointima formation in mouse carotid ligation model. Thromb Haemost. 2006;95(1):128–33.
78. Anggrahini DW, Emoto N, Nakayama K, Widyantoro B, Adiarto S, Iwasa N, et al. Vascular endothelial cell-derived endothelin-1 mediates vascular inflammation and neointima formation following blood flow cessation. Cardiovasc Res. 2009;82(1):143–51. doi:10.1093/cvr/cvp026.
79. Chang PC, Wu HL, Lin HC, Wang KC, Shi GY. Human plasminogen kringle 1–5 reduces atherosclerosis and neointima formation in mice by suppressing the inflammatory signaling pathway. J Thromb Haemost. 2010;8(1):194–201. doi:10.1111/j.1538-7836.2009.03671.x.
80. Tolbert T, Thompson JA, Bouchard P, Oparil S. Estrogen-induced vasoprotection is independent of inducible nitric oxide synthase expression: evidence from the mouse carotid artery ligation model. Circulation. 2001;104(22):2740–5.
81. Sirsjo A, Lofving A, Hansson GK, Wagsater D, Tokuno S, Valen G. Deficiency of nitric oxide synthase 2 results in increased neointima formation in a mouse model of vascular injury. J Cardiovasc Pharmacol. 2003;41(6):897–902.
82. Furuno Y, Morishita T, Toyohira Y, Yamada S, Ueno S, Morisada N, et al. Crucial vasculoprotective role of the whole nitric oxide synthase system in vascular lesion formation in mice: Involvement of bone marrow-derived cells. Nitric Oxide Biol Chem. 2011;25(3):350–9. doi:10.1016/j.niox.2011.06.007.
83. Satoh K, Matoba T, Suzuki J, O'Dell MR, Nigro P, Cui Z, et al. Cyclophilin A mediates vascular remodeling by promoting inflammation and vascular smooth muscle cell proliferation. Circulation. 2008;117(24):3088–98. doi:10.1161/CIRCULATIONAHA.107.756106.
84. Sugimoto R, Warabi E, Katayanagi S, Sakai S, Uwayama J, Yanagawa T, et al. Enhanced neointimal hyperplasia and carotid artery remodelling in sequestosome 1 deficient mice. J Cell Mol Med. 2010;14(6B):1546–54. doi:10.1111/j.1582-4934.2009.00914.x.
85. Lombardi JV, Naji M, Larson RA, Ryan SV, Naji A, Koeberlein B, et al. Adenoviral mediated uteroglobin gene transfer to the adventitia reduces arterial intimal hyperplasia. J Surg Res. 2001;99(2):377–80. doi:10.1006/jsre.2001.6209.
86. Sun L, Ishida T, Okada T, Yasuda T, Hara T, Toh R, et al. Expression of endothelial lipase correlates with the size of neointima in a murine model of vascular remodeling. J Atheroscler Thromb. 2012;19(12):1110–27.
87. Wu YJ, Sala-Newby GB, Shu KT, Yeh HI, Nakayama KI, Nakayama K, et al. S-phase kinase-associated protein-2 (Skp2) promotes vascular smooth muscle cell proliferation and neointima formation in vivo. J Vasc Surg. 2009;50(5):1135–42. doi:10.1016/j.jvs.2009.07.066. S0741-5214(09)01477-3 [pii].
88. Kyuragi R, Matsumoto T, Harada Y, Saito S, Onimaru M, Nakatsu Y, et al. BubR1 Insufficiency Inhibits Neointimal Hyperplasia Through Impaired Vascular Smooth Muscle Cell Proliferation in Mice. Arterioscler Thromb Vasc Biol. 2015;35(2):341–7. doi:10.1161/ATVBAHA.114.304737.
89. Yuan Y, Liao L, Tulis DA, Xu J. Steroid receptor coactivator-3 is required for inhibition of neointima formation by estrogen. Circulation. 2002;105(22):2653–9.

90. Arkenbout EK, de Waard V, van Bragt M, van Achterberg TA, Grimbergen JM, Pichon B, et al. Protective function of transcription factor TR3 orphan receptor in atherogenesis: decreased lesion formation in carotid artery ligation model in TR3 transgenic mice. Circulation. 2002;106(12):1530–5.
91. Squadrito F, Deodato B, Bova A, Marini H, Saporito F, Calo M, et al. Crucial role of nuclear factor-kappaB in neointimal hyperplasia of the mouse carotid artery after interruption of blood flow. Atherosclerosis. 2003;166(2):233–42.
92. Ruusalepp A, Yan ZQ, Carlsen H, Czibik G, Hansson GK, Moskaug JO, et al. Gene deletion of NF-kappaB p105 enhances neointima formation in a mouse model of carotid artery injury. Cardiovasc Drugs Ther. 2006;20(2):103–11. doi:10.1007/s10557-006-6755-7.
93. van Keulen JK, Timmers L, van Kuijk LP, Retnam L, Hoefer IE, Pasterkamp G, et al. The Nuclear Factor-kappa B p50 subunit is involved in flow-induced outward arterial remodeling. Atherosclerosis. 2009;202(2):424–30. doi:10.1016/j.atherosclerosis.2008.05.049.
94. Yoshida T, Kaestner KH, Owens GK. Conditional deletion of Kruppel-like factor 4 delays downregulation of smooth muscle cell differentiation markers but accelerates neointimal formation following vascular injury. Circ Res. 2008;102(12):1548–57. doi:10.1161/CIRCRESAHA.108.176974.
95. Yoshida T, Yamashita M, Horimai C, Hayashi M. Deletion of Kruppel-like factor 4 in endothelial and hematopoietic cells enhances neointimal formation following vascular injury. J Am Heart Assoc. 2014;3(1), e000622. doi:10.1161/JAHA.113.000622.
96. Wang X, Hu G, Gao X, Wang Y, Zhang W, Harmon EY, et al. The induction of yes-associated protein expression after arterial injury is crucial for smooth muscle phenotypic modulation and neointima formation. Arterioscler Thromb Vasc Biol. 2012;32(11):2662–9. doi:10.1161/ATVBAHA.112.254730.
97. Rodriguez-Calvo R, Guadall A, Calvayrac O, Navarro MA, Alonso J, Ferran B, et al. Overexpression of neuron-derived orphan receptor-1 (NOR-1) exacerbates neointimal hyperplasia after vascular injury. Hum Mol Genet. 2013;22(10):1949–59. doi:10.1093/hmg/ddt042.
98. Won KJ, Jung SH, Lee CK, Na HR, Lee KP, Lee DY, et al. DJ-1/park7 protects against neointimal formation via the inhibition of vascular smooth muscle cell growth. Cardiovasc Res. 2013;97(3):553–61. doi:10.1093/cvr/cvs363.
99. Kurakula K, Vos M, Otermin Rubio I, Marinkovic G, Buettner R, Heukamp LC, et al. The LIM-only protein FHL2 reduces vascular lesion formation involving inhibition of proliferation and migration of smooth muscle cells. PLoS One. 2014;9(4), e94931. doi:10.1371/journal.pone.0094931.
100. Talasila A, Yu H, Ackers-Johnson M, Bot M, van Berkel T, Bennett MR, et al. Myocardin regulates vascular response to injury through miR-24/-29a and platelet-derived growth factor receptor-beta. Arterioscler Thromb Vasc Biol. 2013;33(10):2355–65. doi:10.1161/ATVBAHA.112.301000.
101. Myers DL, Harmon KJ, Lindner V, Liaw L. Alterations of arterial physiology in osteopontin-null mice. Arterioscler Thromb Vasc Biol. 2003;23(6):1021–8.
102. Johnson JL, Dwivedi A, Somerville M, George SJ, Newby AC. Matrix metalloproteinase (MMP)-3 activates MMP-9 mediated vascular smooth muscle cell migration and neointima formation in mice. Arterioscler Thromb Vasc Biol. 2011;31(9):e35–44. doi:10.1161/ATVBAHA.111.225623.
103. Ota R, Kurihara C, Tsou TL, Young WL, Yeghiazarians Y, Chang M, et al. Roles of matrix metalloproteinases in flow-induced outward vascular remodeling. J Cereb Blood Flow Metab. 2009;29(9):1547–58. doi:10.1038/jcbfm.2009.77.
104. Choi ET, Khan MF, Leidenfrost JE, Collins ET, Boc KP, Villa BR, et al. Beta3-integrin mediates smooth muscle cell accumulation in neointima after carotid ligation in mice. Circulation. 2004;109(12):1564–9. doi:10.1161/01.CIR.0000121733.68724.FF.
105. Spencer JA, Hacker SL, Davis EC, Mecham RP, Knutsen RH, Li DY, et al. Altered vascular remodeling in fibulin-5-deficient mice reveals a role of fibulin-5 in smooth muscle cell

proliferation and migration. Proc Natl Acad Sci U S A. 2005;102(8):2946–51. doi:10.1073/pnas.0500058102.
106. Resch ZT, Simari RD, Conover CA. Targeted disruption of the pregnancy-associated plasma protein-A gene is associated with diminished smooth muscle cell response to insulin-like growth factor-I and resistance to neointimal hyperplasia after vascular injury. Endocrinology. 2006;147(12):5634–40. doi:10.1210/en.2006-0493.
107. Bale LK, Resch ZT, Harstad SL, Overgaard MT, Conover CA. Constitutive expression of pregnancy-associated plasma protein-A in arterial smooth muscle reduces the vascular response to injury in vivo. Am J Physiol Endocrinol Metab. 2013;304(2):E139–44. doi:10.1152/ajpendo.00376.2012.
108. Moura R, Tjwa M, Vandervoort P, Cludts K, Hoylaerts MF. Thrombospondin-1 activates medial smooth muscle cells and triggers neointima formation upon mouse carotid artery ligation. Arterioscler Thromb Vasc Biol. 2007;27(10):2163–9. doi:10.1161/ATVBAHA.107.151282.
109. Chapman SL, Sicot FX, Davis EC, Huang J, Sasaki T, Chu ML, et al. Fibulin-2 and fibulin-5 cooperatively function to form the internal elastic lamina and protect from vascular injury. Arterioscler Thromb Vasc Biol. 2010;30(1):68–74. doi:10.1161/ATVBAHA.109.196725.
110. Hu L, Cheng XW, Song H, Inoue A, Jiang H, Li X, et al. Cathepsin K activity controls injury-related vascular repair in mice. Hypertension. 2014;63(3):607–15. doi:10.1161/HYPERTENSIONAHA.113.02141.
111. Min SK, Min SI, Jeong EM, Cho SY, Ha J, Kim SJ, et al. Intimal hyperplasia in loop-injured carotid arteries is attenuated in transglutaminase 2-null mice. J Korean Med Sci. 2014;29(3):363–9. doi:10.3346/jkms.2014.29.3.363.
112. Nurminskaya M, Beazley KE, Smith EP, Belkin AM. Transglutaminase 2 promotes PDGF-mediated activation of PDGFR/Akt1 and beta-catenin signaling in vascular smooth muscle cells and supports neointima formation. J Vasc Res. 2014;51(6):418–28. doi:10.1159/000369461.
113. Kotha J, Zhang C, Longhurst CM, Lu Y, Jacobs J, Cheng Y, et al. Functional relevance of tetraspanin CD9 in vascular smooth muscle cell injury phenotypes: a novel target for the prevention of neointimal hyperplasia. Atherosclerosis. 2009;203(2):377–86. doi:10.1016/j.atherosclerosis.2008.07.036.
114. Li Y, Takeshita K, Liu PY, Satoh M, Oyama N, Mukai Y, et al. Smooth muscle Notch1 mediates neointimal formation after vascular injury. Circulation. 2009;119(20):2686–92.
115. Redmond EM, Liu W, Hamm K, Hatch E, Cahill PA, Morrow D. Perivascular delivery of Notch 1 siRNA inhibits injury-induced arterial remodeling. PLoS One. 2014;9(1), e84122. doi:10.1371/journal.pone.0084122.
116. Wu X, Zou Y, Zhou Q, Huang L, Gong H, Sun A, et al. Role of Jagged1 in arterial lesions after vascular injury. Arterioscler Thromb Vasc Biol. 2011;31(9):2000–6. doi:10.1161/ATVBAHA.111.225144. ATVBAHA.111.225144 [pii].
117. Song Z, Jin R, Yu S, Nanda A, Granger DN, Li G. Crucial role of CD40 signaling in vascular wall cells in neointimal formation and vascular remodeling after vascular interventions. Arterioscler Thromb Vasc Biol. 2012;32(1):50–64. doi:10.1161/ATVBAHA.111.238329.
118. Willecke F, Tiwari S, Rupprecht B, Wolf D, Hergeth S, Hoppe N, et al. Interruption of classic CD40L-CD40 signalling but not of the novel CD40L-Mac-1 interaction limits arterial neointima formation in mice. Thromb Haemost. 2014;112(2):379–89. doi:10.1160/TH13-08-0653.
119. Yu W, Liu-Bryan R, Stevens S, Damanahalli JK, Terkeltaub R. RAGE signaling mediates post-injury arterial neointima formation by suppression of liver kinase B1 and AMPK activity. Atherosclerosis. 2012;222(2):417–25. doi:10.1016/j.atherosclerosis.2012.04.001.
120. Dammanahalli KJ, Stevens S, Terkeltaub R. Vanin-1 pantetheinase drives smooth muscle cell activation in post-arterial injury neointimal hyperplasia. PLoS One. 2012;7(6), e39106. doi:10.1371/journal.pone.0039106.

121. Kureha F, Satomi-Kobayashi S, Kubo Y, Kinugasa M, Ishida T, Takai Y, et al. Nectin-like molecule-5 regulates intimal thickening after carotid artery ligation in mice. Arterioscler Thromb Vasc Biol. 2013;33(6):1206–11. doi:10.1161/ATVBAHA.113.301425.
122. Serrano RL, Yu W, Terkeltaub R. Mono-allelic and bi-allelic ENPP1 deficiency promote post-injury neointimal hyperplasia associated with increased C/EBP homologous protein expression. Atherosclerosis. 2014;233(2):493–502. doi:10.1016/j.atherosclerosis.2014.01.003.
123. Simpkins AN, Rudic RD, Roy S, Tsai HJ, Hammock BD, Imig JD. Soluble epoxide hydrolase inhibition modulates vascular remodeling. Am J Physiol Heart Circ Physiol. 2010;298(3):H795–806. doi:10.1152/ajpheart.00543.2009.
124. Furgeson SB, Simpson PA, Park I, Vanputten V, Horita H, Kontos CD, et al. Inactivation of the tumour suppressor, PTEN, in smooth muscle promotes a pro-inflammatory phenotype and enhances neointima formation. Cardiovasc Res. 2010;86(2):274–82. doi:10.1093/cvr/cvp425.
125. Li W, Li H, Sanders PN, Mohler PJ, Backs J, Olson EN, et al. The multifunctional Ca2+/calmodulin-dependent kinase II delta (CaMKIIdelta) controls neointima formation after carotid ligation and vascular smooth muscle cell proliferation through cell cycle regulation by p21. J Biol Chem. 2011;286(10):7990–9. doi:10.1074/jbc.M110.163006.
126. Li L, Zhang HN, Chen HZ, Gao P, Zhu LH, Li HL, et al. SIRT1 acts as a modulator of neointima formation following vascular injury in mice. Circ Res. 2011;108(10):1180–9. doi:10.1161/CIRCRESAHA.110.237875.
127. Yang G, Li H, Tang G, Wu L, Zhao K, Cao Q, et al. Increased neointimal formation in cystathionine gamma-lyase deficient mice: role of hydrogen sulfide in alpha5beta1-integrin and matrix metalloproteinase-2 expression in smooth muscle cells. J Mol Cell Cardiol. 2012;52(3):677–88. doi:10.1016/j.yjmcc.2011.12.004.
128. Liu S, Xie Z, Zhao Q, Pang H, Turk J, Calderon L, et al. Smooth muscle-specific expression of calcium-independent phospholipase A2beta (iPLA2beta) participates in the initiation and early progression of vascular inflammation and neointima formation. J Biol Chem. 2012;287(29):24739–53. doi:10.1074/jbc.M112.340216.
129. Zhou J, Li YS, Nguyen P, Wang KC, Weiss A, Kuo YC, et al. Regulation of vascular smooth muscle cell turnover by endothelial cell-secreted microRNA-126: role of shear stress. Circ Res. 2013;113(1):40–51. doi:10.1161/CIRCRESAHA.113.280883.
130. Zhang RN, Zheng B, Li LM, Zhang J, Zhang XH, Wen JK. Tongxinluo inhibits vascular inflammation and neointimal hyperplasia through blockade of the positive feedback loop between miR-155 and TNF-alpha. Am J Physiol Heart Circ Physiol. 2014;307(4):H552–62. doi:10.1152/ajpheart.00936.2013.
131. Li P, Zhu N, Yi B, Wang N, Chen M, You X, et al. MicroRNA-663 regulates human vascular smooth muscle cell phenotypic switch and vascular neointimal formation. Circ Res. 2013;113(10):1117–27. doi:10.1161/CIRCRESAHA.113.301306.

Chapter 4
Photochemically Induced Endothelial Injury

Yuji Matsumoto and Kazuo Umemura

Abstract Thrombosis and intimal hyperplasia occur in the development of restenosis after coronary angioplasty or the progression of atherosclerosis. The development and use of animal models are thus important for understanding the mechanisms involved in thrombus formation and intimal thickening and for evaluating potential therapies. Photochemically induced thrombosis and neointima formation following endothelial injury are initiated by the reactions between a photosensitizer, rose bengal, and green light (wavelength, 540 nm). The basic mechanism for endothelial injury in this model is that the photoexcited dye produces a singlet molecular oxygen by "photodynamic type II" energy transfer to molecular oxygen. This highly reactive oxygen species may react with structural proteins and lipids in the cell membrane to initiate direct peroxidation reactions leading to endothelial membrane damage, thus providing the initial stimulus for platelet thrombus formation, followed by intimal hyperplasia. The models of such vascular diseases created in the mouse are valuable especially since a variety of transgenic or gene knockout mice is now available for identifying factors involved in the development of thrombosis and intimal hyperplasia.

Keywords Photochemical reactions • Endothelial injury • Thrombosis • Neointimal hyperplasia

4.1 Introduction

Experimental animal models of thrombosis and intimal hyperplasia after endothelial injury are necessary for understanding the mechanisms involved in thrombus and/or neointima formation and for evaluating antithrombotic and thrombolytic preparations as potential therapeutic agents. Over the past few decades, several experimental approaches to induce in vivo arterial thrombosis in animals have been described (reviewed in reference [1]). Those which involve endothelial injury in vivo include: electric current [2, 3], laser [4, 5], intra-arterial catheters [6, 7],

Y. Matsumoto • K. Umemura (✉)
Department of Pharmacology, Hamamatsu University School of Medicine,
1-20-1 Handayama, Hamamatsu, Shizuoka 431-3192, Japan
e-mail: umemura@hama-med.ac.jp

M. Sata (ed.), *Mouse Models of Vascular Diseases*,
DOI 10.1007/978-4-431-55813-2_4

balloon catheters [8, 9], and chemicals [10, 11]. One major limitation of the invasive methods is that they cannot be applied to small mammals. In the light of such drawbacks, a photochemically induced endothelial injury model has been adapted for routine experimental thrombosis studies. The preliminary evaluation studies, using a wide range of antithrombotic and thrombolytic agents, as well as a review of the related literature, have been the subjects of the book [1]. The model represents a nonmechanical and noninvasive method of achieving vessel wall denudation. More recently, this experimental methodology has been applied to induce intravascular thrombosis in mice [12–18]. Furthermore, our laboratory has adapted this photochemically induced injury model of thrombosis to induce intimal thickening, originally in guinea pigs [19, 20] and rats [21–23] and thereafter in mice [24–29]. The model created in the mouse has considerable advantages over that of other species such as the guinea pig, rat, and rabbit. First, a variety of transgenic or gene knockout mice are now available for identifying factors involved in the development of thrombosis and intimal hyperplasia. Second, the quantity of agents, antibodies, and so on required for investigating stimulation or prevention of thrombosis and intimal hyperplasia may be reasonably small. The thrombosis model can be used to assess dynamics, treatment, or prevention of thrombosis, and it can also be used to assess the later sequelae of thrombosis such as neointima formation, restenosis, or other aspects of later atherosclerotic developments as discussed in Sect. 4.3.

4.2 Photochemically Induced Thrombosis Model

4.2.1 Introduction

Thrombotic complications of vascular disease are the major cause of morbidity and mortality in most developed nations [30, 31]. The mechanisms of thrombus formation may be multiple. Intravascular thrombus formation may follow endothelial injury. An injured area of the vessel wall can initiate activation of platelets and the coagulation cascade. Subendothelial tissue induces platelet shape change which results in platelet adhesion and aggregation to form a platelet-rich thrombus at the site of vessel injury [32]. The model is valuable, firstly, because it can be applied to large as well as small blood vessels and, secondly, because this method leads to remarkably reproducible lesions. Since experimental variability determines the number of animals needed, experiments can be performed with reasonably small numbers of animals. This is especially important for testing therapeutic interventions in prolonged experiments such as the development of neointima and complex atherosclerotic lesions. Thirdly, since this animal model can be mechanistically validated by a variety of techniques including genetic manipulation, such a validation may enhance the extrapolation of results to the mechanisms occurring in analogous human disease.

4.2.2 Photochemical Reactions

The principle of photochemical reactions is shown in Fig. 4.1. A photosensitizer, rose bengal, is known as one of the most efficient generators of singlet molecular oxygen [33]. The basic mechanism for thrombus formation in this model is that the photoexcited dye produces singlet molecular oxygen by "photodynamic type II" energy transfer to molecular oxygen [34]. This highly reactive oxygen species may react with structural proteins and lipids in the cell membrane to initiate direct peroxidation reactions leading to endothelial membrane damage, thus providing the initial stimulus for platelet thrombus formation.

In collaboration with Hamamatsu Photonics K.K. (Shizuoka, Japan), the green light irradiation system, L-4887, was designed and developed by our laboratory [1]. The optical system of this apparatus is shown in Fig. 4.2. The light source is a short-arc-type super-quiet xenon lamp. The xenon lamp was selected in order to achieve the high brightness and stable light intensity necessary for irradiating a small area. The light is concentrated and prefiltered by an elliptical reflector which has a special coating to absorb infrared and ultraviolet radiation. The remaining visible light is spectrally modified by filters to produce pure green light of bandwidth 80 nm, centered at 540 nm. Elimination of infrared and ultraviolet radiations is essential, as these can heat up and damage biological tissues. The green light is then directed to a flexible optic fiber as the irradiating probe. The intensity of irradiation is controlled by an optical aperture. Alternative green light sources have also been described, e.g., a 200-fiber optic cable as green light source (530–590 nm) [35].

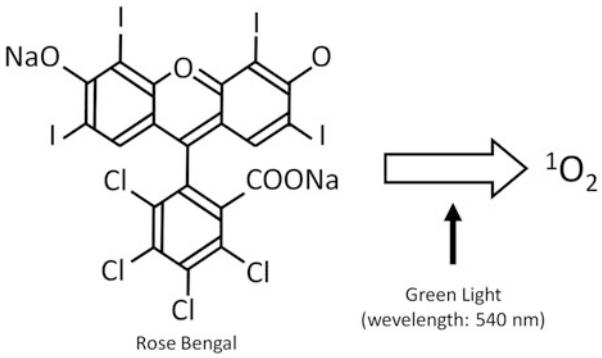

Fig. 4.1 The principle of photochemical reactions. Rose bengal, which belongs to the dye class of photosensitizers, is an efficient photosensitizer of the photodynamic type (type II), producing singlet molecular oxygen ($^1O_2$). For the photoexcitation of rose bengal, the green light absorption maximum is close to 540 nm. The singlet oxygen produced then reacts with endothelial cell components, resulting in endothelial cell injury

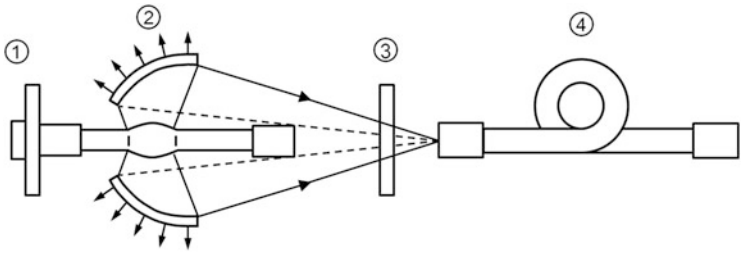

Fig. 4.2 Diagram of the optical system of L-4887, the irradiation apparatus. (*1*) Super-quiet xenon lamp, (*2*) elliptical reflector, (*3*) green filter with heat-absorbing capacity, and (*4*) flexible optic fiber. The light from the short-arc-type xenon lamp is reflected by the elliptical reflector and directed to the optic fiber via filters. Infrared and ultraviolet radiations are eliminated by the reflector and the filters. Pure green light is produced by a spectral cutoff filter. Conventional xenon lamps consume the cathode itself during prolonged use and must be replaced periodically. The super-quiet xenon lamp, however, has a special durable cathode to avoid such problems

4.2.3 Technical Aspects

Our photochemically induced thrombosis model is a modification of the technique described by Watson et al. [36] to induce focal thrombosis in cerebral vessels in the rat. In this model, a small segment of an exposed artery in an experimental animal is irradiated with green light in the presence of an intravenously administered photosensitizer such as rose bengal. Within a few minutes, the irradiated segment becomes occluded by a thrombus. We have described our approach to the femoral arteries of mice previously in great detail [12–14, 37, 38]. Briefly, animals are anesthetized with sodium pentobarbital (80 mg/kg, i.p.). A cannula is inserted into the jugular vein of each animal for injection of rose bengal. Then the right or left femoral artery is exposed, and a pulsed Doppler flow probe (PDV-20; Crystal Biotech, Hopkinton, MA, USA) is placed on it for monitoring blood flow (Fig. 4.3). Transillumination with green light (wavelength, 540 nm) is achieved using a xenon light with both a heat-absorbing filter and a green filter (model L-4887; Hamamatsu Photonics K.K., Shizuoka, Japan). Irradiation is directed via an optic fiber positioned approximately 5 mm away from a segment of the intact femoral artery proximal to the flow probe. Irradiation at an intensity of 0.9 W/cm^2 is started when the baseline blood flow is stable and then rose bengal (15 mg/kg) is injected for 5 min. Irradiation is continued until the blood flow stopped. The femoral artery is considered occluded when the blood flow has stopped for more than 1 min. The time to occlusion is taken from the start of the rose bengal infusion to the cessation of blood flow (Fig. 4.4).

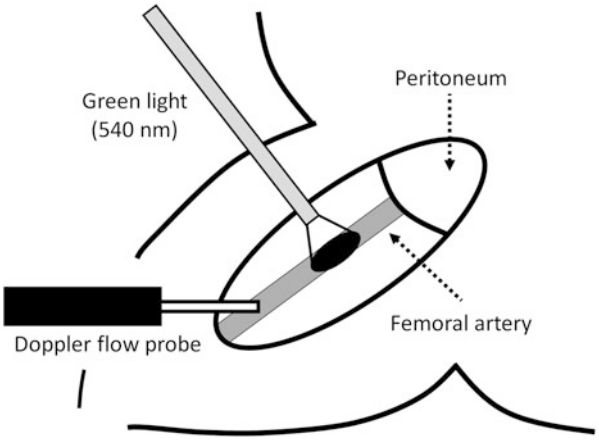

Fig. 4.3 Schematic illustration of photochemically induced thrombosis (PIT) model in the femoral artery. Either the right or left femoral artery is exposed surgically under anesthesia. Blood velocity is measured continuously by a pulsed Doppler flow probe distal to the inguinal ligament. Transillumination with green light (wavelength, 540 nm) is achieved by a xenon lamp. The light is directed by an optic fiber mounted on a micromanipulator so that its head is approximately 5 mm above the intact femoral artery, proximal to the flow probe. Rose bengal (15 mg/kg) is then injected via the contralateral femoral vein, and transillumination with green light continued until the vessel is thrombotically occluded. The femoral artery is assumed to be occluded when the blood flow has completely ceased

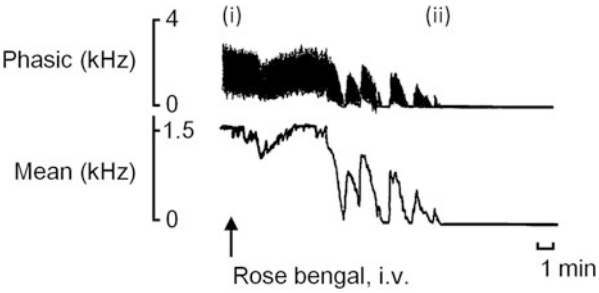

Fig. 4.4 Representative tracings of phasic and mean blood flow in a femoral artery, before and after injection of rose bengal under green light irradiation. (i) Immediately before and after injection of rose bengal 15 mg/kg, iv. (ii) Ten minutes after the initiation of the photochemical reaction. The blood flow of the irradiated artery decreased gradually with time and ceased completely about 10 min after the injection of rose bengal with green light irradiation

4.2.4 Histology of the Thrombotic Response

Light microscopic observation of the femoral artery following the cessation of blood flow reveals that the arterial lumen was occluded with a platelet-rich thrombus at the site of the photochemical reaction (irradiated segment). A representative cross section of the occluded femoral artery is shown in Fig. 4.5. The mouse

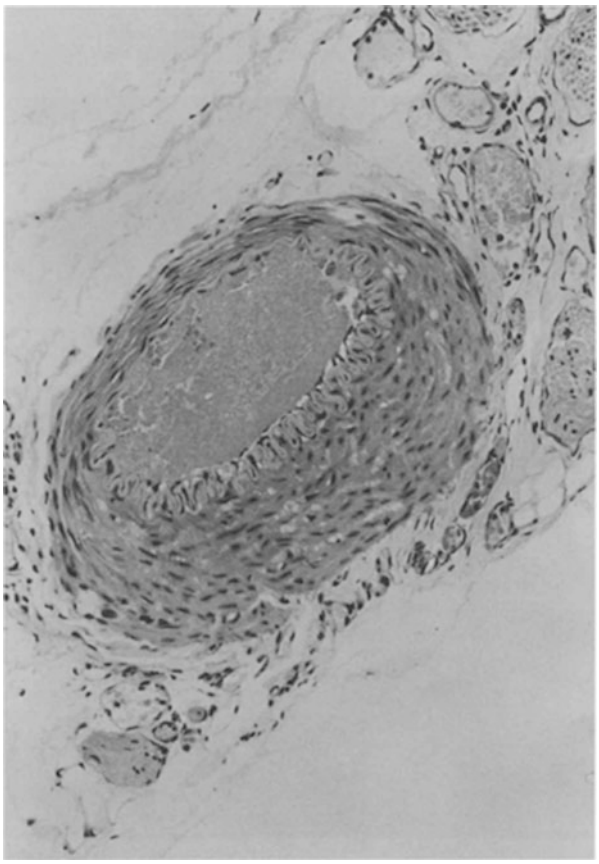

Fig. 4.5 Light microscopic view of a cross section of occluded guinea pig femoral artery which had been irradiated with green light (the site of photochemical reaction). As seen, the arterial lumen is completely occluded by a platelet-rich thrombus. The cross section is stained with hematoxylin and eosin (Reproduced with permission from Ref. [58])

femoral artery became thrombotically occluded (cessation of blood flow) about 10 min after systemic rose bengal injection and green light irradiation. Twenty-four hours later, spontaneous reflow, observed in all mice, had recovered to 86 % of the baseline level [24].

The scanning electron photomicrograph in Fig. 4.6a shows a full view of the femoral artery occluded by a thrombus. Figure 4.6b is a view at higher magnification of a part of Fig. 4.6a. In this model, the thrombus was composed of distorted red blood cells and leukocytes trapped in a fibrin mesh, together with a large number of aggregated platelets (Fig. 4.6b).

4.2.5 Conclusion

This model involves a photochemical reaction between systemically administered rose bengal and transluminal green light, which cause endothelial injury followed

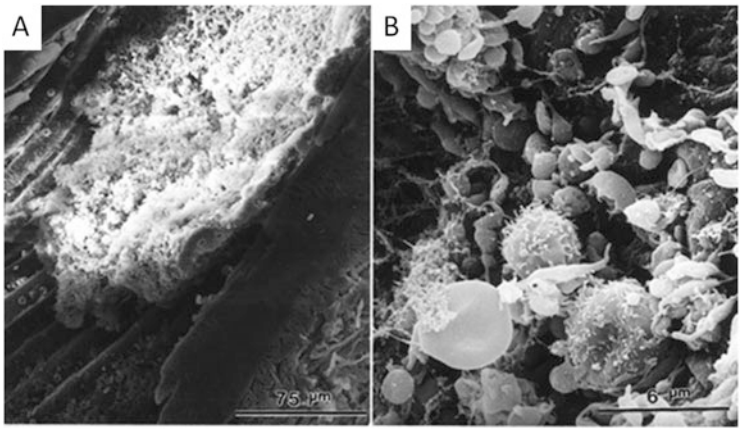

Fig. 4.6 Scanning electron photomicrographs of mouse femoral artery surface immediately after photochemically induced endothelial injury. In panels **a** and **b**, the thrombus is composed of deformed red blood cells and leukocytes trapped in a large amount of fibrin, together with numerous aggregated platelets. Panel **b** is a higher magnification of panel **a** (Reproduced with permission from Ref. [24])

by platelet adhesion, aggregation, and formation of a platelet- and fibrin-rich thrombus at the site of the reaction. The model represents a nonmechanical approach to induce vascular endothelial denudation. The photochemical technique is simple, fast, and reproducible. It has been used originally in guinea pigs [39–41] and rats [42–44]. Thereafter, the methodology has been adapted to induce intravascular thrombosis in mice [12–14]. However, this model can also be broadly applied to any mammalian species from mice to primates [45–47]. Thrombus formation in different species will be easily controlled by rose bengal concentration and the green light intensity. This photochemical thrombosis model has now been widely used in many kinds of genetically altered mice (reviewed in reference [48]). However, it should be mentioned that a number of transgenic mice display phenotypic variability in thrombosis severity depending on the strain background [48]. - Strain-related genetic differences may also influence on the degree of photochemically induced intimal hyperplasia as discussed in Sect. 4.3. The possibility to use genetically altered animals is important, since it allows to characterize mechanisms occurring in vivo.

4.3 Photochemically Induced Arterial Intimal Thickening Model

4.3.1 Introduction

It is well known that intimal thickening occurs with the development of restenosis after percutaneous coronary intervention and the progression of atherosclerosis. To date, several experimental approaches to induce intimal thickening have been reported. These include endothelial injury induced by a flexible wire [49], a balloon catheter [50], air-drying [51], and laser injury [52]. Such injuries do lead to neointimal formation in arteries by removing the endothelium and they can be used to study atherosclerosis and restenosis after angioplasty. However, they all involve procedures that are relatively complicated and difficult to control with respect to the extent of vascular injury [53]. In the light of this situation, establishment of a simple and more reproducible animal model of intimal thickening in response to endothelial injury is very desirable. It could facilitate to gain insight into the pathophysiology of neointimal formation after vascular injury and to assess potential therapies. We have therefore adapted the thrombosis model after photochemically induced endothelial injury to induce intimal thickening originally in guinea pigs [19, 20] and rats [21–23] and thereafter in mice [24–28]. Moreover, the longer duration of these experiments may cause logistic problems, especially if therapeutic interventions should be tested. The mouse model offers an important advantage in this context.

4.3.2 Preparation of the Photochemically Induced Intimal Thickening Model

The procedure for inducing a transluminal thrombus in the mouse femoral artery is largely the same as described above. However, the main interest is focused on late sequelae of endothelial lesion and thrombosis. Therefore, the methods for assessing the outcome differ from the thrombosis model proper. The irradiated segment of the femoral artery is considered to be occluded by a platelet- and fibrin-rich thrombus when blood flow has completely stopped. Thirty minutes later the wound is closed, and the animal is returned to its cage, after it has recovered from anesthesia. Twenty-four hours later, the mice are reanesthetized, and spontaneous reflow is confirmed by monitoring the blood flow in the femoral artery. In photochemically induced thrombosis, spontaneous reflow is affected by the duration of photoirradiation, rose bengal concentration, green light intensity, and thickness of the vessel wall. Under our experimental conditions, spontaneous reflow occurred in all mice within 24 h after thrombotic occlusion of the femoral artery [24].

4.3.3 Histology on Light Microscopy

A typical pattern of intimal thickening after photochemically induced endothelial injury is shown in Fig. 4.7. Twenty-one days after the photochemical injury, an extensive neointima had formed in the subendothelial layers throughout the injured arterial segment. The neointima extended from the borders between uninjured and injured sites (positions A and E in Fig. 4.7) into the injured center (position C in

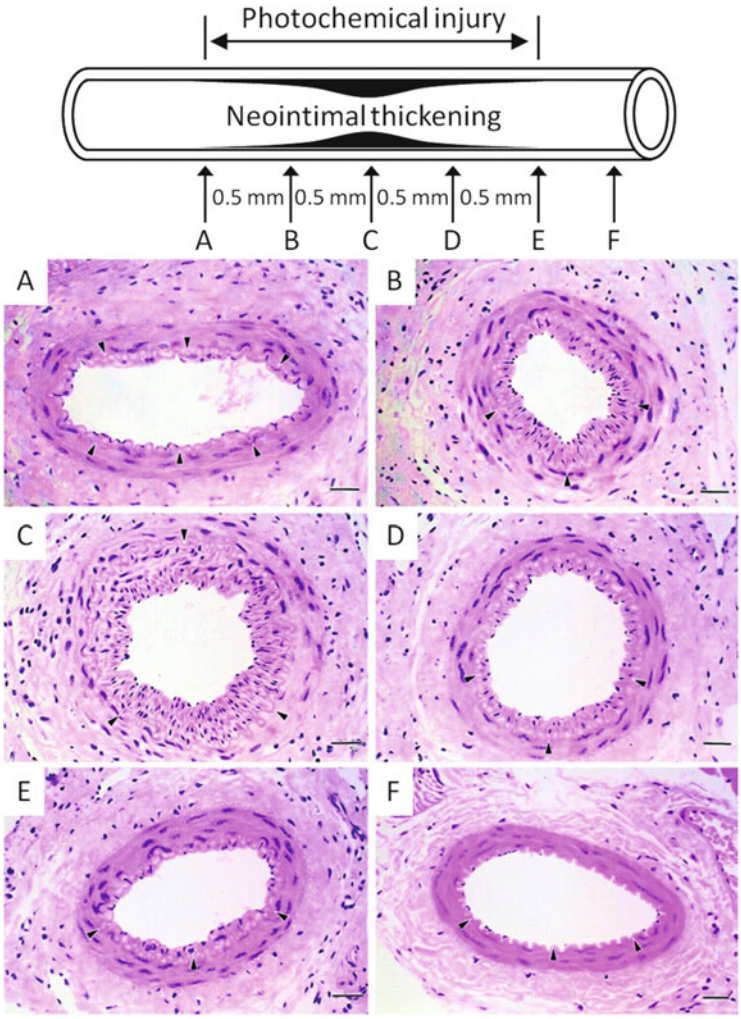

Fig. 4.7 Light photomicrographs of serial histological cross sections from mouse femoral artery 21 days after photochemical injury. **a** to **e** and **f** are cross sections from injured and uninjured vessels, respectively. Internal elastic lamina is indicated by *arrowheads* in **a** to **f**. Hematoxylin and eosin stain, bars = 50 μm (Reproduced with permission from Ref. [24])

Fig. 4.7). On the other hand, neointimal formation was not observed at the normal site (position F in Fig. 4.7). This process was quantified by measuring the intima-media ratio at almost equally spaced positions across the injured segment in Fig. 4.7. Position C in Fig. 4.7 had a significantly thickened neointima compared with neighboring positions [24]. Within 24 h after endothelial injury, the number of medial smooth muscle cells (SMCs) had decreased by about 28 % compared with uninjured controls, and the loss of medial SMCs was apparent in some sections after endothelial injury (Table 4.1). Seven days after injury, SMCs, which had migrated from the media, were present in the neointima and it became gradually thicker, coincident with its repopulation by cells. Neointimal formation reached a maximum of 21 days after endothelial injury and remained unchanged for as long as 42 days after the injury. Within 2 days after endothelial injury, the luminal area decreased, reflecting vasoconstriction due to the disappearance of endothelium-dependent vasodilation, but this initial decrease in the luminal area was reversed at 7 days after injury. Thereafter, with neointimal proliferation, the luminal area of the vessel decreased, but the medial area remained unchanged throughout the observation period (Table 4.1).

4.3.4 Histology on Scanning Electron Microscopy

The scanning electron photomicrographs in Fig. 4.8 show mouse femoral arteries before and after photochemically induced endothelial injury. One day after the thrombotic occlusion, spontaneous thrombolysis had occurred, but numerous activated platelets were still seen adherent to the injured arterial wall (Fig. 4.8a). After 3 days, in addition to platelets, leukocytes were also present and had formed a monolayer on the injured vessel wall (Fig. 4.8b). Seven days after the injury, no leukocytes were seen in the damaged area, but a few platelets were still seen adherent to the exposed subendothelial matrix (Fig. 4.8c). Twenty-one days after the operation, no blood cells were present on the luminal surface (Fig. 4.8d). Figure 4.8e shows the characteristic cobblestone-like intact endothelial cells of the vessel wall of an uninjured artery.

4.3.5 Immunohistology

Immunostaining for smooth muscle α-actin revealed a progressive increase in the area of media and/or neointima, which was positive for smooth muscle α-actin as shown in Fig. 4.9a–c. There were only a few α-actin-positive areas in the neointima at 7 days after the injury (Fig. 4.9a). At day 14 and day 21, however, almost the entire neointima was positive for α-actin (Fig. 4.9b, c). The extracellular matrix (ECM) deposition surrounding SMCs in the neointima was confirmed by Masson's trichrome staining. There was only a small amount of ECM in the neointima at

Table 4.1 Time course of changes in intimal and medial cells; luminal, intimal, and medial areas; and intima-media ratio after photochemically induced endothelial injury

		Time after injury					
	Control	24 h	2 days	7 days	14 days	21 days	42 days
Intimal cells	0 ± 0	0 ± 0	0 ± 0	$31 \pm 5^{\#}$	$70 \pm 8^{\$}$	$72 \pm 8^{\$}$	$83 \pm 15^{\$}$
Medial cells	46 ± 3	34 ± 2	38 ± 5	44 ± 3	45 ± 3	42 ± 2	41 ± 3
Area ($\times$ 0.01 mm^2)							
Luminal	1.879 ± 0.226	1.519 ± 0.427	$0.617 \pm 0.093^{\#}$	1.653 ± 0.638	1.518 ± 0.258	1.204 ± 0.208	1.267 ± 0.166
Intimal	0 ± 0	0 ± 0	0 ± 0	$0.239 \pm 0.079^{*}$	$0.301 \pm 0.049^{\#}$	$0.609 \pm 0.079^{\$}$	$0.662 \pm 0.094^{\$}$
Medial	0.941 ± 0.047	0.859 ± 0.058	0.935 ± 0.044	1.245 ± 0.079	1.216 ± 0.149	1.014 ± 0.073	1.136 ± 0.159
I/M ratio	0 ± 0	0 ± 0	0 ± 0	0.180 ± 0.046	$0.276 \pm 0.058^{\#}$	$0.622 \pm 0.086^{\$}$	$0.661 \pm 0.121^{\$}$
n	10	8	10	9	10	10	8

Reproduced with permission from Ref. [24]
I/M ratio indicates intima-media ratio. Data are presented as the mean $\pm$ SEM
$^{*}P < 0.05$, $^{\#}P < 0.01$, and $^{\$}P < 0.001$ vs. control

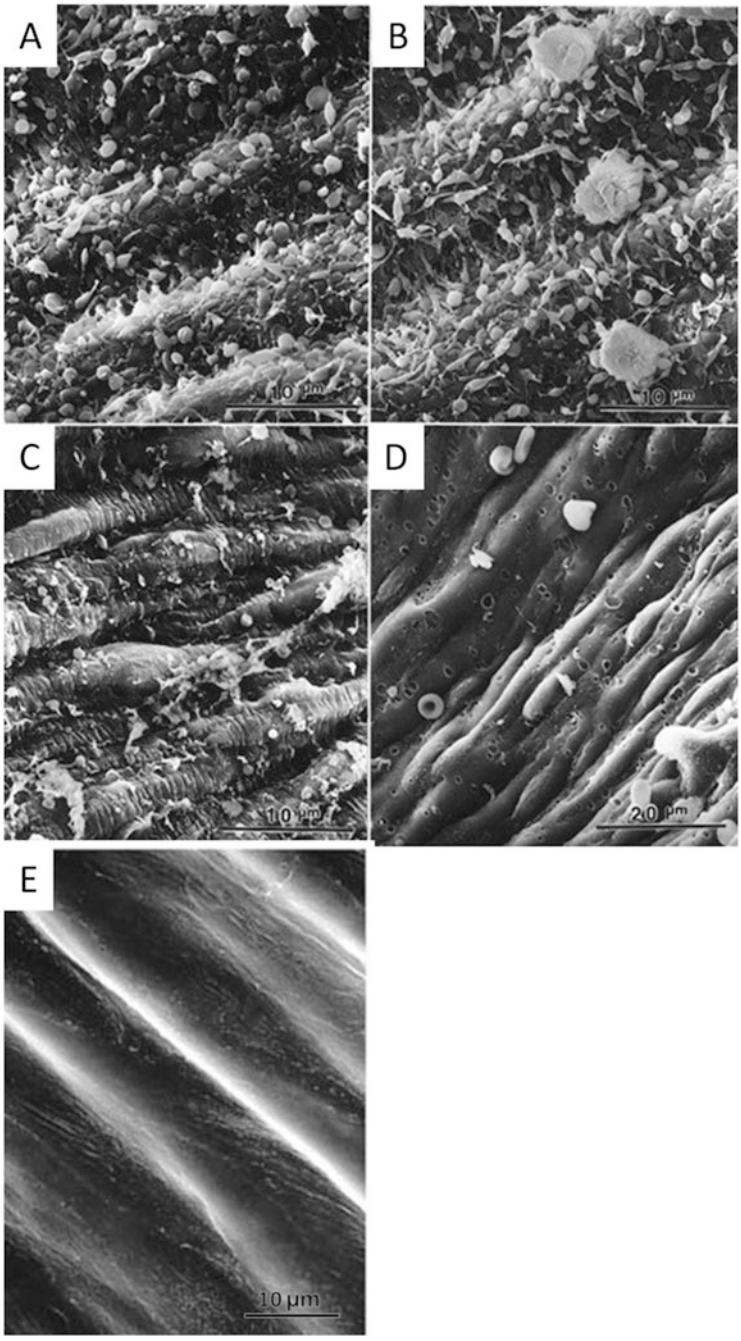

Fig. 4.8 Scanning electron photomicrographs of mouse femoral arteries after photochemically induced endothelial injury. Femoral arteries were harvested at 1 (**a**), 3 (**b**), 7 (**c**), and 21 (**d**) days after injury. (**a**) Spontaneous thrombolysis within 24 h of thrombus occlusion of the vessel is shown. Numerous activated platelets are still evident adherent to injured surface. (**b**) Platelets and leukocytes have formed a monolayer on injured surface. (**c**) No leukocytes are visible on injured

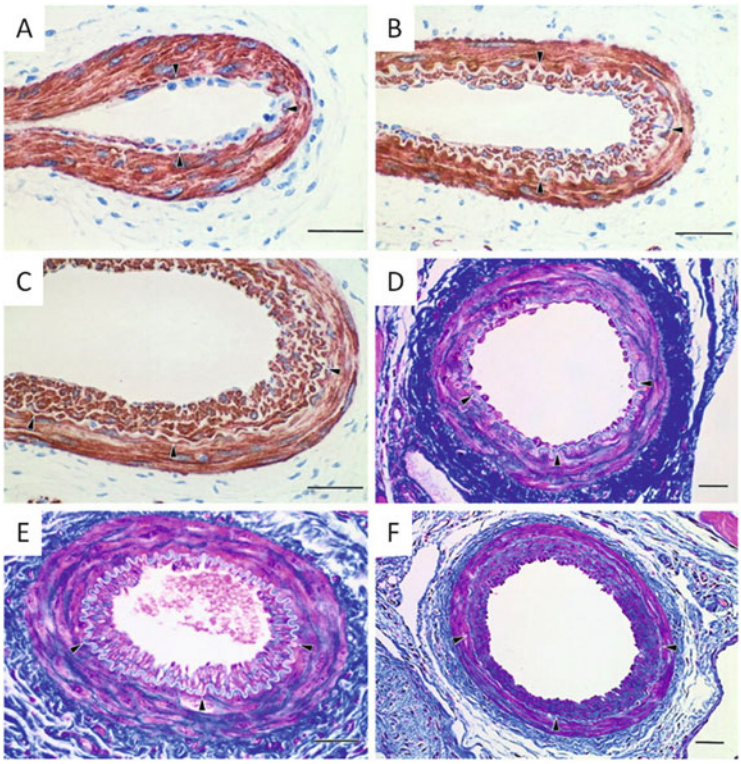

Fig. 4.9 Light photomicrographs of immunostained or Masson's trichrome-stained cross sections from mouse femoral arteries at various times after endothelial injury. **a**, **b**, and **c** were immunostained with alpha-actin monoclonal antibody to reveal smooth muscle cells. **d**, **e**, and **f** were stained with Masson's trichrome reagent to indicate presence of extracellular matrix surrounding smooth muscle cells in the neointima and media of injured arteries. **a** and **d**: 7 days after injury; **b** and **e**: 14 days after injury; **c** and **f**: 21 days after injury. Internal elastic lamina is indicated by *arrowheads* in **a** to **f**. Extracellular matrix and smooth muscle cells are stained blue and red, respectively. In immunostained cross sections, nuclei are stained blue with Mayer's hematoxylin. Bars = 50 μm (Reproduced with permission from Ref. [24])

7 days after injury (Fig. 4.9d). Beyond 14 days after injury, however, the amount of ECM in the neointima was increased (Fig. 4.9e, f). These findings suggest that the neointima that has formed after the vascular injury is composed mainly of SMCs and ECM.

Arterial cell proliferation was evaluated by bromodeoxyuridine (BrdU) staining, which is positive for cells undergoing DNA synthesis [24]. The maximum level of

Fig. 4.8 (continued) surface, but a few platelets remain. (**d**) Blood cells on arterial injured surface are observed no longer. (**e**) Before the endothelial injury, intact endothelial cells are seen (Reproduced with permission from Ref. [24, 27])

SMC proliferation in the medial layer was detected 2 days after vessel wall injury, followed by a gradual decrease to baseline level by day 21. BrdU-positive cells in the intima were first observed 7 days after the endothelial injury and were maximal at this point. The ratio of BrdU labeling thereafter decreased in a time-dependent manner.

4.3.6 Endothelial Regeneration

As shown in Fig. 4.10a, no blue-stained area was observed in the uninjured vessel, indicating no endothelial damage. Endothelial cells (ECs) from the photoirradiated segment were completely absent immediately after the endothelial injury that was revealed by Evans blue staining (Fig. 4.10b). ECs originating from the uninjured

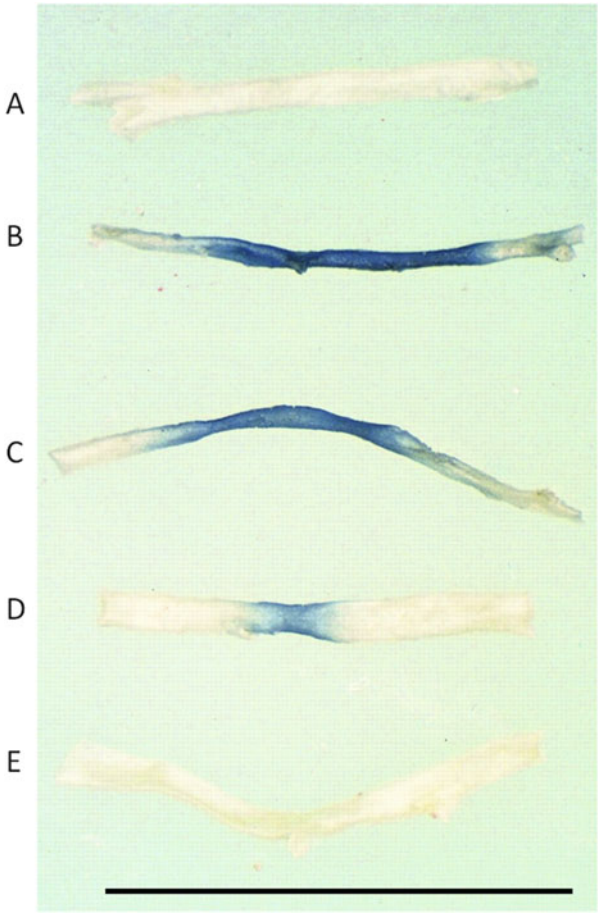

Fig. 4.10 Photographs showing Evans blue staining of mouse femoral arteries after photochemically induced endothelial injury. (**a**) Control (no blue staining in uninjured artery) (**b**): immediately after injury (**c**, **d**, and **e**) are 2, 7, and 21 days after injury, respectively. Evans blue dye penetrated the injured segment immediately after endothelial injury. Blue-stained areas gradually decreased thereafter and were absent by 21 days after injury, at which time endothelial regeneration was complete. Bar = 5 mm (Reproduced with permission [24])

borders grew into the injured center, and the reendothelialization was complete within 21 days after injury (Fig. 4.10c–e).

4.3.7 Conclusion

The model represents a nonmechanical and noninvasive approach to achieve vessel wall denudation, which is different from models using flexible wire [49], balloon catheter [50], air-drying [51], and laser injury [52]. In our model, neointima formation after photochemical injury reflects migration of SMCs from the media to the intima within the arterial wall, proliferation of SMCs in the intima, and excessive production of ECM by SMCs [54]. A number of studies have reported that certain growth factors, including platelet-derived growth factor [55], basic fibroblast growth factor [56], interleukin-1β [54], thrombin [57], activated platelets, and leukocytes or the injured ECs themselves, may interact with the neointimal SMCs in an autocrine or paracrine manner to promote SMC migration and proliferation, thus contributing to the neointima formation. Current pharmacological therapy for preventing the development of restenosis after percutaneous coronary intervention or the progression of atherosclerosis is limited at present. As well as the mouse photochemical thrombosis model, which has been extensively investigated [48], the photochemically induced intimal thickening model with vast genetic and molecular resources should promise not only to discover new and previously unanticipated mechanisms but also thus to bring new therapies.

References

1. Nakashima M. A novel photochemical model for thrombosis research and evaluation of antithrombotic and thrombolytic agents. New York: Churchill Livingstone; 1994.
2. Romson JL, Haack DW, Lucchesi BR. Electrical induction of coronary artery thrombosis in the ambulatory canine: a model for in vivo evaluation of anti-thrombotic agents. Thromb Res. 1980;17(6):841–53.
3. Massad L, Plotkine M, Capdeville C, Boulu RG. Electrically induced arterial thrombosis model in the conscious rat. Thromb Res. 1987;48(1):1–10.
4. Seiffge D, Weithmann KU. Surprising effects of the sequential administration of pentoxifylline and low dose acetylsalicylic acid on thrombus formation. Thromb Res. 1987;46(2):371–83.
5. Grant L, Becker FF. Mechanisms of inflammation. I. Laser-induced thrombosis, a morphologic analysis. Proc Soc Exp Biol Med. 1965;119(4):1123–9.
6. Cattaneo M, Winocour PD, Somers DA, Groves HM, Kinlough-Rathbone RL, Packham MA, et al. Effect of ticlopidine on platelet aggregation, adherence to damaged vessels, thrombus formation and platelet survival. Thromb Res. 1985;37(1):29–43.
7. Moore S, Friedman RJ, Singal DP, Gauldie J, Blajchman MA, Roberts RS. Inhibition of injury induced thromboatherosclerotic lesions by anti-platelet serum in rabbits. Thromb Haemost. 1976;35(1):70–81.

8. Klement P, Borm A, Hirsh J, Maraganore J, Wilson G, Weitz J. The effect of thrombin inhibitors on tissue plasminogen activator induced thrombolysis in a rat model. Thromb Haemost. 1992;68(1):64–8.
9. Steele PM, Chesebro JH, Stanson AW, Holmes Jr DR, Dewanjee MK, Badimon L, et al. Balloon angioplasty. Natural history of the pathophysiological response to injury in a pig model. Circ Res. 1985;57(1):105–12.
10. Mayer Jr JE, Hammond GL. Dipyridamole and aspirin tested against an experimental model of thrombosis. Ann Surg. 1973;178(1):108–12.
11. Kurz KD, Main BW, Sandusky GE. Rat model of arterial thrombosis induced by ferric chloride. Thromb Res. 1990;60(4):269–80.
12. Suzuki Y, Kondo K, Ikeda Y, Umemura K. Antithrombotic effect of geniposide and genipin in the mouse thrombosis model. Planta Med. 2001;67(9):807–10.
13. Kondo K, Suzuki Y, Ikeda Y, Umemura K. Genistein, an isoflavone included in soy, inhibits thrombotic vessel occlusion in the mouse femoral artery and in vitro platelet aggregation. Eur J Pharmacol. 2002;455(1):53–7.
14. Cheng J, Kondo K, Suzuki Y, Ikeda Y, Meng X, Umemura K. Inhibitory effects of total flavones of Hippophae rhamnoides L on thrombosis in mouse femoral artery and in vitro platelet aggregation. Life Sci. 2003;72(20):2263–71.
15. Grad E, Golomb M, Koroukhov N, Lawson JA, Lotan C, Fitzgerald GA, et al. Aspirin reduces the prothrombotic activity of C-reactive protein. J Thromb Haemost. 2009;7(8):1393–400.
16. Danenberg HD, Szalai AJ, Swaminathan RV, Peng L, Chen Z, Seifert P, et al. Increased thrombosis after arterial injury in human C-reactive protein-transgenic mice. Circulation. 2003;108(5):512–5.
17. Nagashima M, Yin ZF, Zhao L, White K, Zhu Y, Lasky N, et al. Thrombin-activatable fibrinolysis inhibitor (TAFI) deficiency is compatible with murine life. J Clin Invest. 2002;109(1):101–10.
18. Kalish Y, Malyutin Z, Shai E, Dana M, Avraham L, Jahshan N, et al. A mouse model to study thrombotic complications of thalassemia. Thromb Res. 2015;135(3):521–5.
19. Hirata Y, Umemura K, Kondoh K, Uematsu T, Nakashima M. Experimental intimal thickening studies using the photochemically induced thrombosis model in the guinea-pig femoral artery. Atherosclerosis. 1994;107(1):117–24.
20. Umemura K, Nishiyama H, Kikuchi S, Kondo K, Nakashima M. Inhibitory effect of a novel orally active GP IIb/IIIa inhibitor, SC-54684A on intimal thickening in the guinea pig femoral artery. Thromb Haemost. 1996;76(5):799–806.
21. Umemura K, Watanabe S, Kondo K, Hashimoto H, Nakashima M. Inhibitory effect of prostaglandin E1 on intimal thickening following photochemically induced endothelial injury in the rat femoral artery. Atherosclerosis. 1997;130(1–2):11–6.
22. Kikuchi S, Umemura K, Kondo K, Nakashima M. Tranilast suppresses intimal hyperplasia after photochemically induced endothelial injury in the rat. Eur J Pharmacol. 1996;295 (2–3):221–7.
23. Takiguchi Y, Nagano M, Ikeda Y, Nakashima M. Early administration of YT-146, an adenosine A2 receptor agonist, inhibits neointimal thickening after rat femoral artery endothelium injury. Eur J Pharmacol. 1995;281(2):205–7.
24. Kikuchi S, Umemura K, Kondo K, Saniabadi AR, Nakashima M. Photochemically Induced Endothelial Injury in the Mouse as a Screening Model for Inhibitors of Vascular Intimal Thickening. Arterioscler Thromb Vasc Biol. 1998;18(7):1069–78.
25. Miyazawa N, Watanabe S, Matsuda A, Kondo K, Hashimoto H, Umemura K, et al. Role of histamine H1 and H2 receptor antagonists in the prevention of intimal thickening. Eur J Pharmacol. 1998;362(1):53–9.
26. Kondo K, Umemura K, Miyaji M, Nakashima M. Milrinone, a phosphodiesterase inhibitor, suppresses intimal thickening after photochemically induced endothelial injury in the mouse femoral artery. Atherosclerosis. 1999;142(1):133–8.

27. Shimazawa M, Kondo K, Hara H, Nakashima M, Umemura K. Sulfatides, L- and P-selectin ligands, exacerbate the intimal hyperplasia occurring after endothelial injury. Eur J Pharmacol. 2005;520(1–3):118–26.
28. Shimazawa M, Watanabe S, Kondo K, Hara H, Nakashima M, Umemura K. Neutrophil accumulation promotes intimal hyperplasia after photochemically induced arterial injury in mice. Eur J Pharmacol. 2005;520(1–3):156–63.
29. Hokamura K, Inaba H, Nakano K, Nomura R, Yoshioka H, Taniguchi K, et al. Molecular analysis of aortic intimal hyperplasia caused by Porphyromonas gingivalis infection in mice with endothelial damage. J Periodontal Res. 2010;45(3):337–44.
30. Raskob GE, Angchaisuksiri P, Blanco AN, Buller H, Gallus A, Hunt BJ, et al. Thrombosis: a major contributor to global disease burden. Arterioscler Thromb Vasc Biol. 2014;34 (11):2363–71.
31. Meadows TA, Bhatt DL. Clinical aspects of platelet inhibitors and thrombus formation. Circ Res. 2007;100(9):1261–75.
32. Moncada S, Vane JR. Arachidonic acid metabolites and the interactions between platelets and blood-vessel walls. N Engl J Med. 1979;300(20):1142–7.
33. Vandeplassche G, Bernier M, Thone F, Borgers M, Kusama Y, Hearse DJ. Singlet oxygen and myocardial injury: ultrastructural, cytochemical and electrocardiographic consequences of photoactivation of rose bengal. J Mol Cell Cardiol. 1990;22(3):287–301.
34. Saniabadi AR. Photosensitisers and photochemical reactions. In: Nakashima M, editor. A novel photochemical model for thrombosis research and evaluation of antithrombotic and thrombolytic agents. New York: Churchill Livingstone; 1994. p. 1–19.
35. Hearse DJ, Kusama Y, Bernier M. Rapid electrophysiological changes leading to arrhythmias in the aerobic rat heart. Photosensitization studies with rose bengal-derived reactive oxygen intermediates. Circ Res. 1989;65(1):146–53.
36. Watson BD, Dietrich WD, Busto R, Wachtel MS, Ginsberg MD. Induction of reproducible brain infarction by photochemically initiated thrombosis. Ann Neurol. 1985;17(5):497–504.
37. Hirata Y, Takiguchi Y, Wada K, Matsuno H, Umemura K, Uematsu T, et al. Roles of platelet-activating factor, thromboxane A2, ADP and thrombin in thrombogenesis in the guinea pig. Eur J Pharmacol. 1993;231(3):421–5.
38. Saniabadi AR, Umemura K, Matsumoto N, Sakuma S, Nakashima M. Vessel wall injury and arterial thrombosis induced by a photochemical reaction. Thromb Haemost. 1995;73 (5):868–72.
39. Wada K, Umemura K, Nishiyama H, Saniabadi AR, Takiguchi Y, Nakano M, et al. A chemiluminescent detection of superoxide radical produced by adherent leucocytes to the subendothelium following thrombolysis: studies with a photochemically induced thrombosis model in the guinea pig femoral artery. Atherosclerosis. 1996;122(2):217–24.
40. Hirata Y, Umemura K, Takiguchi Y, Uematsu T, Nakashima M. A thrombosis model for evaluating thrombolytic agents in the guinea-pig: comparison of t-PA, scu-PA and a novel thrombolytic agent, staphylokinase, on thrombolytic activity. Blood Coagul Fibrinolysis. 1993;4(4):569–75.
41. Nishiyama H, Umemura K, Wada K, Nakashima M. Antithrombotic Effect of a New Glycoprotein IIb/IIIa Antagonist, SC-52012A: Studies in two Guinea-pig Thrombosis Models. Platelets. 1995;6(5):283–7.
42. Takiguchi Y, Wada K, Nakashima M. Comparison of the inhibitory effects of the TXA2 receptor antagonist, vapiprost, and other antiplatelet drugs on arterial thrombosis in rats: possible role of TXA2. Thromb Haemost. 1992;68(4):460–3.
43. Takiguchi Y, Wada K, Nakashima M. Hemodynamic effects on thrombogenesis and platelet aggregation in spontaneously hypertensive rats. Clin Exp Hypertens. 1993;15(1):197–208.
44. Matsuno H, Uematsu T, Umemura K, Takiguchi Y, Wada K, Nakashima M. Effects of vapiprost, a novel thromboxane receptor antagonist, on thrombus formation and vascular patency after thrombolysis by tissue-type plasminogen activator. Br J Pharmacol. 1992;106 (3):533–8.

45. Kaku S, Umemura K, Mizuno A, Yano S, Suzuki K, Kawasaki T, et al. Evaluation of a GPIIb/IIIa antagonist YM337 in a primate model of middle cerebral artery thrombosis. Eur J Pharmacol. 1998;345(2):185–92.
46. Maeda M, Takamatsu H, Furuichi Y, Noda A, Awaga Y, Tatsumi M, et al. Characterization of a novel thrombotic middle cerebral artery occlusion model in monkeys that exhibits progressive hypoperfusion and robust cortical infarction. J Neurosci Methods. 2005;146(1):106–15.
47. Ikeda S, Harada K, Ohwatashi A, Kamikawa Y, Yoshida A, Kawahira K. A new non-human primate model of photochemically induced cerebral infarction. PLoS One. 2013;8(3):e60037.
48. Westrick RJ, Winn ME, Eitzman DT. Murine models of vascular thrombosis (Eitzman series). Arterioscler Thromb Vasc Biol. 2007;27(10):2079–93.
49. Lindner V, Fingerle J, Reidy MA. Mouse model of arterial injury. Circ Res. 1993;73(5):792–6.
50. Clowes AW, Clowes MM. Kinetics of cellular proliferation after arterial injury. II. Inhibition of smooth muscle growth by heparin. Lab Invest. 1985;52(6):611–6.
51. Fishman JA, Ryan GB, Karnovsky MJ. Endothelial regeneration in the rat carotid artery and the significance of endothelial denudation in the pathogenesis of myointimal thickening. Lab Invest. 1975;32(3):339–51.
52. Hanke H, Haase KK, Hanke S, Oberhoff M, Hassenstein S, Betz E, et al. Morphological changes and smooth muscle cell proliferation after experimental excimer laser treatment. Circulation. 1991;83(4):1380–9.
53. Indolfi C, Esposito G, Di Lorenzo E, Rapacciuolo A, Feliciello A, Porcellini A, et al. Smooth muscle cell proliferation is proportional to the degree of balloon injury in a rat model of angioplasty. Circulation. 1995;92(5):1230–5.
54. Liu MW, Roubin GS, King 3rd SB. Restenosis after coronary angioplasty. Potential biologic determinants and role of intimal hyperplasia. Circulation. 1989;79(6):1374–87.
55. Ferns GA, Raines EW, Sprugel KH, Motani AS, Reidy MA, Ross R. Inhibition of neointimal smooth muscle accumulation after angioplasty by an antibody to PDGF. Science. 1991;253(5024):1129–32.
56. Lindner V, Reidy MA. Proliferation of smooth muscle cells after vascular injury is inhibited by an antibody against basic fibroblast growth factor. Proc Natl Acad Sci U S A. 1991;88(9):3739–43.
57. Ip JH, Fuster V, Israel D, Badimon L, Badimon J, Chesebro JH. The role of platelets, thrombin and hyperplasia in restenosis after coronary angioplasty. J Am Coll Cardiol. 1991;17(6 Suppl B):77B–88B.
58. Nishiyama H, Umemura K, Saniabadi AR, Takiguchi Y, Uematsu T, Nakashima M. Enhancement of thrombolytic efficacy of tissue-type plasminogen activator by adjuvants in the guinea pig thrombosis model. Eur J Pharmacol. 1994;264(2):191–8.

Part II
Thrombosis and Hemostasis Models

Chapter 5
Murine Models of Thrombosis and Hemostasis

Brian C. Cooley

Abstract The study of thrombosis and hemostasis has greatly benefited from the development and application of murine models. Thrombosis models have been designed for applications to venous, arterial, and microvascular blood clotting. Common vessels include the infrarenal vena cava, the carotid artery, and several microvessel sites based on thin tissue layers. Methods of analysis range from simple weight/length measurements or time for an occlusive thrombus to grow to more sophisticated intravital fluorescence imaging over time using fluorophore-labeled, thrombus-targeting molecules and cells. Hemostasis models have focused on tail resection designs, to measure the time to hemostatic achievement or collection of blood to measure total volume of blood lost. Other hemostatic models have been designed around injury/transection of the saphenous vein. These many models have been applied with high success to a large variety of transgenic and knockout mouse lines, to determine gene-specific effects on blood clotting under various conditions. Future studies will benefit from appropriate model selection, matching the specific model to the research question.

Keywords Thrombosis • Hemostasis • Thromboembolism • Platelets • Fibrin

5.1 Introduction

The advent of transgenic and gene knockout technologies and their relative ease of application in mice has led to an explosion in utilization of this species in many fields of medical and biological research. The study of thrombosis and hemostasis is exemplary of this transition; prior to the mid-1990s, most in vivo thrombosis and hemostasis models were done in rats, rabbits, and larger animals, whereas the past 15 years have seen the vast majority of studies using murine-adapted models. This chapter will delineate and discuss the various models of note and their utility in the field.

B.C. Cooley, Ph.D. (✉)
Department of Pathology and Laboratory Medicine, Rodent Advanced Surgical Models Core Lab, McAllister Heart Institute, University of North Carolina, Chapel Hill, NC 27599, USA
e-mail: brian_cooley@med.unc.edu

M. Sata (ed.), *Mouse Models of Vascular Diseases*,
DOI 10.1007/978-4-431-55813-2_5

Blood clot formation manifests in two processes: hemostasis (transected/ruptured microvessels or larger-vessel punctures, a desirable process and evolutionarily selected to maintain circulatory integrity) and thrombosis (when clots form inside intact large vessels, blocking flow and limiting circulation regionally with pathologic secondary consequences). Large-vein thrombosis is most commonly encountered in leg and pelvic veins – deep vein thrombosis (DVT) – causing leg pain and swelling and can lead to clot embolization that can disrupt lung circulation as pulmonary embolism (PE). Clinical arterial thrombosis develops under many conditions, generally resulting in blockage of inflow to downstream tissues, such as coronary thrombosis and its associated myocardial infarction or carotid/cerebral artery thromboembolism and its associated stroke symptoms. Plaque rupture in atherosclerotic vessels is considered the primary initiator of arterial thrombosis; however, it can be difficult to determine whether it is thrombus at the plaque rupture site, or downstream lodging of a thromboembolus, or even ruptured plaque material – or some combination of these – that causes the final occlusive event. There are many other initiators of both arterial and venous thrombosis, such as vascular trauma, chemotherapeutic access sites, and even surgical vessel repair, to name some of the more common examples. In vivo modeling of these various thrombus inductions and their sequelae is difficult at best and becomes especially problematic in the very small mouse body size, making such model design quite limited and challenging.

Blood clotting at a vessel surface has two main initiators: tissue factor and collagen. Disruption of the endothelium or complete vessel wall breach causes exposure of both of these elements. Tissue factor is the primary initiator of the well-known coagulation cascade, binding to Factor VIIa to form the extrinsic tenase complex, generating Factor Xa which assembles with Factor Va to form the prothrombinase complex [see Ref # 1–3 for reviews]. This latter enzymatic unit drives the generation of large amounts of thrombin which is the final enzyme that converts fibrinogen to fibrin, the main structural coagulation protein of a clot. Many other pro- and anticoagulation factors are involved in regulating this aspect of clot formation, notably intrinsic tenase, the combination of Factor IXa with its cofactor, VIIIa, as another route for Factor Xa generation. All of the coagulation complexes have greatly enhanced activity when assembled on phospholipid membranes, such as activated/injured endothelium or bound/activated platelets.

Collagen is the other primary initiator of thrombosis [1, 4, 5]. Platelets in circulation bind to collagen through several receptors: direct binding to the integrin receptor $\alpha_2\beta_1$ or the glycoprotein GPVI and indirect binding to the GPIb/IX/V complex. This latter receptor complex has much higher surface presence on platelets (~25,000 copies per platelet) than the other collagen receptors. It binds to von Willebrand factor (vWF) which is found in circulation. vWF is also released by activated platelets and activated/injured endothelium and thus has a high concentration in the vicinity of vessel injury and platelet binding and activation, where a clotting nidus is stimulated to further accrue more platelets. Upon binding/activation, platelets also release other granule contents that stimulate circulating platelets to aggregate via platelet:platelet interactions mediated by the integrin, $\alpha_{IIb}\beta_3$, with

linkage provided by several circulating proteins, notably the highly prevalent fibrinogen molecule. This localized but temporally brief high stimulatory environment causes massive platelet thrombus formation. In the exposed ring of collagen at the end of a transected vessel or puncture site of a larger vessel, this rapid buildup quickly develops into a beneficially occlusive hemostatic plug, which gets reinforced as a fibrin mesh is generated. In a mildly injured large vessel (e.g., arterial catheter insertion/removal), platelet activation/aggregation is limited and subsequently subsides (through platelet disaggregation), but in more severe vessel wall disruption (e.g., plaque rupture), this thrombus buildup can extend across the diameter too quickly, causing a pathologically occlusive event.

There are clear overlapping and reciprocating interactions between coagulation (fibrin formation) and platelet aggregation. Thrombin generated by the coagulation cascade sequence is also a powerful stimulator of platelet activation and aggregation via protease-activated receptors (PARs) on the platelet surface [6]. Reciprocally, platelets provide a vital surface for coagulation complex assembly where the highest activity of coagulation enzymes are localized [7]. Fibrinogen, the precursor of fibrin, is also the primary connecting protein for $\alpha_{IIb}\beta_3$-mediated platelet aggregation [8–10]. This interactive aspect of clot formation is exemplified by the high success and standard use of heparin compounds (Factors Xa and thrombin inhibitors) for many arterial interventions where platelets are known to dominate clot formation [11, 12]. Furthermore, strong clinical evidence has shown that inhibiting platelet aggregation (e.g., with aspirin) can reduce DVT where fibrin clotting is considered to predominate [13–15]. Thus, an understanding of thrombogenesis under any conditions should consider both fibrin- and platelet-based aspects of clot development.

In consideration of murine models of thrombosis and hemostasis, two aspects of study design are of paramount importance – how a clot is formed and how the clot is evaluated. Induction of a clot should have as much clinical relevance/analogy as possible; however, this is often the major shortcoming of experimental studies. Similarly, how the clot is studied – the outcome measure – is an all too often simplified and possibly misleading representation of thrombodynamics. The rest of this chapter will describe the various murine models of thrombosis and hemostasis in most prominent use, critically appraising their utility with these considerations in mind.

5.2 Mouse Models of Venous Thrombosis

Simulating DVT in a mouse is most often done by selecting the largest accessible vein in the mouse, the infrarenal vena cava (IVC). Other veins for model selection have included the iliac, femoral, saphenous, and jugular veins. Some models use injuries to venules of the microvasculature, as models of more general thrombus formation.

5.2.1 IVC Stasis Model

This model [16] is based on rat versions [17] which all relate to the earliest studies of vein occlusion, such as the rabbit-based Wessler model [18]. Upon surgical exposure through a laparotomy, the IVC is simply ligated with a suture just upstream of (distal to) the left renal vein branch site. The model can be done either with or without side and/or back-branch ligations/cauterization; these branches have variable presence and anatomic location [19], which can further vary with mouse strain and gender (females have additional uterine vein branches that enter the IVC in the region of study). A thrombus will subsequently form in the stagnant site (Fig. 5.1) and undergo remodeling over the course of days to weeks.

The major advantages of this model are its relative technical ease and the large size of the clot that can be removed and weighed to give an index of clot size. The length can also be measured as a further index of clot size. Additionally, the clot can be used subsequently for histologic or histomorphometric evaluation [20] or it can be subjected to Western blot analysis for thrombotic component analysis [21].

The primary weakness of this model is its use of abrupt vessel occlusion (via ligature) to induce thrombogenesis. Whereas clinical DVT and related venous thrombosis begin with a thrombus growth which progresses to vessel occlusion, the IVC stasis model uses the opposite – occlusion to induce thrombogenesis. The clot also develops in an upstream direction, opposite to that found with clinical DVT [22, 23]. Thus, the clinical relevance of this reversed thrombotic inductive process and direction of growth is questionable. There can also be considerable variability in clot size/length due to technical differences in model application and mouse vessel anatomic (variability). Of particular note is that operator skill and experience can vary the response; a more traumatic dissection for ligature placement or side/back-branch ligature or cauterization can augment the thrombotic response. The mouse venous system has a great capacity to reroute venous return normally carried by the IVC, and any overlooked small branches can occasionally maintain a flow channel that can prevent thrombus formation.

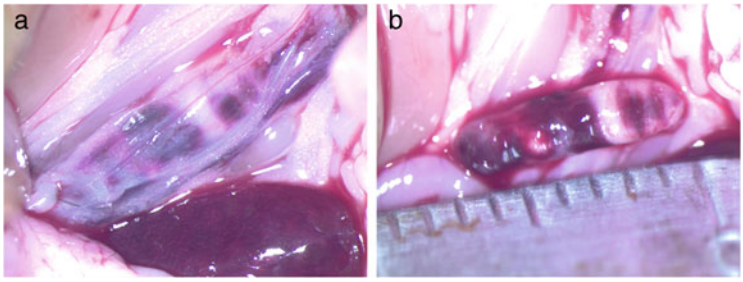

Fig. 5.1 Infrarenal vena cava (IVC) stasis model, showing 48-h thrombus within the IVC (**a**) with ligation site at lower left, and after opening the IVC (**b**), with scale bar showing ~6.5 mm length of a mixed red and white thrombus

5.2.2 IVC Stenosis Model

A modification on complete IVC ligation was developed to create a stenosis [24, 25], a flow restriction of ~90 % of the cross-sectional area just upstream of the left renal vein to induce a low-flow state in the IVC. This is done by placing a spacer tube next to the IVC as the ligature is tied in its infrarenal location and then removing the spacer to create a narrow flow channel through the ligature – a stenosis. The most commonly used spacers are a blunted 30-gauge needle [26, 27], a ~0.36-mm wire [28, 29], or a piece of 5-0 nylon or polypropylene suture [24, 25].

Unlike the complete stasis model, the IVC stenosis model has a less than 100 % thrombosis rate in most hands [26–31]. Efforts to increase the thrombosis rate have focused on side and back-branch ligations/cauterizations [29] as well as the initial model development of introducing a moderate injury by briefly clamping the IVC distal to the ligature with a neurovascular or similar clamp [24, 25]. Work in my lab has found that even this approach is not reliable, with only a ~20 % (3/15) clot formation rate at 24 h, using a large bulldog-style clamp applied for two 15-s periods (Cooley, unpublished data). Others have reported ~50 % clot formation rates without using a clamp injury [31], further suggesting a high variability in clot formation among different operators. Furthermore, when the clot does form, the reported size/weight of the developing thrombus can have a large range and standard error [28], making comparisons among experimental and control groups less rigorous. The model is closer to what is envisioned as simulating clinical DVT due to flow restriction; however, as clinical DVT is believed to develop most often in a downstream direction from a valve pocket, the IVC stenosis thrombus develops in an upstream direction, an oppositely directed scenario which may weaken its clinical relevance. Because of the less than 100 % thrombosis rate, the model may be most useful for evaluating a thrombus-augmenting (prothrombotic) state. This might show both an increase in thrombosis rate and an increase in thrombus size and possibly both outcomes.

5.2.3 IVC Electrolytic Model

The concept of an electrolytic injury, using a mild positive-electric (anodal) current, to stimulate thrombus growth, was originally developed in a dog coronary artery thrombosis model [32]. Diaz and colleagues [33] have recently adapted this model to the mouse IVC. A 25-gauge angled needle with an indwelling silver-coated copper wire is inserted into the IVC near the iliac bifurcation, advancing it proximally and holding it against the inner wall of the IVC. A 250-μA constant anodal current is delivered for 15 min using a Grass stimulator, with cathode grounding to nearby tissue (e.g., skin wound edge), then the needle is removed from the IVC. Thrombus formation is consistently observed at 2 days, using a weight measurement and subsequent protein or microanatomic evaluations

[33]. The primary advantage of this model is that it induces a reliable thrombus under flowing conditions without vessel occlusion, with the thrombus extending downstream from the site of application, thus simulating the purported clinical scenario for DVT development. Disadvantages include (1) the use of a substantial nonphysiologic thrombotic stimulus, an electrolytic injury which is applied to the inside of the vessel; (2) an extra needle puncture site for introducing the 25-gauge needle (adding an additional thrombotic injury); and (3) the need for a relatively expensive constant-current regulated electrical power source to generate the electrolytic induction of thrombus.

5.2.4 Femoral Vein Electrolytic Model

This model uses the same basic electrolytic process as described in the above model to induce a thrombus. The initial model [34] used a smaller microsurgical needle (70–130 μm in diameter) inserted into and against the inner wall of the femoral vein, with a constant voltage source for a shorter time (1–2 min) for thrombus induction. Subsequent studies found that a technically simpler approach [35] yielded a similarly consistent and cleaner thrombus, without adding the needle insertion injury site. The femoral vein is exposed in an anesthetized mouse by simple skin incision and directed retraction, without any other dissection; the vein surface becomes immediately accessible. The blunt end of a 75-μm microsurgical needle (Sharpoint, Surgical Specialties, Reading, PA) with the suture pulled out of the swaged end gives an easily held, iron-containing flat and circular area for contact onto the outer surface of the vein. The anodal (positive-current) end of a 1.5- or 3-V direct current source is easily connected to this wire by holding a connecting wire between the surgeon's gloved finger and the metal instrument that holds the microneedle; the cathode of the power source is attached to local tissue such as the wound edge around the dissected site. Simple manual placement of the blunt end of the needle gently onto the surface of the vein completes the circuit (Fig. 5.2a) and generates a localized free-radical injury that transits through the vein

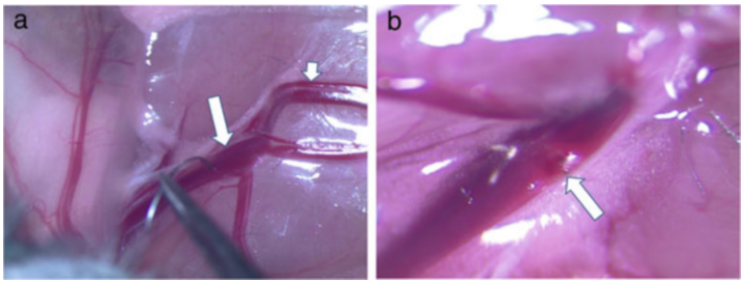

Fig. 5.2 Photomicrographs of mouse femoral vein electrolytic application, showing (**a**) anode-connected blunt microsurgical needle touching surface of femoral vein (*long arrow*; with *short arrow* indicating distal saphenous vessels) and (**b**) visible thrombus seen within the femoral vein 30 min after the electrolytic injury (*long arrow*)

wall to confer thrombogenesis (Fig. 5.2b). A mechanical hand or micromanipulator can also be devised to hold the needle against the vein, though for general, relatively brief applications, hand-holding of the needle is sufficiently steady and consistent.

The contact can be left in place for a variable time, depending on the desired outcome, using a rough equation of [time] × [voltage] to calibrate a consistent injury. A 1.5-V delivery for 30 s yields a consistent, moderate size, nonocclusive thrombus. Even 1–2 s of delivery will induce a small, short-lived thrombotic response, whereas 3 volts applied for 90 s causes a far larger, extended thrombus (Fig. 5.3). This approach, surface-applied electrolytic injury, can be delivered to any vein large enough to have an exposed accessible surface from an intramuscular

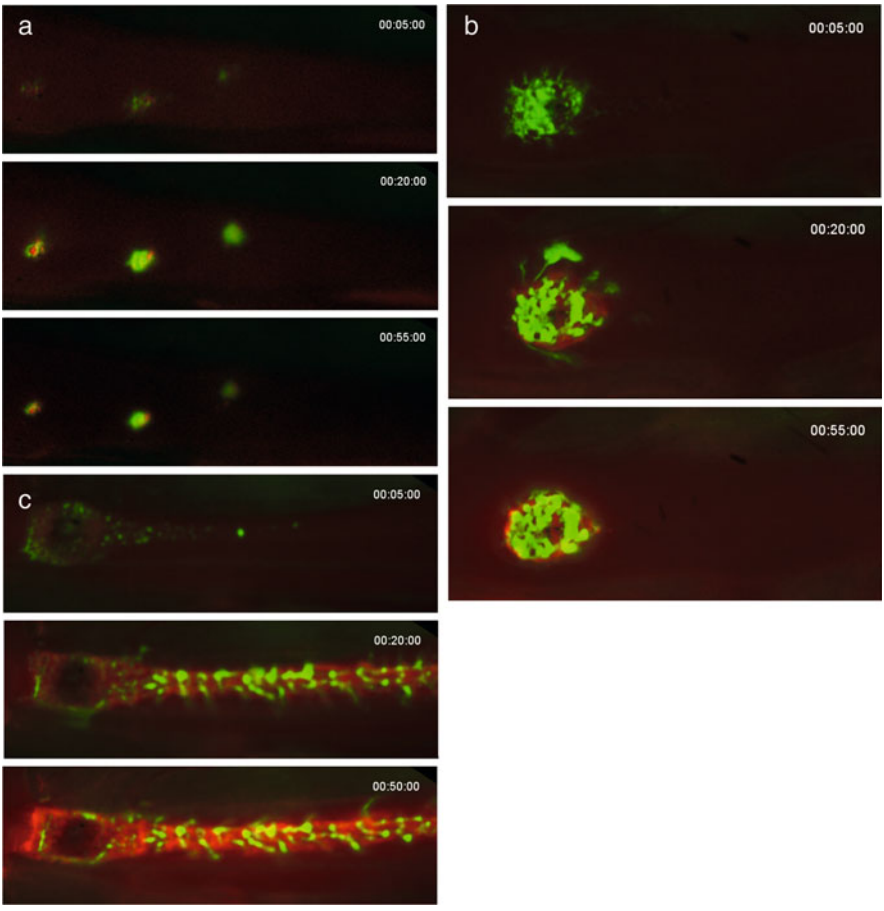

Fig. 5.3 Intravital fluorescence imaging of brief electrolytic injuries to the femoral vein, showing platelet (*green*) and anti-fibrin (*red*) images of the thrombi at 5, 20, and 55 min: (**a**) three regions on the femoral vein surface received 2-s electrolytic injuries with a 1.5-volt application; (**b**) a 30-s injury; and (**c**) a 180-s injury. Flow in the vein is from left to right

venule to the saphenous or epigastric vein (all in the same wound site as the femoral vein exposure) to the IVC.

The major drawback of this model is with the evaluation. The femoral vein is considerably smaller in diameter (0.5–0.6 mm) and shorter in length than the IVC (which is >1 mm in diameter and ~3–4 times longer); this smaller vessel limits the potential size of the ensuing thrombotic mass. Thus, measuring clot weight or length results in too small a datum for separation of experimental groups, with values too close to the limits of scale sensitivity and precise surgical extraction. The thrombus is also very small for other useful applications, such as Western blot analysis. To obtain a reasonable measure of thrombus size, histomorphometric analysis can be applied [34, 36] which involves a complete sectioning of the thrombus and careful area measurements of the clot at evenly spaced cross sections throughout the series, summing the areas to yield a volume estimate. The laborious process also only provides one time point per sample (as in the IVC models) taken at the time of harvest.

To overcome the limitations associated with femoral vein thrombosis in a mouse, an intravital fluorescence imaging system (Fig. 5.4) was developed in concert with the model [35]. A basic dissecting or operating microscope is used, either with inbuilt fluorescence capacity or with a custom-configured system integrated with a non-fluorescence/operating microscope (as developed by the author [35]). This system uses a 100-mm objective lens that allows magnification up to 100X and yields a 2.4 × 3.2 mm field in a C-mounted low-light digital camera, providing sufficient resolution for relatively fine features of thrombodynamic changes. The long working distance of the objective lens permits surgical manipulations before or during imaging. A filter wheel is incorporated between the

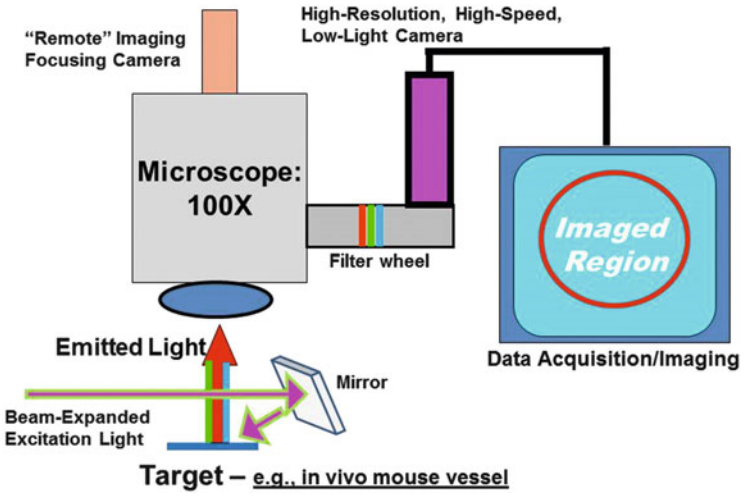

Fig. 5.4 Schematic of custom-designed intravital fluorescence imaging system. The excitation light (e.g., beam-expanded lasers) reflects off a mirror to the surgical field to induce emission in the target vessel, with image capture through a microscope-filter-camera-computer combination

microscopic optical path and the camera to allow flexible selection of emission-specific filters. An array of lasers for specific excitation wavelengths are combined with beam expanders (defocusing lenses) that spread each ~1-mm laser beam to a sufficiently large diameter (2–3 cm) to evenly illuminate the desired field of image capture. A shuttering system is used to limit this illumination via strobe synchronization with the camera shutter, to minimize photo-bleaching. The camera should have controls to permit digital video capture with control of both exposure time and between-exposure delays: this allows time-lapse video capture of a slow-growing thrombus. The lasers can be arrayed with horizontal beam paths adjacent to the microscope, using a mirror system to deflect the light onto the microscopic field of view (i.e., the surgical site of thrombus induction).

For imaging a thrombus, a multitude of fluorophore-linked, thrombus-targeting compounds can be generated to query a variety of aspects about thrombodynamics. The number of fluorophores used in the same thrombus imaging session is primarily limited by the laser and filter sets available and their relative exclusivity. A standard setup [35] is to use a blue or green-yellow fluorophore matched with a red/near-infrared set, using one color for platelet labeling and one for an anti-fibrin antibody, which allows image acquisition for the two dominant structural components of a thrombus. Antibodies or peptides with binding affinities to a number of thrombus-specific targets can be fluorophore labeled and injected systemically, with thrombus site imaging to capture accumulating label. Platelets can be isolated from a donor mouse and membrane labeled for subsequent injection and detection of their accumulation. A standard approach [37–43] is to label platelets with rhodamine 6G or Vybrant DiD (Invitrogen), excited with green (532 nm) or red (650 nm) wavelengths, respectively, with simultaneous injection of a red- or green-labeled anti-fibrin antibody, respectively; this allows simultaneous evaluation of both platelet and fibrin development in a growing thrombus.

The primary advantages of this imaging approach combined with the electrolytic injury are multifold:

1. The surgical exposure and thrombus induction are simple and quick (under 5 min).
2. The thrombotic induction is clean, without any extravascular bleeding (e.g., from puncture holes) which can obscure imaging or give false-positive viewing of an intravascular thrombus.
3. The electrolytic injury can be varied to generate larger or smaller clots simply by changing the applied voltage and/or the time of application.
4. The developing thrombus can be imaged continuously for both qualitative and quantitative offline analysis.
5. Offline analysis yields a direct quantitative evaluation of each fluorophore-linked thrombotic element over time, providing a wealth of data from each assay. By selecting a laser-excitation power density that optimizes image capture of a given fluorophore without camera saturation, the area of fluorescence can be combined with the average pixel intensity of each fluorophore to offer a relative net total fluorescence in each image (with background subtraction). By

quantitating every image over time, the thrombodynamic profile for a given thrombus-targeting compound is generated. Adjustments can also be made for mouse weight (to estimate blood volume) and amount of injected fluorophore to permit normalizing of a group of data for between-animal and between group quantitative/statistical comparisons [35].
6. The same in vivo model can be evaluated with different combinations of thrombus-targeting compounds (various platelet-specific receptors/integrins, coagulation cascade components and coagulation complex assemblies, and other cellular and plasma-carried elements [35]).
7. Time-lapse image series can be developed into videos that speed up the viewing of an extended thrombodynamic process, thus showing, for example, a 1 h thrombotic growth and stabilization in around 15 s, overlaying images for color-specific identification of each thrombotic element.

5.2.5 Other Venous Models

Mechanical, chemical, and laser-injury induction mechanisms have been used on murine veins to stimulate thrombosis, though these approaches are less common and yield more variability in the thrombosis response. Pinching a vein [44] with forceps or a clamp will cause a mechanical injury to the wall with subsequent intraluminal thrombus development at the injury site. Ferric chloride has been used to generate a free-radical injury [45, 46], similar to the electrolytic injury, generally applied by placing a ferric chloride-saturated filter on the vessel surface for a brief (1–3 min) period; this method is more established in arterial thrombosis models (see below). Difficulty with reproducibility is a main contributor to the less frequent use of these models.

5.3 Arterial Thrombosis Models

There are three models of arterial thrombosis that are most commonly done in the mouse, all three of which use a form of free-radical generation to stimulate thrombosis. Several other models have also been developed but are less commonly used due to variability, technical difficulty, or both. All of these models are most often done in the common carotid artery, primarily because of the ease of dissecting and isolating a long, unbranched length for the manipulations.

5.3.1 *Ferric Chloride Model*

Originally described for the rat carotid artery [47], this model is easily adapted to the smaller mouse counterpart [48, 49]. The basic model uses a filter paper strip, usually 1×2 mm, which is soaked in a ferric chloride solution with a concentration by weight of 2–20 % [50]. This saturated strip is laid onto the surface of the common carotid artery for a specified period of time (generally 1–3 min). After its removal and washing of the vessel, flow in the artery is monitored with a flow probe (e.g., Transonic cuff) or similar ultrasound Doppler system. The outcome measure is most often the "time to occlusion" (TTO), the time from initial filter paper placement with baseline flow until the rate of flow approaches zero. Because of the difficulty in determining an absolute zero flow state with the available instrumentation, and because the fall in flow is generally rapid as it passed through 50 % and 25 % of baseline, the TTO is often based on the time to reach 50 % or 25 % of the baseline flow. Depending on the ferric chloride concentration and application time, and the particular mouse phenotype or antithrombotic treatment, some vessels may not undergo significant or even any flow reduction; a final end-assay time of 30 min is generally sufficient to identify whether or not an occlusive thrombus will develop. Most vessels that occlude remain occluded without any re-establishment of flow over the 30-min observation (Fig. 5.5). Some phenotypes/therapies will result in an unstable thrombus, for which an apparent TTO develops but partial or complete flow restoration is seen, sometimes showing the phenomenon repeatedly over 30 min. Decisions on how to treat these nonstandard data [51] should be made, ideally prior to running an assay. This model often requires a substantial number of animals per phenotypic group to obtain a suitable data set for comparison to other groups [52].

While ease of technical application and data collection has made this a popular model, there are several experimental drawbacks. As with many free radical-based injury models, the mechanism of injury which leads to thrombogenesis is

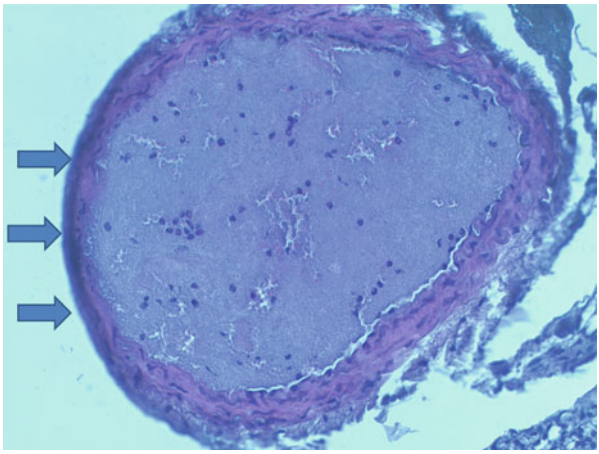

Fig. 5.5 Histologic cross section (H&E stain) of murine carotid artery 30 min after ferric chloride injury to vessel surface (*blackened* wall indicated by *arrows on left*). Thrombus is mostly composed of platelets, with occasional leukocytes and pockets of red blood cells

incompletely understood [53, 54]. The data are non-Gaussian in nature, with a general limit on the shortest TTO and an infinite upper TTO that requires an arbitrary cutoff. Furthermore, the TTO is an indirect measure of thrombosis, the time at which a thrombus gets large and stable enough to occlude flow in the vessel. A slow-growing but thrombo-resistant clot might yield a longer TTO, which would be misinterpreted as a hypothrombotic response; conversely, a rapid-growing but possibly unstable clot may still yield an early occlusion (short TTO) that is interpreted as hyper- or prothrombotic. There is often a lag in the first few minutes before any substantial thrombus develops [55], even under prothrombotic conditions, making discernment of shorter TTOs from control TTOs difficult. Thus, despite its extensive utility, the ferric chloride model as an assay must be critically appraised in each application.

5.3.2 Rose Bengal Model

Intense light in a wavelength range of ~500–600 nm will stimulate singlet oxygen production by Rose bengal. When light is illuminated onto a localized area of the carotid artery of a Rose bengal-injected mouse, the generated singlet oxygen will confer molecular damage at the inner vessel surface, with subsequent thrombogenesis [56–58]. The light is generally applied continuously to maintain the damaging effect. The concentration of circulating Rose bengal plus the illumination intensity (power density, usually delivered by a 540-nm nitrogen laser) is calibrated to yield an occlusive thrombus, using the TTO (as with the ferric chloride model) as an endpoint measure (monitored with a flow probe). The TTO is generally longer than that for the ferric chloride model under similar phenotypic/pharmacologic conditions, suggesting that a milder but prolonged injury is needed to generate an occlusive thrombus with this model. Indeed, the need for continuous laser irradiation/stimulation implies that a somewhat different thrombodynamic process may be operative. The thrombotic occlusion can, as with the ferric chloride model, undergo cyclic reflow [57]. The equipment (laser) adds more to the setup for model development, but otherwise, it is quite similar to the ferric chloride in application, advantages, and shortcomings.

5.3.3 Arterial Electrolytic Injury Model

Surface application of an electrolytic injury can be done on the mouse carotid artery [35], similar to the description above in the venous version of the model. A stronger "dose" of electrolysis (iron deposition) is needed for the thicker-walled artery to generate a substantial injury; generally 3 V for 30 s is sufficient to create a large but nonocclusive thrombus, using a slightly larger microsurgical needle (130–140 μm in diameter) for charge delivery. The same intravital imaging approach (Fig. 5.4) as

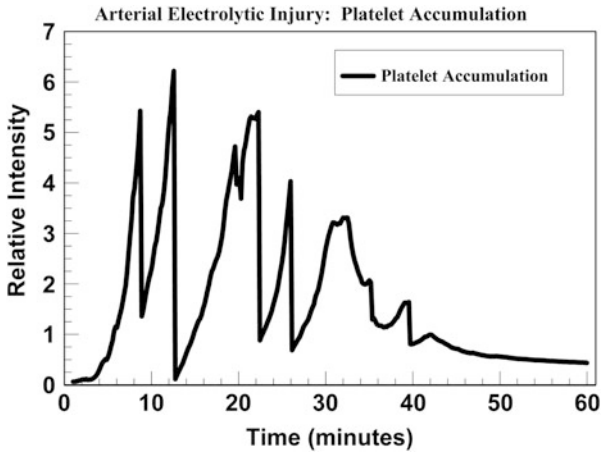

Fig. 5.6 Graph showing the relative intensity of fluorescently labeled platelets at the site of a 30-s electrolytic injury applied to the surface of a murine carotid artery. Data were collected from images captured every 10 s, over the course of 60 min starting 1 min after the initiation of the brief electrolytic injury. Four clearly evident abrupt embolic events can be seen (rapid falls in the intensity), with the second embolus at approximately 12.5 min showing virtually complete thromboembolism

with the venous system is used for outcomes measures, selecting from a variety of potential thrombus-targeting, fluorophore-labeled compounds/cells. A simplified version of imaging can also be used, exploiting the "white" nature of the platelet thrombus and its exclusion of red blood cells to permit direct-light viewing/imaging of the developing clot and using an area measurement of this white region as an estimate for 3-dimension clot size/mass [59].

The primary drawback to this model is the relatively unstable nature of the thrombus attachment site. This instability often causes partial or near-complete thromboembolism, with subsequent regrowth [35]; this embolic/regrowth process may occur repeatedly over the window of observation, though it has not been found to extend beyond 90–120 min (Cooley, unpublished findings). The massive nature of the embolism and thrombogenic regrowth are intriguing phenomena, but they play havoc with efforts to achieve quantitative consistency in a group series, often translating into sharp drops in otherwise smooth and consistent data sets [55] (e.g., in a 1-h imaging series, Fig. 5.6).

5.3.4 Other Arterial Models

In efforts to generate simple or more clinically analogous models, several other approaches have been developed. Mechanical injury mechanisms have been applied to the carotid artery using either a hard, brief pinch [60, 61] or severe

ligation (with immediate removal of the ligature) [62] to create localized vessel wall damage. Possibly due to the lack of consistency in injury delivery, these models can display considerable variability. They also have a rapid onset and resolution in comparison to the free-radical injury-based models, generally peaking in thrombus growth by ~3 min and becoming quiescent by 10–15 min [55].

Recent approaches to develop more clinical relevance in arterial thrombosis models have used atherogenic mouse lines, with injury applied to the pathologic lesions that develop at the internal/external carotid artery bifurcation. Mechanical [62, 63] or acoustic/ultrasound [64] disruption of the atherosclerotic lesion site can stimulate thrombus growth. Difficulties with these models are encountered with consistency and the poor access of the distal regions of these vessels for subsequent imaging. Another inherent shortcoming is that the atherosclerotic lesion in this portion of the carotid artery of an atherogenic mouse may lack similarity to the vulnerable human plaque lesions and their subsequent spontaneous ruptures.

5.4 Models Applicable to Both Arteries and Veins

While many of the above-described models use similar injury mechanisms for stimulating both arterial and venous thrombosis, these often use different outcome measures (e.g., flow in arteries versus clot harvest for analysis in veins). Some models have been developed for more direct comparison between arteries and veins, such as the electrolytic injury model described above, which has been used to compare arterial and venous thrombosis in the same experiment [41, 42]. A model of collagen-stimulated thrombosis was recently developed, with applications to both arterial and venous thrombosis using intravital fluorescence imaging in both for an outcome measure [65]. Another model of thrombosis uses sutured repairs of the femoral artery and vein, for which the small vessel size makes these repairs prone to thrombose, has also been described [66, 67]. This model has direct analogy to vascular surgical repairs which are subject to thrombotic occlusion. Intravital fluorescence imaging can be used for quantitative outcome measures at the vessel repair sites [67].

5.5 Microvessel Thrombosis Models

Two main tissue structures in mice have been used for thrombosis assays in smaller microvessels: the cremaster muscle [68, 69] and the mesenteric fascial/connective tissue [49, 70]. The mouse ear has also been described in a thrombosis model [71]. The arterioles and venules in these thin tissues can be viewed with standard fluorescence or confocal microscopy at high resolution, selecting vessels that are 30–200 μm in diameter for evaluation. Thrombosis is induced without vessel disruption/transection by either precise laser injury to the wall [68, 71] or by

illuminating the vessel with excitation light specific to an injected fluorophore (e.g., fluorescein [69, 70]), both models conferring heat injury, or by regional application of ferric chloride [49], either in solution or by brief application of a saturated piece of filter paper onto the tissue. Fluorescence imaging of the thrombotic site(s) is typically used to identify and quantitate accrual of fluorophore-labeled thrombus-targeting compounds. These approaches have been used successfully to identify many novel aspects of thrombogenesis. Their application requires a high-quality fluorescence or confocal microscopic system which may need to be dedicated specifically for in vivo applications (depending upon institutional/IACUC-established regulations). The high resolution and 3-dimensional image acquisition that can be achieved with confocal microscopy provides profound insight into the initiation and subsequent thrombogenic response in these injured microvessels.

One of the main critiques of these models is that the vasculature is not analogous to the large vessel in which clinical thrombotic complications develop. In this sense, studies of microvessel "thrombosis" may have stronger relevance for hemostasis, which is primarily a phenomenon of microvessel thrombotic occlusion. Indeed, the time to peak thrombus growth in the arterioles, 1–3 min [68, 71], is more along the lines of hemostatic bleeding times (generally under 2 min; see below), whereas sustained thrombotic responses of an hour or more, and often many days, are typically encountered with the murine large-vessel thrombosis models described in the previous sections. Nevertheless, these models remain a useful tool and source of insight for investigating intravascular thrombosis.

5.6 Hemostasis Models

There are two main models for evaluating hemostatic potential in mice. The most popular to date is the tail transection model, which has several variations. A relatively new model has been described using a transected saphenous vein.

5.6.1 Tail Transection Models

The basic model uses an anesthetized mouse and a sharp scalpel or razor blade to transect the tail tip at a defined length, generally between 1 and 5 mm from the end [72–74]. Bleeding from the tip is monitored until cessation, recording the time until complete hemostasis. This is most reproducibly done by hanging the tail in a 37 °C, saline-based solution within a tube, with maintenance of animal body temperature as well. The blood that emerges can be easily observed until bleeding stops, recording the time for hemostasis. The blood can also undergo quantitation by measuring the hemoglobin content collected in the solution during the bleeding [74], using spectrophotometric or similar measurement for quantitation (and adjusting for initial hematocrit of the animal). An alternative "dry" method uses a filter paper for blotting the transected tip at regular intervals (e.g., 10 or 30 s) until

no more spotting is seen on the filter paper, with the last visible blood spot used to determine the hemostasis time [75]. The major drawbacks of these models are their potential variability and the outcome of only one data point per mouse, limiting the experimental potential of each mouse with this assay. An advantage is that the assay can be done with survival of the animal, which can have the tail tip treated to prevent recurrent bleeding, allowing recovery from the blood loss for subsequent use in other studies.

5.6.2 Saphenous Vein Bleeding Model

An alternate bleeding model was developed by Whinna and colleagues [45, 76] in an effort to provide a more reproducible and larger working data set per mouse in a hemostasis assay. In this model, an anesthetized mouse undergoes saphenous vein exposure through a medial skin incision on the leg. Using a dissecting microscope for observation, the vein is first punctured with a hypodermic needle or partially transected with microscissors. A small longitudinal cut (~200–300 μm) is then made in the distal direction along the vein starting at the puncture/transection site. A tapered wick or sponge is used to absorb the emerging blood until the bleeding stops, recording the time from initial bleeding induction until cessation. The small clot in the opening is then immediately (or after a defined interval [77]) disrupted by gently scraping it out with the tip of a small hypodermic needle, stimulating rebleeding. The process of sponging until cessation and removing the recurrent clot is repeated, over the course of 30 min, recording the time to achieve hemostasis after each clot disruption maneuver. Thus, a series of hemostatic times is generated for each mouse, which can be averaged to yield a final hemostatic time with less mouse-to-mouse variability for a given phenotype or antithrombotic treatment. The data in a given group of mice can be combined into a group average hemostasis time, which is relatively comparable to tail bleeding times for more distal tail-tip amputations. Alternatively, each mouse can have the data transformed into the number of hemostatic events over a 30-min period, which is simply a count of the number of these events – both types of data are directly obtained from each other by the formula:

$$[30\ \text{min}]/[\#\ \text{of hemostatic events}] = [\text{average bleeding time for a mouse}].$$

5.6.3 Other Hemostasis Models

A pinpoint of laser light (~540 nm wavelength) can be used at a high power density and in a brief pulse to punch a small hole in a vein wall, with subsequent development of a hemostatic clot [78], generally combining this approach with fluorescence imaging of labeled cells/proteins at the laser-injury site (as described above). In another model, a 30-gauge needle can be used to make a puncture into the knee capsule, stimulating bleeding, with the extent of bleeding evaluated by

visual inspection using a Likert scale of 0–3 for characterizing the ensuing hemorrhage [79].

5.7 Model Selection

There are clearly a relatively large selection of models that can be used to evaluate thrombosis and hemostasis, developed for application in the murine system. How a particular investigator selects which model(s) to apply to his/her particular research question(s) will depend upon several factors:

1. *Available equipment or costs to purchase*: Often functional or used dissecting microscopes are available, though the quality of these can vary greatly, as can that for microsurgical instruments needed for the fine tissue manipulations. Availability of fluorescence imaging systems at sufficient resolution that can be used for intravital procedures may be a limiting factor at some institutions. For example, whole-animal imaging lacks any meaningful resolution for murine thrombosis models, especially in comparison to what can be obtained by confocal microscopy.
2. *Available technical expertise*: Having adequately trained staff to run the experiments is critical for reproducibility. Establishing a given procedure in a lab will require careful validation under previously established/published conditions. If a PI or staff member has no experience with a given model, learning to do it may need to be done from another investigator or lab where the model is well-established.
3. *Matching the model to the question*: There are no perfect models of either thrombosis or hemostasis. For this reason, model selection is at best an approximation based on assumptions and speculation with regard to clinical analogy and appropriateness. Clearly, venous thrombosis models will be most relevant for studying questions related to venous thrombosis, and similarly for arterial and microvessel thrombosis and hemostasis. A broader approach is often recommended, using two or more models that are judged to have the most relevance to the problem. If general thrombotic questions are posed, not specific to large versus small vessels or venous versus arterial systems, then selecting at least one model applicable to each vessel type may be in order.

5.8 Conclusions

Many murine models of relevance to thrombosis and hemostasis have been developed. Each has its strengths and limitations. Appropriate selection is essential for addressing the basic-science and/or clinically relevant questions of a given study plan.

References

1. Loscalzo J, Schafer AI, editors. Thrombosis and hemorrhage. 3rd ed. Philadelphia: Lippincott Williams & Wilkens; 2003.
2. Smith SA, Travers RJ, Morrissey JH: How it all starts: initiation of the clotting cascade. Crit Rev Biochem Mol Biol. 2015; Early Online: 1–11
3. Owens 3rd AP, Mackman N. Tissue factor and thrombosis: the clot starts here. Thromb Haemost. 2010;104:432–9.
4. Varga-Szabo D, Pleines I, Nieswandt B. Cell adhesion mechanisms in platelets. Arterioscler Thromb Vasc Biol. 2008;28:403–12.
5. Nuyttens BP, Thijs T, Deckmyn H, Broos K. Platelet adhesion to collagen. Thromb Res. 2011;127 Suppl 2:S26–9.
6. Alberelli MA, De Candia E. Functional role of protease activated receptors in vascular biology. Vascul Pharmacol. 2014;62:72–81. doi:10.1016/j.vph.2014.06.001.
7. Ahmad SS, London FS, Walsh PN. The assembly of the factor X-activating complex on activated human platelets. J Thromb Haemost. 2003;1:48–59.
8. Nachman RL, Leung LL. Complex formation of platelet membrane glycoproteins IIb and IIIa with fibrinogen. J Clin Invest. 1982;69:263–9.
9. Niewiarowski S, Kornecki E, Budzynski AZ, Morinelli TA, Tuszynski GP. Fibrinogen interaction with platelet receptors. Ann N Y Acad Sci. 1983;408:536–55.
10. Weisel JW, Nagaswami C, Vilaire G, Bennett JS. Examination of the platelet membrane glycoprotein IIb-IIIa complex and its interaction with fibrinogen and other ligands by electron microscopy. J Biol Chem. 1992;267:16637–43.
11. Bucx JJ, de Scheerder I, Beatt K, van den Brand M, Suryapranata H, de Feyter PJ, et al. The importance of adequate anticoagulation to prevent early thrombosis after stenting of stenosed venous bypass grafts. Am Heart J. 1991;121:1389–96.
12. Clagett GP, Sobel M, Jackson MR, Lip GY, Tangelder M, Verhaeghe R. Antithrombotic therapy in peripheral arterial occlusive disease: the seventh ACCP conference on antithrombotic and thrombolytic therapy. Chest. 2004;126 Suppl 3:609S–26.
13. Imperiale TF, Speroff T. A meta-analysis of methods to prevent venous thromboembolism following total hip replacement. JAMA. 1994;271:1780–5.
14. Lotke PA, Lonner JH. The benefit of aspirin chemoprophylaxis for thromboembolism after total knee arthroplasty. Clin Orthop Relat Res. 2006;452:175–80.
15. Dorr LD, Gendelman V, Maheshwari AV, Boutary M, Wan Z, Long WT. Multimodel thromboprophylaxis for total hip and knee arthroplasty based on risk assessment. J Bone Joint Surg Am. 2007;89:2648–57.
16. Myers DD, Hawley AE, Farris DM, Wrobleski SK, Thanaporn P, Schaub RG, et al. P-selectin and leukocyte microparticles are associated with venous thrombogenesis. J Vasc Surg. 2003;38:1075–89.
17. Downing LJ, Strieter RM, Kadell AM, Wilke CA, Brown SL, Wrobleski SK, et al. Neutrophils are the initial cell type identified in deep venous thrombosis induced vein wall inflammation. ASAIO J. 1996;42:M677–82.
18. Deykin D, Wessler S. Activation product, factor IX, serum thrombotic accelerator activity, and serum-induced thrombosis. J Clin Invest. 1964;43:160–6.
19. Diaz JA, Farris DM, Wrobleski SK, Myers DD, Wakefield TW. Inferior vena cava branch variations in C57BL/6 mice have an impact on thrombus size in an IVC ligation (stasis) model. J Thromb Haemost. 2015;13:660–4.
20. Myers Jr D, Farris D, Hawley A, Wrobleski S, Chapman A, Stoolman L, et al. Selectins influence thrombosis in a mouse model of experimental deep venous thrombosis. J Surg Res. 2002;108:212–21.
21. Deatrick KB, Eliason JL, Lynch EM, Moore AJ, Dewyer NA, Varma MR, et al. Vein wall remodeling after deep vein thrombosis involves matrix metalloproteinases and late fibrosis in a mouse model. J Vasc Surg. 2005;42:140–8.

22. Nordstrom M, Lindblad B. Autopsy-verified venous thromboembolism within a defined urban population – the city of Malmo, Sweden. APMIS. 1998;106:378–84.
23. Chau KY, Yuen ST, Wong MP. Clinicopathological pattern of pulmonary thromboembolism in Chinese autopsy patients. Comparison with Caucasian series. Pathology. 1997;29:263–6.
24. Singh I, Smith A, Vanzieleghem B, Collen D, Burnand K, Saint-Remy J-M, Jacquemin M. Antithrombotic effects of controlled inhibition of factor VIII with a partially inhibitory human monoclonal antibody in a murine vena cava thrombosis model. Blood. 2002;99:3235–40.
25. Singh I, Burnand KG, Collins M, Luttun A, Collen D, Boelhouwer B, Smith A. Failure of thrombus to resolve in urokinase-type plasminogen activator gene-knockout mice. Rescue by normal bone marrow-derived cells. Circulation. 2003;107:869–75.
26. Wang JG, Geddings JE, Aleman MM, Cardenas JC, Chantrathammachart P, Williams JC, et al. Tumor-derived tissue factor activates coagulation and enhances thrombosis in a mouse xenograft model of human pancreatic cancer. Blood. 2012;119:5543–52.
27. Brill A, Fuchs TA, Chauhan AK, Yang JJ, De Meyer SF, Kollnberger M, et al. Von Willebrand factor-mediated platelet adhesion is critical for deep vein thrombosis in mouse models. Blood. 2011;117:1400–7.
28. von Bruhl ML, Stark K, Steinhart A, Chandraratne S, Konrad I, Lorenz M, et al. Monocytes, neutrophils, and platelets cooperate to initiate and propagate venous thrombosis in mice in vivo. J Exp Med. 2012;209:819–35.
29. Brandt M, Schonfelder T, Schwenk M, Becker C, Jackel S, Reinhardt C, et al. Deep vein thrombus formation induced by flow reduction in mice is determined by venous side branches. Clin Hemorheol Microcirc. 2014;56:145–52.
30. Modarai B, Burnand KG, Sawyer B, Smith A. Endothelial progenitor cells are recruited into resolving venous thrombi. Circulation. 2005;111:2645–53.
31. Geddings J, Aleman MM, Wolberg A, von Br€uhl ML, Massberg S, Mackman N. Strengths and weaknesses of a new mouse model of thrombosis induced by inferior vena cava stenosis: communication from the SSC of the ISTH. J Thromb Haemost. 2014;12:571–3.
32. Romson JL, Haack DW, Lucchesi BR. Electrical induction of coronary artery thrombosis in the ambulatory canine: a model for in vivo evaluation of anti-thrombotic agents. Thromb Res. 1980;17:841–53.
33. Diaz JA, Hawley AE, Alvarado CM, Berguer AM, Baker NK, Wrobleski SK, et al. Thrombogensis with continuous blood flow in the inferior vena cava. A novel mouse model. Thromb Haemost. 2010;104:366–75.
34. Cooley BC, Szema L, Chen CY, Schwab JP, Schmeling G. A murine model of deep vein thrombosis: characterization and validation in transgenic mice. Thromb Haemost. 2005;94:498–503.
35. Cooley BC. In vivo fluorescence imaging of large-vessel thrombosis in mice. Arterioscler Thromb Vasc Biol. 2011;31:1351–6.
36. Cooley BC, Chen CY, Hess R, Schmeling G. Incomplete resolution of deep vein thrombosis under reduced flow conditions. Thromb Res. 2013;131:55–8.
37. Maroney SA, Cooley BC, Ferrel JP, Bonesho CE, Nielsen LV, Johansen PB, et al. Absence of hematopoietic tissue factor pathway inhibitor mitigates bleeding in mice with hemophilia. Proc Natl Acad Sci U S A. 2012;109:3927–31.
38. Smith AS, Choi SH, Collins JNR, Travers RJ, Cooley BC, Morrissey JH. Inhibition of polyphosphate as a novel strategy for preventing thrombosis and inflammation. Blood. 2012;120:5103–10.
39. Kuether EL, Fahs SA, Cooley BC, Schroeder JA, Montgomery RR, Wilcox DA, et al. Lentivirus-mediated platelet gene therapy of murine hemophilia A with pre-existing anti-FVIII immunity. J Thromb Haemost. 2012;10:1570–80.
40. Zhi H, Rauova L, Hayes V, Gao C, Boylan B, Newman DK, et al. Cooperative integrin/ITAM signaling in platelets enhances thrombus formation in vitro and in vivo. Blood. 2013;121:1858–67.

41. Cooley BC, Herrera AJ. Cross-modulatory effects of clopidogrel and heparin on platelet and fibrin incorporation in thrombosis. Blood Coagul Fibrinolysis. 2013;24:593–8.
42. Aleman MM, Walton BL, Byrnes JR, Wang JG, Heisler MJ, Machlus KR, Cooley BC, Wolberg AS. Elevated prothrombin promotes venous, but not arterial, thrombosis in mice. Arterioscler Thromb Vasc Biol. 2013;33:1829–36.
43. Ellery PER, Maroney SA, Cooley BC, Luyendyk JP, Zogg M, Weiler H, Mast AE. A balance between TFPI and thrombin-mediated platelet activation is required for murine embryonic development. Blood. 2015;125:4078–84.
44. Pierangeli SS, Liu XW, Barker JH, Anderson G, Harris EN. Induction of thrombosis in a mouse model by IgG, IgM and IgA immunoglobulins from patients with the antiphospholipid syndrome. Thromb Haemost. 1995;74:1361–7.
45. Buyue Y, Whinna HC, Sheehan JP. The heparin-binding exosite of factor IXa is a critical regulator of plasma thrombin generation and venous thrombosis. Blood. 2008;112:3234–41.
46. Wang X, Smith PL, Hsu MY, Ogletree ML, Schumacher WA. Murine model of ferric chloride-induced vena cava thrombosis: evidence for effect of potato carboxypeptidase inhibitor. J Thromb Haemost. 2006;4:403–10.
47. Kurz KD, Main BW, Sandusky GE. Rat model of arterial thrombosis induced by ferric chloride. Thromb Res. 1990;60:269–80.
48. Fay WP, Parker AC, Ansari MN, Zheng X, Ginsburg D. Vitronectin inhibits the thrombotic response to arterial injury in mice. Blood. 1999;93:1825–30.
49. Denis C, Methia N, Frenette PS, Rayburn H, Ullman-Cullere M, Hynes RO, Wagner DD. A mouse model of severe von Willebrand disease: defects in hemostasis and thrombosis. Proc Natl Acad Sci U S A. 1998;95:9524–9.
50. Wang K, Xu L. An optimized murine model of ferric chloride-induced arterial thrombosis for thrombosis research. Thromb Res. 2005;115:95–100.
51. Kwon I, Hong S-Y, Kim YD, Nam HS, Kang S, Yang SH, et al. Thrombolytic effects of the snake venom disintegrin saxatilin determined by novel assessment methods: a FeCl3-induced thrombosis model in mice. PLoS One. 2013;8:e81165. doi:10.1371/journal.pone.0081165.
52. Kerlin B, Cooley BC, Isermann BH, Hernandez I, Sood R, Zogg M, et al. Cause-effect relation between hyperfibrinogenemia and vascular disease. Blood. 2004;103:1728–34.
53. Tseng M, Dozier A, Haribabu B, Graham UM. Transendothelial migration of ferric ion in $FeCl_3$ injured murine common carotid artery. Thromb Res. 2006;118:275–80.
54. Eckly A, Hechler B, Freund M, Zerr M, Cazenave JP, Lanza F, et al. Mechanisms underlying FeCl3-induced arterial thrombosis. J Thromb Haemost. 2011;9:779–89.
55. Cooley BC. Murine arterial thrombus induction mechanism influences subsequent thrombodynamics. Thromb Res. 2015;135:939–43.
56. Kawasaki T, Kaida T, Vermylen AJ, Hoylaerts MF. A new animal model of thrombophilia confirms that high plasma factor VIII levels are thrombogenic. Thromb Haemost. 1999;81:306–11.
57. Eitzman DT, Westrick RJ, Nabel EG, Ginsburg D. Plasminogen activator inhibitor-1 and vitronectin promote vascular thrombosis in mice. Blood. 2000;95:577–80.
58. Matsuno H, Kozawa O, Niwa M, Ueshima S, Matsuo O, Collen D, Uematsu T. Differential role of components of the fibrinolytic system in the formation and removal of thrombus induced by endothelial injury. Thromb Haemost. 1999;81:601–4.
59. Kusada A, Isogai N, Cooley BC. Electric injury model of murine arterial thrombosis. Thromb Res. 2007;121:103–6.
60. Cooley BC, Gould JS. Experimental models for evaluating antithrombotic therapies in replantation microsurgery. Microsurgery. 1987;8:230–3.
61. Pierangeli SS, Barker JH, Stikovac D, Ackerman D, Anderson G, Barquinero J, et al. Effect of human IgG antiphospholipid antibodies on an in vivo thrombosis model in mice. Thromb Haemost. 1994;71:670–4.

62. Schulz C, Konrad I, Sauer S, Orschiedt L, Koellnberger M, Lorenz R, et al. Effect of chronic treatment with acetylsalicylic acid and clopidogrel on atheroprogression and atherothrombosis in ApoE-deficient mice in vivo. Thromb Haemost. 2008;99:190–5.
63. Kuijpers MJE, Gilio K, Reitsma S, Nergiz-Unal R, Prinzen L, Heeneman S, et al. Complementary roles of platelets and coagulation in thrombus formation on plaques acutely ruptured by targeted ultrasound treatment: a novel intravital model. J Thromb Haemost. 2009;7:152–61.
64. Hechler B, Gachet C. Comparison of two murine models of thrombosis induced by atherosclerotic plaque injury. Thromb Haemost. 2011;105 Suppl 1:S3–12.
65. Cooley BC. Collagen-induced thrombosis in murine arteries and veins. Thromb Res. 2013;131:49–54.
66. Cooley BC, Daley RA. Murine microvascular anastomosis model of thrombosis. Thromb Res. 1999;96:157–9.
67. Shi G, Meister D, Daley RA, Cooley BC. Thrombodynamics of microvascular repairs: effects of antithrombotic therapy on platelets and fibrin. J Hand Surg [Am]. 2013;38:1784–9.
68. Falati S, Gross P, Merrill-Skoloff G, Furie BC, Furie B. Real-time in vivo imaging of platelets, tissue factor and fibrin during arterial thrombus formation in the mouse. Nat Med. 2002;8:1175–81.
69. Rumbaut RE, Bellera RV, Randhawa JK, Shrimpton CN, Dasgupta SK, Dong JF, et al. Endotoxin enhances microvascular thrombosis in mouse cremaster venules via a TLR4-dependent, neutrophil-independent mechanism. Am J Physiol Heart Circ Physiol. 2006;290:H1671–9.
70. Chang M-C, Huang T-F. In vivo effect of a thrombin-like enzyme on platelet plug formation in mesenteric microvessels of mice. Thromb Res. 1994;73:31–8.
71. Rosen ED, Raymond S, Zollman A, Noria F, Sandoval-Cooper M, Shulman A, et al. Laser-induced noninvasive vascular injury models in mice generate platelet- and coagulation-dependent thrombi. Am J Pathol. 2001;158:1613–22.
72. Kaiser B, Markwardt F. Antithrombotic and haemorrhagic effects of the naturally occurring thrombin inhibitor hirudin. Folia Haematol Int Mag Klin Morphol Blutforsch. 1988;115:41–6.
73. Beviglia L, Poggi A, Rossi C, McLane MA, Calabrese R, Scanziani E, et al. Mouse antithrombotic assay. Inhibition of platelet thromboembolism by disintegrins. Thromb Res. 1993;71(4):301–15.
74. Broze GJ, Yin Z-F, Lasky N. A tail vein bleeding time model and delayed bleeding in hemophiliac mice. Thromb Haemost. 2001;85:747–8.
75. Iwatsuki Y, Kawasaki T, Hayashi K, Moritani Y, Nii T, et al. Combined effects of a factor Xa inhibitor YM466 and a GPIIb/IIIa antagonist YM128 on thrombosis and neointima formation in mice. Thromb Haemost. 2004;92:1221–8.
76. Pastoft AE, Lykkesfeldt J, Ezban M, Tranholm HC, Whinna HC, Laurizen B. A sensitive venous bleeding model in haemophilia A mice: effects of two recombinant FVIII products (N8 and Advate). Haemophilia. 2012;18:782–8.
77. Sehgal A, Barros S, Ivanciu L, Cooley B, Qin J, Racie T, et al. An RNAi therapeutic targeting antithrombin to rebalance the coagulation system and promote hemostasis in hemophilia. Nat Med. 2015;21:492–7. doi:10.1038/nm.3847.
78. Getz TM, Piatt R, Petrich BG, Monroe D, Mackman N, Bergmeier W. Novel mouse hemostasis model for real-time determination of bleeding time and hemostatic plug composition. J Thromb Haemost. 2015;13:417–25.
79. Øvlisen K, Kristensen AT, Valentino LA, Hakobyan N, Ingerslev J, Tranholm M. Hemostatic effect of recombinant factor VIIa, NN1731 and recombinant factor VIII on needle-induced joint bleeding in hemophilia A mice. J Thromb Haemost. 2008;6:969–75.

Part III
Transplant-Associated Atherosclerosis

Chapter 6
Murine Heart Transplantation and Graft Arterial Disease

Jun-ichi Suzuki, Masahito Ogawa, and Mitsuaki Isobe

Abstract Although more than 116,000 heart transplantations have been performed worldwide to date, graft arterial disease (GAD), which is a phenomenon of chronic rejection, is still a serious problem. Because GAD involves entire allograft arteries, angioplasty and bypass grafting are not practical treatment options. Therefore, GAD is the biggest long-term limitation in cardiac allograft recipients. Because the cause of GAD is mostly immunologic, several cytokines, chemokines, and adhesion molecules play a critical role in the process. Although there has been no established clinical strategy for preventing or treating GAD, recent investigations have proved some promising methodologies. In this article, we described a protocol of murine cardiac transplantation and pathological characteristics of GAD.

Keywords Heart transplantation • Chronic rejection • Adhesion molecule • Cytokine • Gene therapy

6.1 Introduction

Heart transplantation is a common surgical procedure in humans; almost 116,000 heart transplantations have been performed worldwide over the past 40 years [1]. However, graft arterial disease (GAD), which is a phenomenon of chronic rejection, is still a serious problem [1, 2]. Because GAD involves entire allograft arteries, angioplasty and bypass grafting are not practical treatment options. Therefore, GAD is the biggest long-term limitation in heart transplant recipients. GAD in cardiac allografts is especially problematic because hearts exhibit more severe diseases than other transplanted organs [3–5].

Several cytokines and adhesion molecules promote rejection; GAD is characterized by intimal thickening comprised of proliferative smooth muscle cells

J.-i. Suzuki (✉)
Department of Advanced Clinical Science and Therapeutics, Graduate School of Medicine, The University of Tokyo, 7-3-1 Hongo, Bunkyo, Tokyo 113-8655, Japan
e-mail: junichisuzuki-circ@umin.ac.jp

M. Ogawa • M. Isobe
Department of Cardiovascular Medicine, Tokyo Medical and Dental University, Bunkyo, Tokyo, Japan

M. Sata (ed.), *Mouse Models of Vascular Diseases*,
DOI 10.1007/978-4-431-55813-2_6

(SMCs) and extracellular matrix (ECM) with relatively intact internal and external elastic laminae. Although the cause of GAD is mostly immunologic, nonimmune pathways also contribute to its development. Inflammatory cells, such as lymphocytes, macrophages, neutrophils, and eosinophils, are all variably present in evolving lesions. In early stages, there is a subendothelial accumulation of mononuclear cell infiltration associated with markers of endothelial cell (EC) activation. Because endothelial or perivascular cellular immune injury induces persistent allograft vascular damage, inflammatory cells and activated ECs secrete growth factors to recruit and activate SMCs [3, 6–9]. Recently, the intimal SMCs in GAD lesions are known to derive in part from circulating host cells. Although these cells share a number of markers with medial SMCs, they are modulated cells with a proliferative and synthetic phenotype [3, 6, 10, 11].

In this article, we outlined the protocol of murine cardiac transplantation and the pathological characteristics of GAD.

6.2 Clinical Findings of GAD

Because transplanted hearts are denervated, clinical symptoms for ischemia are not useful to diagnose GAD. Coronary angiography (CAG) is still a standard methodology for the diagnosis of GAD in clinical settings. However, CAG is relatively insensitive and underestimates the lesions because GAD involves vessels diffusely. Instead, intravascular ultrasound (IVUS) and coronary computed tomography (CT) are preferred methods to quantitatively assess intimal thickening. IVUS is one of the most sensitive tools for diagnosis of GAD because it reveals both actual lumen diameter and thickness of the neointima. The examinations proved the high frequency of GAD; 90 % of patients develop GAD within 10 years. Of note, GAD development does not correlate with episodes or severity of cellular rejection and that vascular lesions occur despite adequate immunosuppression to prevent acute rejection [4, 12]. However, the procedure is invasive and is associated with a risk of complication. In contrast, CT can provide a comprehensive and noninvasive evaluation of GAD. It may be useful as a single noninvasive test not only for GAD evaluation but also for allograft function and other complications [13].

6.3 A Protocol of Murine Heterotopic Cardiac Transplantation

As an experimental model of GAD, transplantation of heterotopic cardiac allografts has been developed in mice. The animal model has demonstrable usefulness in studies of the pathophysiology of rejection. The histological findings are similar to the acute and chronic rejection seen in clinical heart transplantation. Here, we

demonstrate the representative protocol of murine heterotopic cardiac transplantation.

6.3.1 Donor Heart Preparation

1. Inject pentobarbital to anesthetize the donor mouse.
2. Immobilize the mouse using arm and leg restraints.
3. Wipe the skin with alcohol.
4. Open the abdominal cavity by making a transverse incision.
5. Cut the diaphragm and lift the anterior chest wall to expose the heart using clips (Fig. 6.1).
6. Make an incision on the posterior lateral thoracic cavity on the left and right sides of the chest.
7. Place a loose 5-0 silk suture around the inferior vena cava (IVC).
8. Insert it into the right atrium.
9. Inject 1.0 cc of 4 °C heparinized saline into the IVC.
10. Ligate the IVC with the 5-0 silk suture.
11. Isolate the right superior vena cava (SVC) in a similar fashion.
12. Ligate it with 5-0 silk suture.
13. Roll the heart toward the animals' right side and isolate the left SVC.
14. Ligate and divide it with a 5-0 silk suture to expose the left pulmonary artery (PA).

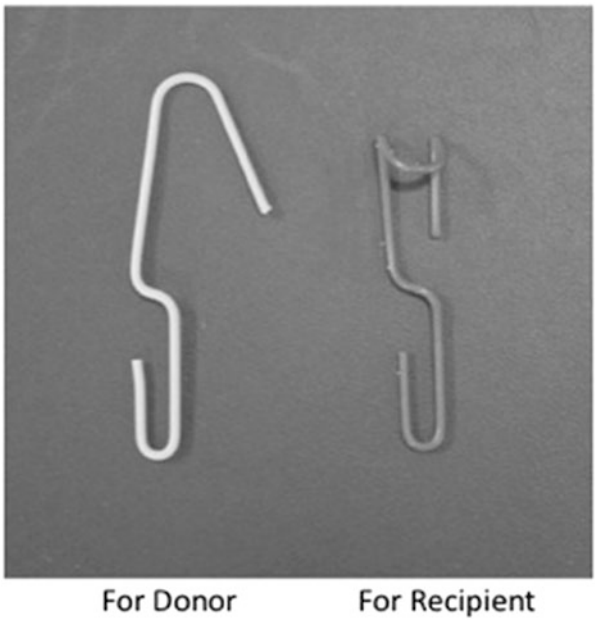

Fig. 6.1 Representative clips for donor (*left*) and recipient (*right*) preparation during the murine heart transplant surgery

15. Use micro-scissors to divide the aorta proximal to the right brachiocephalic artery.
16. Reflect the aortic cuff to expose the PA trunk and the left and right branches of the PA.
17. Divide the PA trunk as distally as possible.
18. Place a 5-0 silk suture around the base of the heart and tie.
19. The heart is then cut free at the base and placed in 4 °C saline.

6.3.2 Heart Implantation into the Recipient Mice

1. Anesthetize the recipient mice with pentobarbital.
2. Immobilize the mouse using arm and leg restraints.
3. Wipe the skin with alcohol and drape in a sterile fashion.
4. Make a midline vertical abdominal incision and enter the abdominal cavity using clips (Fig. 6.1).
5. Retract the bowel on to the chest and keep it wrapped in a sterile, moist gauze.
6. Isolate the abdominal aorta and IVC below the renal vessels (Fig. 6.2).
7. Use 10-0 nylon suture to ligate any lumbar vessels within the field.
8. Use micro-clips to nip the inferior followed by the superior vessels.
9. Form an aortotomy with a 30 G needle in order to enter the lumen of the aorta.
10. Extend the incision with fine micro-scissors to a length of approximately 2 mm.
11. Perform an end-to-side anastomosis of the donor aorta to the recipient aorta in the following fashion.
12. Place a 10-0 nylon suture stay stitch on the donor aorta and on the inferior angle of the incision in the recipient aorta and tie.
13. Place a second 10-0 nylon suture opposite the first in the donor aorta and the superior corner of the incision in the abdominal aorta and tie.

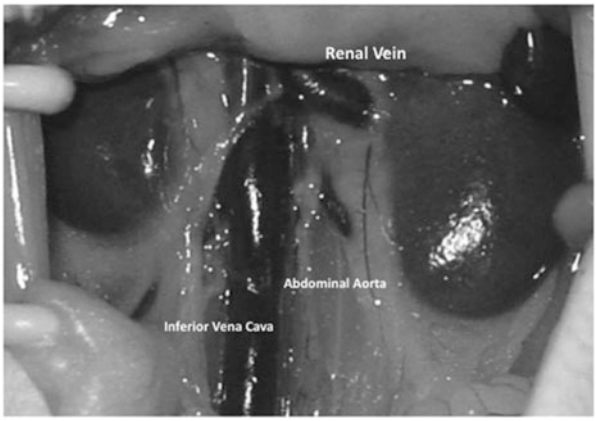

Fig. 6.2 A representative photo of the recipient abdominal aorta, inferior vena cava, and renal vessels

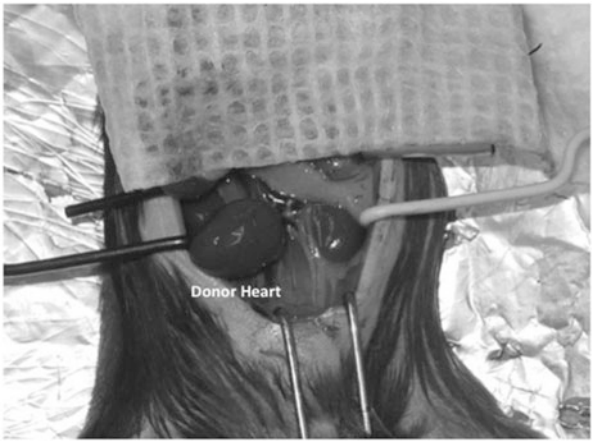

Fig. 6.3 A representative photo of the donor heart after transplantation

14. Make a running suture line from superior to inferior in the lateral wall of the aorta and tie with the previously placed stay stitch.
15. Perform an end-to-side anastomosis of the donor pulmonary artery to the recipient IVC in the following fashion.
16. Puncture the IVC with a 30 G needle and extend the incision for approx. 2 mm with fine micro-scissors.
17. Tie the donor pulmonary artery to the inferior corner of the incision in the IVC with 10-0 nylon.
18. Place a second 10-0 nylon opposite the first in the donor artery and the superior corner of the incision in the IVC and tie.
19. Make a running suture line between the pulmonary artery and the IVC and tie.
20. Release the distal micro-clip to reestablish venous flow.
21. Once hemostasis of the venous anastomosis is observed, the proximal micro-clip is gradually loosened and the arterial anastomosis observed for hemostasis.
22. When both anastomoses are considered secure, remove the micro-clips from the mouse (Fig. 6.3).
23. Return the bowel to the abdomen.
24. Use 6-0 silk suture to close the abdominal wall in two layers.
25. Recover the animal on a warming blanket.

6.4 Pathology of GAD

6.4.1 Immunological Features and Risk Factors

Pathologically, GAD involves the entire length of the transplanted arterial vasculature. GAD is characterized by concentric intimal thickening comprised of SMCs and ECM, with relatively intact internal and external elastic laminae. The vascular

media and adventitia are relatively unaffected, while inflammatory cells are variably present in evolving lesions. Calcification and atheroma formation are also uncommon. It is known that the clinical risk factors for GAD are as follows: donor history of hypertension, induction therapy with IL-2 antagonist or OKT3, pretransplant diagnosis of coronary artery disease, increasing number of HLA-DR mismatches, and so on. Other risk factors include obesity, diabetes, hyperlipidemia, viral infection, and hyperhomocysteinemia [3].

Allografts are subject to multiple injuries, such as immune and nonimmune factors. Although many pathological factors contribute to GAD development, any of the various injuries can independently induce GAD. Immune injury is known to play a critical role in GAD pathogenesis. Although cellular immune responses have a central role in GAD development, humoral injury is also recognized as a critical component. The predominant effector cells are macrophages; they secrete proinflammatory cytokines that influence smooth muscle-like cell (SMLC) and fibroblast proliferation. It also enhances ECM synthesis which results in GAD formation. Recipient T cells require two signals to be activated; one signal involves host T-cell receptor interaction with the donor major histocompatibility complex, and another signal involves ligation of costimulatory molecules. The nature and efficiency of both signals affect the development of GAD [14, 15]. Nonimmune risk factors, including ischemia, diabetes, and hypertension, correlate with intimal thickening of GAD. Periods of ischemia are significantly important for promoting GAD; these effects are attributable to ischemic EC, which increases local platelet accumulation. EC ischemic injury can also increase the major histocompatibility complex and adhesion molecule expression [16, 17]. *Cytomegalovirus* is known to be associated with an increased incidence of GAD, which is linked to wound repair and angiogenesis [18, 19].

6.4.2 Altered Myosin Heavy Chain Isoforms

We reported that there are three types of smooth muscle myosin heavy chain (MHC) isoforms expressed in vascular SMCs: SMl, SM2, and SMemb. SMl is expressed throughout early developmental stages to mature stages, and SM2 is expressed only after birth. These two isoforms are specific to SMCs, whereas SMemb is a non-muscle-type MHC isoform that is expressed in embryonic SMCs of fetal aorta and proliferating SMCs. The expression of these MHC isoforms can be a useful molecular marker for detection of pathological conditions in acute or chronic rejection. We showed that the coronary arteries had significant intimal thickening, as indicated in pathological samples in rat allografts taken on day 35 from FK506-treated recipients. Monkey allografts harvested on day 44 treated with anti-leukocyte function-associated antigen (LFA)-1 mAb showed severe GAD with perivascular cell infiltration. Immunohistochemically, SM2 was positive in the media of coronary arteries in native rat hearts and isografts. In FK506-treated rat allografts harvested on day 35, SM2 expression was eliminated in both the media

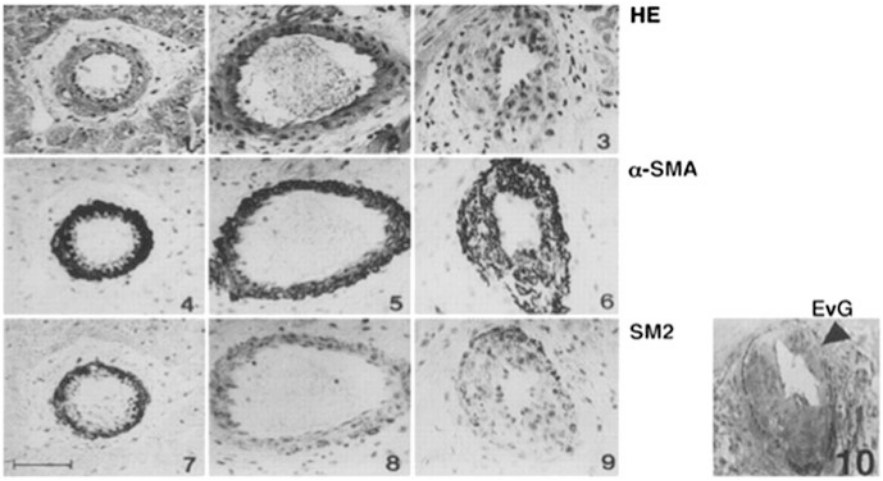

Fig. 6.4 Microscopic findings of rat coronary arteries. Panels at *top* (*1* through *3*) were stained with hematoxylin and eosin (HE), those in the *middle* (*4* through *6*) with anti-α-SMA antibody, and those at *bottom* (*7* through *9*) with anti-SM2 antibody. Elastica van Gieson staining was used to demonstrate intimal thickening (*10*). Both α-SMA and SM2 are expressed in the cells of the medial layer of native heart (*left*, *1*, *4*, and *7*). The allograft harvested on day 14 with FK506 treatment (*middle*, *2*, *5*, and *8*) does not show intimal thickening; however, SM2 expression in the cells of the medial layer was reduced. The allograft harvested on day 35 with FK506 treatment (*right*, *3*, *6*, *9*, and *10*) shows intimal thickening, and SM2 expression was also reduced in the medial layer and thickened intima. An arrowhead in panel *10* shows internal elastic lamina. Scale bar = 50 μm (From Ref. [10])

and thickened intima. However, a reduced SM2 expression was also observed in the media, even in the area lacking the intimal thickening in the FK506-treated rat allografts on day 14. The expression of α-SMA was observed both in the media and in the proliferative intima of all the coronary arteries (Fig. 6.4). In native monkey hearts, SMemb was negative in the media of coronary arteries. However, SMemb was expressed in thickened intima and media in monkey coronary arteries harvested on day 44 (Fig. 6.5). Transmission electron microscopy showed severe intimal thickening of graft coronary arteries in the allograft from FK506-treated rats on day 35. Thickened intima consisted of phenotypically modulated SMCs: some had abundant actin filaments, caveolas, and dense bodies similar to the normal phenotype. Others showed abundant mitochondria and endoplasmic reticula. Reduced actin filaments demonstrated phenotypic modulation (Fig. 6.6). We demonstrated that chronic rejection is characterized by diffuse coronary arteriosclerosis formed by diffuse intimal thickening that consists of proliferative vascular SMCs with phenotypic modulation. Because the proliferation of SMCs is regulated by sustained immune responses, the phenotypic modulation of SMCs can be a sensitive indicator of chronic rejection. In the study, we demonstrated that enhanced SMemb expression and reduced SM2 expression in the media as well as in the thickened intima of coronary arteries were shown in chronically rejected cardiac

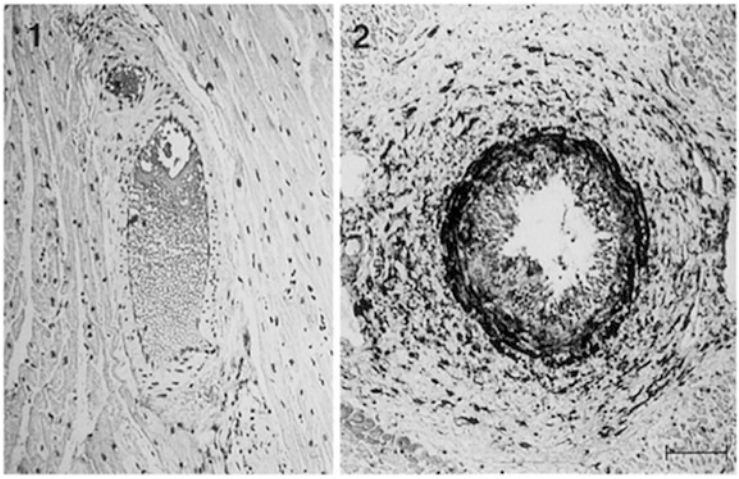

Fig. 6.5 Microscopic findings of monkey coronary arteries stained with anti-SMemb antibody (*1*, native monkey heart; *2*, transplanted monkey heart with anti-LFA-1 mAb treatment harvested on day 44). Although SMemb was not expressed in the native monkey heart, SMemb-positive cells were observed not only in perivascular lesions but also in the thickened intima and media in the transplanted monkey heart. Scale bar = 50 μm (From Ref. [10])

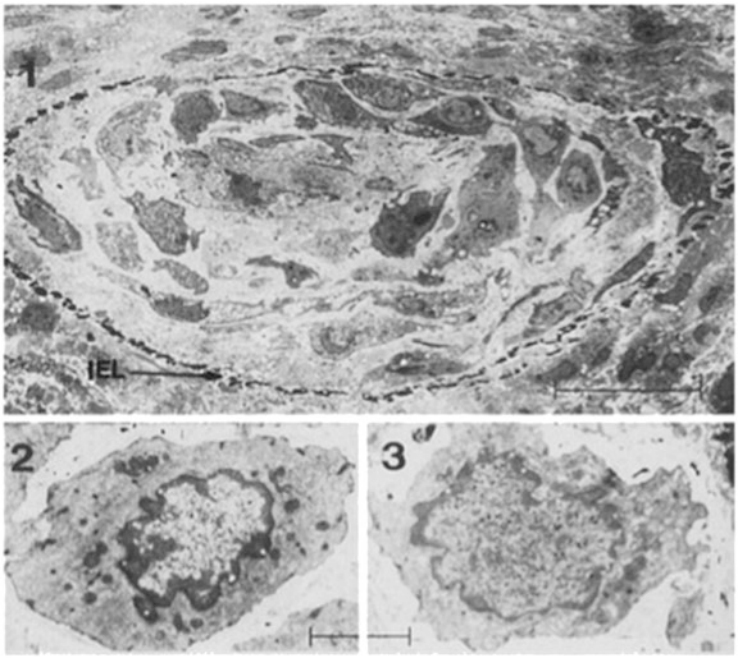

Fig. 6.6 Transmission electron microscopic findings of a coronary artery occluded by intimal thickening (*1*, transplanted rat heart with FK506 treatment on day 35) (IEL indicates internal elastic lamina). The smooth muscle cells that composed the thickened intima demonstrated phenotypes similar to normal cells (*2*) or phenotypic modulation (*3*). 1, scale bar = 10 μm; 2 and 3, scale bar = 1 μm (From Ref. [10])

allografts. These cells were phenotypically modulated SMCs with proliferative states characterized by abundant organelles on electron microscopy, indicating the altered expression of MHC in early chronic rejection. Altered MHC expression was also observed in the media even in the area without intimal thickening. The usefulness of this approach in sensitive detection of phenotypic modulation, before morphological changes occur, was clearly shown. We also noticed altered MHC expression present simultaneously in both endomyocardial arterioles and epicardial coronary arteries of chronically rejected allografts. This result suggested that chronic rejection could be demonstrated by altered MHC isoform expression in endomyocardial arterioles. Therefore, altered MHC expression in GAD is an early sign of chronic rejection [10].

6.4.3 Costimulatory Signals

Costimulatory signals are important for stimulation of T cells and inflammatory cell recruitment into allografts [20]. It has been reported that GAD correlates with expression of adhesion molecules, including intracellular adhesion molecule (ICAM)-1, vascular cell adhesion molecule (VCAM)-1, E-selectin, and P-selectin [21, 22]. Besides facilitating EC interactions, lymphocyte integrins can also act as costimulatory molecules during antigen presentation. Although blockade of ICAM-1 and LFA-1 interactions induced allograft tolerance [23], the effect of the signal blockade on GAD development was not clarified. To prove the effect, we treated C3H/He mice that received cardiac allografts from BALB/c mice with anti-ICAM-1 plus anti-LFA-1 mAbs for the first 5 days after transplantation. For control studies, FK506 was administered daily to other allograft recipients. Allografts were harvested on day 60.Immunohistochemical analysis was used to detect the expression of ICAM-1 and VCAM-1, and in situ reverse transcriptase–polymerase chain reaction (RT-PCR) was performed to detect platelet-derived growth factor (PDGF)-B mRNA expression in the graft arteries. We found that allografts from mice that received FK506 treatment daily showed significant neointimal thickening with increased expression of ICAM-1, VCAM-1, and PDGF-B mRNA, whereas there was almost no intimal thickening and ICAM-1, VCAM-1, and PDGF-B mRNA expression in the mice that received anti-ICAM-1 plus anti-LFA-1 mAbs. We concluded that short-term blockade of ICAM-1 and LFA-1 adhesion not only induced immunologic tolerance to cardiac allografts but also prevented GAD [24] (Fig. 6.7).

It has also been reported that cytotoxic T-lymphocyte-associated protein-4 (CTLA-4) blockade of B7-CD28 interactions attenuated GAD [25]. The inducible costimulator (ICOS) molecule on T cells could also influence GAD development by directly interacting with ICOS-ligand on medial SMC activated by interleukin (IL)-1β [26, 27]. We also revealed that blockade of selectin [28], LIGHT [29], and 4-1BB [30] attenuated GAD, whereas programmed death-1 (PD-1) blockade accelerated the development [31]. Because each costimulatory signal has a different

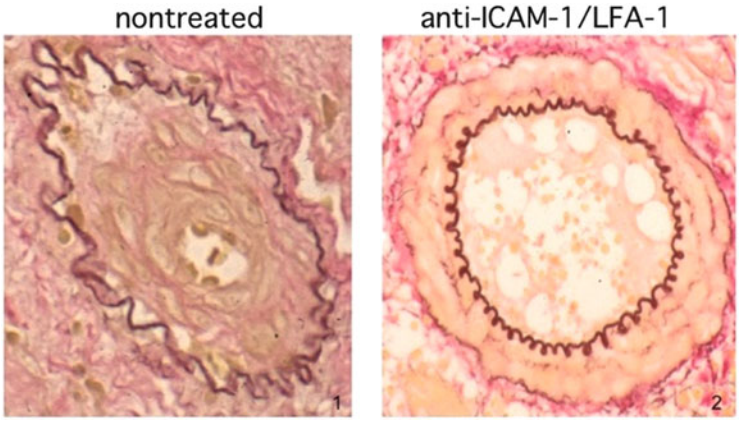

Fig. 6.7 Representative GAD findings of nontreated (*1*) and anti-ICAM-1 and LFA-1 antibody treated (*2*) arteries are demonstrated (From Ref. [24])

effect on GAD development, the anti-costimulatory therapy should investigate different organs and conditions.

6.4.4 Cytokines and Chemokines

Cytokines mediate local and systemic immune responses. Interferon (IFN)-γ is the most important player because it activates macrophages, augments inflammatory cell recruitment, and amplifies immune responses [32]. Despite ongoing acute rejection, the absence of IFN-γ abrogates GAD [33]. In association with the IFN-γ-induced cytokines, the IFN-γ and IL-12 relationship is a critical element in GAD pathogenesis, because medial SMCs synthesize IFN-γ following stimulation by IL-12 and IL-18 [34]. Although IFN-γ blocks medial SMC proliferation in vitro, IFN-γ directly induces intimal hyperplasia in the absence of inflammatory cells [35]. Other proinflammatory cytokines downstream of IFN-γ also play an important role.

Among the proinflammatory cytokines, tumor necrosis factor (TNF) also plays a pivotal role. It is well known that TNF promotes multiple aspects of allograft rejection via binding to type 1 (p55) and type 2 (p75) receptors. To reveal the role of TNF and its receptors on GAD formation, we used TNF type 1 receptor-deficient (TNFR1KO), type 2 receptor-deficient (TNFR2KO), and receptor double-deficient (TNFRDKO) mice to assess the relative roles of TNFR in acute rejection and GAD. Heterotopic cardiac transplantation was performed between C57BL/6 and Balb/c mice (total allomismatch) to assess the effects on graft survival; C57BL/6 and B6.C-H2$^{<bm12>}$KhEg mice (Bm12, class II mismatches) were used to assess the effects on GAD 8 weeks after transplantation. We found that graft survival in the total allomismatch combinations was the same regardless of TNF-receptor

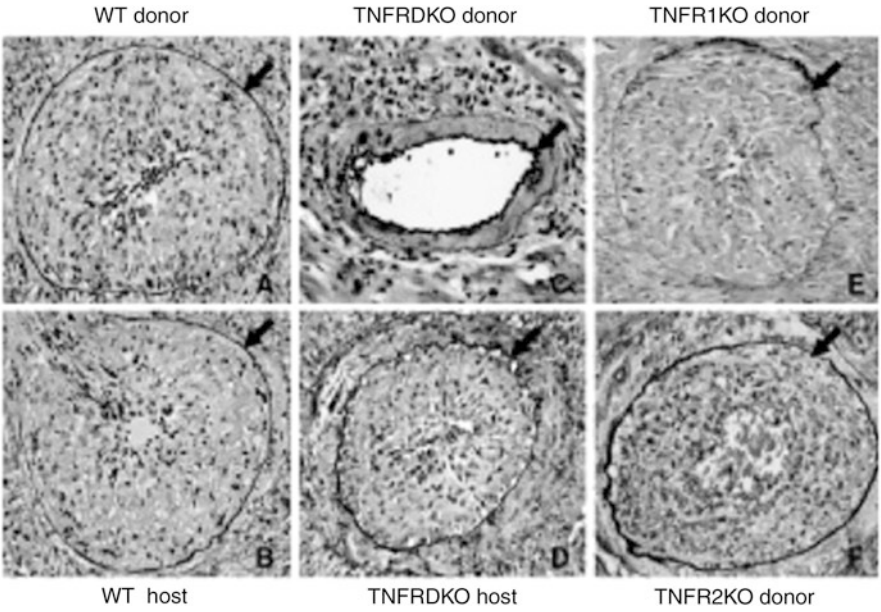

Fig. 6.8 Representative GAD findings are shown. Severe GAD develops by 8 weeks in both WT B/6 donor hearts in Bm12 hosts (**a**), as well as in Bm12 hearts transplanted into WT B/6 hosts (**b**). Major histocompatibility complex class II-mismatched TNFRDKO B/6 allografts implanted into WT Bm12 recipients showed significantly less GAD (**c**) compared to WT B/6 donor hearts. However, the WT Bm12 allografts implanted into TNFRDKO recipients showed severe intimal thickening (**d**), comparable to WT B/6 hosts. Both TNFR1KO (E) and TNFR2KO (F) donor hearts transplanted into Bm12 hosts showed severe GAD comparable to WT combinations (*arrows* indicate internal elastic lamina; original magnification, 200X) (From Ref. [36])

status. In class II mismatches, wild-type (WT) combinations showed severe GAD, and GAD was not diminished when WT hearts were transplanted into TNFRDKO hosts. TNFR1KO donors or TNFR2KO donors had GAD comparable to WT donors; however, GAD was significantly diminished in B/6 TNFRDKO donor hearts. Because host TNF-receptor deficiency did not reduce GAD, the effect was not attributable to TNF signaling on host inflammatory cells. We conclude that both p55 and p75 signals on donor vascular wall cells are involved in the development of GAD, and either TNF receptor is capable of mediating a response that will culminate in GAD [36] (Fig. 6.8).

Chemokines are known to be recruiting and activating inflammatory cells. They are classified in four groups, CC, CXC, XC, and CX3C. The roles of these molecules in acute rejection and GAD have been investigated [37]. RANTES is a well-characterized CC chemokine implicated in both atherosclerotic and GAD pathogenesis [38]. Further chemokines, the IFN-γ-inducible IP10, Mig, and I-TAC, are critical for their strong association with GAD [39, 40]. Moreover, targeted deletion of CCR1 reduced both acute rejection and the development of GAD [41].

6.4.5 *Sources of Cells in GAD*

Although SMLCs are similar in appearance to medial SMCs, they are phenotypically modulated cells with different genetic expression profiles. We revealed that medial SMC exhibits a contractile function, whereas SMLC exhibits a more embryonic, synthetic phenotype [10]. Previously, GAD intimal cells were assumed to derive from the migration and proliferation of donor medial SMC. However, several groups have shown that intimal SMLC can also be of host origin. In animal models, the proportion of host origin SMLC in intimal lesions exceeds 90 % [42–44]. However, in gender-mismatched cardiac allografts, Y-chromosome in situ hybridization identified only 3–15 % host-derived intimal SMLC [45, 46]. These results demonstrate that both host bone marrow and non-bone marrow precursors contribute to the GAD development. Therefore, therapies against GAD may need to account for different cells of origin, routes of recruitment, and differentiation pathways.

6.5 Possible Agents for GAD Prevention

6.5.1 *Immunosuppressants*

Cyclosporin A (CyA) significantly suppressed acute cardiac allograft rejection; however, it was not effective in preventing GAD [47]. Although tacrolimus provides superior prevention of acute rejection compared with CyA, GAD development was similar between CyA- and tacrolimus-treated groups [48]. It has been reported that mycophenolate mofetil (MMF) significantly decreased first-year maximal intimal thickness [49] and the incidence of GAD [50]. Recently, proliferation signal inhibitors are known to have significant effects for preventing GAD. Sirolimus delays the progression of GAD in some clinical trials [51, 52]. Another proliferation signal inhibitor, everolimus, also prevented GAD development [53]. However, as there is no report to demonstrate the long-term effect of proliferation signal inhibitors to suppress GAD, further observation studies are needed.

6.5.2 *AntiHypertensive Drugs*

Calcium channel blockers are known to delay the progression of GAD and enhance coronary vasodilation [54]. Angiotensin-converting enzyme (ACE) inhibitors partially improve allograft endothelial dysfunction, oxidative stress, and endothelin activation. They are also associated with plaque regression and improved graft survival [55, 56]. Recently, a synergistic beneficial effect of a calcium channel blocker and an ACE inhibitor on the development of GAD has been described [57].

We showed that an effect of telmisartan, a potent angiotensin II receptor blocker, was attenuating GAD in murine cardiac allografts. Recently, it was reported that telmisartan could function as a partial agonist of peroxisome proliferator-activated receptor-γ (PPAR-γ) in addition to a blocker of angiotensin II receptor. We investigated the effect of telmisartan on chronic rejection. Hearts from Bm12 mice were transplanted into C57BL/6 mice (class II mismatch), and allografts were harvested at 8 weeks after transplantation. Recipient mice were fed either control chow or chow containing telmisartan from 1 day before transplantation. Proliferation assays of SMCs, which were isolated from the aorta of B/6 mice, were performed. Although severe neointimal hyperplasia developed in allografts from control mice fed chow, neointimal hyperplasia was significantly attenuated in allografts from mice fed chow containing telmisartan. Expression of IFN-γ and IL-15 mRNAs and MMP-2 in allografts was significantly lower in telmisartan-treated mice than in control mice. Proliferation of SMCs in response to fetal bovine serum was suppressed significantly by telmisartan. The PPAR-γ antagonist blocked telmisartan-induced suppression of SMC proliferation. Thus, telmisartan attenuates SMC proliferation via PPAR-γ activity and suppresses neointimal hyperplasia after transplantation. Telmisartan may be useful for suppressing chronic allograft rejection [58].

6.5.3 HMG-CoA Reductase Inhibitors

Studies have shown that HMG-CoA reductase inhibitors (statins) play an important role in the prevention of GAD. The effects of statins are mediated by multiple immunogenic effects. Simvastatin reduced proinflammatory cytokine activity, improved coronary endothelial function, and increased coronary lumen area [59]. We demonstrated that pitavastatin has an effect for prevention of GAD in an animal model. We investigated the role of pitavastatin, a potent HMG-CoA reductase inhibitor, in cardiac allograft rejection and mechanism of GAD suppression. Balb/c mice hearts were transplanted into C3H/He mice (a full allomismatch combination) to assess acute rejection or C57BL/6 hearts into Bm12 (a class II mismatch combination) to examine the extent of GAD. Pitavastatin was orally administered to mice everyday. To assess the effect in acute rejection, mixed lymphocyte reaction (MLR) was performed and cytokine mRNA expression was examined by ribonuclease protection assay (RPA). We found that pitavastatin significantly prolonged allograft survival. Lymphocyte proliferation was inhibited by pitavastatin, and RPA showed downregulation of IL-6 in pitavastatin-treated cardiac allografts. Allografts in the pitavastatin-treated group after 8 weeks showed less GAD compared to the control group. In an in vitro study, pitavastatin suppressed the SMC proliferation in response to activated T cells and inhibited extracellular signal-regulated kinase 1/2 activation. Thus, we concluded that pitavastatin could be effective to suppress GAD development in cardiac transplantation [60] (Fig. 6.9).

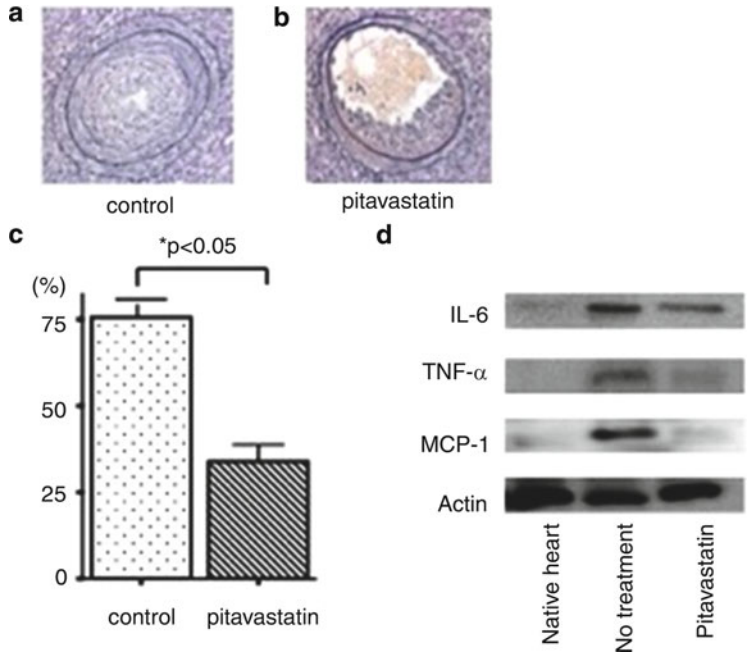

Fig. 6.9 Elastica van Gieson staining of cardiac allografts at 8 weeks after transplantation. (a, control group; b, pitavastatin-treated group) 400x. Panel c demonstrates quantitative results of GAD ($*P < 0.05$), and panel d shows cytokine expressions of cardiac allografts by Western blotting (From Ref. [61])

6.5.4 Pioglitazone

We demonstrated that pioglitazone could prevent GAD in the murine cardiac transplantation. It is well known that pioglitazone activates PPAR-γ and it plays an important role in regulating inflammation. To show their roles on GAD, we administered pioglitazone in a murine cardiac transplantation model. We performed heterotopic murine cardiac transplantation in total allomismatch or major histocompatibility complex class II-mismatched combinations. Recipient mice were given standard chow or chow containing pioglitazone beginning 1 day before cardiac transplantation. In acute rejection, animals given pioglitazone showed significantly longer cardiac allograft survival than that of control mice. Treatment with pioglitazone significantly suppressed the expression of IFN-γ and MCP-1 in the grafts. In chronic rejection, neointimal hyperplasia was significantly lower in allografts from mice treated with pioglitazone than in those from control mice. Pioglitazone-treated allografts showed significantly reduced expression of IFN-γ, IL-10, and MCP-1. We performed MLRs and in vitro proliferation assays of SMCs. Addition of pioglitazone to MLRs inhibited proliferation of T cells. SMCs showed significant proliferation when cocultured with activated splenocytes. This

proliferation was significantly inhibited by addition of pioglitazone. We concluded that pioglitazone prolonged allograft survival and attenuated GAD through suppression of proliferation of SMCs. Pioglitazone may be a novel means to prevent acute and chronic allograft rejection [61].

6.5.5 *Prostaglandin E_2 Receptor 4 Activator*

PGE_2 is a pathogenesis of inflammatory diseases; PGE_2 plays a key role in association of anti-inflammation and immune suppression. EP4, which is a PGE_2 receptor, is known to suppress the production of inflammatory cytokines and chemokines in vitro. Although EP4 agonists prolonged cardiac allograft survival, little has been elucidated the immunological mechanism. We injected a selective EP4 agonist (EP4RAG) into recipient mice with heterotopic cardiac transplantation. EP4RAG significantly prolonged the graft survival compared to the vehicle-treated group. While the vehicle-treated group showed severe myocardial cell infiltration, the EP4RAG-treated group attenuated the development on day 7. EP4RAG suppressed various proinflammatory factors such as cytokines, chemokines, adhesion molecules, and NF-κB compared to the vehicle-treated group. We also demonstrated that EP4RAG suppressed the activation of macrophages, but it did not affect to T lymphocytes in vitro. EP4RAG inhibited the activation of NF-kB compared to the control group. Pharmacological selective EP4 activation suppressed the production of proinflammatory factors via inhibition of NF-kB activity in cardiac transplantation [62].

6.5.6 *Inhibition of Plasminogen Activator Inhibitor-1*

Plasminogen activator inhibitor-1 (PAI-1) is critical in the inflammation and thrombus formation. However, little is known about the effect of PAI-1 in heart transplantation. To clarify the role of PAI-1 in the progression of cardiac rejection, we heterotopically transplanted murine hearts using major mismatch combinations for evaluation of acute rejection and class II mismatch combinations for the GAD. We administered the specific PAI-1 inhibitor (IMD-1622) into murine recipients following cardiac allografts. Nontreated allografts of the major mismatch group were acutely rejected, while the PAI-1 inhibitor prolonged their survival. Although severe cell infiltration and GAD with enhancement of inflammatory factors were observed in untreated allografts of class II mismatch group on day 60, the PAI-1 inhibitor attenuated these changes. The PAI-1 inhibitor is potent for the suppression of both acute rejection and GAD [63] (Fig. 6.10).

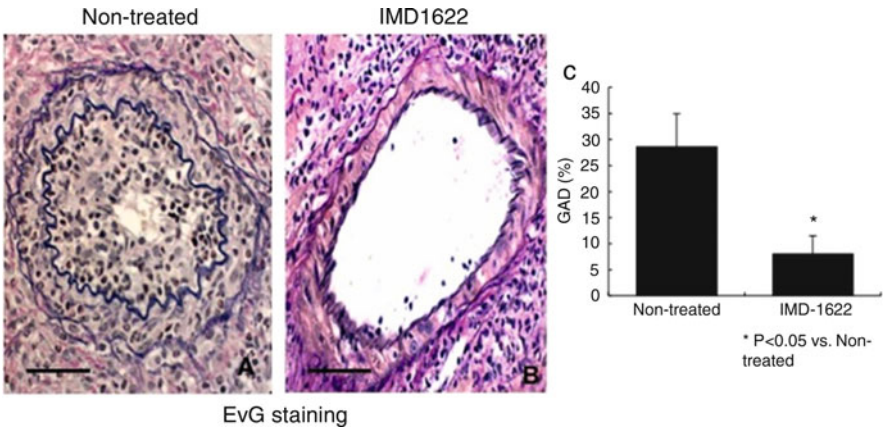

Fig. 6.10 Representative results of Elastica van Gieson staining of the class II mismatch allografts are shown. Heavy neointimal thickening was observed in the coronary arteries of untreated allografts (**a**). In the PAI-1 inhibitor-treated group, arterial intimal thickening was attenuated (**b**). The quantitative result of GAD (C) is demonstrated in the graph (**c**). Scale bars: 50 μm (From Ref. [65])

6.5.7 Macrolide Antibiotics

A major macrolide antibiotic, clarithromycin (CAM), has many biological functions including matrix metalloproteinasis (MMP) regulation. MMPs are critical in the development of inflammation and tissue remodeling. MMP-9 level is associated with the rejection of heart transplantation. However, little is known about the effect of CAM in heart transplantation via MMPs. To clarify the role of MMPs regulated by CAM in the progression of rejection, we orally administered CAM into murine cardiac allograft recipients. Total allomismatch combination and class II mismatch combination were used for the analysis of acute rejection and GAD. CAM improved acute rejection judged by graft survival and by myocardial cell infiltrating area in a total allomismatch combination. CAM-treated allografts showed affected expression of T cells, macrophages, and MMP-9 in immunohistochemistry. Zymography indicated that enhanced MMP activities were observed in nontreated hearts, while CAM suppressed the levels. In chronic rejection, CAM suppressed the development of GAD and myocardial remodeling compared to that of non-treatment. CAM inhibited the expression of MMP-9, while the treatment did not alter the expression of MMP-2 and TIMP-1 in macrophages and SMCs. Inhibition of MMP-9 by CAM was associated with suppression of SMC migration and proliferation. Thus, CAM is useful to suppress GAD because it is critically involved in the prevention of cardiac rejection through the suppression of MMP-9 [64] (Fig. 6.11).

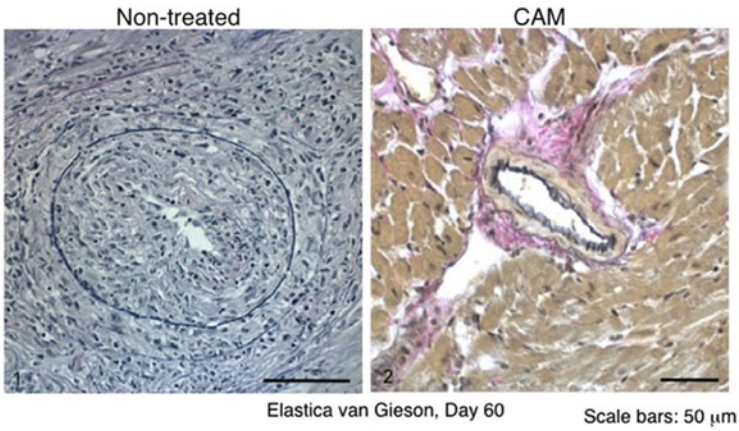

Fig. 6.11 Representative results of Elastica van Gieson staining of the class II mismatch allografts are shown. Although myocardial cell infiltration, fibrosis, and GAD were observed in the nontreated allografts on day 60 (*1*), CAM treatment markedly attenuated them (*2*). Scale bars: 50 μm (From Ref. [66])

6.5.8 Polyphenols

Some natural extracts may have an effect for preventing GAD. Tea catechins have many biological functions; these effects are induced by the suppression of several inflammatory factors. However, effects of catechins on cardiac allograft rejection have not been well investigated. To test the hypothesis that catechins can attenuate ventricular remodeling and GAD in cardiac rejection, we performed oral administration of catechins into murine cardiac recipients. We analyzed the mechanisms using immunohistochemistry, RNase protection assay, gel mobility shift assay, and cell proliferation assay. Although severe myocardial cell infiltration, fibrosis, and GAD with enhancement of inflammatory factors were observed in untreated class II mismatch allografts at day 60, catechins attenuated these changes with altered Th1/Th2 cytokine balances and suppressed NF-kB activation. Catechins are potent agents for the suppression of chronic rejection because they are critically involved in the suppression of proinflammatory signaling pathways [65] (Fig. 6.12). Other substances, such as vitamins and flavonoids, might also have the potential to restore allograft endothelial function [66, 67].

6.6 Gene Therapies for GAD Prevention

Possible targets to prevent GAD are chemokines, cytokines, costimulatory signals, cell proliferation, and apoptosis. It was reported that the induction of transient mixed hematopoietic chimerism leads to long-term heart allograft survival and did not develop GAD in monkeys without chronic immunosuppression [68]. However,

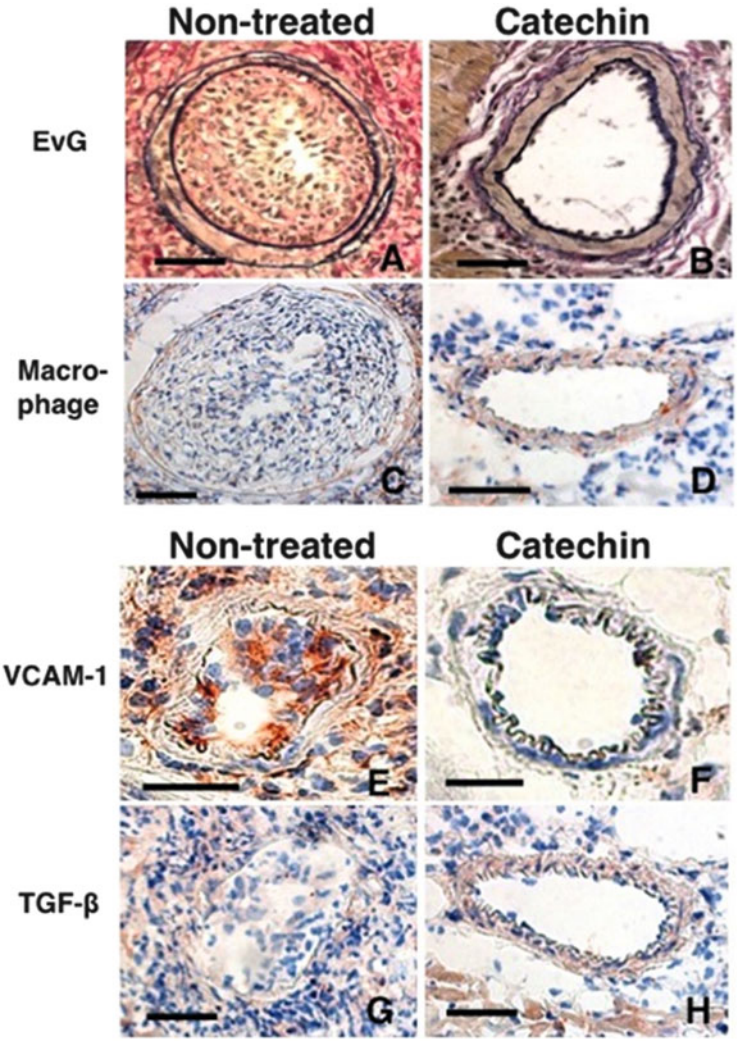

Fig. 6.12 Representative findings of allograft arteries of the class II mismatch group at day 60. *Left panels* show arteries from nontreated mice; *right panels* are from those treated with the catechins. Panels A and B show arteries with Elastica van Gieson staining, and other panels (**c** to **h**) are immunohistochemical findings of the arteries. Severe intimal thickening (**a**) with enhanced expression of macrophages (**c**) and VCAM-1 (**e**) was observed in the nontreated arteries, while suppressed GAD development (**b**) and expression of macrophages (**d**) and VCAM-1 (**f**) was observed in the arteries with catechins. However, TGF-β was faintly expressed in the thickened intima of arteries of nontreated allografts (**g**) as comparable in catechin-treated graft arteries (**h**). Scale bars: 50 μm (From Ref. [67])

tolerance induction and systemic immune modulation may cause adverse effects. Limited treatment on transplant organs is ideal for the long-term survival of recipients. Thus, we have investigated the effects of the limited gene transfer system to allografts for the prevention of GAD [69].

6.6.1 *Antisense Oligodeoxynucleotides for Cell-Cycle Regulation*

Recent progress in DNA technology, such as antisense oligodeoxynucleotides (ODNs) to regulate the transcription of disease-related genes, has an important role in therapeutic applications [70]. Firstly, we selected antisense cyclin-dependent kinase (cdk) 2 kinase ODN because the enzyme plays an important role in cell transition through the G1/S phase [71]. We observed that cdk2 kinase mRNA was elevated in the thickened intima of coronary arteries of murine heterotopic cardiac allografts. We studied the effects of antisense phosphorothioate ODN against this enzyme using gene transfer mediated by a hemagglutinating virus of Japan (HVJ)-liposome complex intraluminally delivered to inhibit the intimal hyperplasia. At 30 days after transplantation, antisense cdk2 kinase ODN treatment had dramatically inhibited neointimal formation in the allografts. Expression of VCAM-1 was also suppressed by antisense cdk2 kinase ODN. However, these effects were not observed in the sense or scrambled ODN-treated allografts. Thus, an intraluminal administration of antisense ODN directed to a specific cell-cycle regulatory gene can inhibit neointimal formation after cardiac transplantation [72] (Fig. 6.13).

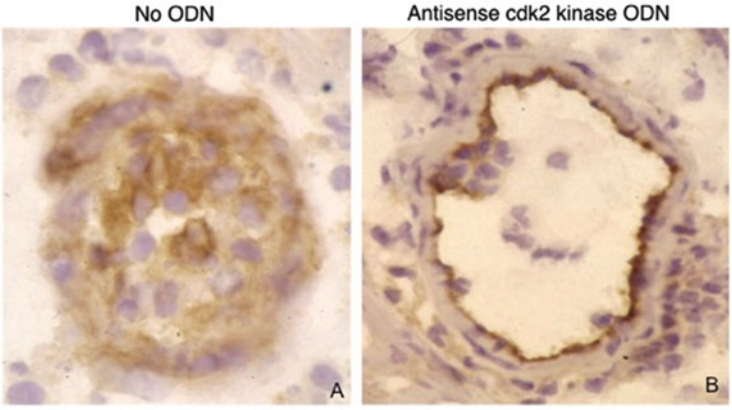

Fig. 6.13 Allograft arteries at day 30 after transplantation with VCAM-1 staining. Antisense cdk2 kinase ODN transfection (**b**) limited intimal thickening and suppressed VCAM-1 expression, whereas the untransfected artery (**a**) showed severe intimal thickening and enhanced VCAM-1 expression (original magnification, x400) (From Ref. [72])

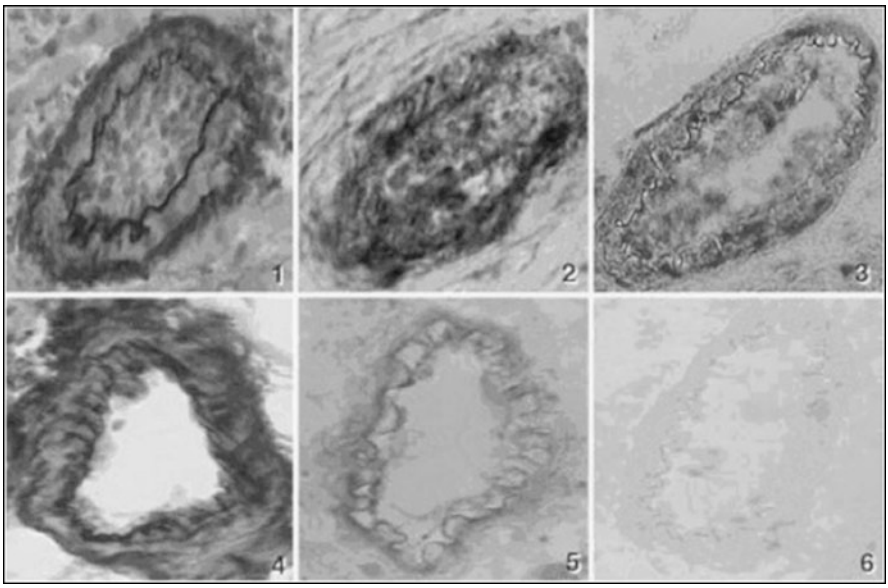

Fig. 6.14 Representative microscopic findings of graft coronary arteries at day 28 after cardiac transplantation. *Upper panels* show nontreated allograft arteries; lower panels are those transfected with antisense PCNA ODN. *Left panels* (*1* and *4*) show graft coronary arteries stained with Elastica van Gieson to demonstrate intimal thickening; *center panels* (*2* and *5*) show VCAM-1 expression using immunohistochemistry; *right panels* (*3* and *6*) show PDGF-B mRNA expression detected by in situ RT-PCR. VCAM-1 and PDGF-B were strongly and diffusely expressed in the thickened intima of the allograft arteries from recipients without ODN transfection, whereas they were almost nonexistent in the allografts transfected with the antisense PCNA ODN (From Ref. [74])

Next, we transfected antisense proliferating-cell nuclear antigen (PCNA) ODN to allografts, because PCNA plays an essential role in cell transition through both the G1/S and G2/M phases [73]. To test the hypothesis that antisense PCNA ODN could prevent allograft arterial intimal hyperplasia, we performed single intraluminal delivery of the antisense or sense PCNA ODN or no transfer into murine cardiac allografts. DBA/2 murine hearts were transfected and transplanted into B10.D2 mice; the allografts were harvested 4 weeks later. Severe intimal thickening with enhanced expression of PCNA was observed in untransfected and sense PCNA ODN-treated allografts, whereas antisense PCNA ODN prevented neointimal formation [74] (Fig. 6.14).

6.6.2 Antisense ODNs for Cell Apoptosis

Next, we targeted apoptosis because it is a prominent feature of atherosclerosis; bcl-x is one of the major antiapoptotic mediators [75]. To test the hypothesis that antisense *bcl-x* ODN is effective in preventing intimal hyperplasia through

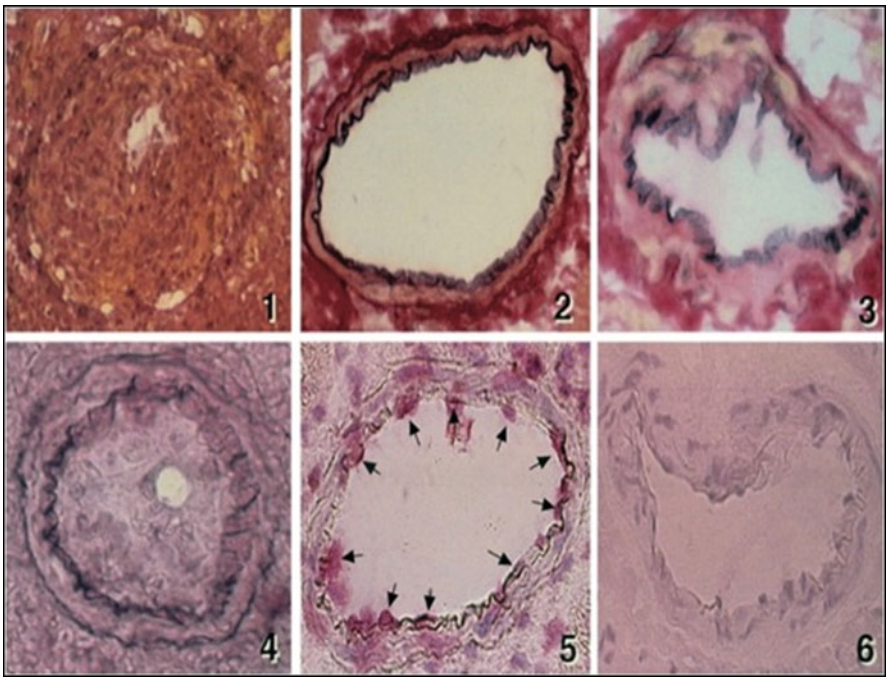

Fig. 6.15 Representative histopathological findings of graft coronary arteries. Upper panels show allograft arteries stained with Elastica van Gieson; lower panels show the arteries with TUNEL assay. Left panels show allograft arteries without ODN transfection; center panels show the arteries with antisense *bcl-x* ODN. Right panels show the arteries of native hearts. No ODN transfection resulted in heavy arterial neointimal formation (*1*) with faint TUNEL positive cells (*4*), while antisense *bcl-x* ODN suppressed neointimal development (*2*) with enhanced TUNEL staining; arrows indicate TUNEL positive cells (*5*). Neither neointimal formation (*3*) nor TUNEL positive cells (*6*) were seen in native heart arteries (original magnification: X400) (From Ref. [76])

enhancing apoptosis after cardiac transplantation, we performed single intraluminal delivery of antisense *bcl-x* ODN into murine cardiac allografts. DBA/2 mouse hearts were transplanted into B10.D2 mice. Sense *bcl-x* ODN and no treatment studies were also performed. Allografts were harvested at 4 weeks after transplantation; all allografts kept beating throughout the period. Coronary intimal thickening had developed in nontreated and sense ODN-transfected allografts at 4 weeks after transplantation with enhanced expression of bcl-x and cell adhesion molecules and suppressed apoptosis. However, antisense *bcl-x* ODN prevented neointimal formation through enhanced apoptosis. These results indicate that apoptosis of vascular SMCs induced by bcl-x is associated with initial hyperplasia after heart transplantation. Antisense *bcl-x* ODN inhibits SMC proliferation by inducing apoptosis in graft coronary arteries [76] (Fig. 6.15).

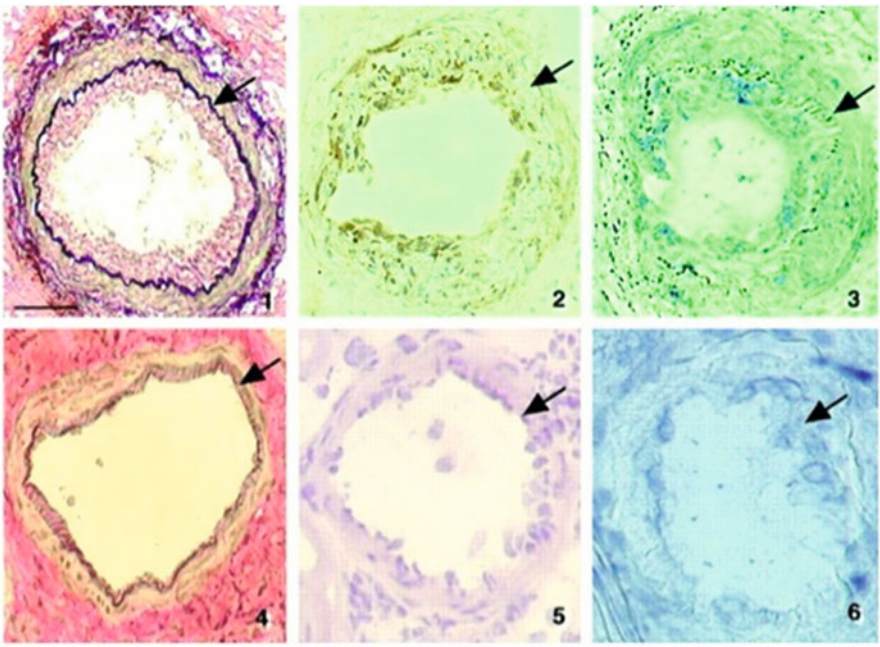

Fig. 6.16 Representative pathological findings of primate allograft arteries at day 28 after transplantation. Top, allograft arteries without any gene transfection; bottom, allograft arteries transfected with E2F decoy. Panels *1* and *4* show coronary arteries stained with EvG to demonstrate intimal thickening. Panels *2* and *5* show PCNA expression revealed by immunohistochemistry, and panels *3* and *6* show cdc2 kinase mRNA expression detected by in situ RT-PCR. PCNA and cdc2 kinase were strongly and diffusely expressed in the thickened intima of the allograft arteries from recipients without decoy transfection, whereas their expression was weak in the allografts transfected with the E2F decoy. Arrows indicate internal elastic lamina. Scale bars: 50 μm (From Ref. [78])

6.6.3 Decoy ODNs for Cell-Cycle Regulation

Transfection of cis-element double-stranded DNA, named "decoy," has been reported to be a useful method for gene therapy. The transcription factor E2F regulates multiple cell-cycle regulatory genes, which are critical to the process of cell growth and proliferation [77]. To test the hypothesis that double-stranded DNA with specific affinity for E2F (E2F decoy) is effective in preventing intimal hyperplasia, we performed ex vivo single intraluminal delivery of E2F decoy into cardiac allografts of mice and Japanese monkeys using the HVJ artificial viral envelope (AVE)–liposome method. Severe intimal thickening was observed, and multiple cell-cycle regulatory genes were enhanced in the untreated allografts. E2F decoy prevented neointimal formation and suppressed these genes for up to 8 weeks. Gel mobility shift assay proved the specific effects of E2F decoy, and reverse transcriptase–polymerase chain reaction documented that neither complication nor dissemination of HVJ into other organs was observed. We demonstrate that ex vivo gene delivery to allografts is a potent strategy to modify allograft gene expression, resulting in the prevention of GAD without systemic adverse effects [78] (Fig. 6.16).

Although the E2F decoy ODN strategies have not yet been used in clinical transplantation, the effects have already been investigated in coronary bypass grafting in clinical settings. It was reported that ex vivo E2F decoy ODN transfection in vascular grafts suppressed neointimal hyperplasia after cardiac bypass surgery [79, 80].

6.6.4 Decoy ODNs for Inflammatory Gene Regulation

Another critical transcription factor, nuclear factor-kappa B (NF-kB), plays a pivotal role in the coordinated transcription of multiple inflammatory genes [81]. To test the hypothesis that NF-kB decoy can attenuate acute rejection and GAD, we performed single intraluminal delivery of NF-kB decoy into murine cardiac allografts using the HVJ-AVE-liposome method. No decoy or scrambled decoy transfer was performed for control. Hearts were heterotopically transplanted from BALB/c to C3H/He mice (major mismatch group) and from DBA/2 to B10. D2 mice (minor mismatch group). Nontreated or scrambled decoy transfected allografts of the major mismatch group were acutely rejected, while NF-kB decoy prolonged their survival. While severe cell infiltration and GAD with enhancement of inflammatory factors were observed in untreated or scrambled decoy-treated allografts of minor mismatch group at day 28, NF-kB decoy attenuated these changes. We conclude that NF-kB is critically involved in the development of acute as well as chronic rejection of the transplanted hearts. NF-kB decoy attenuates both acute rejection and GAD by blocking the activation of several inflammatory genes [82] (Fig. 6.17).

Although the NF-kB decoy ODN has not yet been used in clinical transplantation, we tried the NF-kB decoy ODN transfection in the site of coronary arteries after stent implantation in humans [83–85]. The results demonstrated that the strategy is clinically promising. Thus, further studies should be conducted in other transplant models to explore the clinical utility of this technology for prevention of GAD.

6.7 Summary

Although improved surgical techniques have resulted in excellent graft functions [86], GAD is a remaining problem to be resolved in the treatment. Because heart transplantation has been limited by a severe shortage of donors [87], preventing GAD is critical for prognosis of recipients. In this review article, we described pathological and immunological characteristics of GAD. Several cytokines, chemokines, and adhesion molecules play a critical role in the process. Cell adhesion, migration, and proliferation of the bone marrow and other cells are involved in its development (Fig. 6.18). Although there has been no established

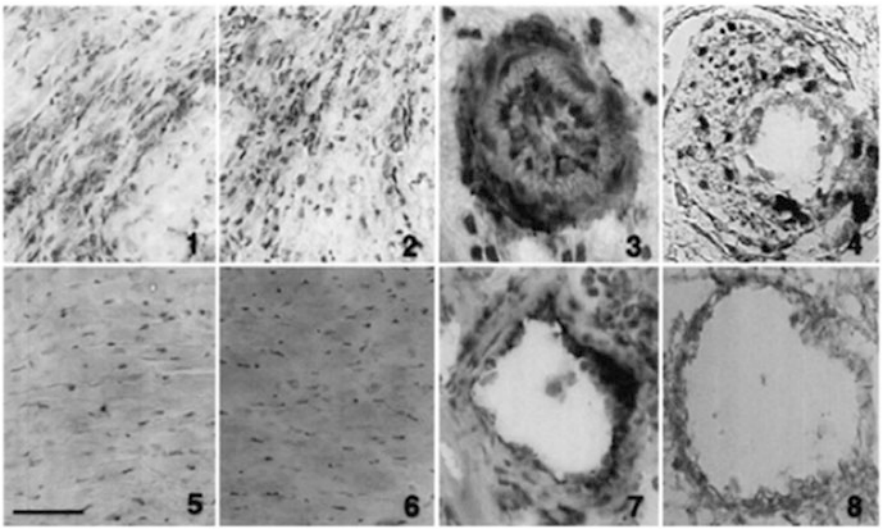

Fig. 6.17 Representative microscopical findings of allografts of the minor mismatch group at day 28. *Upper panels* show allografts from nontreated mice; *lower panels* are from those transfected with NF-kB decoy. Panels *1* and *5* show ICAM-1 expression and *2* and *6* show major histocompatibility complex class I expression using immunohistochemistry. ICAM-1 and major histocompatibility complex class I were strongly and diffusely expressed in the myocardial interstitium of allografts from untreated recipients, while expression was weak in allografts transfected with NF-kB decoy. Panels *3* and *7* show VCAM-1 expression, and *4* and *8* show PDGF-B mRNA expression in graft coronary arteries. They were strongly expressed in the nontreated thickened intima, while expression was weak in the allografts with NF-kB decoy. Scale Bars: 50 μm (From Ref. [82])

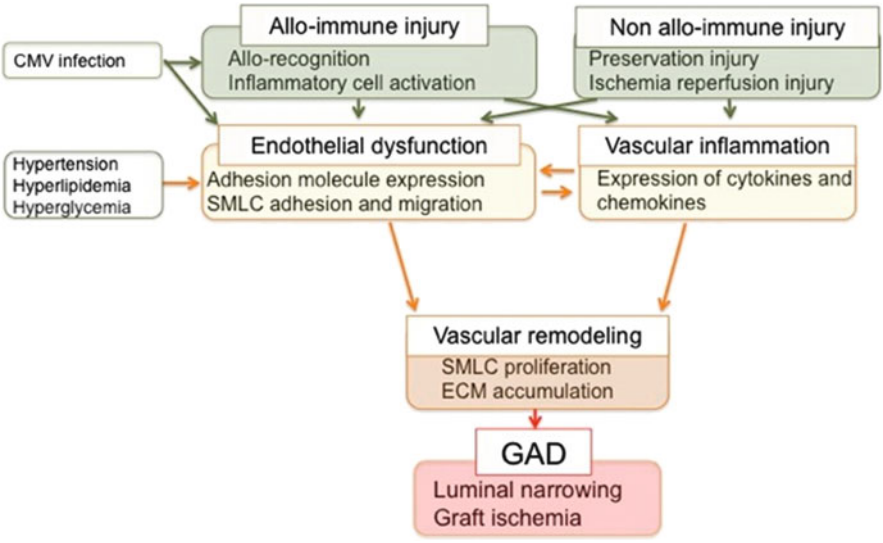

Fig. 6.18 A summary on the pathological and immunological characteristics of GAD is demonstrated. Several cytokines, chemokines, and adhesion molecules play a critical role in the process. Cell adhesion, migration, and proliferation of bone marrow and other cells are involved in its development. *GAD* indicates graft arterial disease, *CMV Cytomegalovirus*, *ECM*, extracellular matrix, *NF-kB* nuclear factor-kappa B, and *SMLC* smooth muscle-like cell

clinical strategy for preventing or treating GAD, recent investigations have proved some promising methodologies. Therefore, further studies are needed to clarify the clinical usefulness for prevention of GAD.

Acknowledgment We thank Ms. Noriko Tamura and Ms. Yasuko Matsuda for their excellent assistance.

References

1. Lund LH, Edwards LB, Kucheryavaya AY, Benden C, Christie JD, Dipchand AI, Dobbels F, Goldfarb SB, Levvey BJ, Meiser B, Yusen RD, Stehlik J, International Society of Heart and Lung Transplantation. The Registry of the International Society for Heart and Lung Transplantation: Thirty-first Official Adult Heart Transplant Report-2014; Focus Theme: Retransplantation. J Heart Lung Transplant. 2014;33:996–1008.
2. Suzuki J, Isobe M, Morishita R, Nagai R. Characteristics of chronic rejection in heart transplantation – important elements of pathogenesis and future treatments-. Circ J. 2010;74:233–9.
3. Mitchell RN. Graft vascular disease: immune response meets the vessel wall. Annu Rev Pathol. 2009;4:19–47.
4. Schmauss D, Weis M. Cardiac allograft vasculopathy: recent developments. Circulation. 2008;117:2131–41.
5. Ramzy D, Rao V, Brahm J, Miriuka S, Delgado D, Ross HJ. Cardiac allograft vasculopathy: a review. Can J Surg. 2005;48:319–27.
6. Mitchell R, Libby P. Vascular remodeling in transplant vasculopathy. Circ Res. 2007;100:967–78.
7. Libby P, Pober J. Chronic rejection. Immunity. 2001;14:387–97.
8. Furukawa Y, Libby P, Stinn J, Becker G, Mitchell R. Cold ischemia enhances cytokine/cell adhesion molecule expression and induces graft arterial disease in isografts, but does not accentuate alloimmune responses of nonimmunosuppressed hosts. Am J Pathol. 2002;160:1077–87.
9. Dhaliwal A, Thohan V. Cardiac allograft vasculopathy: the Achilles heel of long-term survival after cardiac transplantation. Curr Atheroscler Rep. 2006;8:119–30.
10. Suzuki J, Isobe M, Aikawa M, Kawauchi M, Shiojima I, Kobayashi N, et al. Nonmuscle and smooth muscle myosin heavy chain expression in rejected cardiac allografts -A study in rat and monkey models. Circulation. 1996;94:1118–24.
11. Shah R, Mitchell R. The role of stem cells in the response to myocardial and vascular wall injury. Cardiovasc Pathol. 2005;14:225–31.
12. Tuzcu E, Kapadia S, Sachar R, Ziada K, Crowe T, Feng J, et al. Intravascular ultrasound evidence of angiographically silent progression in coronary atherosclerosis predicts long-term morbidity and mortality after cardiac transplantation. J Am Coll Cardiol. 2005;45:1538–42.
13. Bogot NR, Durst R, Shaham D, Admon D. Cardiac CT of the transplanted heart: indications, technique, appearance, and complications. Radiographics. 2007;27:1297–309.
14. Michaels P, Espejo M, Kobashigawa J, Alejos J, Burch C, Takemoto S, et al. Humoral rejection in cardiac transplantation: risk factors, hemodynamic consequences and relationship to transplant coronary artery disease. J Heart Lung Transplant. 2003;22:58–69.
15. Wehner J, Morrell C, Reynolds T, Rodriguez E, Baldwin W. Antibody and complement in transplant vasculopathy. Circ Res. 2007;100:191–203.
16. Caforio A, Tona F, Fortina A, Angelini A, Piaserico S, Gambino A, et al. Immune and nonimmune predictors of cardiac allograft vasculopathy onset and severity: multivariate risk factor analysis and role of immunosuppression. Am J Transplant. 2004;4:962–70.

17. el-Sawy T, Fahmy N, Fairchild R. Chemokines: directing leukocyte infiltration into allografts. Curr Opin Immunol. 2002;14:562–8.
18. Valantine H. The role of viruses in cardiac allograft vasculopathy. Am J Transplant. 2004;4:169–77.
19. Streblow D, Kreklywich C, Andoh T, Moses A, Dumortier J, Smith PP, et al. The role of angiogenic and wound repair factors during CMV-accelerated transplant vascular sclerosis in rat cardiac transplants. Am J Transplant. 2008;8:277–87.
20. Isobe M, Kosuge H, Suzuki J. T cell costimulation in the development of cardiac allograft vasculopathy: Potential targets for therapeutic interventions. Arterioscler Thromb Vasc Biol. 2006;26:1447–56.
21. Denton M, Davis S, Baum M, Melter M, Reinders M, Exeni A, et al. The role of the graft endothelium in transplant rejection: evidence that endothelial activation may serve as a clinical marker for the development of chronic rejection. Pediatr Transplant. 2000;4:252–60.
22. Dietrich H, Hu Y, Zou Y, Dirnhofer S, Kleindienst R, Wick G, et al. Mouse model of transplant arteriosclerosis: role of intercellular adhesion molecule–1. Arterioscler Thromb Vasc Biol. 2000;20:343–52.
23. Isobe M, Yagita H, Okumura K, Ihara A. Specific acceptance of cardiac allograft after treatment with antibodies to ICAM-1 and LFA-1. Science. 1992;255:1125–7.
24. Suzuki J, Isobe M, Yamazaki S, Sekiguchi M. Inhibition of accelerated coronary atherosclerosis with short-term blockade of intercellular adhesion molecule-1 and lymphocyte function-associated antigen-1 in a heterotopic murine model of heart transplantation. J Heart Lung Transplant. 1997;16:1141–8.
25. Furukawa Y, Mandelbrot D, Libby P, Sharpe A, Mitchell R. Association of B7-1 costimulation with the development of graft arterial disease: studies using mice lacking B7-1, B7-2, or B7-1/B7-2. Am J Pathol. 2000;157:473–84.
26. Kosuge H, Suzuki J, Gotoh R, Koga N, Ito H, Isobe M, et al. The induction of immunological tolerance to cardiac allograft by simultaneous blockade of inducible co-stimulator (ICOS) and CTLA4 pathway. Transplantation. 2003;75:1374–9.
27. Kosuge H, Suzuki J, Haraguchi G, Koga N, Maejima Y, Inobe M, et al. Critical role of inducible costimulator signaling in the development of arteriosclerosis. Arterioscler Thromb Vasc Biol. 2006;26:2660–5.
28. Yamazaki S, Isobe M, Suzuki J, Tojo S, Horie S, Okubo Y, et al. Role of selectin-dependent adhesion in cardiac allograft rejection. J Heart Lung Transplant. 1998;17:1007–16.
29. Kosuge H, Suzuki J, Kakuta T, Haraguchi G, Koga N, Futamatsu H, et al. Attenuation of graft arterial disease by manipulation of the LIGHT pathway. Arterioscler Thromb Vasc Biol. 2004;24:1409–15.
30. Saiki H, Suzuki J, Kosuge H, Haraguchi G, Haga T, Maejima Y, et al. Blockade of the 4-1BB pathway attenuates graft arterial disease in cardiac allografts. Int Heart J. 2008;49:105–18.
31. Koga N, Suzuki J, Kosuge H, Haraguchi G, Onai Y, Futamatsu H, et al. The blockade of the interaction between PD-1 and PD-L1 accelerates graft arterial disease in cardiac allografts. Arterioscler Thromb Vasc Biol. 2004;24:2057–62.
32. Tellides G, Pober J. Interferon-γ axis in graft arteriosclerosis. Circ Res. 2007;100:622–32.
33. Nagano H, Mitchell R, Taylor M, Hasegawa S, Tilney N, Libby P. Interferon-γ deficiency prevents coronary arteriosclerosis but not myocardial rejection in transplanted mouse hearts. J Clin Invest. 1997;100:550–7.
34. Gerdes N, Sukhova G, Libby P, Reynolds R, Young J, Schönbeck U. Expression of interleukin-18 and functional IL-18 receptor on vascular endothelial cells, smooth muscle cells, and macrophages: implication for atherogenesis. J Exp Med. 2002;195:245–57.
35. Tellides G, Tereb D, Kirkiles-Smith N, Kim R, Wilson JH, Schechner JS, et al. Interferon-γ elicits arteriosclerosis in the absence of leukocytes. Nature. 2000;403:207–11.
36. Suzuki J, Cole S, Batirel S, Kosuge H, Shimizu K, Isobe M, et al. Tumor necrosis factor receptor–1 and –2 double deficiency reduces graft arterial disease in murine cardiac allografts. Am J Transplant. 2003;3:968–76.

37. Nelson P, Krensky A. Chemokines, chemokine receptors, and allograft rejection. Immunity. 2001;14:377–86.
38. von Hundelshausen P, Weber K, Huo Y, Proudfoot A, Nelson P, Ley K, et al. RANTES deposition by platelets triggers monocyte arrest on inflamed and atherosclerotic endothelium. Circulation. 2001;103:1772–7.
39. Zhao D, Hu Y, Miller G, Luster A, Mitchell R, Libby P. Differential expression of the IFN-γ-inducible CXCR3-binding chemokines, IFN-inducible protein 10, monokine induced by IFN, and IFN-inducible T cell α chemoattractant in human cardiac allografts: association with cardiac allograft vasculopathy and acute rejection. J Immunol. 2002;169:1556–60.
40. van Loosdregt J, van Oosterhout M, Bruggink A, van Wichen D, van Kuik J, de Koning E, et al. The chemokine and chemokine receptor profile of infiltrating cells in the wall of arteries with cardiac allograft vasculopathy is indicative of a memory T–helper 1 response. Circulation. 2006;114:1599–607.
41. Gao W, Topham P, King J, Smiley S, Csizmadia V, Lu B, Gerard CJ, et al. Targeting of the chemokine receptor CCR1 suppresses development of acute and chronic cardiac allograft rejection. J Clin Invest. 2000;105:35–44.
42. Shimizu K, Mitchell R. Stem cell origins of intimal cells in graft arterial disease. Curr Atheroscler Rep. 2003;5:230–7.
43. Hillebrands J, Klatter F, Rozing J. Origin of vascular smooth muscle cells and the role of circulating stem cells in transplant arteriosclerosis. Arterioscler Thromb Vasc Biol. 2003;23:380–7.
44. Hillebrands J, Klatter F, van den Hurk BM, Popa E, Nieuwenhuis P, Rozing J. Origin of neointimal endothelium and α-actin-positive smooth muscle cells in transplant arteriosclerosis. J Clin Invest. 2001;107:1411–22.
45. Glaser R, Lu M, Narula N, Epstein J. Smooth muscle cells, but not myocytes, of host origin in transplanted human hearts. Circulation. 2002;106:17–9.
46. Minami E, Laflamme M, Saffitz J, Murry C. Extracardiac progenitor cells repopulate most major cell types in the transplanted human heart. Circulation. 2005;112:2951–8.
47. Segovia J, Gomez-Bueno M, Alonso-Pulpon L. Treatment of allograft vasculopathy in heart transplantation. Expert Opin Pharmacother. 2006;7:2369–83.
48. Kobashigawa JA, Patel J, Furukawa H, Moriguchi JD, Yeatman L, Takemoto S, et al. Five-year results of a randomized, single-center study of tacrolimus vs microemulsion cyclosporine in heart transplant patients. J Heart Lung Transplant. 2006;25:434–9.
49. Kobashigawa JA, Tobis JM, Mentzer RM, Valantine HA, Bourge RC, Mehra MR, et al. Mycophenolate mofetil reduces intimal thickness by intravascular ultrasound after heart transplant: reanalysis of the multicenter trial. Am J Transplant. 2006;6:993–7.
50. Kaczmarek I, Ertl B, Schmauss D, Sadoni S, Knez A, Daebritz S, et al. Preventing cardiac allograft vasculopathy: long-term beneficial effects of mycophenolate mofetil. J Heart Lung Transplant. 2006;25:550–6.
51. Mancini D, Pinney S, Burkhoff D, LaManca J, Itescu S, Burke E, et al. Use of rapamycin slows progression of cardiac transplantation vasculopathy. Circulation. 2003;108:48–53.
52. Keogh A, Richardson M, Ruygrok P, Spratt P, Galbraith A, O'Driscoll G, et al. Sirolimus in de novo heart transplant recipients reduces acute rejection and prevents coronary artery disease at 2 years: a randomized clinical trial. Circulation. 2004;110:2694–700.
53. Eisen HJ, Tuzcu EM, Dorent R, Kobashigawa J, Mancini D, Valantine-von Kaeppler HA, et al. Everolimus for the prevention of allograft rejection and vasculopathy in cardiac-transplant recipients. N Engl J Med. 2003;349:847–58.
54. Schroeder JS, Gao SZ, Alderman EL, Hunt SA, Johnstone I, Boothroyd DB, et al. A preliminary study of diltiazem in the prevention of coronary artery disease in heart-transplant recipients. N Engl J Med. 1993;328:164–70.
55. Steinhauff S, Pehlivanli S, Bakovic-Alt R, Meiser BM, Becker BF, von Scheidt W, et al. Beneficial effects of quinaprilat on coronary vasomotor function, endothelial oxidative

stress, and endothelin activation after human heart transplantation. Transplantation. 2004;77:1859–65.
56. Bae JH, Rihal CS, Edwards BS, Kushwaha SS, Mathew V, Prasad A, et al. Association of angiotensin-converting enzyme inhibitors and serum lipids with plaque regression in cardiac allograft vasculopathy. Transplantation. 2006;82:1108–11.
57. Erinc K, Yamani MH, Starling RC, Crowe T, Hobbs R, Bott-Silverman C, et al. The effect of combined angiotensin-converting enzyme inhibition and calcium antagonism on allograft coronary vasculopathy validated by intravascular ultrasound. J Heart Lung Transplant. 2005;24:1033–8.
58. Kosuge H, Ishihara T, Haraguchi G, Maejima Y, Okada H, Saiki H, Suzuki J, Isobe M. Treatment with telmisartan attenuates graft arteriosclerosis in murine cardiac allografts. J Heart Lung Transplant. 2010;29:562–7.
59. Wenke K, Meiser B, Thiery J, Nagel D, von Scheidt W, Krobot K, et al. Simvastatin initiated early after heart transplantation: 8-year prospective experience. Circulation. 2003;107:93–7.
60. Suzuki J, Koga N, Kosuge H, Ogawa M, Haraguchi G, Maejima Y, Saiki H, Isobe M. Pitavastatin suppresses acute and chronic rejection in murine cardiac allografts. Transplantation. 2007;83:1093–7.
61. Kosuge H, Haraguchi G, Koga N, Maejima Y, Suzuki J, Isobe M. Pioglitazone prevents acute and chronic cardiac allograft rejection. Circulation. 2006;113:2613–22.
62. Ogawa M, Suzuki J, Kosuge H, Takayama K, Nagai R, Isobe M. The mechanism of anti-inflammatory effects of prostaglandin E_2 receptor 4 activation in murine cardiac transplantation. Transplantation. 2009;87:1645–53.
63. Ogawa M, Suzuki J, Yamaguchi Y, Muto S, Itai A, Hirata Y, Isobe M, Nagai R. The effects of pharmacological plasminogen activator inhibitor-1 inhibition in acute and chronic rejection in murine cardiac allografts. Transplantation. 2011;91:21–6.
64. Ogawa M, Suzuki J, Hishikari K, Takayama K, Tanaka H, Isobe M. Clarithromycin attenuates acute and chronic rejection via MMP suppression in murine cardiac transplantation. J Am Coll Cardiol. 2008;51:1977–85.
65. Suzuki J, Ogawa M, Sagesaka YM, Isobe M. Tea catechins attenuate ventricular remodeling and graft arterial diseases in murine cardiac allografts. Cardiovasc Res. 2006;69:272–9.
66. Fang JC, Kinlay S, Beltrame J, Hikiti H, Wainstein M, Behrendt D, et al. Effect of vitamins C and E on progression of transplant-associated arteriosclerosis: a randomised trial. Lancet. 2002;359:1108–13.
67. Iwanaga K, Hasegawa T, Hultquist DE, Harada H, Yoshikawa Y, Yanamadala S, et al. Riboflavin-mediated reduction of oxidant injury, rejection, and vasculopathy after cardiac allotransplantation. Transplantation. 2007;83:747–53.
68. Kawai T, Cosimi AB, Wee SL, Houser S, Andrews D, Sogawa H, et al. Effect of mixed hematopoietic chimerism on cardiac allograft survival in cynomolgus monkeys. Transplantation. 2002;73:1757–64.
69. Isobe M, Suzuki J. New approaches to the management of acute and chronic cardiac allograft rejection. Jpn Circ J. 1998;62:315–27.
70. Morishita R. Perspective in progress of cardiovascular gene therapy. J Pharmacol Sci. 2004;95:1–8.
71. Tsai LH, Harlow E, Meyerson M. Isolation of the human cdk2 gene that encodes the cycline A and adenovirus E1A associated p33 kinase. Nature. 1991;353:174–7.
72. Suzuki J, Isobe M, Morishita R, Aoki M, Horie S, Okubo Y, et al. Prevention of graft coronary arteriosclerosis by antisense cdk2 kinase oligonucleotide. Nat Med. 1997;3:900–3.
73. Morishita R, Gibbons GH, Ellison KE, Nakajima M, Zhang L, Kaneda Y, et al. Single intraluminal delivery of antisense cdc 2 kinase and proliferating-cell nuclear antigen oligonucleotides results in chronic inhibition of neointimal hyperplasia. Proc Natl Acad Sci U S A. 1993;90:8474–8.

74. Suzuki J, Isobe M, Morishita R, Nishikawa T, Amano J, Kaneda Y. Prevention of cardiac allograft arteriosclerosis using antisense proliferating-cell nuclear antigen oligonucleotide. Transplantation. 2000;70:398–400.
75. Geng YJ, Libby P. Evidence for apoptosis in advanced human atheroma. Colocalization with interleukin-1 beta-converting enzyme. Am J Pathol. 1995;147:251–66.
76. Suzuki J, Isobe M, Morishita R, Nishikawa T, Amano J, Kaneda Y. Antisense bcl-x oligonucleotide induces apoptosis and prevents arterial neointimal formation in murine cardiac allografts. Cardiovasc Res. 2000;45:783–7.
77. Morishita R, Gibbons GH, Horiuchi M, Ellison KE, Nakajima M, Chang L, et al. A gene strategy using a transcription factor decoy of the E2F binding site inhibits smooth muscle proliferation in vivo. Proc Natl Acad Sci U S A. 1995;92:5855–9.
78. Kawauchi M, Suzuki J, Morishita R, Wada Y, Izawa A, Tomita N, et al. Gene therapy for attenuating cardiac allograft arteriopathy using *ex vivo* E2F decoy transfection by HVJ-AVE-liposome method in mice and nonhuman primates. Circ Res. 2000;87:1063–8.
79. Mann MJ, Whittemore AD, Donaldson MC, Belkin M, Conte MS, Polak JF, et al. Ex-vivo gene therapy of human vascular bypass grafts with E2F decoy: the PREVENT single-centre, randomised, controlled trial. Lancet. 1999;354:1493–8.
80. Alexander JH, Hafley G, Harrington RA, Peterson ED, Ferguson Jr TB, Lorenz TJ, et al. Efficacy and safety of edifoligide, an E2F transcription factor decoy, for prevention of vein graft failure following coronary artery bypass graft surgery: PREVENT IV: a randomized controlled trial. JAMA. 2005;294:2446–54.
81. Barnes PJ, Karin M. Nuclear factor-kappaB: a pivotal transcription factor in chronic inflammatory diseases. N Engl J Med. 1997;336:1066–71.
82. Suzuki J, Morishita R, Amano J, Kaneda Y, Isobe M. Decoy against nuclear factor-kappa B attenuates myocardial cell infiltration and arterial neointimal formation in murine cardiac allografts. Gene Ther. 2000;7:1847–52.
83. Suzuki J, Ito H, Gotoh R, Morishita R, Egashira K, Isobe M. Initial clinical cases using an NF-kB decoy at the site of the coronary stenting for prevention of restenosis. Circ J. 2004;68:270–1.
84. Egashira K, Suzuki J, Ito H, Aoki M, Isobe M, Morishita R, for INDOR Study Group. Long-term follow up of initial clinical cases with NF-kB decoy oligodeoxynucleotide transfection at the site of the coronary stenting. J Gene Med. 2008;10:805–9.
85. Suzuki J, Tezuka D, Morishita R, Isobe M. An initial case of suppressed restenosis with NF-kB decoy transfection after PCI. J Gene Med. 2009;11:89–91.
86. Kitamura S, Nakatani T, Kato T, Yanase M, Kobayashi J, Nakajima H, et al. Hemodynamic and echocardiographic evaluation of orthotopic heart transplantation with the modified bicaval anastomosis technique. Circ J. 2009;73:1235–9.
87. Nakatani T, Fukushima N, Ono M, Saiki Y, Matsuda H, Yozu R, Isobe M. The registry report of heart transplantation in Japan (1999–2013). Circ J. 2014;78:2604–9.

Chapter 7
Murine Models of Vein Grafting

Brian C. Cooley

Abstract Vein graft research has increasingly turned to murine models, to exploit the potential of transgenic and knockout mouse lines to study genetically based questions. Several models of murine interpositional vein grafting into arteries have been published, as well as models of vein patch grafting. Models vary on the vein graft source (inferior vena cava, external jugular vein or its distal branches), recipient artery (aorta, carotid, or femoral), and method of engraftment (end-to-end or end-to-side continuous or interrupted suturing or ring-coupling techniques). Outcomes vary considerably, depending on the model employed; neointimal wall thickening is induced that is often comparable to larger vein graft models on an absolute basis, despite the much smaller vessel diameters of mouse vein grafts. Substantial vein graft stenosis is apparently only found with the smaller of these vein graft models. Selecting the appropriate model requires careful consideration of the specific research question to be addressed as well as laboratory expertise with microsurgical techniques.

Keywords Bypass vein grafting • Vein graft stenosis • Neointimal formation

7.1 Introduction

It has become increasingly clear that the complications arising after vein bypass grafting procedures are more complex than had been originally hoped [1, 2]. More sophisticated approaches to basic experimental design are needed to address these complexities for developing more effective therapies to reduce the complication rate.

The major complications encountered with clinical vein grafting are early/acute thrombosis (occlusive failure), more intermediate stage (1–24 months) graft stenosis due to neointimal inward overgrowth, and late-stage (2–10 years) atherogenic lesion formation on the graft, again leading to stenosis [3, 4]. Most experimental studies have focused primarily on vein wall changes that are extrapolated as

B.C. Cooley (✉)
Department of Pathology and Laboratory Medicine, Rodent Advanced Surgical Models Core Lab, McAllister Heart Institute, University of North Carolina, Chapel Hill, NC 27599, USA
e-mail: brian_cooley@med.unc.edu

M. Sata (ed.), *Mouse Models of Vascular Diseases*,
DOI 10.1007/978-4-431-55813-2_7

simulations of the inward "negative" remodeling which progresses to graft stenosis, either with or without a superimposed atherogenic burden.

There are two common assumptions in many of these studies that may be erroneous. Firstly, and most critically, the development of a thickened neointimal wall in an experimental vein graft is often considered the clinically analogous pathology when, in most cases, this type of remodeling should be considered "arterialization," a desirable and beneficial remodeling of the vein in response to the arterial shear flow and high-pressure environment [5]. Many studies have shown methods and therapies that reduce the thickness of this arterialized wall, which may in fact cause the wall to become pathologically too thin. Very few experimental vein graft models develop a truly stenotic lesion [6–8], yet investigators all too often overlook this critical shortcoming of the applied model.

Secondly, the study of atherosclerotic lesion development in the vein graft is assumed to be distinctly separable from the neointimal type of lesion. It is more likely that these two processes, neointimal wall remodeling and atherogenic lesion formation, have overlapping roles, with each contributing to the other's development or modulation or both. Endemic to this overlap is the imprecision of using atherosclerosis-associated wording and terminology to refer to neointima-dominated processes, often without an atherogenic stimulus in the experimental design. Thus, the separation of these potentially distinct pathologic processes needs more precise demarcation in animal models and study design.

7.1.1 Advantages of Mouse Vein Graft Models

The primary, overwhelmingly utilitarian advantage of using the mouse for vein graft research is the availability and application of the many knockout and transgenic mouse lines that have been developed [9, 10]. Very specific gene-based questions can be directly addressed with such animal models. Related to these mouse lines are the numerous syngenic strains of mice that permit transplantation between and among mice on the same strain or that have undergone background crossing into the same strain, obviating complications from immunogenic responses. Thus, cross-transplant strategies can be combined, such as placing a vein from a knockout or transgenic mouse into a wild-type recipient to determine the effect of the particular genetic change restricted to the vein graft cells and, reciprocally, placing a wild-type graft into a knockout/transgenic recipient to modify the systemic/circulatory environment for an otherwise normal graft [11, 12]. The availability of marker gene mice and breeding possibilities that generate cell lineage tracing tissues permits tracking of specific cell types and their sources [13, 14]. These mouse lines have the potential to be combined with bone marrow or fetal liver transplants for specific manipulations of hematopoietic cells [14] to determine their role in the vein graft response.

7.1.2 Disadvantages of Murine Vein Graft Models

A central drawback to the mouse model in general is its questionable clinical relevance to human (patho)physiology. In particular for vein graft studies, it is currently not possible to attempt experimental versions for exact replication of clinical procedures – whether for coronary artery bypass or lower limb arterial bypass surgery – due to the small vessel sizes and nonparallel anatomy for the mouse vascular structures. The small mouse body size and concomitant vessel diameters make any type of vein graft especially challenging from a technical standpoint. Furthermore, the response of a vein placed into the rapid pulsatile flow in a mouse is another source of difference.

7.2 Models: Technical Aspects

The published models for mouse vein graft studies can be divided on the basis of interpositional surgical technique, ring-coupled versus sutured, and end-to-end versus end-to-side versus patch graft repairs. These grafts can also segregate on the basis of donor graft source (vena cava, jugular, femoral, or posterior facial vein) or recipient site (aorta, carotid, or femoral artery). Most applications have used a harvested vein segment or patch from a donor animal which is transplanted into a separate recipient animal.

7.2.1 Ring-Coupled Vein Graft Model

Zou and colleagues [15] developed a simplified method for interpositioning a large vein into the common carotid artery. The basis of this approach is the incorporation of a thin-walled polyethylene or similar synthetic ring (e.g., cut from tubing) of an inner diameter approximating that of the unstretched artery. The common carotid artery is clamped or occluded at proximal and distal sites and an appropriate segment is resected. Two rings are brought into place, one for each end of the artery. To create an anastomosis to a vein end, the transected end of the artery is fed through the ring and everted back and over the outside of the ring. The vein end is then slipped over the everted artery on the ring and a 8-0 nylon suture is placed as a ligature around the ring, securing both vessels onto the ring in a leak-proof anastomosis. The same procedure is done at the other end of the vein graft, coupling it to the other transected arterial end to complete the interpositioning of the graft. While the carotid artery is the primary recipient vessel of choice, the model can also be done in the abdominal aorta, though this presents a more invasive surgical procedure due to the intra-abdominal exposure/access and lower body ischemia from the aortic clamping.

The thoracic inferior vena cava (IVC) is found within the thoracic cavity just below the heart, has no branches, is easy to isolate with sufficient length, and has a diameter amenable to this procedure, making it the ideal choice for vein graft source. It must be obtained from a donor mouse upon euthanasia. The graft can tolerate a moderate ischemic interval even at room temperature in a saline-based physiologic solution. The external jugular vein is another graft source, though limited length and the presence of branches make it a less consistent vein donor source.

7.2.2 End-to-Side Sutured IVC Graft

This model was developed by Zhang and colleagues at Duke University [16]. It is similar to the ring-coupled model in its donor/recipient choices of IVC and carotid artery. The carotid is occluded with temporary occlusion clamps or 5-0 silk suture (temporary ligatures), placed at proximal and distal extremes on the dissected artery. Two arteriotomies ("side" windows) are created just within each occlusion site. Each vein end is then anastomosed to an arteriotomy in end-to-side fashion, orienting the vein so that the subsequent arterial flow in it will be in the same direction as the original venous flow. The repairs are done with 11-0 nylon using running stitches. The carotid artery is doubly ligated with 5-0 silk between the anastomoses and the artery is transected between these ligatures. Thus, the arterial ends retract, stretching the vein slightly in the gap, whereupon reflow is established.

7.2.3 End-to-End Vein Graft Models to Abdominal Aorta

Diao and associates [17] developed an alternative vein graft model placed into the abdominal aorta using 11-0 nylon suture in interrupted-stitch fashion for creating two end-to-end anastomoses to join the artery ends to the vein graft. They used the external jugular vein harvested from the same mouse for the graft source, in an autologous transplant. Salzberg and colleagues [18] described a technically similar model but used a donor mouse to provide the thoracic IVC as the donor graft, identical to the previously described models.

7.2.4 Posterior Facial Vein to Femoral Artery Model

I developed an independent model [11] which has similarities to the last set of sutured models. It uses two end-to-end, interrupted-stitch anastomoses with 11-0 nylon to join the arterial and vein graft ends (Figs. 7.1 and 7.2a). The posterior facial vein is found just distal to and feeding into the external jugular vein

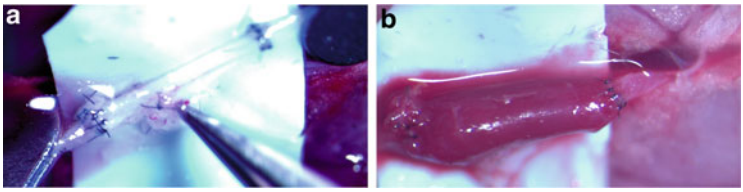

Fig. 7.1 Posterior facial vein graft interpositioned to the femoral artery, showing (**a**) completed anastomoses (interrupted 11-0 sutures, 8 per anastomosis), with forceps adjacent to small ligated branch in middle of graft and (**b**) graft with flow immediately after completing the anastomoses (flow is from *left* to *right*). The dilated vein is approximately 0.6 mm in diameter, while the femoral artery is 0.2 mm in diameter

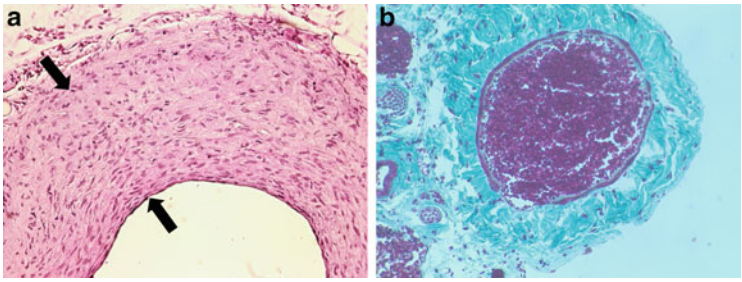

Fig. 7.2 (**a**) H&E cross section of proximal portion of vein graft (4-week harvest), showing neointimal extent between *black arrows*. (**b**) Masson stain of cross-sectioned posterior facial vein prior to harvest from the neck (blood filling lumen to hold it open); note very thin medial layer (one-cell layer thick)

(Fig. 7.2b), within the loose subcutaneous tissue of the neck; the mouse vein anatomy is essentially identical with rat vein anatomy in this tissue region [19] and does not directly parallel human anatomy. It is the larger of two main branches that conjoin at the origin of the jugular vein and it has few or usually only one minor branch along a ~1 cm length; this small branch should be ligated (Fig. 7.1a) or cauterized prior to graft reflow. While autologous grafting is easily achieved, the model has more often been used with donor graft harvest from one mouse and transplantation to a recipient mouse; this approach permits two grafts to be harvested from a donor, taken from the pair of veins found bilaterally, which can be a valuable technical step when scarcity of donor mice is a factor. The femoral artery of a recipient mouse is dissected and clamped widely, resecting a small portion, then the vein is brought in and anastomosed with 11-0 nylon using approximately eight interrupted stitches per anastomosis (Fig. 7.1). Because of the fragility of the vein, it should be minimally handled and not mechanically dilated at any point; simply placing it into the femoral wound with a physiologic solution facilitates lumen exposure, with the walls floating apart to permit lumen identification, using a high-magnification microscope (60X or greater). The procedure may take time to master, but with experience the graft can be harvested in

less than 5 min and grafted to the artery in ~40 min (total recipient surgery time of ~60 min).

7.2.5 Patch Graft Models

A model of vein oval patch graft to an artery has been described by two groups, using autologous transplantation of a piece of jugular vein to replace a portion of resected arterial wall. Although not a true vein bypass-analogous graft, this model provides some insight into the response of a vein wall in an arterial environment. Shi and associates [20] used a single incision in the ventral neck to access both the jugular vein for obtaining the graft and exposure of the carotid artery for placement. Sakaguchi and colleagues [21] transferred the same graft to the abdominal aorta. Both groups described using 11-0 suture in a single, continuous running stitch for engraftment into an arteriotomy/side window.

7.3 Technical Comparisons

The various combinations of donor vein and recipient artery selection and the method of graft anastomosis are limited, though this may play a profound role in the subsequent response designed to mimic clinical vein grafting (Table 7.1). Zhou et al. [15] and Zhang et al. [16] both use the same vessels, grafting the IVC into the carotid artery but with very different anastomotic techniques. Diao et al. [17] and Salzberg et al. [18] used a suturing technique that differed from that of Zhang et al. [15], placing interrupted stitches in end-to-end fashion rather than continuous running stitches in end-to-side configuration and adding variations in graft/recipient combinations. In the model developed in my lab [11], perhaps the smallest vein used, the posterior facial vein is grafted into the smallest of arteries in these models – the common femoral artery – using interrupted end-to-end suturing. The patch graft models use more common vessels but deviate from true interpositional vein grafting. Though none of these models replicate clinical vein graft-to-artery scenarios, the femoral artery model can be argued to share more features of lower extremity artery bypass surgery, involving a muscular-type artery that in fact matches a clinical site for these procedures.

The suture-based techniques [11, 15–18] offer the most clinical analogy, though the ring-coupled approach of Zou and colleagues [15] is the simplest to perform. An inherent weakness of this model is the abrupt diametric transitions from the arterial ends where they enter the vein through the inner diameter of the ring, creating a 90° geometric jump to the larger diameter of the outer edge of the ring. This deviation from the other models, which attempt to create a smoother transitional interface from artery to vein and back to artery, may lead to potentially non-pathophysiologic results, at least in terms of paralleling clinical vein graft responses.

Table 7.1 List of published murine vein graft models and their relative characteristics, merits, and expected/estimated outcomes

Model	Ring-coupled	End-to-side suturing	End-to-end suturing	End-to-end suturing	End-to-end suturing	Patch graft	Patch graft
Originator	Zou et al. [15]	Zhang et al. [16]	Diao et al. [17]	Salzberg et al. [18]	Cooley [11]	Shi et al. [20]	Sakaguchi et al. [21]
Recipient artery	Carotid	Carotid	Abdominal aorta or carotid	Abdominal aorta	Femoral artery	Carotid	Abdominal aorta
Donor vein	Inferior vena cava	Inferior vena cava	External jugular vein	Inferior vena cava	Posterior facial vein	External jugular vein	External jugular vein
Anastomosis	Mechanical ring	Continuous 11-0 suture	Interrupted 11-0 suture	Interrupted 11-0 suture	Interrupted 11-0 suture	Continuous 11-0 suture	Continuous 11-0 suture
Procedure time (graft harvest + interpositioning)	Total = 60 min	Total = 20 + 90 min	68 min aortic clamp time	30–50 min aortic clamp time	Total = 5 + 45–55 min	50 min	Total = 40 min
Success rate (patency)	86–90%	>95 % with experience	89 %	(83 %)	70–80% with experience	87 %	92 %
Vein: artery diametric ratio	Not determined	2.3:1	1.9:1 (carotid) 1.4:1 (aorta)	Not determined	~3:1	Not applicable	Not applicable
Neointimal thickness	(~220 μm)	91 μm	Not determined	110 μm	~103 μm	Not determined	Not determined
Lumen area reduction	Not determined	(~16 %)	(~20 %)	Not determined	~78 % (proximal end)	Not determined	~65 %

Another consideration is the handling and treatment of the vein graft, from harvest to arterial flow. Dilating or otherwise stretching the vein may match what some clinical surgeons do, but there has been an effort over the past 30 or more years to minimize handling and related sources of iatrogenic trauma to the vein – the so-called no-touch technique [22–24]. The ring-coupled method describes mechanically stretching the IVC over the ring for its placement. Though the rest of the published models lack details on vein handling, in the case of my model, the handling is nearly no-touch, with only the needle passage having a direct trauma to the vein wall; the vein is isolated from the neck without touching or flushing it, allowing incubation in a heparinized solution to gently clear the blood without clotting and using the same solution at the recipient site to float the vein open for identifying the lumen and to facilitate stitch placement. Whether the other models use a similar approach would be valuable to learn.

The technique of experimental vein grafting for model selection must take two other aspects under consideration: time for the procedure (i.e., throughput) and success rate (acute graft patency). The published accounts for the procedural times differ in their start and stop points (Table 7.1), though most models describe times that appear to lead to total times of 40–70 min, with perhaps longer times for the end-to-side model of Zhang and colleagues [16]. These times are clearly dependent upon operator experience and microsurgical proficiency. In the case of my model, the initial effort took 2.5 h, but rapidly fell to under 1.5 h, and approximately 1 h with further experience; this time includes all steps, from graft harvest in a donor to final recipient site closure.

Another consideration is the acute success rate – graft patency following the procedure (Table 7.1). Most models report greater than 85 %, approaching 100 % for some [16] as experience is gained. The model I developed is an exception, with success rates slightly lower at 70–80 %, even with extensive experience. There thus may be trade-offs between speed of completing the procedure and successful outcome.

The major outcome measure for which these models were primarily designed is neointimal inward remodeling of the graft wall – the major complication of clinical vein grafting. As mentioned previously, this neointimal growth is often mistakenly attributed to the influence from simple transference of venous tissue to arterial flow/shear and pressure. Many studies in larger animal models of vein graft neointimal development have found relatively little net wall thickening, with very few models showing true stenotic lesion formation. The primary induction of excessive neointimal growth occurs at sites of perturbed or oscillatory flow and not at high-shear, laminar flow regions. Thus, in evaluating murine vein grafts, analysis should be directed at models and sites within models where such perturbed flow can be expected.

The transitions from the artery to the vein and back from the vein to the artery are the most likely sites of predicted flow alterations. Indeed, some of the reported models have shown such differential responses, with greater neointimal thickening in the graft adjacent to the anastomotic junctures [11, 16]. Another criterion for predicting such altered flow is the diametric ratio of the vein to the artery

(Table 7.1). This is seen to be approximately 2:1 for the IVC grafts placed into the carotid artery, with a lower ratio for placement into the aorta. The posterior facial vein grafted into the femoral artery has an even greater ratio of ~3:1, which is further supported by the strong difference in neointimal response in the proximal and distal portions of the graft in comparison to the mid-graft regions.

7.4 Outcome Measures

The primary outcome measurements are based around direct or surrogate markers of graft stenosis. Measuring neointimal wall thickness is most often used (Table 7.1), with some models including medial or combined neointimal and medial wall thickness as parameters. The neointimal wall thickness that develops by 4–8 weeks ranges from ~100 to 220 μm in reports using these models [11, 15, 16, 18]. Intriguingly, these thicknesses are comparable to many reports for published absolute thicknesses from larger rat and rabbit vein models [25–28]; this provides further support to justify using murine models in vein graft research. A direct measure of luminal areas from cross-sectioned grafts is the most relevant reflection of true graft stenosis (Table 7.1). For reported or derived estimates from published figures, this level of stenosis can range from 15–20% [16, 17] to 65–78% [11, 20]. In the model I developed, this level of stenosis can be severe (Fig. 7.3) and results in stenotic occlusion of the graft by 4 weeks in 3–6% of grafts that were initially patent [11, 29].

Another important issue has been the determination of the origin of the stenosis-contributing neointimal cells. Whereas until recently, non-murine models have not been able to determine these sources reliably [30], the use of murine transgenic

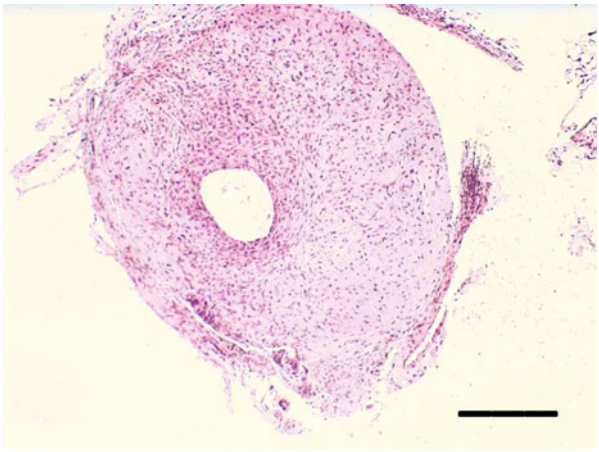

Fig. 7.3 Highly stenotic H&E-stained vein graft cross section, harvested at 4 weeks; bar = 100 μm

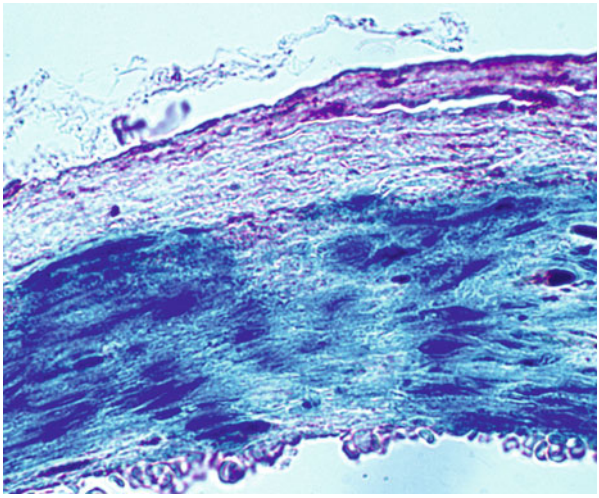

Fig. 7.4 Vein graft from transgenic mouse constitutively expressing LacZ, grafted into wild-type mouse and harvested at 4 weeks, with X-galactosidase staining (*blue*) and hematoxylin counterstaining, demonstrating dominant presence of vein graft-originating neointimal cells

lines has permitted in-depth assessment of neointimal cell sources. Despite this valuable tool, the potential sources of these cells remain an area of controversy. Indeed, the identified sources have ranged from graft-extrinsic cells, presumptively blood-borne "pluripotent" cells or peri-adventitial cells migrating into the lumen [12, 31–34], to a predominance of graft-intrinsic cells (Fig. 7.4) [11]. The source for cells may be dependent upon vein graft handling, since a gentle technique can preserve the endothelial layer to a large extent [11]. Furthermore, recent work has shown that vein-originating endothelial cells can transdifferentiate into smooth muscle-like neointimal cells, contributing approximately half of the neointimal cells within the lesion [13]. Thus, technical considerations of vein graft models may have a direct influence upon how the neointima develops in these grafts.

7.5 Atherosclerotic Lesion Development

The distinction of atherosclerotic lesion formation within the vein graft wall versus neointimal development is important because of the differences in these pathophysiologic processes [1–4]. Unfortunately, most studies in murine systems that have used atherogenic models have not drawn this distinction very precisely, at times confusing the terms and analyses [31, 33, 35–37]. There may be differential responses of neointima in an atherogenic environment, but distinguishing non-atherosclerotic from atherosclerotic wall lesions needs to be more carefully appraised (Fig. 7.5).

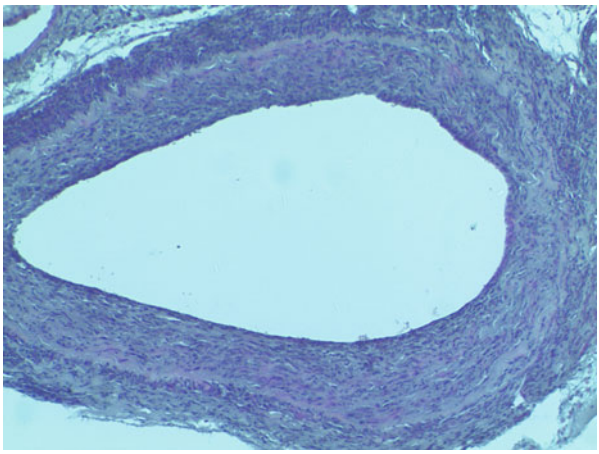

Fig. 7.5 Wild-type vein graft transplanted into an ApoE-null mouse on high-fat diet (atherogenic), with 4-week harvest, showing similar extent of neointimal formation in comparison to non-atherogenic conditions

7.6 Summary

In conclusion, there are several published models of vein grafts that have been developed in mice. These models offer unique opportunities for investigating vein graft complications. The appropriate selection of specific model for the research question(s) and how to evaluate the outcome are important considerations for future studies in the field.

References

1. Hess CN, Lopes RD, Gibson CM, et al. Saphenous vein graft failure after coronary artery bypass surgery: insights from PREVENT IV. Circulation. 2014;130:1445–51.
2. Aranki SF, Tatooles AJ. Disconnect between vein graft failure and clinical events after coronary artery bypass graft surgery. Circulation. 2014;130:1439–41.
3. Motwani JG, Topol EJ. Aortocoronary saphenous vein graft disease: pathogenesis, predisposition, and prevention. Circulation. 1998;97:916–31.
4. Halabi AR, Alexander JH, Shaw LK, et al. Relation of early saphenous vein graft failure to outcomes following coronary artery bypass surgery. Am J Cardiol. 2005;96:1254–9.
5. Cooley BC. Experimental vein graft research: a critical appraisal of models. Heart Res Open J. 2015;2:53–9. http://dx.doi.org/10.17140/HROJ-2-110
6. Abbasi K, Shalileh K, Anvari MS, et al. Perivascular nitric oxide delivery to saphenous vein grafts prevents graft stenosis after coronary artery bypass grafting: a novel sheep model. Cardiology. 2011;118:8–15.
7. Shiroma H, Kusaba A. Ultrastructural features of progressive intimal hyperplasia at the distal end-to-side anastomosis of vein grafts. Cardiovasc Surg. 1996;4:393–8.
8. Saito T, Iguchi A, Tabayashi K. Irradiation inhibits vascular anastomotic stenosis in a canine model. Gen Thorac Cardiovasc Surg. 2009;57:406–12.
9. Capecchi MR. The new mouse genetics: altering the genome by gene targeting. Trends Genet. 1989;5:70–6.

10. Gierut JJ, Jacks TE, Haigis KM. Strategies to achieve conditional gene mutation in mice. Cold Spring Harb Protoc. 2014;4:339–49.
11. Cooley BC. Murine model of neointimal formation and stenosis in vein grafts. Arterioscler Thromb Vasc Biol. 2004;24:1180–5.
12. Hu Y, Mayr M, Metzler B, Erdel M, Davison F, Xu Q. Both donor and recipient origins of smooth muscle cells in vein graft atherosclerotic lesions. Circ Res. 2002;91:e13–20.
13. Cooley BC, Nevado J, Mellad J, et al. TGF-β signaling mediates endothelial to mesenchymal transition (EndMT) during vein graft remodeling. Sci Transl Med. 2014;6:227ra234.
14. Maroney SA, Cooley BC, Ferrel JP, Bonesho CE, Mast AE. Murine hematopoietic cell tissue factor pathway inhibitor limits thrombus growth. Arterioscler Thromb Vasc Biol. 2011;31:821–6.
15. Zou Y, Dietrich H, Hu Y, Metzler B, Wick G, Xu Q. Mouse model of venous bypass graft arteriosclerosis. Am J Pathol. 1998;153:1301–10.
16. Zhang L, Hagen PO, Kisslo J, Peppel K, Freedman NJ. Neointimal hyperplasia rapidly reaches steady state in a novel murine vein graft model. J Vasc Surg. 2002;36:824–32.
17. Diao Y, Xue J, Segal MS. A novel mouse model of autologous venous graft intimal hyperplasia. J Surg Res. 2005;126:106–13.
18. Salzberg SP, Filsoufi F, Anyanwu A, von Harbou K, Karlof E, Carpentier A, et al. Increased neointimal formation after surgical vein grafting in a murine model of type 2 diabetes. Circulation. 2006;114:I302–1307.
19. Greene EC. Anatomy of the rat. Philadelphia: Macmillan Publishing Co.; 1935.
20. Shi C, Patel A, Zhang D, et al. Plasminogen is not required for neointima formation in a mouse model of vein graft stenosis. Circ Res. 1999;84:883–90.
21. Sakaguchi T, Asai T, Belov D, et al. Influence of ischemic injury on vein graft remodeling: role of cyclic adenosine monophosphate second messenger pathway in enhanced vein graft preservation. J Thorac Cardiovasc Surg. 2005;129:129–37.
22. Gottlob R. The preservation of the venous endothelium by 'dissection without touching' and by an atraumatic technique of vascular anastomosis. The importance for arterial and venous surgery. Minerva Chir. 1977;32:693–700.
23. Adcock OT, Adcock GL, Wheeler JR, Gregory RT, Snyder SO, Gayle RG. Optimal techniques for harvesting and preparation of reversed autogenous vein grafts for use as arterial substitutes: a review. Surgery. 1984;96:886–94.
24. Tsui JCS, Souza DSR, Filbey D, Bomfim V, Dashwood MR. Preserved endothelial integrity and nitric oxide synthase in saphenous vein grafts harvested by a 'no-touch' technique. Br J Surg. 2001;88:1209–15.
25. Tennant M, McGeachie JK. Adaptive remodelling of smooth muscle in the neo-intima of vein-to-artery grafts in rats: a detailed morphometric analysis. Anat Embryol. 1993;187:161–6.
26. Mann MJ, Gibbons GH, Kernoff RS, et al. Genetic engineering of vein grafts resistant to atherosclerosis. Proc Natl Acad Sci U S A. 1995;92:4502–6.
27. Wolff RA, Tomas JJ, Hullett DA, et al. Macrophage depletion reduces monocyte chemotactic protein-1 and transforming growth factor-β1 in healing rat vein grafts. J Vasc Surg. 2004;39:878–88.
28. Suggs WD, Olson SC, Mandani D, Petal S, Veith FJ. Antisense oligonucleotides to c-fos and c-jun inhibit intimal thickening in a rat vein graft model. Surgery. 1999;126:443–9.
29. Cooley BC. Differential neointimal response in vein grafts and wire-injured arteries. Circ J. 2007;71:1649–52.
30. Dilley RJ, McGeachie JK, Tennant M. The role of cell proliferation and migration in the development of a neo-intimal layer in veins grafted into arteries, in rats. Cell Tissue Res. 1992;269:281–7.
31. Hu Y, Zhang Z, Torsney E, Afzal AR, Davison F, Metzler B, Xu Q. Abundant progenitor cells in the adventitia contribute to atherosclerosis of vein grafts in ApoE-deficient mice. J Clin Invest. 2004;113:1258–65.

32. Zhang L, Freedman NJ, Brian L, Peppel K. Graft-extrinsic cells predominate in vein graft arterialization. Arterioscler Thromb Vasc Biol. 2004;24:470–6.
33. Xu Q, Zhang Z, Davison F, Hu Y. Circulating progenitor cells regenerate endothelium of vein graft atherosclerosis, which is diminished in ApoE-deficient mice. Circ Res. 2003 Oct 17;93 (8):e76-86.
34. Zhang L, Brian L, Freedman NJ. Vein graft neointimal hyperplasia is exacerbated by CXCR4 signaling in vein graft-extrinsic cells. J Vasc Surg. 2012;56:1390–7.
35. Hu Y, Xu Q. New mouse model of vein bypass graft atherosclerosis. Heart Lung Circ. 2002;11:182–8.
36. Liu S, Li Y, Zhang Z, Xie F, et al. α1-Adrenergic receptors mediate combined signals initiated by mechanical stretch stress and norepinephrine leading to accelerated mouse vein graft atherosclerosis. J Vasc Surg. 2013;57:1645–56.
37. Chen Y, Wong MM, Campagnolo P, et al. Adventitial stem cells in vein grafts display multilineage potential that contributes to neointimal formation. Arterioscler Thromb Vasc Biol. 2013;33:1844–51.

Part IV
Hyperlipidemia-Induced Atherosclerosis

Chapter 8
Mouse Models of Atherosclerosis

Hiroshi Iwata, Jun-ichiro Koga, Julius Decano, Jung Choi, Andrew K. Mlynarchik, Peter C. Mattson, Elena Aikawa, and Masanori Aikawa

Abstract Atherosclerosis is a chronic inflammatory disorder in arteries, and its complications cause major clinical problems such as acute myocardial infarction and stroke, leading to global health threats. Particularly, activated macrophages participate in multiple steps of atherogenesis from the initiation, to the lesion progression, to the onset of acute complications. To examine its molecular mechanisms and develop new therapies, experimental models of atherosclerosis play important roles. Due to the availability of various genetically altered strains, mouse models of atherosclerosis enormously contribute to testing specific biological hypotheses. Mouse models of atherosclerosis also help to evaluate and monitor the effects of new therapies. This chapter briefly discusses the history of the development of animal models of atherosclerosis and summarizes several mouse strains commonly used in atherosclerosis research. As do clinical trials, preclinical studies should employ multidisciplinary approaches to provide the unambiguous evidence that supports a biological hypothesis or examine the effects of a new therapy from various angles. We thus describe the experimental protocols of atherosclerosis research in mice that covers several disciplines, including ultrasonography, molecular imaging of macrophage activation, histological analyses, and biochemical assays.

H. Iwata • J. Decano • J. Choi • A.K. Mlynarchik • P.C. Mattson
Center for Interdisciplinary Cardiovascular Sciences, Cardiovascular Division, Harvard Medical School, Brigham and Women's Hospital, 3 Blackfan st, CLS, Floor 11, Boston, MA 02115, USA

J.-i. Koga
Center for Excellence in Vascular Biology, Cardiovascular Division, Harvard Medical School, Brigham and Women's Hospital, Boston, MA, USA

E. Aikawa • M. Aikawa (✉)
Center for Interdisciplinary Cardiovascular Sciences, Cardiovascular Division, Harvard Medical School, Brigham and Women's Hospital, 3 Blackfan st, CLS, Floor 11, Boston, MA 02115, USA

Center for Excellence in Vascular Biology, Cardiovascular Division, Harvard Medical School, Brigham and Women's Hospital, Boston, MA, USA
e-mail: maikawa@rics.bwh.harvard.edu

M. Sata (ed.), *Mouse Models of Vascular Diseases*,
DOI 10.1007/978-4-431-55813-2_8

Keywords Atherosclerosis • Macrophages • Molecular imaging • Ultrasonography • Histology

8.1 Introduction

Atherosclerosis is a chronic inflammatory disease. Inflammation is integral to the pathophysiology in the development and progression of atherosclerosis [1, 2]. Atherosclerosis is accelerated by dyslipidemia, clinically defined as elevated plasma levels of low-density lipoprotein (LDL), very-low-density lipoprotein (VLDL), and triglycerides and low levels of high-density lipoprotein (HDL). In dyslipidemia, monocytes in circulation infiltrate vascular lesions, differentiate into macrophages, and become foam cells by taking up oxidized lipoproteins. Macrophage foam cells release various proinflammatory cytokines and chemokines, which promote further inflammatory processes in neighboring cells (e.g., dysfunction of endothelial cells, proliferation, migration, and excessive extracellular matrix production in smooth muscle cells), the recruitment of additional monocytes, and further activation of macrophages [3, 4]. Inflammation in atherosclerotic plaques also contributes to the onset of acute events, including acute myocardial infarction and stroke, through enhancing the instability and thrombogenicity [5–7]. Since initial contributions to in vivo models of atherosclerosis in cholesterol-fed rabbits made by Nikolai Anitschkov and others in the nineteenth century [8], animal studies have helped to understand the mechanisms of atherosclerosis and develop new therapies. Although various species (e.g., nonhuman primates, rabbit, dog, swine, guinea pig, hamster, rat) are useful depending on the goals of each study, mouse is most frequently used. This chapter will describe experimental protocols of mouse models of chronic atherosclerosis. Mouse genes are named according to the International Committee on Standardized Genetic Nomenclature for Mice (e.g., *Apoe*−/− instead of apoE−/−) [9].

8.2 Mouse Strains for Atherosclerosis Research

Major reasons why mice have been dominantly used compared to other animals include (1) less difficulty for genetic engineering, (2) cost effectiveness due to shorter gestational period, (3) smaller size, and (4) relatively faster progression of atherosclerotic lesions. It should also be noted that mice and humans significantly differ in various parameters related to atherogenesis. In mice, heart rates are much higher than humans (550–700 in mice and 60–100 in humans), although blood pressure is comparable [10]. Furthermore, major lipoprotein in mice is HDL while LDL in humans. One possible reason of this difference is the lack of cholesteryl ester transfer protein (CETP) in mice. Nevertheless, mice, particularly genetically altered strains, are useful to test the specific biological hypothesis.

A study by Pagen et al. compared the development of atherosclerosis among three wild-type mouse strains C57Bl/6J, BALB/c, and C3H fed by an atherogenic high-fat diet [11], and they found C57/Bl6J was most susceptible for atherogenesis. Manipulation of certain genes related to lipid metabolism alters the lipid profile and accelerates the development of atherosclerotic lesions. The two most frequently used genetically altered mouse strains are apoE and LDL receptor-deficient (*Apoe*−/− [12]and the *Ldlr*−/− [13]) mice. *Apoe*−/− mice are spontaneously hypercholesterolemic (300–500 mg/dl) and develop significant atherosclerotic lesions on a normal chow diet. Atherogenesis can develop faster with a high-fat/high-cholesterol diet, such as Western diet, Paigen diet [14], and atherogenic diet [15], which increase plasma cholesterol levels beyond 1000 mg/dl. Lesions develop in the aortic root, the arch, the innominate artery, and other branches of the aorta and bifurcation of renal arteries. On a normal chow diet, early-stage foam cell lesions develop within 10 weeks of age. Later than 15 weeks of age, they progress into atherosclerotic lesions. And, beyond 20 weeks, they become advanced fibrous lesions. High-fat/high-cholesterol feeding accelerates this time course. Moreover, high-fat/high-cholesterol diets promote cholesterol crystal, necrotic core, and calcification. As a potential disadvantage of the use of *Apoe*−/− mice, plasma cholesterol is mostly carried by lipoprotein remnants, instead of LDL, which plays a central role in human atherosclerosis. Elevation of plasma lipoprotein levels in *Apoe*−/− mice is mainly caused by the lack of the lipoprotein ligand for the major cell-surface receptors, which are responsible for high-affinity plasma lipoprotein clearance. Many studies have used the *Ldlr*−/− mice [16]. The advantage of using Ldlr−/− mice in atherosclerosis study is that deficiency of LDL receptor does not have multitude of functions other than lipoprotein uptake and clearance. *Ldlr*−/− mice on a regular chow diet do not have substantial hyperlipidemia and develop only mild atherosclerotic lesions. On a high-fat/high-cholesterol diet, however, *Ldlr*−/− mice develop marked hypercholesterolemia and atherosclerotic lesions within 20 weeks. Thus, unlike *Apoe*−/− mice, one can turn on the atherogenic milieu in a group of *Ldlr*−/− mice by beginning a high-fat/high-cholesterol diet at any given time point.

Ldlr−/− deficiency has been coupled with transgenic *Apob*, such as a deficiency of the ApoB100-editing enzyme apoBec-1 [17] and human apoB100 transgenic [18], to yield mice that develop extensive atherosclerotic lesions in hypercholesterolemia (300 mg/dL) with large numbers of small *Apob*-100-containing lipoproteins even in normal chow diet. ApoE*3 Leiden mice expressing a variant of human apoE3 with low affinity for the LDL receptor develop atherosclerotic lesions [19, 20]. LDL receptor and apoE double-mutant mice (*Apoe*−/−*Ldlr*−/− mice) represent more severe hypercholesterolemia and atherosclerotic lesions than single *Apoe*−/− mice [21]. As mice do not have CETP that decreases HDL levels in humans, studies have utilized a mouse strain expressing human CETP transgene in combination with *Ldlr*−/− [22], human apoB100 transgenic [23], or ApoE*3 Leiden mice [24] to produce atherosclerotic lesions. Proprotein convertase subtilisin/kexin type 9 (PCSK9) increases plasma LDL cholesterol levels by degrading LDL receptor in the liver [25]. Two recent studies demonstrated that the induction

Table 8.1 Mouse Models of Atherosclerosis

Mouse models	Diets	Reported duration for atherosclerotic lesion formation	Reference no.
Apoe−/−	Normal chow diet	16–20 weeks old	[72]
Human ApoE*3 Leiden transgenic	High-fat/high-cholesterol diet	16 weeks	[20]
Ldlr−/−	High-fat/high-cholesterol diet	16–20 weeks	[13]
Ldlr−/− x human apoB-100 transgenic	High-fat/high-cholesterol diet	24 weeks	[73]
Ldlr−/− x Apobec-1−/−	Normal chow diet	8 months (32 weeks) old	[17]
Apoe−/− x Ldlr−/−	Normal chow diet	14 weeks old	[18]
Mouse Apoa2 transgenic	High-fat/high-cholesterol diet	11–12 weeks	[74]
Human apoB transgenic	High-fat/high-cholesterol diet	18 weeks	[75]
Ldlr−/− x human CETP transgenic	High-fat/high-cholesterol diet	3 months (12 weeks)	[22]
Apoe−/− x human CETP transgenic	High-fat/high-cholesterol diet	3 months (12 weeks)	[76]
Human apoE*3 Leiden transgenic x human CETP transgenic	High-fat/high-cholesterol diet	19 weeks	[77]
Human apoB transgenic x human CETP transgenic	High-fat/high-cholesterol diet	20 weeks	[23]
PCSK9 gain-of-function mutants (adeno-associated viral vectors)	High-fat/high-cholesterol diet	12 weeks	[26]
SR-BI KO/ApoeR61(h/h)	High-fat/high-cholesterol diet	4 weeks	[28, 29]

of PCSK9 mediated by adeno-associated virus (AAV) induces hypercholesterolemia and atherosclerosis under high-fat diet without gene manipulation even in a relatively early time point (12 weeks) [26, 27]. Mice with homozygous mutations in the high-density lipoprotein receptor SR-BI (scavenger receptor class B, type I) and apolipoprotein E genes (SR-BI KO/ApoeR61(h/h) mice) fed with a low-fat diet

exhibit a constellation of pathologies shared with human atherosclerotic coronary heart disease (CHD): hypercholesterolemia, occlusive coronary atherosclerosis, myocardial infarctions, cardiac dysfunction (heart enlargement, reduced systolic function and ejection fraction, and ECG abnormalities), and premature death (mean age 6 weeks) [28, 29] (Table 8.1).

8.3 Atherogenic Diets

Depending on the main purpose of each study, different strategies to induce atherosclerosis in mice may be used. A series of diets are commercially available (Research Diets, Harlan Laboratories, and Purina Diets), which promote the development of atherosclerosis. Here, we review the common types that have been used in many studies. It should also be noted that an appropriate choice of a mouse model is important in conjunction with the diet for successful study.

- Normal chow diet, or otherwise known as the "control diet" in animal experiments, provides sufficient nutrition. Usually composed of ground ingredients such as corn, oats, wheat, and soybean meal, this grain- or cereal-based diet is designed to meet the requirements of a healthy rodent diet (along with other additives such as vitamins, minerals, and fat). An animal group fed with an atherogenic diet may be paired with another group with a control diet with no added cholesterol and fat. Such a control diet should ideally use purified chow rather than regular chow, as contents of regular chow vary depending on the season, which may influence on the results of experiments [30].
- The Western diet is a purified diet composed of 20 % milk fat/butter fat, 34 % sucrose, and 0.2 % cholesterol and is widely available. Fat and cholesterol amounts can be modified to higher levels. It is popularly used with genetically manipulated mouse strains, such as *Ldl*r−/− and *Apoe*−/− and others.
- Another common diet is the "Paigen" atherogenic diet (a hybrid diet created by mixing a natural ingredient mouse diet in a 3:1 ratio with "Thomas-Hartroft" diet) which consists of 16 % fat (half derived from cocoa butter), 1.25 % cholesterol, and 0.5 % sodium cholate.
- "Clinton/Cybulsky" AIN-76A semi-purified high-fat diet which contains 17 % cocoa butter and 1.25 % cholesterol (category: D12108C, Research Diets) compared to the "standard" AIN-76A rodent diet.

To effectively induce quantifiable atherosclerotic plaques in mice, it is crucial to understand and pick which nutrients you may wish to add/deduct from the rodent diet before starting the administration. Addition of dietary cholesterol is a key factor for promoting atherosclerosis in especially some genetically modified mouse strain [31]. Ishibashi et al. have indicated that the greater the increase in lipid-rich diet in *Ldlr*−/− mice, the greater the increase in plasma cholesterol can be achieved [32]. Added dietary cholate for atherosclerosis studies in LDLR −/− mice was reported to be controversial due to its toxic hepatic metabolic effects [33].

8.4 Feeding Study Protocol

Before starting any animal experiment, approval of the experiment via animal research protocol by a local institutional committee for animal care and use/NIH is required. All federal regulations and institutional policies need to be fully abided.

The materials needed for an administration protocol are genetically altered mice (e.g., *Ldlr*−/−, *Apoe*−/−) and wild-type mice (for control group) of at 6–10 weeks of age (and at least 18 g in body weight) and the prepared diet. Depending on goals of each study, the diet can be composed of either chow or high-fat diet with/without additive cholesterol. The diet can be customized as well to test a compound of interest or a drug. For safer measures, it is always recommended to have the diet irradiated for sterility before administering it to the animals. The prepared diets should last for 3–6 months in cold storage, but if testing out a drug/compound, one needs to take into account the shelf life of the compound mixed in with the diet. The activity level of the compound may also alter when going through the milling process (heating and cooling).

With 6–10-week-old *Ldlr*−/− mice, high-fat/high-cholesterol diet administration (ad lib) should be between a minimum of 4 weeks and ~20 weeks (study end point) to induce substantial levels of plaque formation within the aorta and carotid arteries. *Apoe*−/− mice on the other hand do not require such extensively long diet administration to see similar amount of plaque formation, due to the strain's trait of possessing severe spontaneous hypercholesterolemia earlier in age, in comparison to its Ldlr−/− counterpart. Even if fed with a milder "high-fat" diet, *Apoe*−/− mice are known to induce severe hypercholesterolemia [34].

8.5 Ultrasound Imaging of the Carotid Artery

The development of high-resolution ultrasound imaging has helped translational and preclinical researchers noninvasively visualize in vivo tissue structure and physiology [35]). This makes it an excellent and clinically relevant tool for small animal imaging to measure surrogate end points. High frame rate ultrasonography and advanced echocardiography have been made accessible to laboratories worldwide largely due to the efforts of VisualSonics through their line of high-resolution micro-ultrasound machines (e.g., Vevo 2100, Vevo LAZR, Vevo 3100). Imaging the vasculature, including the aorta, brachiocephalic, and carotid arteries, with intact physiologic blood flow, is critical for accurate morphometric analyses in mouse models of atherosclerosis. High temporal resolution accorded by this modality provides data such as vascular wall motion velocities, displacement, distensibility, and stiffness through a speckle-based tracking algorithm in VisualSonics' Vevo®Vasc Advanced Analysis software package [36]. Their high-frequency transducers (e.g., MS 700 of the Vevo 2100) combined with a stepping motor (minimum of 10 μm steps) can produce detailed 3D image data set from serial slices of 2D B

mode, color Doppler, contrast, or power Doppler images. Targets such as the neointima can be segmentally traced for accurate in vivo volumetric measurements. In addition, the MS 700 having a center frequency of 50 MHz and bandwidth of 30–70 MHz can image the mouse carotid artery with an axial resolution of 30 μm and a lateral resolution of 70 μm. A clear delineation of the intima-media border can be visualized in the atherosclerotic vessel, which appears as a thin black line "sandwiched" between a slightly hyper-echoic (gray) adventitia and a very hyper-echoic (white) endothelial/intima layer.

Following protocol is an example of acquiring a short-axis and a long-axis B mode, ECG-based kilohertz visualization (EKV) image, and 3D B-mode image of the mouse carotid artery.

Materials

- Vevo 2100 and MS 700 Transducer (VisualSonics)
- Vevo Integrated Rail System III (VisualSonics)
- ECG platform and physiologic monitor
- Transducer clamp
- Oxygen/medical air tank
- Inhalational anesthesia system
- Isoflurane
- Transmission gel
- Lubricant
- ECG electrode cream
- Depilatory cream
- Cotton-tipped applicators
- Kim wipes
- Mice on pro-atherogenic or the control diet

Protocol

1. Turn on the Vevo 2100 machine and allow it to fully initiate.
2. Attach physiologic monitor to the Vevo 2100 and turn it on. Attach MS 700 to the transducer port and then initialize the scanhead.
3. Set the platform temperature to 37 °C on the physiologic monitor.
4. Fill to 80 % capacity the anesthesia vaporizer chamber with isoflurane and open the air tank.
5. Set air flow to 1 l/min and isoflurane output to 2–3 %
6. Place the mouse inside the anesthesia induction chamber. Secure airflow lines and direct isoflurane gas to the chamber. Allow 3–6 min for full sedation.
7. Transfer the mouse onto the ECG platform in the supine position. Fit the animal's snout into the nasal cone. Switch the isoflurane line toward the cone and reduce isoflurane to 1–1.2 %.
8. Place ECG electrode cream onto the four metal ECG leads on the platform and then secure the paws of the mouse onto these leads using tape.

9. Coat the rectal temperature sensor with lubricant before gently inserting into the mouse to monitor its temperature.
10. Check the physiologic monitor and confirm the heart rate remains between 400 and 600 beats per minute and the temperature is close to 37 °C. For heart rate <400 bpm, reduce isoflurane to 0.8–0.9 %.
11. Make sure the animal's respiratory rate (RR) is between 50 and 80 cycles per minute. If <40 cpm, reduce the isoflurane. RR and ECG tracing can easily be seen on-screen during live scanning.
12. Apply depilatory cream onto the neck region of the mouse from the submandibular area down to the sternal area extending to the lateral edges of the mouse's neck. Massage the cream onto the fur using the cotton-tipped applicator and wait for 3–6 min.
13. Remove the cream with detached fur using wet Kim wipes. Continue wiping with fresh wipes until all cream is gone revealing a hairless neck area. Dry the area.
14. Place transmission gel onto the neck area and position the scanhead where the midportion of the common carotid artery is located, 0.5–1.0 cm above the skin of the neck. Make sure the horizontal plane of the transducer is perpendicular to the axis of the carotid.
15. Press scan button to image live. The image is short-axis view or transverse section of the artery.
16. The notched ridge on one side of the scanhead orients the imager to the image seen. This ridge corresponds to the vertical line beside a small dot located in the top left corner of the image window. This orients the probe position relative to the image.
17. Locate midsection of the common carotid artery, which appears as a circular object pulsating on each side of the midline trachea. Change to color Doppler to confirm arterial pulsations inside the arterial lumen. If no pulsations are seen, adjust the pulse repetition frequency (PRF) to a lesser value using the "velocity" turn-knob.
18. Center the target in the image window and reduce image width and depth while pushing the transducer nearer to the artery so as to "zoom in" on the artery. Adjust image focus using focal zone-type and depth rocker switches.
19. Maximize the differential appearance (echogenicity) of the neointima, media, and adventitia of the artery by reducing the transmission power to the desired level while keeping the gain at 32 dB.
20. Record cine loop of several frames (e.g., 300 or 800 frames). To get an EKV image, make sure the heart rate is regular and then switch to EKV acquisition mode. The EKV image is much more polished than a B-mode image. Its clarity depends on the EKV acquisition frequency which can range from 1000 Hz to 10,000 Hz. A higher EKV frequency will have longer acquisition time. The resulting EKV image is a reconstruction of multiple successive M-mode lines of image taken from the left edge of the acquisition window all through the right edge for every time frame within the ECG cycle.

21. One can also take an M-mode image of the cross section. This allows acquisition of very high temporal images of the anterior and posterior vessel wall as it moves during several cardiac cycles. This movement and displacement may be affected by arterial distensibility, elasticity, or stiffness. Simply place the M-mode sector sampler exactly at the middle of the arterial section. Record cine loop.
22. For a long-axis B-mode image, the probe is simply rotated in place by 90°. During B mode, the image window is adjusted by increasing the image width until the carotid bifurcation is seen. The artery should be in the most horizontal position for imaging. Any tissue plane is most clearly seen when they are directly perpendicular to the axis of insonation (long axis of the transducer). Adjust the mouse platform accordingly.
23. Record cine loop and an EKV image if desired.
24. All B-mode and EKV images can also be processed offline using the Vevo®Vasc Advance Analysis software for speckle tracking to measure several parameters like intima-media thickness (IMT); distensibility; elastance; shear stress; pulse propagation velocity; sector- or layer-specific motion parameters like radial, rotational, and tangential velocity; displacement; and lumen diameter changes.
25. To get a 3D image of the artery, attach the Vevo 3D stepping motor to the rail system with the transducer clamp attached below the mini rail of the stepping motor. Position the transducer accordingly. Attach the motor connector cable to the back panel of the Vevo 2100 and initiate the motor through the software.
26. Locate the artery and center it as closely as possible.
27. Press the 3D button.
28. Set up the 3D mode using the guide below:

3D parameter	Description
Scan distance	Distance in millimeters that the 3D motor stage will traverse for image acquisition
Step size	Sets the incremental distance between successive 2D images which affects the amount of detail contained in the 3D image and acquisition time

29. Start scanning. Once done, store cine loop.
30. Load the 3D image as directed in the screen and go to 3D settings for volume rendering. Start tracing of the neointima or the lumen, proceed through the slices, and end as prompted on the screen. Volume will be automatically calculated. Various options in the screen can be used to show different 3D renderings and viewpoints.

8.6 Molecular Imaging

Molecular or functional imaging is a promising tool to visualize biological processes at molecular levels. Technical innovations, such as nanotechnology, have enormously contributed to the development of molecular imaging [37]. Macrophages play central roles in the pathogenesis of atherosclerosis from the initiation to the development and to the onset of acute thrombotic complications of atherosclerosis. Therefore, imaging of macrophages may help to further understand the mechanisms for atherosclerosis. Macrophage imaging may also serve as a powerful preclinical tool to monitor the effects of new therapies. This section briefly reviews several key modalities for molecular imaging of macrophages—magnetic resonance imaging (MRI), nuclear imaging, and near-infrared fluorescence (NIRF) imaging—and then describes a specific protocol of NIRF imaging in macrophage activities in atherosclerotic plaques.

8.6.1 Macrophage Imaging by MRI

Magnetic nanomaterials with iron oxide cores are used as contrast agents for MRI [37]. Superparamagnetic iron oxide (SPIO) nanoparticles and ultrasmall SPIO (USPIO) nanoparticles (<50 nm) represent such materials. Morishige et al. used 3.0 Tesla MRI and USPIO to report that, in rabbit atherosclerosis model, (1) changes of MRI signal intensity correlate with histologically evaluated macrophage accumulation and (2) macrophage imaging with USPIO can monitor the effects of lipid-lowering therapy on plaque [38].

8.6.2 Macrophage Imaging by Nuclear Medicine

Nuclear medicine is a promising modality to visualize macrophage burden and activity in atherosclerotic plaques in patients. PET with ^{18}F-fluorodeoxyglucose (FDG-PET) can visualize cells with active glucose metabolism—macrophages in atherosclerotic plaques—and monitor the effects of drugs [39–41]. FDG-PET is also used in the field of preclinical research. FDG-PET can detect foamy macrophages in atherosclerotic plaques in hyperlipidemic rabbits [42]. Furthermore, a recent study reported new radionuclides targeting mannose receptor, a macrophage product [43]. Macrophages took up 2-deoxy-2-[^{18}F]fluoro-D-mannose (^{18}F-FDM) more efficiently than ^{18}F-FDG, suggesting that ^{18}F-FDM serves as a novel macrophage-targeting tracer.

8.6.3 NIRF Imaging of Macrophages

NIRF with a wavelength of 600–900 nm has several advantages for noninvasive imaging. The absorbance of NIRF signals by H_2O or hemoglobin, which abundantly exists in human bodies, is small and thus penetrates the tissue. By combination with other modalities such as an angioscope, information about tissue surface appearance and protease activity in deeper tissues could be obtained simultaneously [44, 45]. The Jaffer and Tearney groups have developed an intravascular molecular imaging modality [46, 47]. This technology involves a catheter-assisted dual-imaging approach—optical frequency domain imaging (OFDI) and NIRF imaging. This dual-modality intra-arterial catheter can visualize atherosclerotic plaques with high protease activity in the rabbit aorta and porcine coronary arteries and has been in clinical development. In mouse models of atherosclerosis, NIRF images could be acquired by intravital confocal laser microscopy or fluorescence reflectance imaging (FRI) with appropriate laser and detector for NIRF.

8.6.3.1 Macrophage Accumulation

NIRF probes for macrophages are commercially available. AminoSPARK (PerkinElmer) consists of nanoparticles with iron oxide core and is coated with biocompatible polymer. AminoSPARK is taken up by macrophages, thus enabling to visualize phagocytic activity in vivo.

8.6.3.2 Proteinase Activity

Plaque macrophages produce various proteinases including matrix metalloproteinases (MMPs) and cathepsins. The evidence suggests that such matrix-degrading enzymes reduce collagen content in atherosclerotic arteries and weaken mechanical strength of the atherosclerotic plaques [48, 49]. Experimental studies used genetically altered mouse strains to support this theory [50, 51]. Preclinical studies including our own established the feasibility of molecular imaging of matrix-degrading enzymes in atherosclerosis [37, 52, 53].

8.6.3.3 Calcification

Human arteries and aortic valves often contain calcification. Although conventional views considered cardiovascular calcification as an aging-associated passive degenerative process, the recent evidence has recognized that calcification involves active biological processes closely linked with inflammation [16, 54, 55]. In humans, the recent evidence has indicated that coronary artery calcium (CAC) score detected by CT predicts future cardiovascular events [44, 56]. Preclinical evidence suggests that

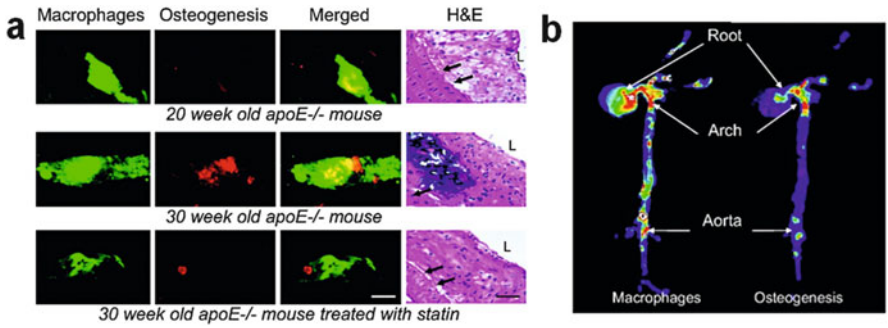

Fig. 8.1 NIRF imaging of macrophages and calcification in mouse atherosclerotic plaques. (**a**) Intravital NIRF imaging of the left carotid artery of *Apoe*−/− mice for osteogenic activity (*green*) and macrophage accumulation (*red*). At 20 weeks of age, osteogenic activity was almost undetectable where macrophages accumulated. 10 weeks later in the same lesion of the same mouse, as macrophage burden had increased, marked osteogenic activity was detected. However, 10 weeks of statin treatment in *Apoe*−/− mice that started at 20 weeks of age suppressed macrophage accumulation and, in parallel, osteogenic activity. (**b**) Co-mapping of macrophages and calcification by FRI. FRI co-localized macrophage accumulation and osteogenic activity in the aortic root and aorta (Reproduced from Aikawa E. et al. [54])

early calcification ("microcalcification") reduces atherosclerotic plaque stability and increases the risk of disruption and thrombus formation [57]. Molecular imaging with the NIRF probes OsteoSense 680 for osteogenic activity and AminoSPARK for macrophages, co-injected in atherosclerotic mice, demonstrated that macrophage accumulation precedes calcification (Fig. 8.1a) [54]. The same study also demonstrated that statin treatment retarded the development of macrophage burden and calcification in parallel (Fig. 8.1b), indicating that anti-inflammatory therapies may prevent calcification and thus cardiovascular events. Figueiredo JL et al. demonstrated that cathepsin S inhibition decreases osteogenic activity in atherosclerotic lesion of *Apoe*−/− mice [58].

Following protocol is an example of an intravital molecular imaging using NIRF probes.

Materials

- Animals: mouse (*Apoe*−/−, *Ldlr*−/− mice, etc.)
- Diet: high-fat/high-cholesterol diet (D12108C, Research Diets)
- NIRF probes: MMPSense 680, AminoSPARK (PerkinElmer)
- Imaging instrument: confocal microscopy (FV1200, Olympus)
- Surgical tools: small spring scissors, forceps, polyethylene tubing, corkboard
- Anesthetic agents: ketamine, xylazine

Protocol

1. Prepare model animals (e.g., high-fat diet-fed *Ldlr*−/− mice).
2. Intravenously inject NIRF probes.

3. 24 or 48 h later, anesthetize the mice.
4. Place the mouse on the corkboard at supine position and cut the neck skin at midline.
5. Separate left and right lobes of thyroid grand by midline incision.
6. Expose trachea and remove connective/fat tissues around the carotid artery.
7. Insert polyethylene tubes under the carotid artery to keep the artery horizontal.
8. Set the mouse on the stage of the microscopy and detect and image the NIRF signals with appropriate wavelength laser.

8.7 Tissue Harvesting

Materials

- Mice (high-fat/high-cholesterol diet fed)
- Phosphate-buffered saline (PBS) (Cat: 12001-680, VWR)
- 0.9 % sodium chloride solution (can be used to substitute the PBS above) (Cat: 85583, Owens and Minor)
- Surgical scissors, sharp-blunt, one pair (Cat: 14001-12, Fine Science Tools)
- Adson forceps, one pair (Cat: 91106-12, Fine Science Tools)
- Dumont #5/45 Forceps (angled), two pairs (Cat: 11251-35, Fine Science Tools)
- Vannas Spring Scissors, one pair (Cat: 91500-09, Fine Science Tools)
- 10 mL syringe (Cat: BD309604, VWR)
- 1 mL syringe (Cat: BD309659, VWR)
- 25-gauge needles (Cat: 305122, VWR)
- Heparin sodium (Cat: 33185, Henry Schein Animal Health)
- Pentobarbital (Euthasol) (Cat: 07-805-9296, Patterson Veterinary)
- Isoflurane (can be used to substitute pentobarbital above) (Cat: 029405, Henry Schein Animal Health)

Protocol

1. Either inject pentobarbital (200 mg/kg IP or approved amount for euthanasia) or place the animal under the effect of isoflurane anesthesia.
2. To first collect whole blood sample for lipid analysis (if blood sampling is not needed, then skip to step 4), hold abdominal skin at midline of the body with Adson forceps and open the abdominal cavity laterally to the diaphragm using surgical scissors—sharp-blunt. Use the forceps (or a cotton swab in substitution) to gently move the digestive tract and other organs to the side to expose the inferior vena cava (IVC) and right kidney.
3. Coat the inner 1 mL syringe and 25G needle with heparin (drawing as much heparin as you can and flushing it all out). Carefully puncture the inferior vena cava (IVC) and draw blood slowly. A 25–30 g mouse should yield approximately 800–1000 uL of blood collection in volume.
4. From below the sternum, carefully open the thoracic cavity anteriorly using surgical scissors until the thyroids are exposed. Both sides of the rib cage should

be retracted to the side to expose the lungs and heart. Diaphragm can be opened further if more "work space" is needed.
5. Using micro scissors, snip the right atrium of the heart, and perfuse the remaining blood from the left ventricle using a 10 mL syringe full of PBS or 0.9 % sodium chloride solution.
6. Remove all other organs and tissues from the body cavity so that only the heart and kidneys are left. Note: take extra caution when removing the lungs, thyroids, and esophagus so that the aorta and carotid arteries are not accidentally damaged. These can be resected using the micro scissors and angled forceps, under a dissecting microscope.
7. Taking care to not damage the aortic arch, hold surrounding connective tissues with the angled forceps and "peel" away (with micro scissors) as much fatty tissue as possible. Free the left subclavian artery, left common carotid artery, and the brachiocephalic artery (can further free the right subclavian and right carotid artery bifurcation if interested). Transect across these three arteries to leave 2–3 mm attached to the aorta. Separate the heart at the aortic root. The abdominal aorta should also be cleaned of connective tissue and fat, all the way down until the internal/external iliac arteries are exposed. Remove the aorta for tissue embedding.

8.8 Histopathological Approaches

Histopathology is an important tool to characterize pathomorphological changes in human and experimental atherosclerosis. To better understand the development of atherosclerosis and atherosclerotic lesion formation and its composition, it is crucial to know the morphology of the tissue and the various pathological processes involved. Histopathology can also examine the effects of new therapies in vivo. These goals can be accomplished through a variety of histological stains, identification of different proteins through immunohistochemistry, and rigorous quantitative analysis. This section will describe how to process the tissue for histological analyses, the different histological stains used to visualize tissue morphology, and how to identify protein targets through immunohistochemistry.

8.8.1 Embedding of Fresh-Frozen Tissue in Optimum Cutting Temperature (OCT) Compound

Tissue preparation is a critical step in obtaining reliable and reproducible results in histopathology. There are two major types of specimen preparation routinely used in staining experiments: paraffin-embedded and fresh-frozen tissue samples. While paraffin embedding has its advantages (e.g., tissue preservation), fresh-frozen embedding is the preferable method, particularly for immunohistochemistry. Unfixed fresh-frozen tissues maintain antigen preservation. This method also

allows more flexibility in post-fixative choice, which can be determined based on a specific experimental goal or the choice of an antibody. This is important because different fixatives (e.g., formalin, paraformaldehyde) may differently affect the reactivity of each antigen. Paraffin embedding of fixed tissues preserves excellent tissue morphology. However, its use for immunohistochemistry may suffer with antigenic masking by a fixative and paraffin embedding (e.g., heat).

One must be extremely careful when freezing tissue. Improper freezing process may cause ice crystal artifacts in the tissue. This often makes morphological interpretation difficult. If tissue is frozen too slowly, large ice crystals can form, producing cracks in the tissue, increasing intracellular and extracellular spaces, the detachment of the tunica intima from the media, and rupturing cell membranes. While "snap freezing" technique using liquid nitrogen allows tissue to be frozen rapidly, tissue often cracks due to the rapid expansion of ice, producing problems later on during sectioning. Liquid nitrogen, in its vapor phase, can also act as an insulator, causing uneven tissue freezing and adding further to ice crystal formation. The ice artifacts due to too slow and too rapid freezing techniques could be overcome by freezing the tissue in chilled/dry ice isopentane (2-methylbutane) (see protocol below). The use of isopentane allows the tissue to freeze without expansion and tissue damage, making it the preferred method for histological and immunohistological applications.

Protocol (Fresh-Frozen Tissue Embedding)

1. Place a container filled with isopentane (2-methylbutane) onto dry ice 15–20 min before embedding so that the isopentane becomes cold.
2. Dissect the tissue (approximately 1×1 cm).
3. Incubate the tissue in optimal cutting temperature (OCT) compound (Tissue-Tek O.C.T. Compound, Sakura Finetek) at room temperature (2–3 changes, 1 min each).
4. Add OCT into a plastic Cryomold.
5. Place tissue in Cryomold with OCT (make sure that tissue is completely covered by OCT).
6. Using long forceps, place the Cryomold into cold isopentane until OCT stops bubbling (~1–3 min).
7. Place frozen mold onto dry ice until isopentane fumes evaporate before going to -80 °C freezer.

Before tissue samples are sectioned, they should be taken out of the -80 °C freezer and placed into the cryostat until the temperature of the tissue falls to the temperature of the cryostat. Sections should be cut in temperatures of around -16 to -22 °C. If cryostat temperature is too low, tissue sections tend to fold during sectioning, making it difficult to get a clean section on the microscope slide. On the other hand, if cryostat temperature is too high, tissue sections will shrivel up during cutting. Therefore, it is crucial to maintain the right cryostat temperature in order to obtain a clean and undamaged tissue section. Furthermore, for immunohistochemical applications, sections are cut in 6–7 μm thickness (thickness can

be adjusted based on each experimental situation). Following cryotomy, slides are left at room temperature for up to 30 min to air dry. The contrast in heat melts OCT on the slide, providing better tissue adhesion. The slides are then stored at −20 °C until further needed.

8.8.2 Collagen and Elastin

Elastin and collagen are major extracellular matrix components that influence the progression of atherosclerosis. In response to inflammation, special enzymes are released that degrade elastin and collagen. This leads to the thinning of the fibrous cap, which ultimately leads to its rupture. The following Masson trichrome stain, picrosirius red stain, and van Gieson stain can highlight these extracellular components in atherosclerotic lesions.

8.8.2.1 Picrosirius Red Stain

Picrosirius red stain is an excellent method to detect fibrillar collagen accumulation and tissue collagenous architecture when viewed under circulatory polarized light [16, 51, 59–61]. To accurately quantify fibrillar collagens, assessment with polarized microscopy is essential, while bright-field assessment may overestimate or underestimate the results [62–65]. The use of polarized light also enables to visualize the collagen fiber orientation and perform quantitative analyses on collagen retardation and red and green hues [50, 66] (Fig. 8.2a).

Protocol (Frozen Sections)

1. Dry slides for 30 min.
2. Place slides in 10 % neutral buffered formalin for 10 min.
3. Rinse slides under running tap water for 5 min.
4. Place slides in distilled water 2 times for 2–3 min.
5. Incubate slides with 0.1 % picrosirius red (pH = 2) for 90 min.
6. Rinse in 0.01 N HCL, 2 times for 2 min.
7. Rinse in distilled water.
8. Rinse slides in 70 % alcohol for 30 s.
9. Rinse slides in 95 % alcohol for 30 s.
10. Rinse slides in 100 % alcohol for 30 s.
11. Place slides in xylene for 3 min.
12. Mount slides using Permount.

Results

(a) Light microscopy

    1. Collagen: Red

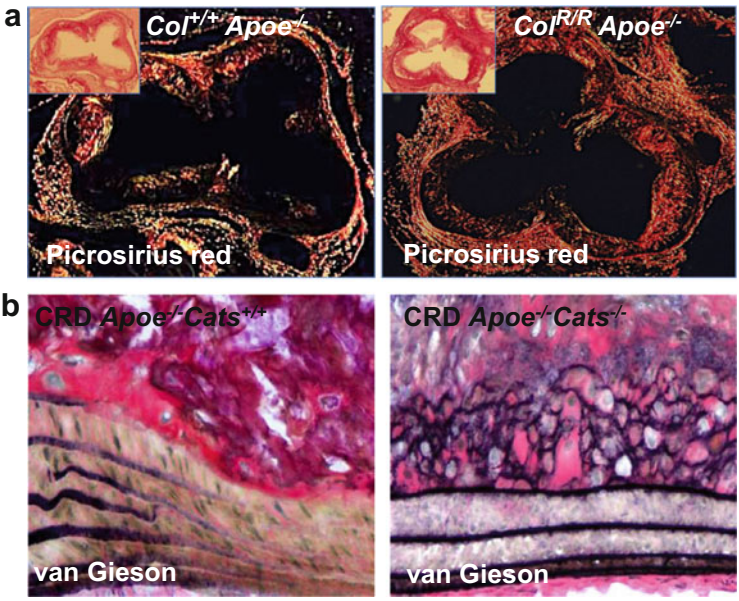

Fig. 8.2 Extracellular matrix staining in mouse atherosclerotic plaques. (**a**) Picrosirius red staining for fibrillar collagen viewed under polarized microscope [50]. Collagen accumulation in the intima of the aortic root of hyperlipidemic *Apoe*−/− mice crossed with collagenase-resistant mutant knock-in mice that express type I collagen that is not cleaved by the MMP family collagenases ($Col^{RR}/apoE^{-/-}$; *right*) was greater than that of mice expressing wild-type collagen type I ($Col^{+/+}/Apoe^{-/-}$; *left*). *Insets*: Picrosirius red staining without polarization. (**b**) van Gieson staining for elastin. Elastin fiber broke in the atherosclerotic plaque of $Apoe^{-/-}$ mice (*left*). Elastin was better preserved in $Apoe^{-/-}$ mice that lacks cathepsin S (*Cats*−/−) mouse atheroma [54] (Reproduced from Fukumoto Y. et al. [50] and Aikawa E. et al. [54])

(b) Polarized microscopy

1. Thick collagen fibers: Yellow, orange
2. Thin collagen fibers: Green

8.8.2.2 van Gieson Stain (Elastic Stain)

The van Gieson stain identifies elastic fibers in the tissue allowing for better understanding of the atherosclerotic plaque morphology often characterized by increased elastin fiber breaks in more advanced lesions [67] (Fig. 8.2b).

Protocol (Frozen Sections)

1. Fix slides in 10 % neutral buffered formalin.

2. Prepare fresh working elastic stain solution.
   (a) Alcoholic hematoxylin solution. . .. . .20 ml
   (b) Ferric chloride solution. . .. . .8 ml
   (c) Weigert's iodine solution. . .. . .8 ml
3. Prepare fresh working differentiating solution.
   (a) Ferric chloride solution. . .. .8 ml
   (b) Deionized or distilled water. . .. .32 ml
4. Hydrate slides in distilled water.
5. Stain slides in working elastic stain solution for 15 min to 1 h.
6. Rinse excess stain off slides in tap water for 1 min.
7. Decolorize sections in working differentiating solution and agitate gently until elastic fibers are blue-black and background is pale gray.
8. Check under microscope.
9. Place slides in sodium thiosulfate solution for 1 min.
10. Rinse slides in distilled water for 30 s.
11. Stain slides in van Gieson stain solution for 1 min.
12. Rinse in 95 % alcohol 3 times for 1 min each.
13. Rinse in 100 % alcohol 2 times for 1 min each.
14. Place slides in xylene 3 times for 1 min each.
15. Mount with Permount.

Results
Elastic Fibers: Black
Nuclei: Black
Collagen: Red
Other Tissue Structures: Yellow

8.8.3 Lipid Stain

Lipids play a major role in various stages of atherogenesis. To highlight overall lipid accumulation in atherosclerotic lesions, we describe the protocol of Oil Red O stain as an example.

Protocol (Frozen Sections)
Oil Red O Preparation (Do this the day before staining.):

1. Add 0.5 g of oil Red O to 100 ml of 100 % propylene glycol (only add a small amount of propylene glycol in the beginning).
2. Gradually add the remainder of propylene glycol stirring periodically.
3. Heat gently until solution reaches 95 °C (Do not allow solution to go over 100 °C).

4. Filter solution through coarse filter paper while still warm.
5. Let solution stand overnight at room temperature.
6. Filter through medium fritted glass filter with aid of vacuum (filter only what you want to use on that day).
7. Refilter if solution becomes turbid.

Staining:

1. Rinse slides in distilled water.
2. Place in absolute propylene glycol for 2 min.
3. Stain in oil Red O solution for 90 min.
4. Differentiate in 85 % propylene glycol solution 3 times for 1 min each.
5. Rinse in 2 changes of distilled water.
6. Stain in Gill's Hematoxylin solution for 1 min.
7. Rinse thoroughly in several changes of distilled water and coverslip using aqueous mounting solution.

Results
Lipids: Red
Nuclei: Blue

8.8.4 Calcification

Calcium deposits are often present in advanced atherosclerotic lesions. The following stains can be used to highlight calcification in tissues: alkaline phosphatase for early calcification and von Kossa and Alizarin Red for late stages of calcification [Aikawa E, Circulation 2007;116:2841–50]. Representative images showing early- and late-stage calcification in mouse atherosclerotic plaques are provided (Fig. 8.3).

8.8.4.1 Alkaline Phosphatase Stain

Activity of alkaline phosphatase, a marker for early-stage calcification, can be visualized using the Vector Red Substrate Kit from Vector Laboratories (SK-5100). The resultant stain is also fluorescent and can be viewed under a polarized light microscope:

1. Dry slides for 20 min.
2. Place slides in tap water for 5 min.
3. Briefly rinse slides in distilled water.
4. Prepare the substrate working solution.
   (a) To 5 ml of 100 mM Tris-HCl, pH 8.5 buffer, add 2 drops of reagent 1 and mix well.
   (b) Add 2 drops of reagent 2 and mix well.
   (c) Add 2 drops of reagent 3 and mix well.

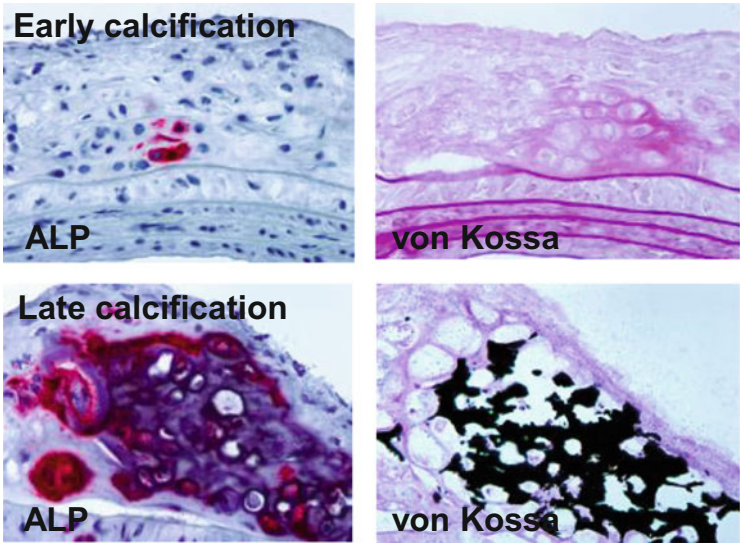

Fig. 8.3 Early and late calcification in mouse atherosclerotic plaques. *Top panels*: Little if any activity of alkaline phosphatase (ALP, red stain) and no calcium deposits (von Kossa) were detected in early calcifying lesions. *Bottom panels*: Lesion with advanced calcification contained high levels of ALP and von Kossa (*black*) signals [67] (Reproduced from Aikawa E. et al. [67])

5. Cover tissue sections with the substrate working solution and leave for 40–60 min.
6. Place slides in Tris-HCl, pH 8.5 buffer for 5 min.
7. Place slides in distilled water.
8. Dip slides in Gill's Hematoxylin 2 times.
9. Wash slides in tap water.
10. Place in Bluing Reagent for 1 min.
11. Wash slides in tap water.
12. Rinse slides in distilled water.
13. Place slides in 95 % ethanol 2 times for 3 min each.
14. Place slides in 100 % ethanol 2 times for 3 min each.
15. Place slides in xylene 2 times for 3 min each.
16. Cover slip slides using Permount.

Results
Alkaline phosphatase enzyme: Red
Nuclei: Blue

8.8.4.2 The von Kossa Stain

The von Kossa stain is used to stain calcium deposits in tissue.

Protocol (Frozen Sections)

1. Dry slides for 20 min.
2. Place slides in 10 % neutral buffered formalin for 10 min.
3. Place slides in tap water for 2 min.
4. Rinse slides through 2 changes of distilled water.
5. Cover tissue sections with 5 % silver nitrate.
6. Place slides under UV light for 10–60 min.
7. Rinse slides in distilled water.
8. Place slides in 5 % sodium thiosulfate for 2–3 min.
9. Rinse slides thoroughly in running tap water.
10. Place slides in nuclear fast red stain for 5 min.
11. Rinse slides in running tap water.
12. Dehydrate slides by placing in 100 % alcohol 3 times.
13. Place in xylene 3 times.
14. Coverslip using Permount mounting medium.

Results
Calcium: Black
Cytoplasm: Pink
Nuclei: Red

8.8.5 Immunohistochemistry

Immunohistochemistry is a powerful tool for identifying and localizing antigens within tissues through the use of antibodies. In atherosclerosis, immunohistochemistry can identify a variety of targets within cell types including macrophages, T cells, endothelial cells, and smooth muscle cells, which contribute to the pathological processes of atherosclerotic lesion development (Fig. 8.4). While the following protocol is a general immunohistochemistry protocol, there can be different variations including type of fixation, incubation steps, and one-step or multiple-step labeling methods. One-step labeling methods involve the label being directly conjugated to the primary antibody. Multiple-step labeling methods involve the label being conjugated to a secondary antibody or the use of an avidin-biotin complex. The protocol given below can easily be adapted to fit one's preferred experimental design.

Immunohistochemistry Protocol (Frozen Sections)

1. Dry slides for 30 min at room temperature.
2. Wash slides 2 times in PBS for 5 min each.
3. Fix slides in 4 % paraformaldehyde for 5 min.
4. Rinse slides in tap water and then wash in PBS 2 times for 5 min each.

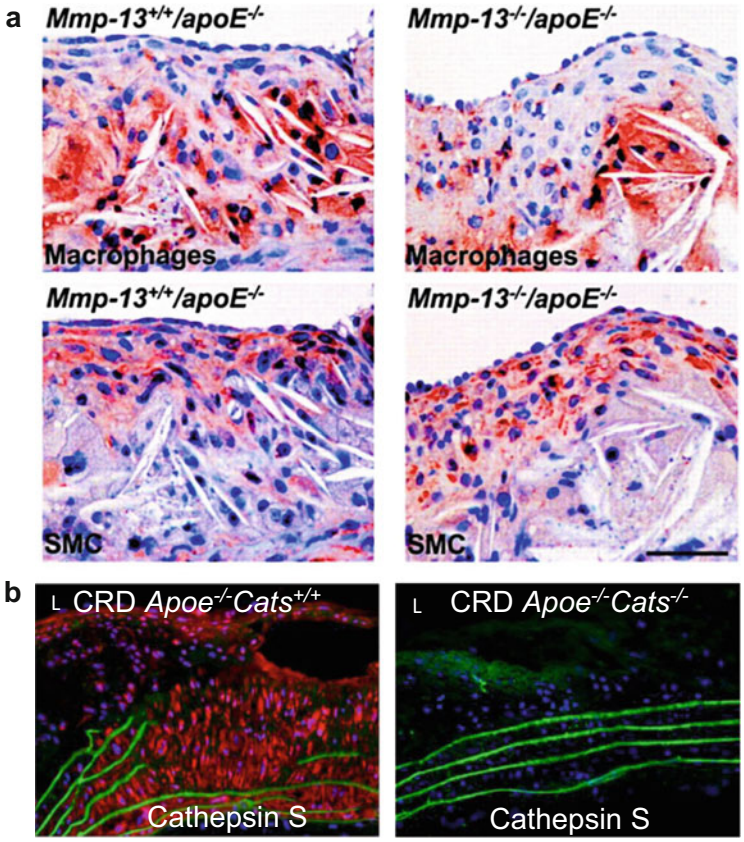

Fig. 8.4 Immunohistochemistry of matrix-degrading enzymes in mouse atherosclerotic plaques. (**a**) Immunostain for macrophages (*top*, *red* reaction product) and smooth muscle cells (SMCs; *bottom, red*) in the atherosclerotic plaques of *Apoe*$^{-/-}$ and MMP-13-deficient (*Mmp13*−/−) mice [50]. (**b**) Immunofluorescence identified increased cathepsin S expression (*red fluorescence*) in the atheroma of *Apoe*−/− mice as compared to undetectable levels in those with cathepsin S deficiency (Cats−/−) [67] (Reproduced from Deguchi J et al. [50] and Aikawa E. et al. [67])

5. Place slides in H_2O_2 solution for 3 min to inhibit endogenous peroxidase activity.
6. Wash well in distilled water.
7. Wash with PBS for 5 min.
8. Prepare a moisture chamber with soaked paper towels.
9. Cover each tissue section with appropriate blocking serum (4 % normal serum, depending on primary antibody source) for 30 min in moisture chamber.
10. Tap off blocking serum and cover each section with primary antibody (diluted in the blocking serum) and incubate for 90 min.
11. Tap off primary antibody solution and wash 2 times in PBS for 5 min each.

12. Cover each section with appropriate secondary antibody solution. Incubate for 45 min.
13. Tap off secondary antibody solution and wash slides 2 times in PBS for 5 min each.
14. Cover each section with streptavidin peroxidase for 30 min.
15. Wash slides 2 times in PBS for 5 min each.
16. Cover sections with AEC Substrate/Chromogen solution and check reaction under microscope.
17. Rinse slides in tap water 2 times for 5 min each.
18. Counterstain with Gill's Hematoxylin solution for 1 min.
19. Rinse in tap water for 5–10 min.
20. Place in bluing solution for 1 min.
21. Rinse in tap water.
22. Coverslip with aqueous mounting medium.

8.8.6 Immunofluorescence

Using fluorescent labels is another powerful tool to visualize proteins but more on a subcellular level (Fig. 8.4). It is mainly used to identify where the protein is expressed within the cell. Immunofluorescence is also useful for double or triple labeling. Typically, tissue sections are incubated with a secondary antibody that is conjugated with a fluorochrome label or avidin-biotin complexes. Tissue sections can also directly be incubated in primary antibodies that are fluorescently conjugated, decreasing the number of steps in the protocol and avoiding cross-reactivity and high background staining. Tissue sections are viewed under a fluorescent microscope equipped with filters for imaging fluorochromes based on their emission and excitation characteristics. Common fluorescent dyes used in immunohistochemistry include fluorescein (e.g. FITC, green, excitation 494 nm, emission 521 nm) and rhodamine (e.g., Texas Red, red, excitation 595 nm, emission 615 nm). Alexa Fluor dyes are also common, with their excitation and emission spectra covering the visible spectrum and extending into the infrared (e.g., Alexa Fluor 350, blue; Alexa Fluor 488, green; Alexa Fluor 594, red; Alexa Fluor 680, near-infrared). The following protocol is routinely used in our laboratory and also includes steps for single and double labeling.

Immunofluorescence Protocol for Frozen Sections (Single and Double Labeling)

1. Fix slides in 4 % paraformaldehyde for 5 min and wash slides in H_2O followed by PBS two times for 5 min each.
2. Incubate slides in 4 % species-appropriate normal serum for 30 min to block nonspecific binding of primary antibody.
3. Apply primary antibody diluted in 4 % species-appropriate normal serum and incubate for 90 min.
4. Wash slides in PBS three times for 5 min each.

5. Apply biotinylated secondary antibody diluted in 4 % species-appropriate normal serum and incubate for 45 min.
6. Wash slides in PBS three times for 5 min each.
7. Apply streptavidin-conjugated Texas Red and incubate for 20 min.
8. Wash slides in PBS three times for 5 min each.

   For single labeling, continue to step 11.
   For double labeling, continue to step 9.

9. For double labeling, sections after first part of staining undergo two blocking procedures:

   (a) Treatment with an avidin/biotin blocking kit (Vector): incubate in solution A for 15 min followed by 15 min of washing in PBS; incubate in solution B for 15 min followed by 15 min of washing in PBS.
   (b) Block with 4 % appropriate normal serum for 20 min.

10. For the second antigen, apply primary antibody overnight in +4 °C fridge, followed by washing in PBS three times for 5 min each the next day. Apply biotinylated secondary antibody for 45 min, wash in PBS three times for 5 min each, and then apply streptavidin-conjugated FITC and incubate for 20 min. Wash in PBS three times for 5 min each.
11. Counterstain nuclei with DAPI for 2 min.
12. Coverslip slides and store in box at +4 °C.

8.8.7 Counterstaining

Counterstaining is an important step following immunohistochemistry to show a direct contrast between the antigen expression (labeled enzymatically) and the overall tissue morphology including nuclei. It can also indicate whether the antigen is localized in the nuclei or the cytoplasm. In general, hematoxylin is useful because it provides a good contrast when 3-amino-9-ethylcarbazole (AEC) is used as a chromogen, showing a blue counterstain, while the antigen expression is shown in red/brown. Because chromogens such as AEC are soluble in alcohol, it is recommended that nonalcoholic hematoxylins (Gill's) be used for counterstaining.

8.8.8 Data Interpretation

In order to properly interpret the results of immunohistochemistry, many different factors must be taken into consideration. Type of fixation, tissue processing, sectioning, and staining all could influence the results. Specific signal usually shows in the cytoplasm, nuclei, or the cell membrane, while nonspecific background staining tends to show in connective tissue, adipocytes, and collagen.

Background staining is often associated with excessive concentrations of a primary antibody; the use of polyclonal antibodies; staining of cells that have undergone damage, necrosis, or autolysis; and poor blocking of endogenous enzymatic activity. Fixation is also a crucial factor where a short fixation time can preserve the antigens but may sacrifice the tissue morphology. On the other hand, a longer fixation time will preserve the morphology but may alter, mask, deplete, or destroy the antigens. Thus, careful optimization of these various factors that can influence the results is critical. Proper interpretation of results also highly depends on the skill and experience levels of the reader.

8.8.9 Quantification

In order to analyze and quantify histological staining including immunohistochemistry, one would first capture digital images and then calculate the percent area that is positive for a specific stain or the number of signals (e.g., positive cells, positive nuclei). While this is a common and useful method, several factors, including the quality of images and observer subjectivity, limit the power of this method. Therefore, we recently developed a new method involving a hue, saturation, value (HSV) color space program named *Color Selection HSV* to accurately quantify and analyze histological stains [68]. This method allows researchers to acquire quantitative data that is objective and independent of section thickness and has little sample-to-sample variation. This new program quantifies histological stains by separating colors of an image not only into the typical red, blue, green (RBG) color space but also a hue, saturation, and value color space. This HSV color space can be attained using the program to convert the RGB dimensions into HSV dimensions through a mathematical formula. Then, the program automatically extracts certain colors from the images by identifying every pixel that falls within a specific threshold range in both color spaces. The program then can count the total number of pixels that fall into the thresholds and display the number as a percentage of the region of interest selected [68].

8.8.10 Detection of Pathobiological Processes and Cellular Events in Atherosclerotic Lesion Development

The development of atherosclerotic lesions results from various pathological processes involving several cell types including macrophages and smooth muscle cells. Several cell types including macrophages, endothelial cells, and smooth muscle cells contribute to atherogenesis through their production of promoters or suppressors of inflammation, matrix remodeling, and thrombogenesis. In order to identify a major source of such factors and characterize their expression patterns in each cell

type, an appropriate marker must be used. The following are common markers for macrophages and smooth muscle cells.

8.8.10.1 Macrophages

- CD68: a commonly used macrophage marker; expressed by human monocytes and tissue macrophages
- F4/80 (mouse): a commonly used macrophage marker
- Mac-1/Mac-3: monoclonal antibodies against the human mannose receptor, a specific marker for macrophages
- CD163: a specific marker of macrophages that can be used in paraffin-embedded tissue samples and is not restricted to "mature" macrophages
- Ly6C: a marker for early-stage atherosclerosis

8.8.10.2 Smooth Muscle Cells

- Alpha smooth muscle actin (α-SMA): a general marker of smooth muscle cells, expressed in differentiated and undifferentiated smooth muscle cells and myofibroblasts
- Calponin: highly expressed in terminally differentiated and non-proliferating smooth muscle cells
- Caldesmon: a marker of fully differentiated and non-proliferating smooth muscle cells
- Smoothelin: a structural protein of differentiated, contractile smooth muscle cells
- SM22 (transgelin): a marker of differentiating smooth muscle cells
- SM1: a smooth muscle myosin heavy chain (MHC) isoform; a strict marker of differentiated smooth muscle cells
- SM2: a smooth muscle MHC isoform; the most strict marker for mature smooth muscle cells

8.8.10.3 Other Targets

Other targets for immunohistochemistry include cytokines and chemokines, including interleukin 1β (IL-1β), tumor necrosis factor α (TNFα), fibroblast growth factor (FGF), platelet-derived growth factor (PDGF), and chemokine (C-C motif) ligand 2 (CCL2)/monocyte chemotactic protein 1 (MCP1). As discussed, extracellular matrix is subject to degradation by proteolytic enzymes such as metalloproteinases (MMPs) and cathepsins during tissue remodeling. Among these enzymes are 3 mammalian collagenases that initiate the degradation of interstitial collagen: MMP-1/collagenase-1, MMP-8/collagenase-2, and MMP-13/collagenase-3. MMP-13 seems to play a dominant role in collagen remodeling in mouse

atherosclerosis [50, 53]. Other key proteolytic enzymes that can be detected by immunostaining include gelatinases (MMP-2 and MMP-9) and elastases (cathepsin S and cathepsin L) [58, 67]. The antibodies for these enzymes are readily available from various sources.

8.9 Biochemical Analyses

8.9.1 RNA Extraction

This procedure, whose purpose is to isolate RNA from atherosclerotic tissues for downstream application in gene expression studies, is similar to that described in previous literature [69]. Briefly, the procedure consists of both homogenization and phase separation stages.

Materials
- Mice with induced atherosclerosis
- 1.5 mL tubes (DNase/RNase-Free)
- Pipette tips (DNase/RNase-Free)
- TRIzol (Invitrogen, Carlsbad, CA, USA)
- Chloroform (Sigma-Aldrich, St. Louis, MO, USA)
- Isopropyl alcohol (Sigma-Aldrich, St. Louis, MO, USA)
- UltraPure DNase/RNase-Free Distilled Water (Life technologies, Carlsbad, CA, USA)
- 75 % Ethanol (diluted in UltraPure Water above)
- NanoDrop 2000 (NanoDrop Technologies, Wilmington, DE, USA)
- RNeasy Micro Kit (Valencia, CA, USA)
- RNAlater RNA Stabilization Reagent (Valencia, CA, USA)

Protocol

1. Tissue samples are homogenized in 0.5–1 ml of TRIzol for every 50–100 mg of sample. Cells are lysed on a plate and incubated for several minutes and then collected into 1.5 ml tubes.
2. 0.2 ml of chloroform per 1 ml of TRIzol is then added, and the samples are centrifuged at no more than 12,000×g for 15 min at 4 °C.
3. The aqueous phase is carefully transferred to a fresh tube, followed by the addition of 0.5 ml of isopropyl alcohol per 1 ml of TRIzol.
4. Samples are incubated at room temperature for 10 min and then centrifuged at no more than 12,000xg for 10 min at 4 °C.
5. Following removal of the supernatant, 1 ml of 75 % ethanol is added to wash the RNA pellet.
6. Samples are centrifuged at no more than 7,500xg for 5 min at 4 °C, and then the supernatant is again removed and the RNA pellet is briefly dried.

7. The last step is to dissolve RNA in DNase-Free and RNase-Free water with variable elution volume.
8. RNA concentration is then measured with NanoDrop 2000, followed by immediate use of RNA or storage at −80 °C.
9. Other options for RNA extraction include Qiagen's RNeasy Micro Kit and Qiagen's RNAlater RNA Stabilization Reagent. RNeasy consists of a column method in which samples are initially lysed and homogenized. After ethanol is added to improve binding conditions, the lysate is placed on a silica membrane to which only the RNA binds. A desired volume of water is then added to elute the pure RNA. This is a convenient procedure but more costly.
10. RNA later consists of premeasured RNA Stabilization Reagent within TissueProtect Tubes in which tissues are immersed directly following their harvesting.
11. In all cases, the samples can subsequently be held in storage at −80 °C.

8.10 Reverse Transcription Quantitative Polymerase Chain Reaction (RT-qPCR)

The goal of RT-PCR is to convert the RNA garnered from extraction into cDNA, in order to then quantitatively measure the levels of gene expression. This is carried out similarly to that described in previous literature [69]. The procedure comprises a reverse transcription protocol—to convert RNA to cDNA—and a quantitative polymerase chain reaction to amplify and measure cDNA.

Materials
- Template: Total RNA from atherosclerotic mice (1 μg/tube)
- Reverse transcriptase (Quanta BioSciences, Gaithersburg, MD)
- qScript Reaction Mix (5X) (Quanta BioSciences, Gaithersburg, MD)
- Nuclease-free water (Quanta BioSciences, Gaithersburg, MD)
- Thermal cycler (GeneAmp® PCR System 9700)
- 0.2 mL tubes
- Pipetman
- Nuclease-free pipet tips
- cDNA from Reverse Transcription
- PerfeCTa FastMix II ROX (Quanta BioSciences, Gaithersburg, MD)
- TaqMan® Gene Expression Assays or SYBR® Green dye for your target genes (Life Technologies, Carlsbad, CA, USA)
- Distilled water
- Applied Biosystems 7900HT Fast Real-Time PCR system
- MicroAmp Optical 384-Well Reaction Plate
- MicroAmp 96- and 384-Well Optical Adhesive Film

Protocol
Reverse Transcription of RNA to cDNA

1. RNA is converted into cDNA via reverse transcription of 1000 ng RNA in a 20 uL solution.
2. 10 uL of this solution is a master mix consisting of 5 uL nuclease-free water, 4 uL qScript Reaction Mix (5x), and 1 uL reverse transcriptase. The remaining 10 uL consists of up to 1000 ng RNA with supplemental dilution in nuclease-free water.
3. These samples are then briefly vortexed and spun down, before being placed in the GeneAmp® PCR System 9700 with the following preset cycles: 22 °C for 5 min, 42 °C for 30 min, 85 °C for 5 min, and 4 °C for any remaining time.

Quantitative Polymerase Chain Reaction (RT-qPCR)

1. 2 µl cDNA from the previous step is inserted on a MicroAmp Optical 384-Well Reaction Plate, followed by 5 µl PerfeCTa Fast Mix, 0.2 µl TaqMan Gene Expression assays that serve as primers/probes for the selected genes of interest, and 2.8 µl distilled water.
2. Plate is sealed with MicroAmp 384-Well Optical Adhesive Film and spun down at 1000 rpm for 1 min. The following preset cycles are used on the PCR system: 95 °C for 30 min, 95 °C for 30 min.

8.10.1 Protein Extraction

In order to analyze proteins that are relevant to studying atherosclerosis in mice, one must first isolate them from the tissue. As mentioned in previous literature [70], this is a relatively straightforward procedure that takes advantage of radioimmunoprecipitation assay buffer (RIPA buffer) to extract the proteins that will be used in downstream testing, proteomics, and analysis.

Materials
- 10X RIPA (Cell Signaling Technology, Beverly, MA, USA)
- HPLC Water (Fisher Scientific, Hampton, New Hampshire, USA)
- Protease Inhibitor Cocktail-I (50 µl) (Sigma-Aldrich, St. Louis, MO, USA)

Protocol
The tissue sample is thoroughly minced and then subjected to RIPA buffer, made of the constituents listed above. This will separate the sample into a soluble layer (desired) and an insoluble layer (can be discarded) over the course of 30 min of incubation on ice. As previous literature touches upon, these extracts can be cleaned up if desired by removing any additional buffers, detergents, salts, and other contaminants.

8.10.2 Western Blotting

The mission of this procedure is to prove the expression of a particular protein of interest in atherosclerotic tissues. Previous literature reviews the use of the Western blot to determine expression of CD59 protein in a mouse model [71]. There are also manufacturer's instructions for how to use iBlot in a Western blot (https://tools.lifetechnologies.com/content/sfs/manuals/iblot2_device_qrc.pdf). The procedure possesses a SDS-PAGE protocol, a blotting protocol, and a blocking step via antibody reaction.

Materials

- Extracted proteins from atherosclerotic mice
- SDS-PAGE Materials (Bio-Rad Laboratories, Hercules, CA, USA)
- iBlot (Life Technologies, Carlsbad, CA, USA)
- Blocking materials (primary antibody, secondary antibody, TBS-T buffer)

Protocol

1. Extracted proteins from the previous protocol are washed twice with cold PBS, lysed for 2 h while sitting on ice, and centrifuged to remove undesirable and insoluble materials.
2. Gels are placed into slots within a tank with 1X running buffer, and protein samples are then added into the wells.
3. The power supply is then set to 20 mA/ gel and the samples undergo SDS-PAGE. The power supply is then shut off when the run is nearly complete (when the dye front is proximal to the bottom edge of the gel).
4. For the blotting stage, at least two different methods have proven to work well. The traditional approach, known as the standard wet transfer, utilizes the layering of filter paper, gel, and the membrane, which are all submerged in a solution of transfer buffer.
5. This sandwich of layers is bound together and placed in a transfer tub with buffer to which a power supply is directed to promote protein migration to the membrane. This current can be applied overnight for best results.
6. On the other hand, the more costly alternative is called the rapid transfer technique with iBlot technology. Anode and cathode stacks are carefully layered on the bottom and top of the gel, respectively, in the iBlot machine, along with the iBlot Filter Paper and disposable sponge according to the manufacturer's instructions. After running in the iBlot machine, the gels are blocked with a proper blocking solution and incubated at room temperature for 1 h.
7. The membrane is then washed in TBS-T 3 times for 5 min each time. They next undergo an antibody reaction when incubated with a primary antibody and blocking solution again for 1 h at room temperature.
8. The membrane is then washed in TBS-T 3 times for 5 min each time. They undergo another reaction when incubated with a secondary antibody and blocking solution for 1 h at room temperature.

References

1. Glass CK, Witztum JL. Atherosclerosis. The road ahead. Cell. 2001;104:503–16.
2. Ross R. Atherosclerosis – an inflammatory disease. N Engl J Med. 1999;340:115–26.
3. Galkina E, Ley K. Immune and inflammatory mechanisms of atherosclerosis. Annu Rev Immunol. 2009;27:165–97.
4. Hansson GK, Libby P. The immune response in atherosclerosis: a double-edged sword. Nat Rev Immunol. 2006;6:508–19.
5. Ley K, Miller YI, Hedrick CC. Monocyte and macrophage dynamics during atherogenesis. Arterioscler Thromb Vasc Biol. 2011;31:1506–16.
6. Libby P, Aikawa M. Stabilization of atherosclerotic plaques: new mechanisms and clinical targets. Nat Med. 2002;8:1257–62.
7. Moore KJ, Sheedy FJ, Fisher EA. Macrophages in atherosclerosis: a dynamic balance. Nat Rev Immunol. 2013;13:709–21.
8. Anitschkow N, Chalatow S. Classics in arteriosclerosis research: on experimental cholesterin steatosis and its significance in the origin of some pathological processes. translated by Mary Z. Pelias, 1913. Arteriosclerosis. 1983;3:178–82.
9. Maltais LJ, Blake JA, Eppig JT, Davisson MT. Rules and guidelines for mouse gene nomenclature: a condensed version. International Committee on Standardized Genetic Nomenclature for Mice. Genomics. 1997;45:471–6.
10. Mattson DL. Comparison of arterial blood pressure in different strains of mice. Am J Hypertens. 2001;14:405–8.
11. Paigen B, Holmes PA, Mitchell D, Albee D. Comparison of atherosclerotic lesions and HDL-lipid levels in male, female, and testosterone-treated female mice from strains C57BL/6, BALB/c, and C3H. Atherosclerosis. 1987;64:215–21.
12. Piedrahita JA, Zhang SH, Hagaman JR, Oliver PM, Maeda N. Generation of mice carrying a mutant apolipoprotein E gene inactivated by gene targeting in embryonic stem cells. Proc Natl Acad Sci U S A. 1992;89:4471–5.
13. Ishibashi S, Herz J, Maeda N, Goldstein JL, Brown MS. The two-receptor model of lipoprotein clearance: tests of the hypothesis in "knockout" mice lacking the low density lipoprotein receptor, apolipoprotein E, or both proteins. Proc Natl Acad Sci U S A. 1994;91:4431–5.
14. Nishina PM, Verstuyft J, Paigen B. Synthetic low and high fat diets for the study of atherosclerosis in the mouse. J Lipid Res. 1990;31:859–69.
15. Zhang SH, Reddick RL, Burkey B, Maeda N. Diet-induced atherosclerosis in mice heterozygous and homozygous for apolipoprotein E gene disruption. J Clin Invest. 1994;94:937–45.
16. Fukuda D, Aikawa E, Swirski FK, Novobrantseva TI, Kotelianski V, Gorgun CZ, Chudnovskiy A, Yamazaki H, Croce K, Weissleder R, Aster JC, Hotamisligil GS, Yagita H, Aikawa M. Notch ligand delta-like 4 blockade attenuates atherosclerosis and metabolic disorders. Proc Natl Acad Sci U S A. 2012;109:E1868–77.
17. Powell-Braxton L, Veniant M, Latvala RD, Hirano KI, Won WB, Ross J, Dybdal N, Zlot CH, Young SG, Davidson NO. A mouse model of human familial hypercholesterolemia: markedly elevated low density lipoprotein cholesterol levels and severe atherosclerosis on a low-fat chow diet. Nat Med. 1998;4:934–8.
18. Veniant MM, Withycombe S, Young SG. Lipoprotein size and atherosclerosis susceptibility in Apoe(−/−) and Ldlr(−/−) mice. Arterioscler Thromb Vasc Biol. 2001;21:1567–70.
19. van Vlijmen BJ, van den Maagdenberg AM, Gijbels MJ, van der Boom H, HogenEsch H, Frants RR, Hofker MH, Havekes LM. Diet-induced hyperlipoproteinemia and atherosclerosis in apolipoprotein E3-Leiden transgenic mice. J Clin Invest. 1994;93:1403–10.
20. Leppanen P, Luoma JS, Hofker MH, Havekes LM, Yla-Herttuala S. Characterization of atherosclerotic lesions in apo E3-leiden transgenic mice. Atherosclerosis. 1998;136:147–52.
21. Witting PK, Pettersson K, Ostlund-Lindqvist AM, Westerlund C, Eriksson AW, Stocker R. Inhibition by a coantioxidant of aortic lipoprotein lipid peroxidation and atherosclerosis

in apolipoprotein E and low density lipoprotein receptor gene double knockout mice. FASEB J. 1999;13:667–75.
22. Masucci-Magoulas L, Goldberg IJ, Bisgaier CL, Serajuddin H, Francone OL, Breslow JL, Tall AR. A mouse model with features of familial combined hyperlipidemia. Science. 1997;275:391–4.
23. Zuckerman SH, Evans GF, Schelm JA, Eacho PI, Sandusky G. Estrogen-mediated increases in LDL cholesterol and foam cell-containing lesions in human ApoB100xCETP transgenic mice. Arterioscler Thromb Vasc Biol. 1999;19:1476–83.
24. de Vries-van der Weij J, Zadelaar S, Toet K, Havekes LM, Kooistra T, Rensen PC. Human CETP aggravates atherosclerosis by increasing VLDL-cholesterol rather than by decreasing HDL-cholesterol in APOE*3-Leiden mice. Atherosclerosis. 2009;206:153–8.
25. Lagace TA, Curtis DE, Garuti R, McNutt MC, Park SW, Prather HB, Anderson NN, Ho YK, Hammer RE, Horton JD. Secreted PCSK9 decreases the number of LDL receptors in hepatocytes and in livers of parabiotic mice. J Clin Invest. 2006;116:2995–3005.
26. Bjorklund MM, Hollensen AK, Hagensen MK, Dagnaes-Hansen F, Christoffersen C, Mikkelsen JG, Bentzon JF. Induction of atherosclerosis in mice and hamsters without germline genetic engineering. Circ Res. 2014;114:1684–9.
27. Roche-Molina M, Sanz-Rosa D, Cruz FM, Garcia-Prieto J, Lopez S, Abia R, Muriana FJ, Fuster V, Ibanez B, Bernal JA. Induction of sustained hypercholesterolemia by single adeno-associated virus-mediated gene transfer of mutant hPCSK9. Arterioscler Thromb Vasc Biol. 2015;35:50–9.
28. Braun A, Zhang S, Miettinen HE, Ebrahim S, Holm TM, Vasile E, Post MJ, Yoerger DM, Picard MH, Krieger JL, Andrews NC, Simons M, Krieger M. Probucol prevents early coronary heart disease and death in the high-density lipoprotein receptor SR-BI/apolipoprotein E double knockout mouse. Proc Natl Acad Sci U S A. 2003;100:7283–8.
29. Zhang S, Picard MH, Vasile E, Zhu Y, Raffai RL, Weisgraber KH, Krieger M. Diet-induced occlusive coronary atherosclerosis, myocardial infarction, cardiac dysfunction, and premature death in scavenger receptor class B type I-deficient, hypomorphic apolipoprotein ER61 mice. Circulation. 2005;111:3457–64.
30. Wang H, Tranguch S, Xie H, Hanley G, Das SK, Dey SK. Variation in commercial rodent diets induces disparate molecular and physiological changes in the mouse uterus. Proc Natl Acad Sci U S A. 2005;102:9960–5.
31. Maganto-Garcia E, Tarrio M, Lichtman AH. Mouse models of atherosclerosis. Curr Protoc Immunol. 2012;Chapter 15:Unit 15.24 1–23.
32. Ishibashi S, Goldstein JL, Brown MS, Herz J, Burns DK. Massive xanthomatosis and atherosclerosis in cholesterol-fed low density lipoprotein receptor-negative mice. J Clin Invest. 1994;93:1885–93.
33. Getz GS, Reardon CA. Diet and murine atherosclerosis. Arterioscler Thromb Vasc Biol. 2006;26:242–9.
34. van Ree JH, van den Broek WJ, Dahlmans VE, Groot PH, Vidgeon-Hart M, Frants RR, Wieringa B, Havekes LM, Hofker MH. Diet-induced hypercholesterolemia and atherosclerosis in heterozygous apolipoprotein E-deficient mice. Atherosclerosis. 1994;111:25–37.
35. Pistner A, Belmonte S, Coulthard T, Blaxall B. Murine echocardiography and ultrasound imaging. J Vis Exp. 2010;42:2100.
36. Larsson M, Heyde B, Kremer F, Brodin LA, D'Hooge J. Ultrasound speckle tracking for radial, longitudinal and circumferential strain estimation of the carotid artery--an in vitro validation via sonomicrometry using clinical and high-frequency ultrasound. Ultrasonics. 2015;56:399–408.
37. Weissleder R, Nahrendorf M, Pittet MJ. Imaging macrophages with nanoparticles. Nat Mater. 2014;13:125–38.
38. Morishige K, Kacher DF, Libby P, Josephson L, Ganz P, Weissleder R, Aikawa M. High-resolution magnetic resonance imaging enhanced with superparamagnetic nanoparticles measures macrophage burden in atherosclerosis. Circulation. 2010;122:1707–15.

39. Rudd JH, Narula J, Strauss HW, Virmani R, Machac J, Klimas M, Tahara N, Fuster V, Warburton EA, Fayad ZA, Tawakol AA. Imaging atherosclerotic plaque inflammation by fluorodeoxyglucose with positron emission tomography: ready for prime time? J Am Coll Cardiol. 2010;55:2527–35.
40. Tahara N, Kai H, Nakaura H, Mizoguchi M, Ishibashi M, Kaida H, Baba K, Hayabuchi N, Imaizumi T. The prevalence of inflammation in carotid atherosclerosis: analysis with fluorodeoxyglucose-positron emission tomography. Eur Heart J. 2007;28:2243–8.
41. Tahara N, Kai H, Yamagishi S, Mizoguchi M, Nakaura H, Ishibashi M, Kaida H, Baba K, Hayabuchi N, Imaizumi T. Vascular inflammation evaluated by [18F]-fluorodeoxyglucose positron emission tomography is associated with the metabolic syndrome. J Am Coll Cardiol. 2007;49:1533–9.
42. Ishino S, Ogawa M, Mori I, Nishimura S, Ikeda S, Sugita T, Oikawa T, Horiguchi T, Magata Y. 18F-FDG PET and intravascular ultrasonography (IVUS) images compared with histology of atherosclerotic plaques: 18F-FDG accumulates in foamy macrophages. Eur J Nucl Med Mol Imaging. 2014;41:624–33.
43. Tahara N, Mukherjee J, de Haas HJ, Petrov AD, Tawakol A, Haider N, Tahara A, Constantinescu CC, Zhou J, Boersma HH, Imaizumi T, Nakano M, Finn A, Fayad Z, Virmani R, Fuster V, Bosca L, Narula J. 2-deoxy-2-[18F]fluoro-D-mannose positron emission tomography imaging in atherosclerosis. Nat Med. 2014;20:215–9.
44. Erbel R, Mohlenkamp S, Moebus S, Schmermund A, Lehmann N, Stang A, Dragano N, Gronemeyer D, Seibel R, Kalsch H, Brocker-Preuss M, Mann K, Siegrist J, Jockel KH, Heinz Nixdorf Recall Study Investigative G. Coronary risk stratification, discrimination, and reclassification improvement based on quantification of subclinical coronary atherosclerosis: the Heinz Nixdorf Recall study. J Am Coll Cardiol. 2010;56:1397–406.
45. Sevick-Muraca EM. Translation of near-infrared fluorescence imaging technologies: emerging clinical applications. Annu Rev Med. 2012;63:217–31.
46. Ughi GJ, Verjans J, Fard AM, Wang H, Osborn E, Hara T, Mauskapf A, Jaffer FA, Tearney GJ. Dual modality intravascular optical coherence tomography (OCT) and near-infrared fluorescence (NIRF) imaging: a fully automated algorithm for the distance-calibration of NIRF signal intensity for quantitative molecular imaging. Int J Cardiovasc Imaging. 2015;31:259–68.
47. Yoo H, Kim JW, Shishkov M, Namati E, Morse T, Shubochkin R, McCarthy JR, Ntziachristos V, Bouma BE, Jaffer FA, Tearney GJ. Intra-arterial catheter for simultaneous microstructural and molecular imaging in vivo. Nat Med. 2011;17:1680–4.
48. Libby P. Molecular bases of the acute coronary syndromes. Circulation. 1995;91:2844–50.
49. Shah PK. Molecular mechanisms of plaque instability. Curr Opin Lipidol. 2007;18:492–9.
50. Deguchi J, Aikawa E, Libby P, Vachon JR, Inada M, Krane SM, Whittaker P, Aikawa M. Matrix metalloproteinase-13/collagenase-3 deletion promotes collagen accumulation and organization in mouse atherosclerotic plaques. Circulation. 2005;112:2708–15.
51. Fukumoto Y, Deguchi JO, Libby P, Rabkin-Aikawa E, Sakata Y, Chin MT, Hill CC, Lawler PR, Varo N, Schoen FJ, Krane SM, Aikawa M. Genetically determined resistance to collagenase action augments interstitial collagen accumulation in atherosclerotic plaques. Circulation. 2004;110:1953–9.
52. Deguchi J, Aikawa M, Tung CH, Aikawa E, Kim DE, Ntziachristos V, Weissleder R, Libby P. Inflammation in atherosclerosis: visualizing matrix metalloproteinase action in macrophages in vivo. Circulation. 2006;114:55–62.
53. Quillard T, Tesmenitsky Y, Croce K, Travers R, Shvartz E, Koskinas KC, Sukhova GK, Aikawa E, Aikawa M, Libby P. Selective inhibition of matrix metalloproteinase-13 increases collagen content of established mouse atherosclerosis. Arterioscler Thromb Vasc Biol. 2011;31:2464–72.
54. Aikawa E, Nahrendorf M, Figueiredo JL, Swirski FK, Shtatland T, Kohler RH, Jaffer FA, Aikawa M, Weissleder R. Osteogenesis associates with inflammation in early-stage atherosclerosis evaluated by molecular imaging in vivo. Circulation. 2007;116:2841–50.

55. New SE, Aikawa E. Molecular imaging insights into early inflammatory stages of arterial and aortic valve calcification. Circ Res. 2011;108:1381–91.
56. Martin SS, Blaha MJ, Blankstein R, Agatston A, Rivera JJ, Virani SS, Ouyang P, Jones SR, Blumenthal RS, Budoff MJ, Nasir K. Dyslipidemia, coronary artery calcium, and incident atherosclerotic cardiovascular disease: implications for statin therapy from the multi-ethnic study of atherosclerosis. Circulation. 2014;129:77–86.
57. Hutcheson JD, Maldonado N, Aikawa E. Small entities with large impact: microcalcifications and atherosclerotic plaque vulnerability. Curr Opin Lipidol. 2014;25:327–32.
58. Figueiredo JL, Aikawa M, Zheng C, Aaron J, Lax L, Libby P, de Lima Filho JL, Gruener S, Fingerle J, Haap W, Hartmann G, Aikawa E. Selective cathepsin S inhibition attenuates atherosclerosis in apolipoprotein E-deficient mice with chronic renal disease. Am J Pathol. 2015;185:1156–66.
59. Aikawa M, Rabkin E, Okada Y, Voglic SJ, Clinton SK, Brinckerhoff CE, Sukhova GK, Libby P. Lipid lowering by diet reduces matrix metalloproteinase activity and increases collagen content of rabbit atheroma: a potential mechanism of lesion stabilization. Circulation. 1998;97:2433–44.
60. Fujihara Y, Koyama H, Nishiyama N, Eguchi T, Takato T. Gene transfer of bFGF to recipient bed improves survival of ischemic skin flap. Br J Plast Surg. 2005;58:511–7.
61. Rabkin E, Aikawa M, Stone JR, Fukumoto Y, Libby P, Schoen FJ. Activated interstitial myofibroblasts express catabolic enzymes and mediate matrix remodeling in myxomatous heart valves. Circulation. 2001;104:2525–32.
62. Sweat F, Puchtler H, Rosenthal SI. Sirius Red F3ba as a stain for connective tissue. Arch Pathol. 1964;78:69–72.
63. Junqueira LC, Bignolas G, Brentani RR. Picrosirius staining plus polarization microscopy, a specific method for collagen detection in tissue sections. Histochem J. 1979;11:447–55.
64. Puchtler H, Meloan SN, Waldrop FS. Are picro-dye reactions for collagens quantitative? Chemical and histochemical considerations. Histochemistry. 1988;88:243–56.
65. Puchtler H, Waldrop FS, Valentine LS. Polarization microscopic studies of connective tissue stained with picro-sirius red FBA. Beitr Pathol. 1973;150:174–87.
66. Aikawa E, Whittaker P, Farber M, Mendelson K, Padera RF, Aikawa M, Schoen FJ. Human semilunar cardiac valve remodeling by activated cells from fetus to adult: implications for postnatal adaptation, pathology, and tissue engineering. Circulation. 2006;113:1344–52.
67. Aikawa E, Aikawa M, Libby P, Figueiredo JL, Rusanescu G, Iwamoto Y, Fukuda D, Kohler RH, Shi GP, Jaffer FA, Weissleder R. Arterial and aortic valve calcification abolished by elastolytic cathepsin S deficiency in chronic renal disease. Circulation. 2009;119:1785–94.
68. Yabusaki K, Faits T, McMullen E, Figueiredo JL, Aikawa M, Aikawa E. A novel quantitative approach for eliminating sample-to-sample variation using a hue saturation value analysis program. PLoS One. 2014;9:e89627.
69. Ahmed S, Shaffer A, Geddes T, Studzinski D, Mitton K, Pruetz B, Long G, Shanley C. Evaluation of optimal RNA extraction method from human carotid atherosclerotic plaque. Cardiovasc Pathol. 2015;24:187–90.
70. Ngoka LC. Sample prep for proteomics of breast cancer: proteomics and gene ontology reveal dramatic differences in protein solubilization preferences of radioimmunoprecipitation assay and urea lysis buffers. Proteome Sci. 2008;6:30.
71. Li B, Xu YJ, Chu XM, Gao MH, Wang XH, Nie SM, Yang F, Lv CY. Molecular mechanism of inhibitory effects of CD59 gene on atherosclerosis in ApoE (−/−) mice. Immunol Lett. 2013;156:68–81.
72. Zhang SH, Reddick RL, Piedrahita JA, Maeda N. Spontaneous hypercholesterolemia and arterial lesions in mice lacking apolipoprotein E. Science. 1992;258:468–71.
73. Sanan DA, Newland DL, Tao R, Marcovina S, Wang J, Mooser V, Hammer RE, Hobbs HH. Low density lipoprotein receptor-negative mice expressing human apolipoprotein B-100 develop complex atherosclerotic lesions on a chow diet: no accentuation by apolipoprotein(a). Proc Natl Acad Sci U S A. 1998;95:4544–9.

74. Warden CH, Hedrick CC, Qiao JH, Castellani LW, Lusis AJ. Atherosclerosis in transgenic mice overexpressing apolipoprotein A-II. Science. 1993;261:469–72.
75. Purcell-Huynh DA, Farese Jr RV, Johnson DF, Flynn LM, Pierotti V, Newland DL, Linton MF, Sanan DA, Young SG. Transgenic mice expressing high levels of human apolipoprotein B develop severe atherosclerotic lesions in response to a high-fat diet. J Clin Invest. 1995;95:2246–57.
76. Linclauen LA, Holotcheff IJ. Wrist arthrodesis: indication and results. Ned Tijdschr Geneeskd. 1975;119:697–703.
77. Westerterp M, van der Hoogt CC, de Haan W, Offerman EH, Dallinga-Thie GM, Jukema JW, Havekes LM, Rensen PC. Cholesteryl ester transfer protein decreases high-density lipoprotein and severely aggravates atherosclerosis in APOE*3-Leiden mice. Arterioscler Thromb Vasc Biol. 2006;26:2552–9.

Part V
Aneurysm in the Aorta

Chapter 9
Angiotensin II-Induced Aortic Aneurysms in Mice

Hong Lu, Deborah A. Howatt, Anju Balakrishnan, Jessica J. Moorleghen, Debra L. Rateri, Lisa A. Cassis, and Alan Daugherty

Abstract Angiotensin II (AngII) infusion into mice induces both abdominal and thoracic aortic aneurysms. Continuous delivery of AngII is achieved by subcutaneous implantation of osmotic pumps. The accumulated experience of many laboratories has provided templates for standardizing procedures to enhance reproducibility of data in the quantification and characterization of AngII-induced aortic aneurysms. This chapter provides suggestions for standard protocols, experimental designs, execution, and data interpretation. It includes discussion of the confounding issues in quantifying compositional characteristics of AngII-induced aortic aneurysms.

Keywords Angiotensin II • Aortic aneurysms • Infusion • Mouse

9.1 Introduction

Aortic aneurysms are region-specific permanent dilations that invoke a risk for sudden death through rupture-induced exsanguination. Common locations for aortic aneurysms in humans are abdominal aortic aneurysms (AAAs) and thoracic aortic aneurysms (TAAs). AAAs most frequently occur in the infrarenal region,

H. Lu
Saha Cardiovascular Research Center, University of Kentucky, BBSRB Room B249, 741 South Limestone, Lexington, KY 40503-0509, USA

Department of Physiology, University of Kentucky, Lexington, KY, USA

D.A. Howatt • A. Balakrishnan • J.J. Moorleghen • D.L. Rateri
Saha Cardiovascular Research Center, University of Kentucky, BBSRB Room B206, 741 South Limestone, Lexington, KY 40503-0509, USA

L.A. Cassis
Department of Pharmacology and Nutritional Sciences, University of Kentucky, Lexington, KY, USA

A. Daugherty (✉)
Saha Cardiovascular Research Center, University of Kentucky, BBSRB Room B243, 741 South Limestone, Lexington, KY 40503-0509, USA

Department of Physiology, University of Kentucky, Lexington, KY, USA
e-mail: Alan.Daugherty@uky.edu

M. Sata (ed.), *Mouse Models of Vascular Diseases*,
DOI 10.1007/978-4-431-55813-2_9

whereas TAAs are predominant in the aortic root and ascending aortic region. Known risk factors for human AAAs include male gender, aging, and smoking [1–4], whereas there is frequently a genetic basis for human TAAs [5].

Angiotensin II (AngII) infusion was first noted to promote formation of AAAs in the suprarenal region of LDL receptor −/− mice [6] that were subsequently observed in apoE −/− mice [7]. The reproducibility of AngII inducing AAAs has been demonstrated by publications from many laboratories (reviewed in [8]). The pathology of AngII-induced AAAs shares several features of human AAAs, including pronounced lumen expansion, elastin breaks, thrombosis, extracellular matrix fragmentation, and accumulation of many types of leukocytes (macrophages, B and T lymphocytes) [9, 10]. Also consistent with the human disease, the incidence of AngII-induced AAAs is significantly greater in male than in female mice [11, 12] and is augmented by coadministration of nicotine [13], a major component in cigarettes. While age is a major risk factor for AAAs in humans, currently no studies have demonstrated age-related effects in the formation of AngII-induced AAAs in mice. Obesity has also been associated with the presence of AAAs in humans and in AngII-infused mice [14, 15]. Finally, hypercholesterolemia augments AngII-induced AAAs in mice [8, 16], which is consistent with risk factors for human AAAs [1–4].

In addition to AngII inducing AAAs, profound dilation also occurs in the thoracic aorta. The AngII-induced dilation is primarily in the ascending aortic region, with medial pathology also occurring just distal to the left subclavian artery branch [17]. While AngII-induced TAAs share a common feature of pronounced lumen expansion with AAAs, the pathology between these two locations is markedly different. Specifically, AngII-induced TAAs exhibit an early presence of intraluminal thrombus, extensive and concentric elastin fragmentation, a relative lack of leukocytic accumulation, and a gradient of tissue disruption across the media with the most severe being in the adventitial aspect [18–20]. These pathological features of AngII-induced TAAs are distinct from those observed in AngII-induced AAAs [9, 18–20].

Relative to other commonly used mouse models of AAAs, such as periaortic application of calcium chloride [21] or intra-aortic perfusion with elastase [22], subcutaneous infusion of AngII is an easier procedure that does not require surgical entry into the body cavity. Moreover, infusion of AngII has the benefit of enabling the concomitant study of both AAAs and TAAs (Fig. 9.1), as well as atherosclerosis when AngII is infused to hypercholesterolemic mice. In addition, infusion rates of AngII that induce these vascular pathologies in mice typically elevate blood pressure, although these increases do not have a direct effect on aneurysm formation and progression [23]. Therefore, infusion of AngII in mice provides a good model to compare and contrast mechanisms of several vascular diseases in response to interventions. In this chapter, we provide guidance on the design, execution, and reporting of studies on AngII-induced aortic aneurysms.

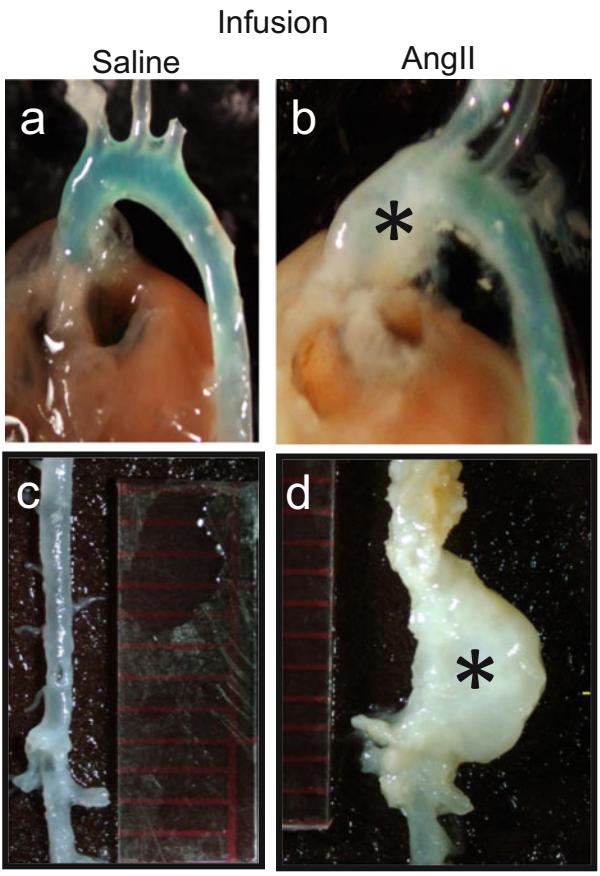

Fig. 9.1 AngII infusion in mice induces both thoracic and abdominal aortic aneurysms. Male mice were infused with either saline or AngII (1000 ng/kg/min) for 4 weeks. Thoracic and abdominal aortas dissected from mice infused with saline (**a** and **c**). Thoracic and abdominal aortas dissected from mice infused with AngII (**b** and **d**). *Asterisks* (*) indicate aneurysmal area. *Light green color* (**a** and **b**) is 2 % agarose gel containing dye that is introduced into the aortic lumen to maintain patency and improve visualization

9.2 Selection of Mice and Infusion Rate of AngII

The initial study reported that AngII infusion at a rate of 500 ng/kg/min induced AAAs in male LDL receptor −/− mice at the age of 5 months [6]. Our subsequent study infused 1000 ng/kg/min to female apoE −/− aged 6 months fed with a normal laboratory diet [7]. Later studies have demonstrated pronounced male gender preference in hypercholesterolemic mice [11, 12]. Studies have also demonstrated that AngII infusion induces AAAs in normocholesterolemic C57BL/6 mice, but the incidence is 5–10 times lower than hypercholesterolemic mice [16, 24–26]. In contrast, fat-enriched diet or genetic obesity promotes AngII-induced AAAs in C57BL/6 mice without pronounced hypercholesterolemia [15]. The basis for hypercholesterolemia promoting AAAs is attributable to increased apoB-containing lipoproteins [16]. Although aging is a critical risk factor for human AAAs, there has been no systematic study demonstrating changes in incidence or severity of

AngII-induced AAAs with increasing age. Most studies have been performed on mice that are ~8–12 weeks old.

Mouse selection for the study of AngII-induced AAAs can vary depending on the hypothesis of the experimental study. For example, if administration of a drug or manipulation of a gene of interest is expected to reduce AngII-induced AAAs, it is preferable to have a robust presence of the disease in the placebo or vehicle group. This would be achieved using hypercholesterolemic male mice infused with 1000 mg/kg/min or higher of AngII. If the experimental outcome is expected to promote AAAs, the presence of AAAs can be reduced in controls by reducing AngII infusion rate and/or using normocholesterolemic mice.

In contrast to profound contributions of hypercholesterolemia and male gender to AngII-induced AAAs, AngII-induced TAAs are not associated with increases in plasma cholesterol concentrations or gender differences [20]. Therefore, if AngII-induced TAAs are the focus of a proposed experiment, normocholesterolemic mice of either gender can be used. As with AngII-induced AAAs, an infusion rate of 500 ng/kg/min or less is preferable if augmentation of AngII-induced TAAs is expected, whereas an infusion rate of 1000 ng/kg/min is desirable if the outcome is attenuation of AngII-induced TAAs.

9.3 Determination of AngII Infusion Rate and Selection of Pump Models

Development of a protocol to permit consistent infusion rates of AngII is a critical aspect of experimental design. AngII mass to be infused is calculated after determination of infusion rate and study duration [27]. Infusion is performed using an Alzet (DURECT Corporation) osmotic pump model selected from those listed in Table 9.1. Selection of a pump model for a specific experiment is based on infusion rate, study duration, and mouse body weight. Although most reported studies use an AngII infusion rate of 1000 ng/kg/min for 28 days, infusion rates and study duration can vary depending on experimental purpose. Insights into selecting AngII rates are provided in Sect. 9.2. If early changes prior to overt aortic aneurysm formation are the focus of an investigation, infusions of AngII for less than 10 days will suffice [9]. If advanced stages of AAAs are the focus of a study, longer infusion intervals can be performed by sequential replacement of pumps [18, 28]. In addition to infusion duration, an important determinant to the selection of Alzet pump used is mouse body weight (Table 9.1).

Different pump models have various priming intervals to initiate peptide delivery. For example, model 2004 pumps initiate extrusion 40 h after filling, when

Table 9.1 Alzet osmotic pump models commonly used in mice

Pump model	1007D	2001	1002	2002	1004	2004	2006
Infusion duration (days)	7	7	14	14	28	28	42
Mouse weight (g)	>10	>20	>10	>20	>10	>20	>20

submersed in saline at 37 °C or implanted subcutaneously. In our standard protocol, we implant pumps after incubation in saline at 37 °C for 12–24 h on the basis that mice have 16–28 h to recover from the surgery prior to AngII delivery. However, if prolonged infusion of AngII (more than 4 or 6 weeks) is needed, this requires replacement with a second pump that should be primed to immediately deliver AngII on implantation. In this case, a filled model 2004 must be immersed in saline and incubated at 37 °C for at least 40 h before the implantation surgery.

Although increases of blood pressure do not contribute to AngII-induced AAAs or TAAs [20, 23, 29], we routinely measure systolic blood pressure at baseline (prior to pump implantation) and during AngII infusion since blood pressure is one parameter that demonstrates effective AngII delivery [30]. Therefore, we recommend measuring blood pressure as a routine procedure before and during AngII infusion. A second validation is measurement of plasma renin concentrations that are decreased during AngII infusion [31].

9.4 Quantification of Aortic Aneurysms

9.4.1 Death Due to Aortic Rupture

Death due to aortic rupture has been a consistent finding during AngII infusion, and it should be qualified in all studies. Analysis of aortic rupture rate or survival curve for the entire study duration is a useful indicator of aneurysm rupture in response to an intervention [28, 32]. Since mice infused with AngII may die of either abdominal or thoracic aortic rupture, it is important to perform a necropsy soon after death to define the location of aortic rupture since pathologies of AngII-induced AAAs and TAAs differ considerably.

9.4.2 Ultrasonography

Ultrasonography is the most convenient and cost-efficient manner of screening for aortic aneurysms in humans [33–35]. In humans, although luminal diameter of 3 cm or above in the infrarenal region is commonly defined as an AAA, an aneurysm is also defined as exceeding the normal luminal diameter of the artery by 50 % [36]. Both sagittal and transverse screens are commonly used, accompanied by color Doppler flow recognition in humans.

Ultrasonography has also been used frequently in mouse aortic aneurysm studies to quantify aortic dilation [28, 37–42]. A major benefit of this method is the ability to sequentially quantify luminal dilation in a live mouse [20, 29, 37]. Any of the VisualSonics models (Vevo 660, 770, or 2100) provide sufficient resolution to

determine lumen dimensions of the suprarenal aorta. Although long-axis screening is reported in several studies, accuracy requires demonstrating that lumen diameter is recorded from the midpoint of the vessel to provide maximum diameter. Also, the potential for tortuous regions after AngII infusion can complicate accurate measurement. Hence, it is likely that short-axis screen provides more precise measurements of abdominal aortic dilations in mice.

For these measurements, mice are sedated with isoflurane and their abdominal surface depilated and placed dorsally in a supine position. AngII-induced AAAs are located in the suprarenal region. The left renal artery provides a landmark to ensure consistent screening in the same location. After identifying the left renal artery, two-dimensional images (B mode) can be acquired starting above the right renal artery with Cine loops. Our standard protocol requires acquisition of Cine loops of 100 frames/suprarenal aortic region. The 100 frames are used to determine the maximal luminal diameter of suprarenal aortas. Measurement accuracy of ultrasonographic images depends largely on user skill, knowledge, and experience. It is preferable that two independent, well-trained operators analyze images in a blinded manner. The frequency for ultrasound screening is variable dependent on the experimental design. To monitor the progression of AAAs, suprarenal aortas can be screened at relatively frequent intervals [28, 37].

Ultrasonography has also been used frequently to monitor and determine aortic root and ascending aortic dilations in mouse models [20, 29, 41, 42]. Because of depth of penetration and width of the aortic root and ascending aorta, use of a VisualSonics Vevo 2100 is preferable to acquire these images. There is an enhanced level of technical skill needed to measure TAAs relative to AAAs.

To provide some quality control of ultrasonographic measurements, it is suggested that aortic dimensions acquired by this noninvasive process be compared to direct visualization and measurements of aortas after termination, as described in Sects. 9.4.3 and 9.4.4.

9.4.3 Aortic Tissue Processing

Blood is usually drawn from anesthetized mice through a right ventricular puncture to collect either serum or plasma for biochemical measurements. These measurements typically include concentrations of total cholesterol and cytokines. As noted above, we commonly measure plasma renin concentrations to confirm effective AngII delivery.

For mice infused with AngII for 4 weeks or less, after perfusion with saline to remove blood, aortas are dissected carefully and placed in a fixative solution (e.g., 10 % neutrally buffered formalin) for more than 24 h. For mice infused with AngII for more than 4 weeks, especially those infused with AngII for 12 weeks, it is helpful to excise aortas after pressure perfusion with a fixative solution at ~100 mmHg and injection of 2 % (wt/vol) agarose to maintain aortic patency [18, 28]. Adventitial tissues are then removed carefully to expose the gross structure

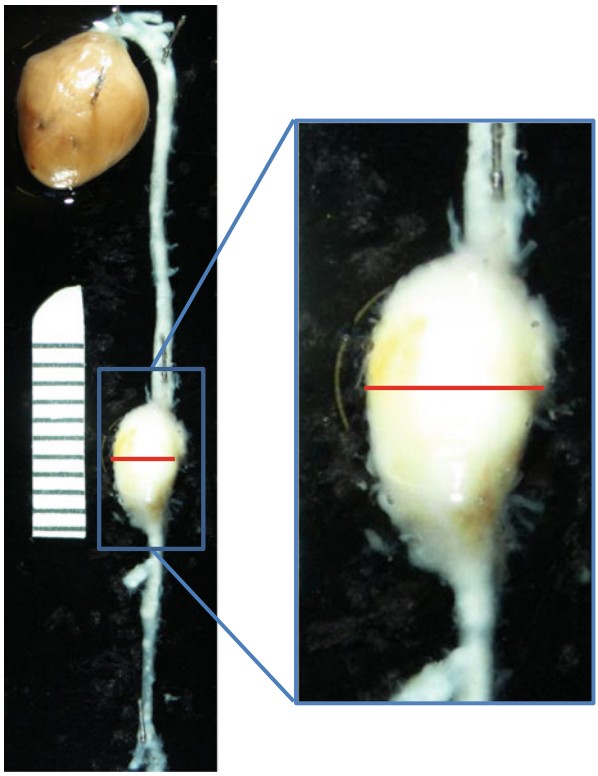

Fig. 9.2 Maximal outer width measurement of the suprarenal aorta. Example shown is an aorta from a male LDL receptor −/− mouse infused with AngII 1000 ng/kg/min for 4 weeks. The *red line* on the abdominal aorta represents maximal outer width of the suprarenal region

(outer boundary of the medial layers) of the aorta. Subsequently, aortas are pinned on black wax to acquire aortic images for maximal ex vivo measurements of suprarenal regions (Fig. 9.2). After completion of this measurement, aortas are unpinned and cut open longitudinally (Fig. 9.3a) through the inner curvature and outer curvature with midline cutting through the three major branches (innominate, left common carotid, and left subclavian) of the aortic arch region as described in the literature [43]. Aortas are then pinned to expose intimal surface of the ascending, arch, and descending part of the thoracic aorta on black wax. For TAAs, images are acquired for en face measurements of intimal surface areas (Fig. 9.3b).

9.4.4 Ex Vivo Imaging

Measurement of the maximal outer width is the most commonly used measurement for AngII-induced AAAs. Measurements can easily be recorded using a digital imaging system. It is preferable to have two independent observers acquire measurements. The measurement of ex vivo diameter can be used to determine AAA

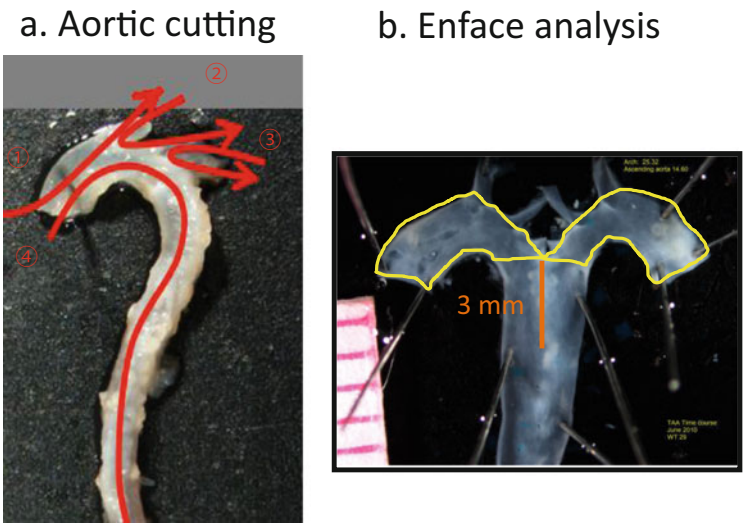

Fig. 9.3 En face analysis for measuring thoracic aortic aneurysms. (**a**). Longitudinal cutting open of aorta. Labeling *1–4* represents the cutting order. *1* represents cutting open the middle of the outer curvature through the innominate artery, *2* through left common carotid artery, and then *3* through left subclavian artery. *4* is cutting open the inner curvature with midline cutting through the entire length of the aorta. (**b**). Definition of area to determine intimal area of the ascending aortic (*yellow box*) and aortic arch (ascending aorta in addition to 3 mm from the branch of the subclavian as illustrated by the *orange* line)

incidence. As with the definition of human AAAs, this requires an arbitrary definition of the absolute size or percent increases that determine AAA presence.

A potential issue of ex vivo measurements is that it only provides a two-dimensional measurement of a three-dimensional aorta and it does not provide information on luminal diameters. To overcome this limitation, AAA volume can be measured using the three-dimensional (3D) imaging function of the Vevo imaging system [28, 38]. 3D mode of the Vevo imaging system acquires a series of 2D "slices" that can be assembled into a 3D dataset using a cube view system. This method can provide both outer and inner volumes of each aortic segment analyzed. For this approach, it is optimal to perform fixation in vivo at physiological pressure to maintain the patency of the lumen. With current software configurations, it is time consuming to measure AAA volume.

In an earlier publication [44], we proposed a classification of AngII-induced AAAs. This was subsequently modified to ease classification and assist in developing statistically robust data [45].

9.4.5 En Face *Imaging*

En face analysis of thoracic aortic dilation can be performed on pinned aortas using image analysis. As shown in Fig. 9.3b, this analysis can arbitrarily be defined as ascending aorta and arch regions to determine site-specific effects. The ascending aorta is defined as the intersection of the base of the left cardiac ventricle to the root of innominate artery, and the aortic arch includes the three major aortic branches (innominate, left common carotid, and left subclavian arteries). Ascending aortic dilation is measured by tracing the outline of the intimal surface area in the ascending and arch regions. As with all measurements, we acquire measurements from two independent operators.

9.5 Characterization of Aortic Aneurysmal Pathologies

9.5.1 Serial Sectioning

Visualization and characterization of pathological changes in aneurysmal tissues is optimally performed by histological and immunocytochemical analyses on serial sections of aortas. AAAs have considerable heterogeneity throughout their length. Meaningful analysis of AAA pathologies requires examining the region of lumen expansion which presents in the early stages of AAA formation as a focal transmural media break across all elastin layers. This should include analysis of regions with normal lumen diameters, although these are not the primary areas of disease initiation. Therefore, it is preferable to section the entire length of AngII-induced AAAs, also including a small portion of normal aortic tissues proximal and distal to the AAA region. An example of a protocol for performing this analysis has been described previously [18]. This includes the collection of serial 10 μm sections throughout the AAA. These sections are placed serially on 10 sequential slides. This process provides slides with 9–12 tissue sections that are located at 100 μm intervals. For a 4 mm long AAA with normal aortic tissues, this entails 40 slides with approximately 400 sections.

Serial sections of the ascending aorta can be acquired in a similar manner as we described for measurements of atherosclerotic lesions [46]. The serial sectioning of the aortic arch provides more challenges due to the curvature of the region and the presence of the three branches. An alternative to short-axis cross sectioning is to perform longitudinal sectioning of the ascending aortic and arch region [20]. While acquisition of longitudinal sections can provide a view of the entire region in a single section, a shortcoming of longitudinal sectioning for measurements is the difficult of acquiring sections of the midsection of the aorta. Acquisition of sections either side of the midline compromises measurements since tissue dimensions are distorted.

9.5.2 Compositional Analyses

Considering the heterogeneity of aortic aneurysmal pathologies, it is important to characterize pathologies in multiple tissue sections. As noted by the description of serial sectioning, this enables multiple sections to be characterized throughout the aortic aneurysmal tissue and enables multiple stains to be performed on serial sections.

9.5.2.1 Histological Analyses

A commonly used histological method is hematoxylin and eosin (H&E) staining. This is a rapid, easy method to visualize and distinguish cells from adjacent extracellular materials in cross-sectioned aortic tissues. There are several other histological methods that are routinely used to characterize pathologies including connective tissue staining with Movat's pentachrome, collagen staining with Gomori trichrome or Picrosirius red, and elastin staining using Verhoeff's hematoxylin method. Extracellular matrices and ground substances of aortic pathologies can be characterized using these histological methods. For example, medial thickness can be quantified by measuring the largest distance perpendicularly between the internal and external elastic laminas of each section with either H&E or any of the other stains. Frequency of elastin breaks can be counted in serial sections using Verhoeff's or Movat's pentachrome stains.

9.5.2.2 Immunostaining

Immunostaining enables identification of many cellular markers such as leukocytes and their subtypes (macrophages and lymphocytes). Specific cellular components of the aortic pathologies can be determined by immunostaining using the antibodies described in Table 9.2 and our previous publication [47]. Specific protein identification in the aortic pathologies can also be performed if authentic antibodies are available.

9.5.2.3 Quantitative Analysis of Histology and Immunostaining

There is an increasing recognition that tissue composition, rather than diameter, is a primary determinant of acute rupture of aortic aneurysms. Therefore, quantification of a specific component in aneurysmal sections has been performed by many investigators to explore mechanisms of progressive aortic dilation and aortic rupture. Quantification is based on immunostaining analysis of a molecule of interest. Currently, there are no widely accepted standards for quantification of immunostaining. Most reported studies use a red, green, and blue (RGB) mode image that relies on an observer-defined threshold. All histological stainings and

Table 9.2 Antibodies commonly used for immunostaining of cellular components in aortic aneurysmal tissues

Cellular components	Information of commonly used antibodies
Leukocytes	Rat CD45 monoclonal antibody (Clone 30-F11, cat# 550539, BD Pharmingen)
Macrophages	Rat CD68 monoclonal antibody (Clone FA-11, cat# MCA1957, AbD Serotec)
T lymphocytes	Rat CD90.2 monoclonal antibody (Clone 30-H12, cat# 553009, BD Pharmingen)
B lymphocytes	Rat CD19 monoclonal antibody (Clone 1D3, cat# 553783, BD Pharmingen)
Endothelial cells	Biotinylated anti-CD31 monoclonal antibody (Clone MEC13.3, cat# 553371, BD Pharmingen)
Smooth muscle cells	Rabbit polyclonal alpha smooth muscle actin antibody (cat# ab5694, ABCAM)

immunostaining result in a range of color intensities that usually require an arbitrary decision to determine the border of the staining. Since the determination of a threshold color intensity that defines positive staining is a subjective decision, it is preferable for two operators to independently acquire data. Additionally, the reliability of measurements will be enhanced by the use of sufficient numbers of serial sections as described at the beginning of Sect. 5.1 to prevent acquisition of data that are subject to sampling error.

Aortic diameter measurements may be combined with compositional analysis to interpret mechanisms of aneurysmal formation. While aortic dilations are standardized and a well-accepted measurement of aortic aneurysms, the many confounding factors noted above may influence quantification and interpretation of compositional analysis. Also, the pronounced changes in tissue composition with aneurysmal development provide challenges to interpreting quantitative data.

9.6 Summary

Reproducibility of aortic aneurysm studies will be optimized by the establishment of standard protocols and experimental designs that consider the multiple variables, including mouse strain, age and gender, as well as AngII infusion rate and duration. Standard protocols for quantification and characterization are also important. These are necessary to enhance consistency of the AAA literature and thereby provide meaningful mechanistic insights into aortic aneurysm formation and progression using AngII infusion approach.

Acknowledgments The authors' research work is supported by grants from the National Institutes of Health, the United States of America (HL107319 to Alan Daugherty, HL107326 to Lisa A. Cassis). The content in this manuscript is solely the responsibility of the authors and does not necessarily represent the official views of the National Institutes of Health.

References

1. Nordon IM, Hinchliffe RJ, Loftus IM, Thompson MM. Pathophysiology and epidemiology of abdominal aortic aneurysms. Nat Rev Cardiol. 2011;8:92–102.
2. Sampson UK, Norman PE, Fowkes FG, Aboyans V, Yanna S, Harrell FE Jr, Forouzanfar MH, Naghavi M, Denenberg JO, McDermott MM, Criqu, MH, Mensah GA, Ezzat, M, Murray C. Global and regional burden of aortic dissection and aneurysms: mortality trends in 21 world regions, 1990 to 2010. Glob Heart. 2014; 9:171–180.e10.
3. Norman PE, Curci JA. Understanding the effects of tobacco smoke on the pathogenesis of aortic aneurysm. Arterioscler Thromb Vasc Biol. 2013;33:1473–7.
4. Sweeting MJ, Thompson SG, Brown LC, Powell JT. Meta-analysis of individual patient data to examine factors affecting growth and rupture of small abdominal aortic aneurysms. Br J Surg. 2012;99:655–65.
5. Lindsay ME, Dietz HC. Lessons on the pathogenesis of aneurysm from heritable conditions. Nature. 2011;473:308–16.
6. Daugherty A, Cassis L. Chronic angiotensin II infusion promotes atherogenesis in low density lipoprotein receptor −/− mice. Ann N Y Acad Sci. 1999;892:108–18.
7. Daugherty A, Manning MW, Cassis LA. Angiotensin II promotes atherosclerotic lesions and aneurysms in apolipoprotein E-deficient mice. J Clin Invest. 2000;105:1605–12.
8. Liu J, Daugherty A, Lu H. Angiotensin II and abdominal aortic aneurysms: an update. Curr Pharm Des. 2015;21(28):4035–48.
9. Saraff K, Babamusta F, Cassis LA, Daugherty A. Aortic dissection precedes formation of aneurysms and atherosclerosis in angiotensin II-infused, apolipoprotein E-deficient mice. Arterioscler Thromb Vasc Biol. 2003;23:1621–6.
10. Daugherty A, Cassis LA, Lu H. Complex pathologies of angiotensin II-induced abdominal aortic aneurysms. J Zhejiang Univ Sci B. 2011;12:624–8.
11. Henriques T, Zhang X, Yiannikouris FB, Daugherty A, Cassis LA. Androgen increases AT1a receptor expression in abdominal aortas to promote angiotensin II-induced AAAs in apolipoprotein E-deficient mice. Arterioscler Thromb Vasc Biol. 2008;28:1251–6.
12. Henriques TA, Huang J, D'Souza SS, Daugherty A, Cassis LA. Orchidectomy, but not ovariectomy, regulates angiotensin II-induced vascular diseases in apolipoprotein E-deficient mice. Endocrinology. 2004;145:3866–72.
13. Maegdefessel L, Azuma J, Toh R, Deng A, Merk DR, Raiesdana A, Leeper NJ, Raaz U, Schoelmerich AM, McConnell MV, Dalman RL, Spin JM, Tsao PS. MicroRNA-21 blocks abdominal aortic aneurysm development and nicotine-augmented expansion. Sci Transl Med. 2012;4:122ra22.
14. Cronin O, Walker PJ, Golledge J. The association of obesity with abdominal aortic aneurysm presence and growth. Atherosclerosis. 2013;226:321–7.
15. Police SB, Thatcher SE, Charnigo R, Daugherty A, Cassis LA. Obesity promotes inflammation in periaortic adipose tissue and angiotensin II-induced abdominal aortic aneurysm formation. Arterioscler Thromb Vasc Biol. 2009;29:1458–64.
16. Liu J, Lu H, Howatt DA, Balakrishnan A, Moorleghen JJ, Sorci-Thomas M, Cassis LA, Daugherty A. Associations of apoAI and apoB-containing lipoproteins with AngII-induced abdominal aortic aneurysms in mice. Arterioscler Thromb Vasc Biol. 2015;35(8):1826–34.
17. Daugherty A, Rateri DL, Charo IF, Owens AP, Howatt DA, Cassis LA. Angiotensin II infusion promotes ascending aortic aneurysms: attenuation by CCR2 deficiency in apoE−/− mice. Clin Sci (Lond). 2010;118:681–9.
18. Rateri DL, Howatt DA, Moorleghen JJ, Charnigo R, Cassis LA, Daugherty A. Prolonged infusion of angiotensin II in apoE(−/−) mice promotes macrophage recruitment with continued expansion of abdominal aortic aneurysm. Am J Pathol. 2011;179:1542–8.
19. Rateri DL, Moorleghen JJ, Knight V, Balakrishnan A, Howatt DA, Cassis LA, Daugherty A. Depletion of endothelial or smooth muscle cell-specific angiotensin II type 1a receptors

does not influence aortic aneurysms or atherosclerosis in LDL receptor deficient mice. PLoS One. 2012;7:e51483.
20. Rateri DL, Davis F, Balakrishnan A, Howatt DA, Moorleghen JJ, O'Connor W, Charnigo R, Cassis LA, Daugherty A. Angiotensin II induces region-specific medial disruption during evolution of ascending aortic aneurysms. Am J Pathol. 2014;184:2586–95.
21. Longo GM, Xiong W, Greiner TC, Zhao Y, Fiotti N, Baxter BT. Matrix metalloproteinases 2 and 9 work in concert to produce aortic aneurysms. J Clin Invest. 2002;110:625–32.
22. Pyo R, Lee JK, Shipley JM, Curci JA, Mao D, Ziporin SJ, Ennis TL, Shapiro SD, Senior RM, Thompson RW. Targeted gene disruption of matrix metalloproteinase-9 (gelatinase B) suppresses development of experimental abdominal aortic aneurysms. J Clin Invest. 2000;105:1641–9.
23. Cassis LA, Gupte M, Thayer S, Zhang X, Charnigo R, Howatt DA, Rateri DL, Daugherty A. Angiotensin II infusion promotes abdominal aortic aneurysms independent of increased blood pressure in hypercholesterolemic mice. Am J Physiol Heart Circ Physiol. 2009;296:H1660–5.
24. Deng GG, Martin-McNulty B, Sukovich DA, Freay A, Halks-Miller M, Thinnes T, Loskutoff DJ, Carmeliet P, Dole WP, Wang YX. Urokinase-type plasminogen activator plays a critical role in angiotensin II-induced abdominal aortic aneurysm. Circ Res. 2003;92:510–7.
25. King VL, Trivedi D, Gitlin JM, Loftin CD. Selective cyclooxygenase-2 inhibition with celecoxib decreases angiotensin II-induced abdominal aortic aneurysm formation in mice. Arterioscler Thromb Vasc Biol. 2006;26:1137–43.
26. Uchida HA, Poduri A, Subramanian V, Cassis LA, Daugherty A. Urokinase-type plasminogen activator deficiency in bone marrow-derived cells augments rupture of angiotensin II-induced abdominal aortic aneurysms. Arterioscler Thromb Vasc Biol. 2011;31:2845–52.
27. Lu H, Howatt DA, Balakrishnan A, Moorleghen JJ, Rateri DL, Cassis LA, Daugherty A. Subcutaneous angiotensin II infusion using osmotic pumps induces aortic aneurysms in mice. J Vis Exp. 2015;103:e53191.
28. Xie X, Lu H, Moorleghen JJ, Howatt DA, Rateri DL, Cassis LA, Daugherty A. Doxycycline does not influence established abdominal aortic aneurysms in angiotensin II-infused mice. PLoS One. 2012;7:e46411.
29. Davis FM, Rateri DL, Balakrishnan A, Howatt DA, Strickland DK, Muratoglu SC, Haggerty CM, Fornwalt BK, Cassis LA, Daugherty A. Smooth muscle cell deletion of low-density lipoprotein receptor-related protein 1 augments angiotensin II-induced superior mesenteric arterial and ascending aortic aneurysms. Arterioscler Thromb Vasc Biol. 2015;35:155–62.
30. Daugherty A, Rateri D, Lu H, Balakrishnan A. Measuring blood pressure in mice using volume pressure recording, a tail-cuff method. J Vis Exp. 2009;1291.
31. Lu H, Balakrishnan A, Howatt DA, Wu C, Charnigo R, Liau G, Cassis LA, Daugherty A. Comparative effects of different modes of renin angiotensin system inhibition on hypercholesterolaemia-induced atherosclerosis. Br J Pharmacol. 2012;165:2000–8.
32. Wang Y, Ait-Oufella H, Herbin O, Bonnin P, Ramkhelawon B, Taleb S, Huang J, Offenstadt G, Combadiere C, Renia L, Johnson JL, Tharaux PL, Tedgui A, Mallat Z. TGF-beta activity protects against inflammatory aortic aneurysm progression and complications in angiotensin II-infused mice. J Clin Invest. 2010;120:422–32.
33. Cosford PA, Leng GC. Screening for abdominal aortic aneurysm. Cochrane Database Syst Rev. 2007;CD002945.
34. Svensjo S, Bjorck M, Wanhainen A. Update on screening for abdominal aortic aneurysm: a topical review. Eur J Vasc Endovasc Surg. 2014;48:659–67.
35. Norman PE, Jamrozik K, Lawrence-Brown MM, Le MT, Spencer CA, Tuohy RJ, Parsons RW, Dickinson JA. Population based randomised controlled trial on impact of screening on mortality from abdominal aortic aneurysm. BMJ. 2004;329:1259.
36. Kent KC. Clinical practice. Abdominal aortic aneurysms. N Engl J Med. 2014;371:2101–8.

37. Barisione C, Charnigo R, Howatt DA, Moorleghen JJ, Rateri DL, Daugherty A. Rapid dilation of the abdominal aorta during infusion of angiotensin II detected by noninvasive high-frequency ultrasonography. J Vasc Surg. 2006;44:372–6.
38. Zhang X, Thatcher S, Wu C, Daugherty A, Cassis LA. Castration of male mice prevents the progression of established angiotensin II-induced abdominal aortic aneurysms. J Vasc Surg. 2015;61:767–76.
39. Maegdefessel L, Spin JM, Tsao PS. New ways to dismantle a ticking time bomb: microRNA 712/205 and abdominal aortic aneurysm development. Arterioscler Thromb Vasc Biol. 2014;34:1339–40.
40. Yoshimura K, Aoki H, Ikeda Y, Fujii K, Akiyama N, Furutani A, Hoshii Y, Tanaka N, Ricci R, Ishihara T, Esato K, Hamano K, Matsuzak M. Regression of abdominal aortic aneurysm by inhibition of c-Jun N-terminal kinase. Nat Med. 2005;11:1330–8.
41. Habashi JP, Doyle JJ, Holm TM, Aziz H, Schoenhoff F, Bedja D, Chen Y, Modiri AN, Judge DP, Dietz HC. Angiotensin II type 2 receptor signaling attenuates aortic aneurysm in mice through ERK antagonism. Science. 2011;332:361–5.
42. Habashi JP, Judge DP, Holm TM, Cohn RD, Loeys BL, Cooper TK, Myers L, Klein EC, Liu G, Calvi C, Podowski M, Neptune ER, Halushka MK, Bedja D, Gabrielson K, Rifkin DB, Carta L, Ramirez F, Huso DL, Dietz HC. Losartan, an AT1 antagonist, prevents aortic aneurysm in a mouse model of Marfan syndrome. Science. 2006;312:117–21.
43. Tangirala RK, Rubin EM, Palinski W. Quantitation of atherosclerosis in murine models: correlation between lesions in the aortic origin and in the entire aorta, and differences in the extent of lesions between sexes in LDL receptor-deficient and apolipoprotein E-deficient mice. J Lipid Res. 1995;36:2320–8.
44. Daugherty A, Manning MW, Cassis LA. Antagonism of AT2 receptors augments angiotensin II-induced abdominal aortic aneurysms and atherosclerosis. Br J Pharmacol. 2001;134:865–70.
45. Wang YX, Cassis LA, Daugherty A. Angiotensin II-induced abdominal aortic aneurysms. In: Xu Q, editor. A handbook of mouse models for cardiovascular disease. Chichester: Wiley; 2006. p. 125–36.
46. Daugherty A, Rateri DL. Development of experimental designs for atherosclerosis studies in mice. Methods. 2005;36:129–38.
47. Lu H, Rateri DL, Daugherty A. Immunostaining of mouse atherosclerosis lesions. Methods Mol Med. 2007;139:77–94.

Chapter 10
Mouse Model of Abdominal Aortic Aneurysm Induced by $CaCl_2$

Hiroki Aoki, Satoko Ohno, Aya Furusho, Michihide Nishihara, Norifumi Nishida, Saki Hirakata, and Koichi Yoshimura

Abstract Abdominal aortic aneurysm (AAA) is a common and fatal disease for which pathogenesis is still uncertain. Reproducible and standardized animal model of AAA is essential to obtain the knowledge of the molecular pathogenesis for developing novel diagnostic and therapeutic strategies. In this regard, $CaCl_2$-induced mouse model of AAA (Ca model) has several advantages. The histopathology of Ca model recapitulates important features of human AAA, including chronic inflammation, progressive destruction of elastic lamellae with preserved triple layers of aortic wall, and expansion of aortic diameter. The procedure has been well established and widely used to decipher the roles of key molecules in AAA. Because Ca model is induced by a simple chemical stimulus, the result is highly reproducible qualitatively and quantitatively once the surgical technique is established. In this section, we describe the step-by-step procedure for creating Ca model of AAA in mice. The standard methods for the evaluation and analysis of the aortic aneurysm are also provided.

Keywords Aorta • Chronic inflammation • Extracellular matrix • Remodeling

10.1 Introduction

Aortic aneurysm is the local weakening and dilation of aortic walls that is driven by chronic inflammation and proteolytic degradation of the extracellular matrix [1]. Although most patients present no clinical symptoms, the degradation and

H. Aoki (✉)
Cardiovascular Research Institute, Kurume University, 67 Asahi-machi, Kurume, Fukuoka 830-0011, Japan
e-mail: haoki@med.kurume-u.ac.jp

S. Ohno • A. Furusho • M. Nishihara • N. Nishida • S. Hirakata
Division of Cardiovascular Medicine, Department of Internal Medicine, Kurume University School of Medicine, Fukuoka, Japan

K. Yoshimura
Department of Surgery and Clinical Science, Yamaguchi University Graduate School of Medicine, Yamaguchi, Japan

M. Sata (ed.), *Mouse Models of Vascular Diseases*,
DOI 10.1007/978-4-431-55813-2_10

expansion of aortic walls advance and eventually result in the abrupt rupture of the aorta and sudden death. The current therapeutic option is limited to replacement of the diseased aorta with an artificial graft either by open surgery or endovascular aneurysm repair (EVAR) using a stent graft. In most of the patients, the aneurysm diameters are small and not suitable for graft replacement due to the low risk of rupture and lack of symptoms. No therapeutic option is available for these patients, and "watchful observation" is the only clinical strategy. The EVAR leaves diseased aortic wall tissue in place, which poses a concern because of remaining inflammation and may lead to future complications such as progression of the aneurysm. Therefore, patients with a small aneurysm or those who have undergone EVAR would benefit from therapies that suppress the inflammation and stabilize the aortic walls.

Extensive studies have aimed to better understand the molecular mechanism of aortic aneurysm, so new diagnostic and therapeutic strategies can be developed. Reliable and reproducible animal models are essential for such studies [2, 3]. The $CaCl_2$-induced abdominal aortic aneurysm model (Ca model) is widely used for deciphering the molecular mechanism and for testing the efficacy of therapeutic interventions [4, 5]. This section includes the detailed protocol for the Ca model as well as a description of some pitfalls. The standard methods for the evaluation and analysis of the aortic aneurysm will also be provided.

10.2 Ca Model of Aortic Aneurysm

The Ca model is induced by the application of $CaCl_2$ solution to the adventitia of the exposed abdominal aorta. This procedure takes about 30 min per mouse for a trained operator. The $CaCl_2$ is thought to make insoluble salts in the tissue that trigger chronic inflammation and promote the development of aortic aneurysm 6–10 weeks after application, eventually causing dilation of the $CaCl_2$-treated segment of the aorta to about twice its normal diameter. Histopathologically, the treated aortic walls recapitulate many of the features in human aortic aneurysm, including the adventitial inflammation with cellular infiltration, activation of inflammatory signaling molecules such as JNK [6] and NF-κB [7], secretion of various matrix metalloproteinases (MMPs) [5], and degradation of medial elastic lamellae (Fig. 10.1).

As an experimental system, the Ca model is highly reproducible qualitatively and quantitatively [3]. Fine-tuning of the inflammation can be achieved by adjusting the time the $CaCl_2$ solution is applied. On the other hand, some limitations of the Ca model are that it does not progress to rupture and develops no atherosclerosis or mural thrombi. The procedure requires careful training of the operator, especially for the exposure of the aorta and removal of the connective tissue surrounding the adventitia. The training of the operator can be lengthy, because it takes 4–6 weeks for the aortic aneurysm to develop. For optimal results, the operator should adjust the procedure based on the extent of inflammation and the

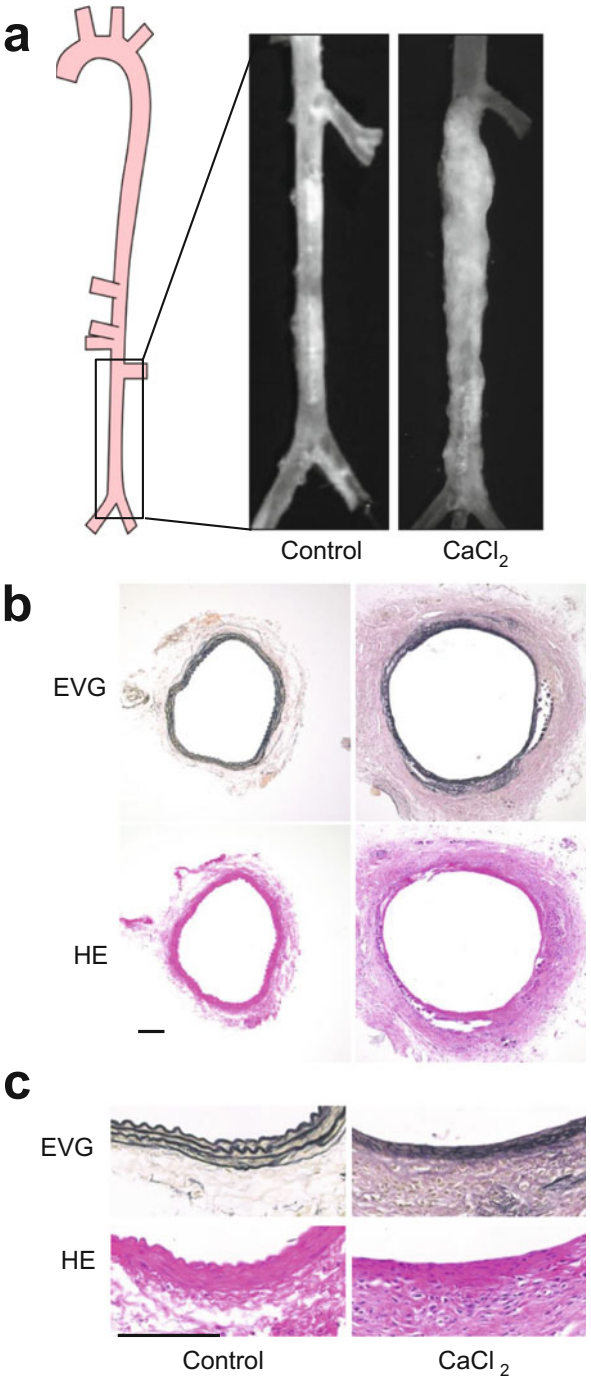

Fig. 10.1 Macroscopic and microscopic images of the Ca model. Macroscopic images (**a**) and microscopic images (**b**, **c**) using Elastica van Gieson (*EVG*) and hematoxylin and eosin (*HE*) stains. Bars indicate 100 μm

dilation of the aorta. To shorten the training period, we suggest observing the aorta 1 week after the $CaCl_2$ treatment. Adventitial inflammation of the entire circumference of the aorta ensures that the isolation and the $CaCl_2$ treatment of the aorta were successful. At this time point, the aneurysm has not fully developed and the elastic lamellae, observed with Elastica van Gieson staining, should not be severely destructed. Once the circumferential inflammation is reproducibly obtained by the $CaCl_2$ treatment, the aorta should be observed 6 weeks after the $CaCl_2$ treatment to verify the aortic aneurysm develops as expected. Adjust the application time of the $CaCl_2$ treatment without changing the surgical procedure to obtain the optimal results. By keeping the surgical technique and the $CaCl_2$ treatment (concentration, volume, and application time) consistent, highly reproducible results can be obtained.

10.3 Tools

The tools and equipment that the authors use for making and analyzing the Ca model (Fig. 10.2) are listed below. The names of the manufacturers and the catalog numbers are provided for selected items as a reference for the readers. Similar products from other manufacturers may be used.

- Cotton wool
- Cotton swabs
- Superfine cotton swabs
- Scissors
- Fine scissors (F.S.T. #14060-09)
- Spring scissors (F.S.T. #15003-08)
- Forceps (F.S.T. #11050-10)
- Microsurgery forceps (F.S.T. #11253-20) × 2
- Needle holder (Roboz #RS-7820)
- Extra-thin pins (F.S.T. Minuten pins #26002-10)
- Syringes (1 mL) with 26G needles
- Infusion set
- Microsurgical needles with 5-0 nylon suture thread
- 100 mm culture dish with black rubber plate and scale
- Stereomicroscope for surgery with shadowless coaxial illumination (Carl Zeiss Stemi DV4 SPOT)
- Microscope equipped with a calibrated digital camera and PC (Leica M165 C)
- Anesthesia apparatus
- Timer
- Fiber optic illuminator or LED illuminator with flexible arms
- Operating table
- Heating plate
- Hair removal cream

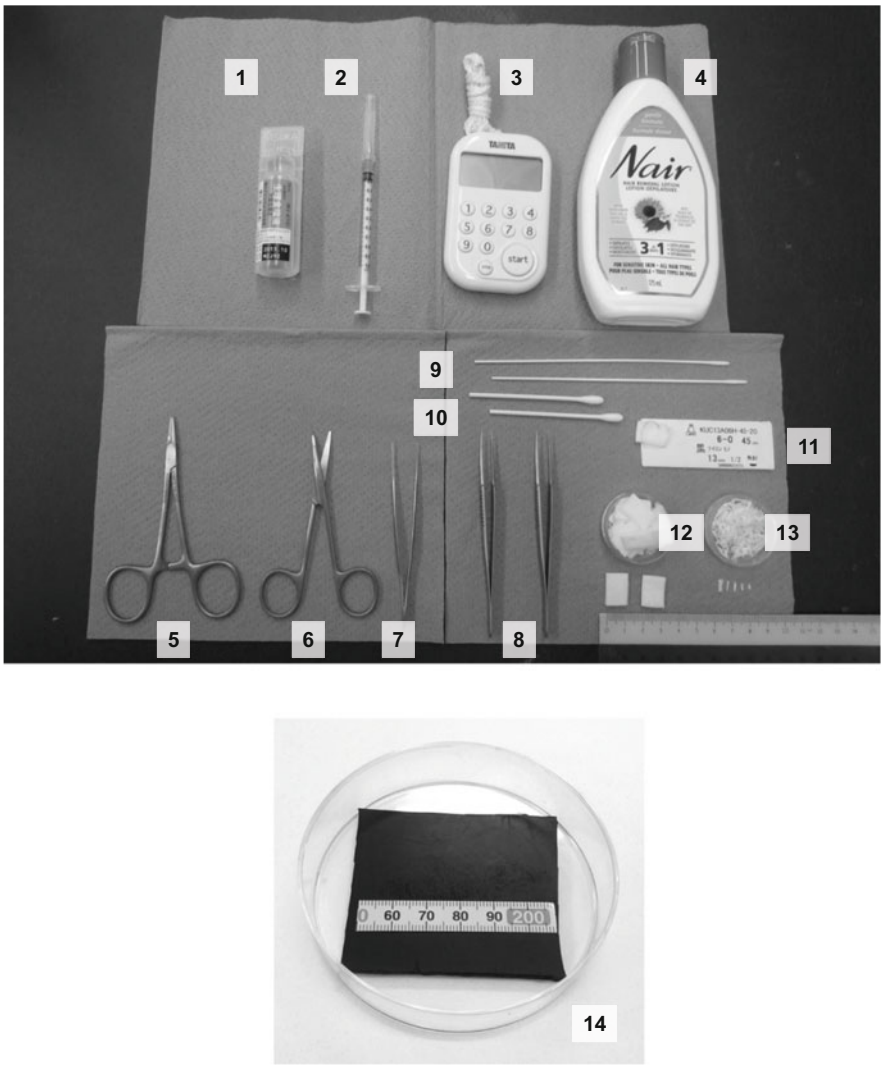

Fig. 10.2 Tools for the Ca model. (*1*) Physiological saline, (*2*) 1 mL syringe with 26G needle, (*3*) timer, (*4*) hair removal cream, (*5*) needle holder, (*6*) scissors, (*7*) forceps, (*8*) microsurgery forceps, (*9*) superfine cotton swabs, (*10*) cotton swabs, (*11*) microsurgical needles with 5-0 nylon suture thread, (*12*) large pieces of cotton, (*13*) small pieces of cotton, (*14*) 100 mm culture plate with rubber plate and scale

- Anesthetics; sodium pentobarbital, isoflurane
- 70 % ethanol for disinfection
- 0.5 M $CaCl_2$ solution
- Physiological saline
- Phosphate-buffered saline (PBS)
- 4 % paraformaldehyde (PFA) in PBS

10.4 Operation Procedure

In this instruction, the left and the right indicate those of the operator, not of the mouse. Fast the mice the day before the surgery. Dilute sodium pentobarbital (50 mg/mL) to 5 mg/mL with saline and administer it intraperitoneally at 0.08–0.1 mL/10 g body weight (40–50 mg/kg body weight) to the mouse for the induction of anesthesia. Maintain the anesthesia with 2 % isoflurane with appropriate adjustment of the concentration. Remove the abdominal hair with hair removal cream. Place the mouse on the operating table in the supine position. Sterilize the abdomen with 70 % ethanol. Make a skin incision of approximately 2.5 cm along the midline and cut the abdominal wall along the linea alba to open the peritoneal cavity (Fig. 10.3).

Using a cotton swab, displace the intestine to the upper right side in the peritoneal cavity to expose the right kidney, inferior vena cava (IVC), and left renal vein (Fig. 10.4). Pay attention not to injure the liver. Put a piece of cotton (1.5×1.0 cm) into the upper and left sides of the abdominal cavity to keep the intestine outside of the operating field. Expose the IVC from the level of the left renal vein to the iliac bifurcation. Aortic beats should be visible on the right side of the IVC. Find two thin blood vessels running in the retroperitoneum in front of the aorta (Figs. 10.4 and 10.5, arrowheads). Using microsurgery forceps, carefully tear

Fig. 10.3 Skin and peritoneal incisions

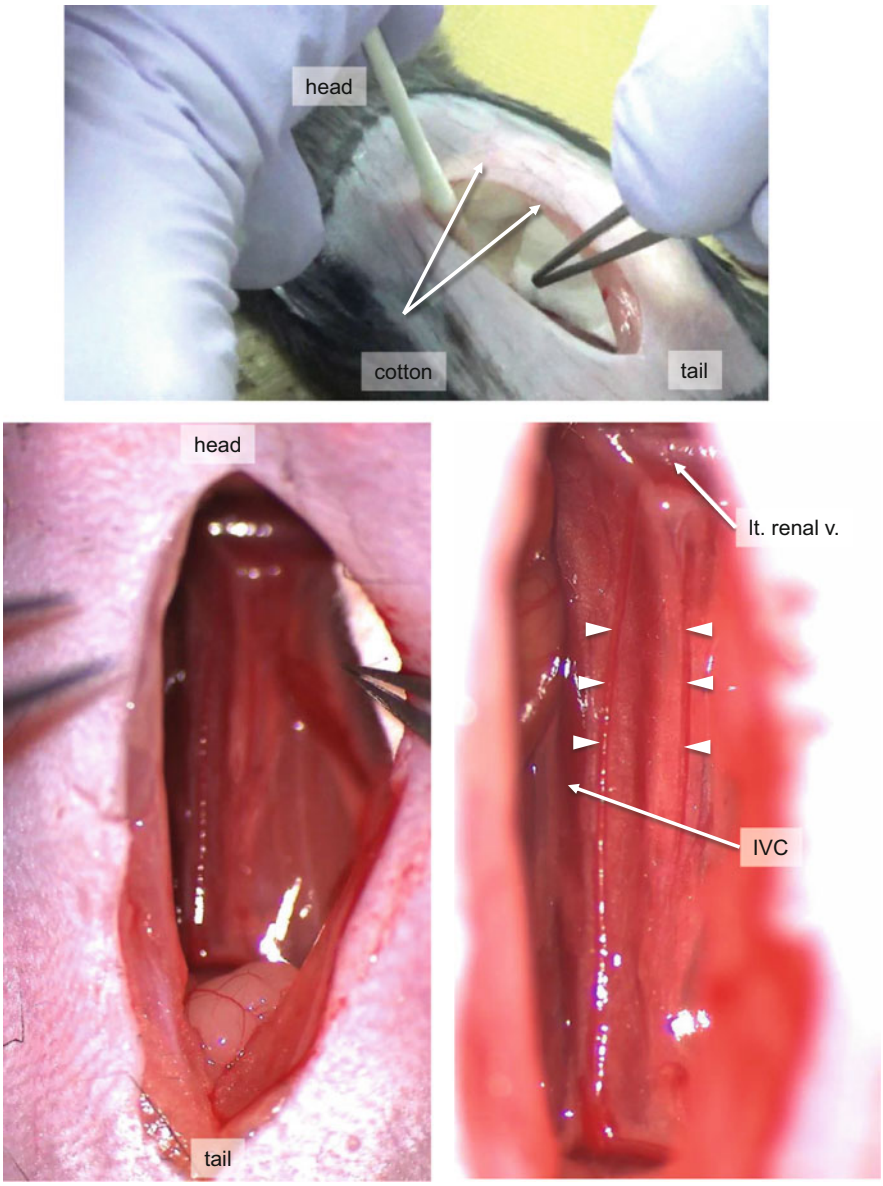

Fig. 10.4 Securing of the operating field

the retroperitoneum covering the aorta between these vessels from the level of the left renal vein to the iliac bifurcation. Then, displace the loose connective tissue covering the aorta (Fig. 10.6). Avoid damaging the blood vessels as it can cause operational death from major bleeding.

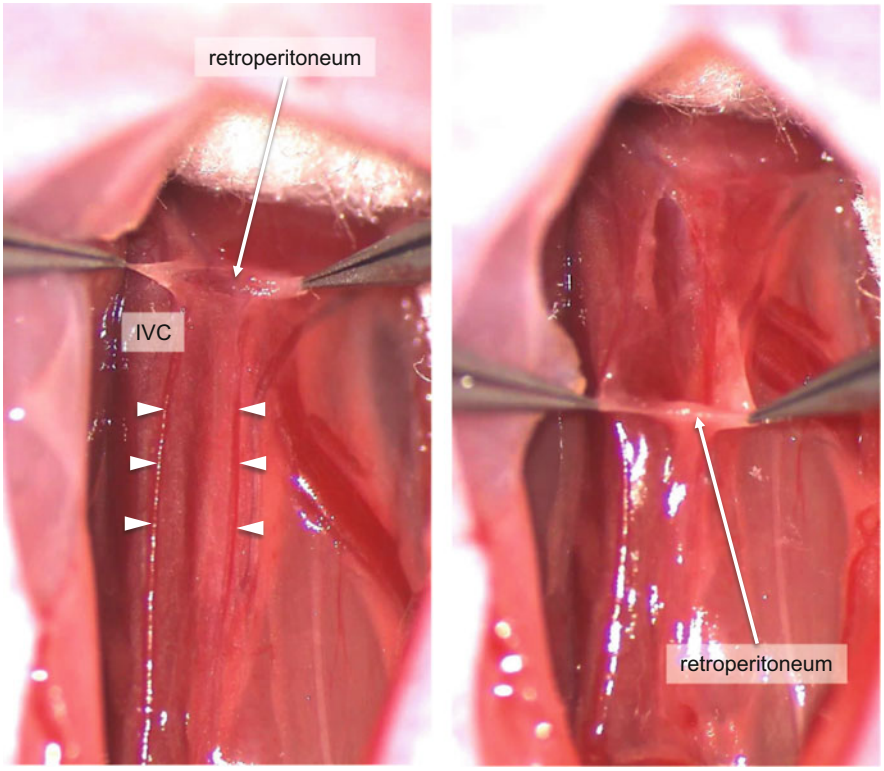

Fig. 10.5 Tearing the retroperitoneum

While gently holding the connective tissue (not aortic wall) on the left side of the midline of the aorta with microsurgery forceps, displace the aorta with slight rotation to the right side to expose the left surface of the aorta (Fig. 10.7). While keeping the aorta displaced, gently tear off the connective tissues and adipose tissues from the left and the back sides of the aorta using microsurgery forceps. Then, repeat the same procedure to expose the right surface of the aorta. The left renal vein sometimes runs close to the aorta. Remove it from the aorta by holding the surrounding connective tissue without touching the veins. It is easy to separate the aorta from the IVC between the level of the left renal vein and the midpoint to the iliac bifurcation. Avoid forceful separation of the lower half of the infrarenal aorta from the IVC, as this portion is packed in thick connective tissue. Pay attention not to injure the lumbar arteries and veins running toward the back.

After adequate removal of the connective tissue surrounding the aorta, gently lift the aorta to see if the IVC can be seen from the right side through the thin connective tissue underneath (Fig. 10.8). After isolating the aorta, wipe off the exudate with a cotton swab. Immerse small pieces of cotton (1×3–4 mm) in 200 μL of 0.5 M $CaCl_2$ solution (Fig. 10.9) and pack them around the isolated

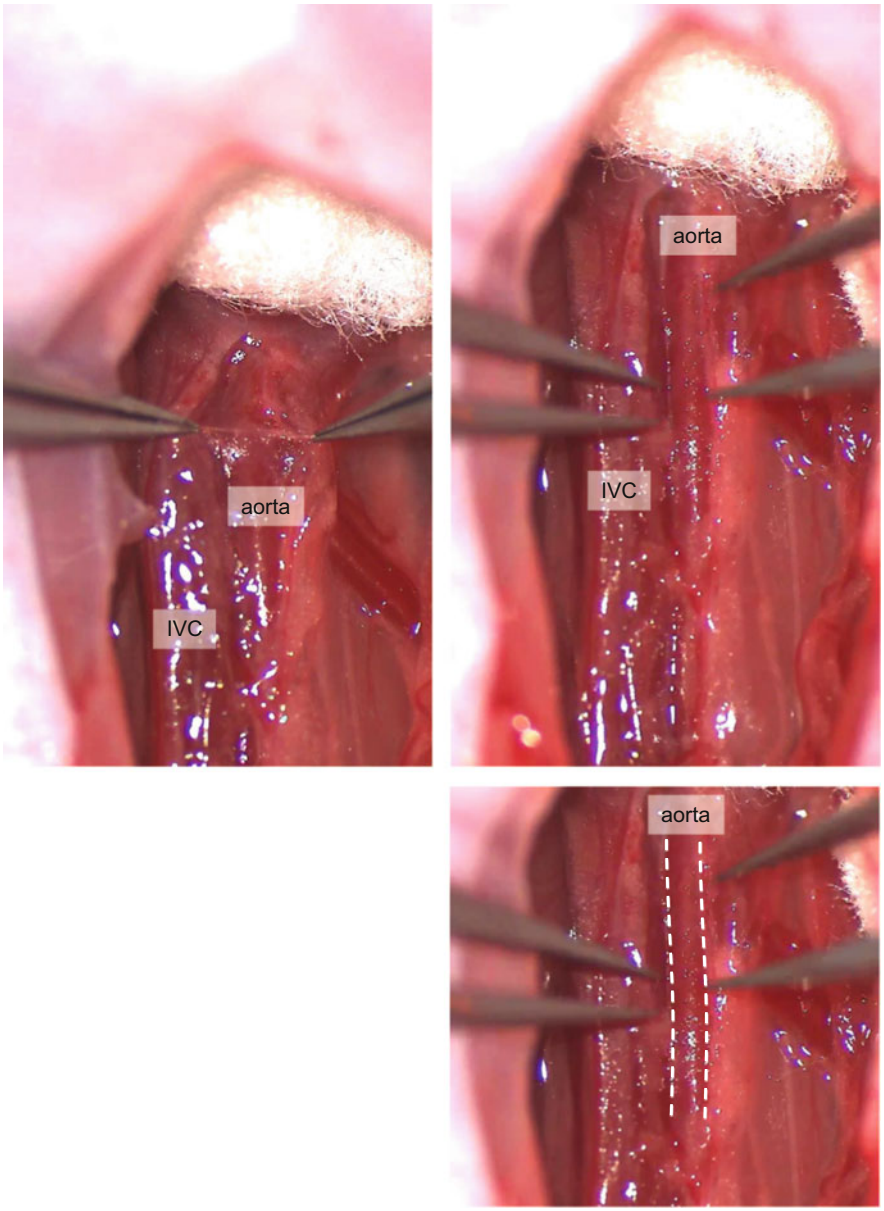

Fig. 10.6 Clearing the connective tissue covering the aorta. *Dashed lines* indicate the aorta

aorta. First, pack the cotton in the back of the aorta, then on the right and left sides, and finally on the front. Pile the $CaCl_2$-soaked large pieces of cotton (2×5 mm) on the aorta in the cavity, which was formed by cutting the retroperitoneum, to a height of approximately 5 mm (Fig. 10.10). Use the entire 200 μL of $CaCl_2$ solution to

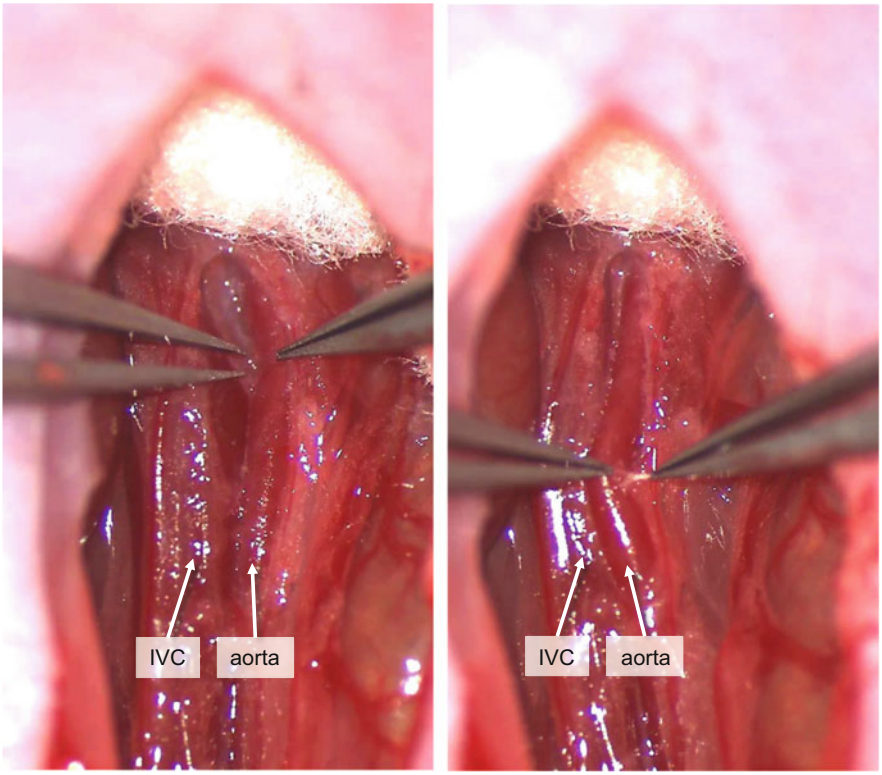

Fig. 10.7 Clearing the left and right sides of the aorta

soak the cotton pieces that are packed around the aorta. Start a timer for 20 min. After the 20 min waiting time, remove all of the cotton surrounding the aorta. Gently wipe the peritoneal and retroperitoneal cavities with a piece of saline-soaked cotton. Remove the two pieces of cotton used to displace the organs. Close the incision of the retroperitoneum and place the organs back to their original positions. Suture the abdominal wall with a continuous suture using 5-0 nylon thread (Fig. 10.11).

10.5 Analysis of the Aortic Aneurysm Model

10.5.1 Perfusion Fixation

Euthanize the animals by intraperitoneal administration of an overdose of pentobarbital. After the thoracotomy, insert a thin plastic cannula, such as the outer catheter of Angiocath™, into the left ventricle of the heart from the apex. Perfuse

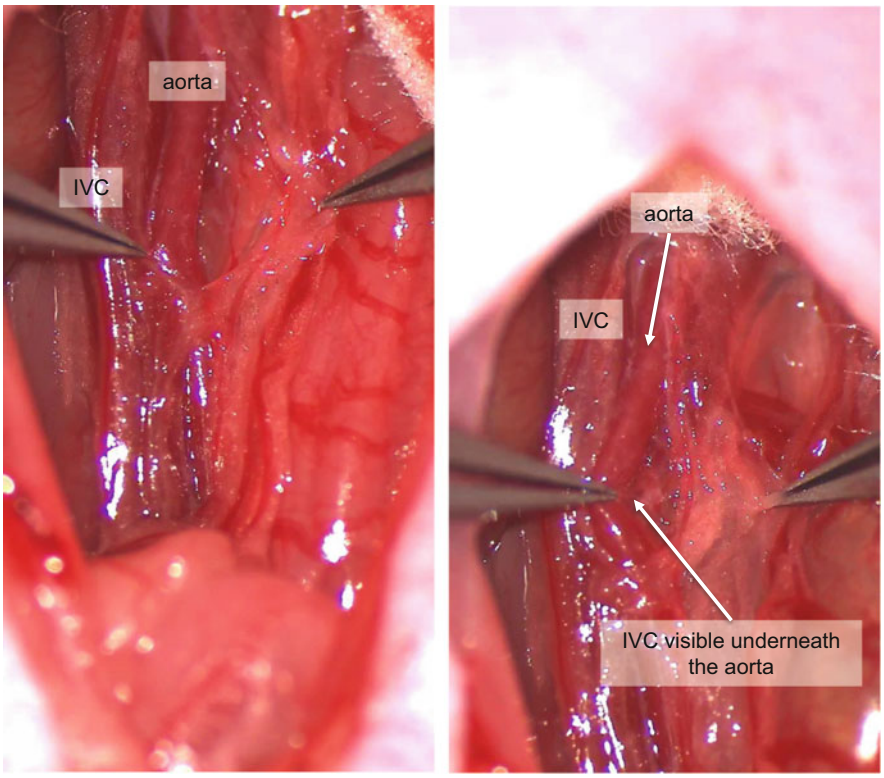

Fig. 10.8 Isolation of the aorta

the animal with PBS at physiological pressure (approximately 80 cm H_2O) using an infusion set. Drain the blood by cutting the free wall of the right atrium. After draining all blood by perfusion, which is indicated by the clear draining fluid from the right atrium, switch the perfusion fluid to 4 % PFA in PBS and continue the perfusion with approximately 2–3 mL to fix the tissue.

10.5.2 Excision of the Aorta

After the perfusion fixation, open the abdominal cavity to excise the abdominal aorta under the stereomicroscope using forceps and fine scissors. Care should be taken not to damage the aortic wall that shows fibrous adhesion to the periaortic tissue because of the inflammation from the aortic aneurysm induced by $CaCl_2$. Stick the excised abdominal aorta to the rubber plate with extra-thin pins. Clear the aorta from the periaortic fibrous tissue under the stereomicroscope using microsurgery forceps and spring scissors. Remove all of the loose connective tissue for accurate morphometry.

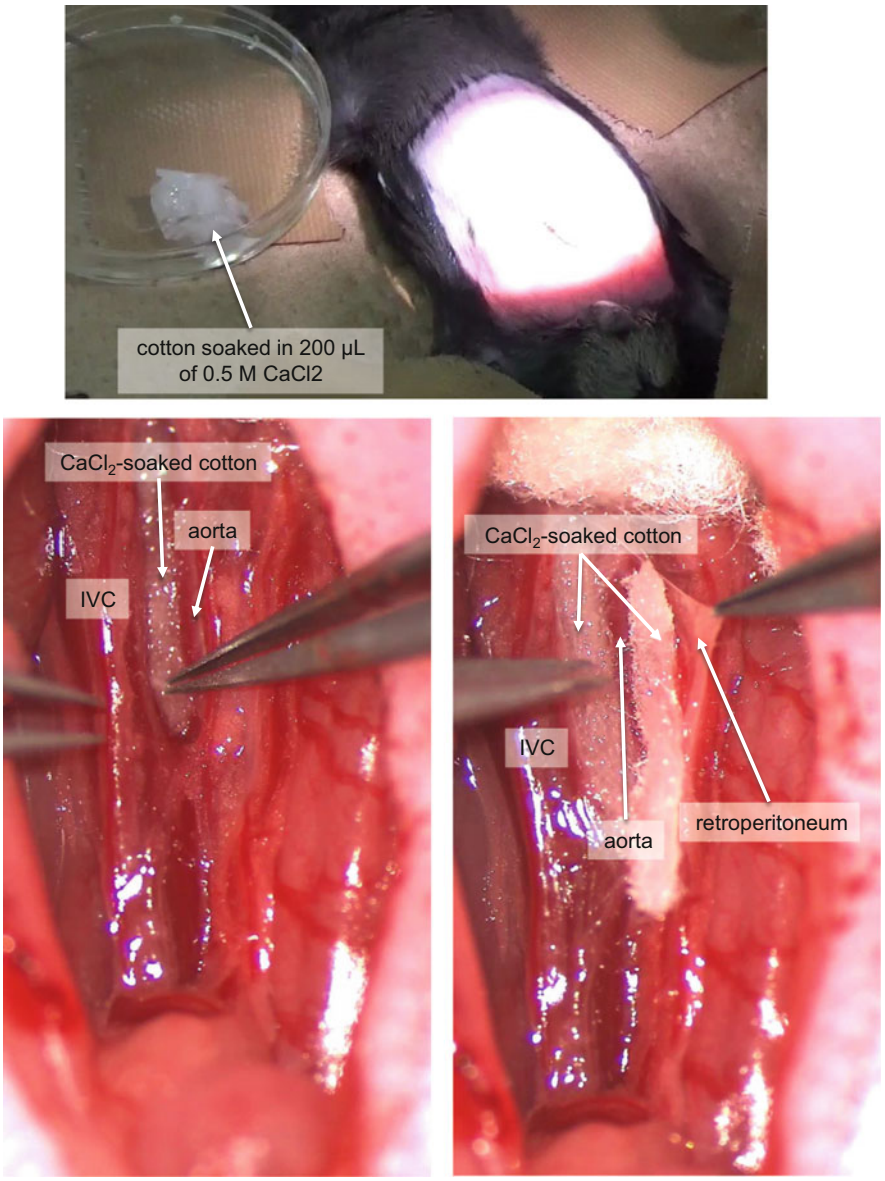

Fig. 10.9 Packing of the $CaCl_2$-soaked cotton

10.5.3 Morphometry

For the morphometry, prepare a plastic dish, such as a 100 mm cell culture plate, with a black rubber plate attached to the bottom. Fill the dish with PBS. Stick the

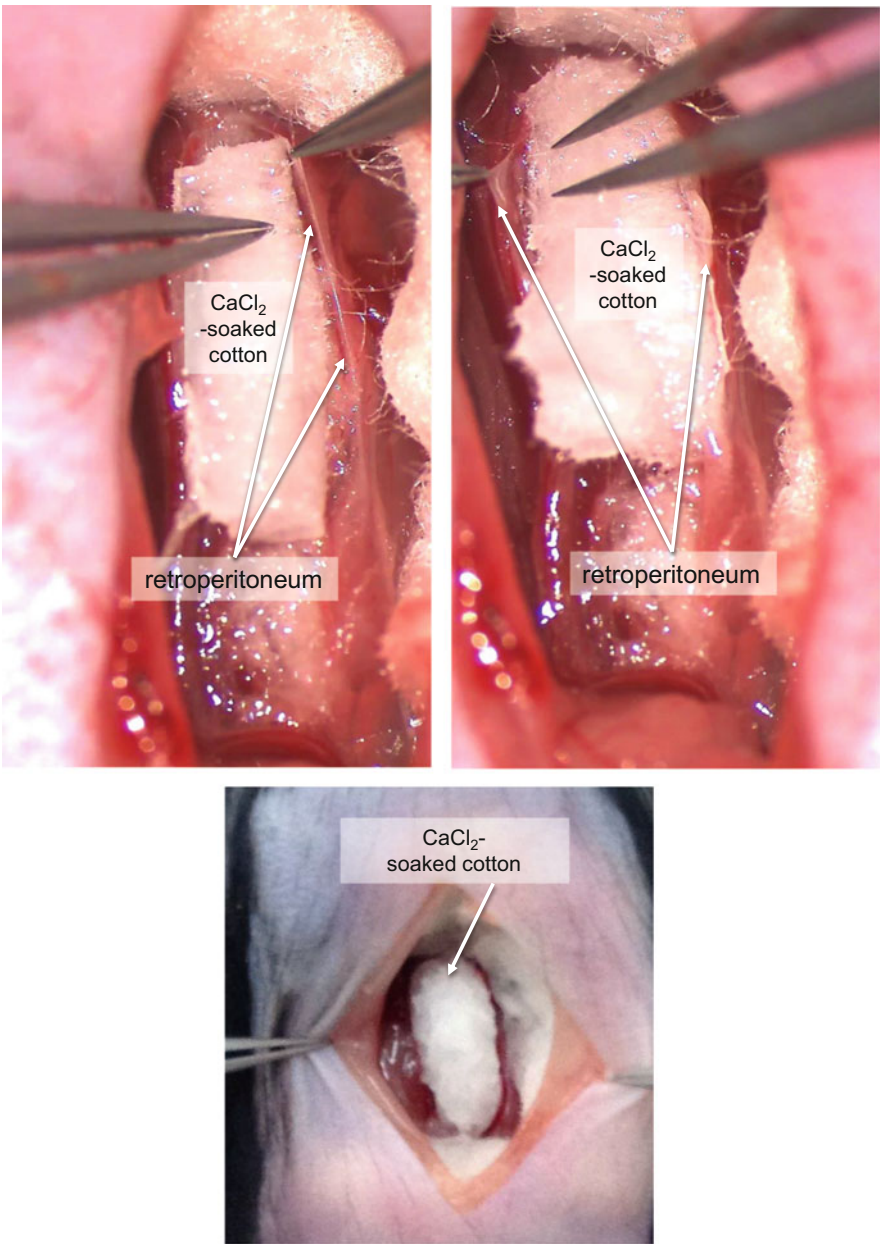

Fig. 10.10 The $CaCl_2$ treatment

aorta to the black rubber plate with extra-thin pins. Place the scale along the aorta. Take pictures of the aorta using the digital camera attached to the stereomicroscope under appropriate illumination from the fiber optic illuminator to avoid unwanted shadows. Perform the morphometric analysis using image analysis software on the

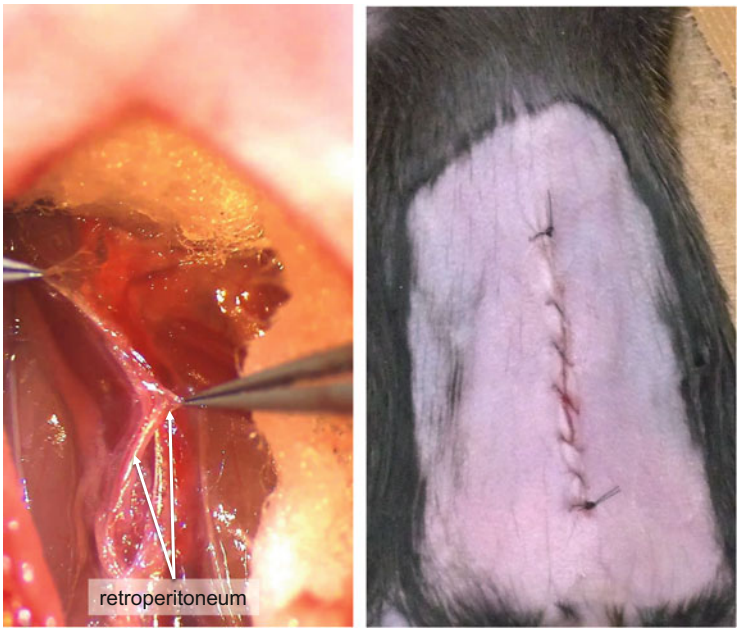

Fig. 10.11 Closing the retroperitoneum and the skin incision

photographs that are calibrated with the scale. A digital imaging system such as Leica M165 C equipped with a calibrated digital camera and PC would be convenient for recording the images and the morphometry.

10.5.4 Histological Analysis

Fix the aorta in 4 % PFA in PBS overnight at 4 °C, followed by 70 % ethanol for at least 1 day before paraffin embedding and sectioning. Alternatively, the aorta may be embedded into Tissue-Tek O.C.T. Compound™ (Sakura Finetek Japan Co., Japan) for cryosectioning. After sectioning, use standard histochemical stains, such as hematoxylin and eosin and Elastica van Gieson (Fig. 10.1). For further analysis, immunostainings may be performed.

10.5.5 Expression of Genes and Proteins

For the expression analyses of genes and proteins, perfusion should be done without PFA or other fixatives, and the tissue should be processed according to the purpose. For mRNA analysis, the tissue may be immersed into an RNA-preserving reagent

such as RNAlater® or snap-frozen in liquid nitrogen for later RNA extraction. For protein analysis, the tissue is snap-frozen in liquid nitrogen. Pulverize the frozen tissue using a homogenizer such as SK-100 (Token Co., Japan), and extract the proteins with an appropriate lysis buffer.

References

1. Curci JA, Baxter BT, Thompson RW. Arterial aneurysms: etiologic considerations. In: Rutherford RB, editor. Vascular surgery. 6th ed. Philadelphia: Saunders; 2005. p. 475–92.
2. Powell J. Models of arterial aneurysm: for the investigation of pathogenesis and pharmacotherapy – a review. Atherosclerosis. [Review]. 1991;87(2–3):93–102.
3. Trollope A, Moxon JV, Moran CS, Golledge J. Animal models of abdominal aortic aneurysm and their role in furthering management of human disease. Cardiovasc Pathol. [Review]. 2011;20(2):114–23.
4. Chiou AC, Bill MPH, Chiu BS, Pearce WH. Murine aortic aneurysm produced by periarterial application of calcium chloride. J Surg Res. 2001;99:371–6.
5. Longo GM, Xiong W, Greiner TC, Zhao Y, Fiotti N, Baxter BT. Matrix metalloproteinases 2 and 9 work in concert to produce aortic aneurysms. J Clin Invest. 2002;110(5):625–32.
6. Yoshimura K, Aoki H, Ikeda Y, Fujii K, Akiyama N, Furutani A, et al. Regression of abdominal aortic aneurysm by inhibition of c-Jun N-terminal kinase. Nat Med. 2005;11(12):1330–8.
7. Miyake T, Aoki M, Masaki H, Kawasaki T, Oishi M, Kataoka K, et al. Regression of abdominal aortic aneurysms by simultaneous inhibition of nuclear factor kappaB and ets in a rabbit model. Circ Res. 2007;101(11):1175–84.

Chapter 11
Mouse Models of Aortic Aneurysm

Miyuki Kanematsu, Yasuhisa Kanematsu, and Tomoki Hashimoto

Abstract A combination of pharmacologically induced hypertension and degeneration of elastic lamina by lysyl oxidase inhibition can cause aneurysm formations at two aneurysm-prone regions of the aorta. This model with or without modification has been successfully used to study pathophysiology of aortic aneurysms. Phenotypic differences between thoracic and abdominal aortic aneurysms in this model may indicate that different pharmacological strategies may be needed to prevent growth and rupture of aneurysms at these two different locations.

Keywords Aortic aneurysm • Hypertension • Animal model • Aneurysm

11.1 Introduction

Rupture of aortic aneurysm results in severe mortality and morbidity. Surgical or endovascular intervention for unruptured aortic aneurysms is to prevent future rupture. However, these procedures still carry significant risks of adverse events. Therefore, pharmacological stabilization of aneurysms that prevents growth and rupture of aortic aneurysms has been proposed [1]. In order to develop such strategy, an animal model that recapitulates key features of human aortic aneurysms is extremely useful.

There is a close association between systemic hypertension and aortic aneurysm formations in humans [2, 3]. In addition, degeneration and disorganization of elastic lamina are characteristic histological changes observed in both thoracic and abdominal aortic aneurysms [4, 5]. Incidence of aortic aneurysms increases with age

M. Kanematsu, M.D.
Department of Surgery, National Hospital Organization Shikoku Medical Center for Children and Adults, Tokushima, Japan

Y. Kanematsu, M.D., Ph.D.
The Department of Neurosurgery (YT, KS, KTK, SN.), School of Medicine, The University of Tokushima, Tokushima, Japan

T. Hashimoto, M.D. (✉)
Department of Anesthesia and Perioperative Care, University of California, 1001 Potrero Avenue, No. 3C-38, San Francisco, CA 94110, USA
e-mail: hashimot@anesthesia.ucsf.edu

M. Sata (ed.), *Mouse Models of Vascular Diseases*,
DOI 10.1007/978-4-431-55813-2_11

[6, 7]. Aging-related degeneration of elastic lamina mat represents a precursory change that precedes aneurysm formation [8].

In animals, degeneration of elastic lamina can be induced by administration of beta-aminopropionitrile (BAPN), an inhibitor of lysyl oxidase [9]. Lysyl oxidase cross-links elastin fibers and collagen fibers. While aging decreases lysyl oxidase activity in humans [10], BAPN is considered as a lathyrogen because its effects closely mimic human aging [11].

11.2 Animal Model

We combined hypertension and degeneration of elastic lamina by lysyl oxidase inhibitor, BAPN, to induce thoracic and abdominal aortic aneurysms in mice [12]. This model has been successfully used by multiple independent groups with or without modifications [13–19].

In this model, hypertension can be induced by two well-established methods of pharmacologically induced hypertension—angiotensin-II-induced hypertension and deoxycorticosterone acetate (DOCA)-salt hypertension. BAPN (150 mg/kg/day), a lysyl oxidase inhibitor, can be administered for the first 2 weeks through a subcutaneously implanted osmotic pump (Alzet, Durect Corp).

Figure 11.1 shows representative aortic aneurysms from this model. Aortic aneurysms in this model develop at the ascending thoracic aorta and abdominal

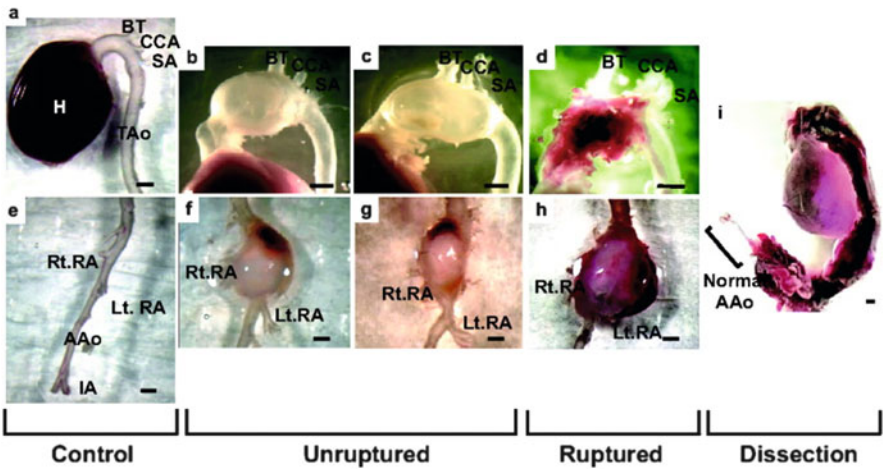

Fig. 11.1 Representative aortic aneurysms. Macroscopically, thoracic and abdominal aortic aneurysms in this model resembled human aortic aneurysms with their site-specific morphology. Thoracic aortic aneurysms were saccular-shaped with localized dilation at the great curvature, while abdominal aortic aneurysms were fusiform-shaped aneurysms with a thick vascular wall. (**a**) normal thoracic aorta; (**b**, **c**) unruptured thoracic aortic aneurysm; (**d**) ruptured thoracic aortic aneurysm; (**e**) normal abdominal aorta; (**f**, **g**) unruptured abdominal aortic aneurysm; (**h**) ruptured abdominal aortic aneurysm; (**i**) dissecting aortic aneurysm. Scale bar: 1 mm (This figure is reproduced with permission from the publisher (Kanematsu and Kanematsu [12]))

aorta, the two locations where most human aortic aneurysms can be found [7, 12]. In addition, thoracic and abdominal aortic aneurysms in this model show site-specific morphological and histological characteristics [12]. Another key advantage of this new model is the use of wild-type mice, which makes it easier to examine roles of different signaling pathways compared to using knockout and transgenic mice.

Using this study, we showed that the combination of hypertension and degeneration of elastic lamina by lysyl oxidase inhibition in mice resulted in formation of aortic aneurysms that recapitulate key features of human aortic aneurysms with site-specific phenotypes. In addition, we showed critical roles of high blood pressure in the formation of aortic aneurysms, establishing a causal link between hemodynamic conditions and aortic aneurysm formation in animals.

Daugherty et al. developed an abdominal aortic aneurysm model in genetically atherosclerosis-prone mice by continuously infusing angiotensin-II [20, 21]. In their angiotensin-II-induced aortic aneurysm model, apolipoprotein E (ApoE)-knockout mice or fat-fed low-density lipoprotein (LDL) receptor knockout mice was used [20, 21]. Morphological and histological characteristics of angiotensin-II-induced abdominal aortic aneurysms in these knockout mice were similar to the abdominal aortic aneurysms in our model, indicating that common molecular mechanisms potentially exist between these two models in respect to abdominal aortic aneurysms. Interestingly, angiotensin-II infusion in ApoE-knockout or LDL receptor knockout mice did not cause thoracic aortic aneurysm [20, 21]. In contrast, aneurysm formation in our model occurred not only in the abdominal aorta but also in the thoracic aorta involving the ascending aorta.

Direct application of calcium chloride to the descending thoracic aorta through thoracotomy can cause aneurysmal formation in the aortic segment that was exposed to calcium chloride [22]. The advantage of the calcium application model is that aneurysmal dilatation occurred in almost all animals [22]. However, the aneurysmal dilatation in their model was mild, i.e., 25 % dilatation comparing to 50 % in our model. More importantly, in our model, both abdominal and thoracic aneurysms were induced by the same pharmacological treatments. Our model may be more suitable for studying differential underlying mechanisms and treatment strategies between thoracic and abdominal aortic aneurysms.

In our model, the aneurysms at the two aneurysm-prone regions were induced by the same systemic pharmacological treatment. However, they exhibited different morphological and histological features that closely resembled human aortic aneurysms at the respective locations. Morphological and histological differences observed between thoracic and abdominal aortic aneurysms in this model may suggest that differential responses to the combination of hypertension and lysyl oxidase inhibition at these two regions of the aorta lead to different phenotypes of aneurysms.

Morphological and histological differences between thoracic and abdominal aortas in this model and in humans may be due to the differences in developmental origins of smooth muscle cells [23, 24]. Embryologically programmed differences of vascular smooth muscle cells may determine the site-specific phenotypes of

aneurysms at the two regions [23–25]. More importantly, different pharmacological strategies may be needed to prevent growth and rupture of aneurysms at these two different locations.

Interestingly, normalization of blood pressure by an antihypertensive agent dramatically reduced the incidence of aneurysms and almost completely abolished histological changes associated with angiotensin-II and BAPN treatment in this model. We were able to reproduce thoracic and abdominal aortic aneurysms when DOCA-salt hypertension was used. Captopril did not reduce the incidence of aortic aneurysm in DOCA-salt-hypertensive mice, further suggesting critical roles of hypertension in this model.

It should be noted that although our mouse model replicated key features of thoracic and abdominal aortic aneurysms in humans, aneurysms in this model did not form spontaneously but were induced by two pharmacological interventions, which potentially bypassed some of the early critical events that lead to aortic aneurysm in humans.

11.3 Conclusions

A combination of pharmacologically induced hypertension and degeneration of elastic lamina by lysyl oxidase inhibition can cause aneurysm formations at two aneurysm-prone regions of aorta. Using this model, we established critical roles of hypertension in the formation of aortic aneurysms. Phenotypic differences between thoracic and abdominal aortic aneurysms in this model may indicate that different pharmacological strategies may be needed to prevent growth and rupture of aneurysms at these two different locations.

Sources of Funding The project described was supported by R01NS055876 (TH) and R01NS082280 (TH) from the National Institute of Neurological Disorders and Stroke (NIH/NINDS).

Disclosures No conflicts.

References

1. Axisa B, Loftus IM, Naylor AR, Goodall S, Jones L, Bell PR, Thompson MM. Prospective, randomized, double-blind trial investigating the effect of doxycycline on matrix metalloproteinase expression within atherosclerotic carotid plaques. Stroke. 2002;33 (12):2858–64. PubMed.
2. Dapunt OE, Galla JD, Sadeghi AM, Lansman SL, Mezrow CK, de Asla RA, Quintana C, Wallenstein S, Ergin AM, Griepp RB. The natural history of thoracic aortic aneurysms. J Thorac Cardiovasc Surg. 1994;107(5):1323–32; discussion 32–3. PubMed.

3. Lederle FA, Johnson GR, Wilson SE, Chute EP, Littooy FN, Bandyk D, Krupski WC, Barone GW, Acher CW, Ballard DJ. Prevalence and associations of abdominal aortic aneurysm detected through screening. Aneurysm Detection and Management (ADAM) Veterans Affairs Cooperative Study Group. Ann Intern Med. 1997;126(6):441–9. PubMed.
4. Tang PC, Coady MA, Lovoulos C, Dardik A, Aslan M, Elefteriades JA, Tellides G. Hyperplastic cellular remodeling of the media in ascending thoracic aortic aneurysms. Circulation. 2005;112(8):1098–105. PubMed.
5. Lopez-Candales A, Holmes DR, Liao S, Scott MJ, Wickline SA, Thompson RW. Decreased vascular smooth muscle cell density in medial degeneration of human abdominal aortic aneurysms. Am J Pathol. 1997;150(3):993–1007. Epub 1997/03/01. PubMed PMID: 9060837; PMCID: 1857880.
6. Albornoz G, Coady MA, Roberts M, Davies RR, Tranquilli M, Rizzo JA, Elefteriades JA. Familial thoracic aortic aneurysms and dissections--incidence, modes of inheritance, and phenotypic patterns. Ann Thorac Surg. 2006;82(4):1400–5. Epub 2006/09/26. doi: S0003-4975(06)01020-4 [pii] 10.1016/j.athoracsur.2006.04.098. PubMed.
7. Isselbacher EM. Thoracic and abdominal aortic aneurysms. Circulation. 2005;111(6):816–28. Epub 2005/02/16. doi: 111/6/816 [pii] 10.1161/01.CIR.0000154569.08857.7A. PubMed.
8. Schlatmann TJ, Becker AE. Histologic changes in the normal aging aorta: implications for dissecting aortic aneurysm. Am J Cardiol. 1977;39(1):13–20. PubMed.
9. McCallum HM. Experimental lathyrism in mice. J Pathol Bacteriol. 1965;89:625–36. PubMed.
10. Behmoaras J, Slove S, Seve S, Vranckx R, Sommer P, Jacob MP. Differential expression of lysyl oxidases LOXL1 and LOX during growth and aging suggests specific roles in elastin and collagen fiber remodeling in rat aorta. Rejuvenation Res. 2008;11(5):883–9. PubMed.
11. Davies I, Schofield JD. Connective tissue ageing: the influence of a lathyrogen (beta-aminopropionitrile) on the life span of female C57BL/Icrfat mice. Exp Gerontol. 1980;15(5):487–94. PubMed.
12. Kanematsu Y, Kanematsu M, Kurihara C, Tsou TL, Nuki Y, Liang EI, Makino H, Hashimoto T. Pharmacologically induced thoracic and abdominal aortic aneurysms in mice. hypertension. 2010;55(5):1267–74. Epub 2010/03/10. doi: HYPERTENSIONAHA.109.140558 [pii] 10.1161/HYPERTENSIONAHA.109.140558. PubMed PMID: 20212272; PMCID: PMC2859958.
13. Remus EW, O'Donnell RE, Jr., Rafferty K, Weiss D, Joseph G, Csiszar K, Fong SF, Taylor WR. The role of lysyl oxidase family members in the stabilization of abdominal aortic aneurysms. Am J Physiol Heart Circ Physiol. 2012;303(8):H1067–75. doi: 10.1152/ajpheart.00217.2012. PubMed PMID: 22904155; PMCID: 3469640.
14. Kurihara T, Shimizu-Hirota R, Shimoda M, Adachi T, Shimizu H, Weiss SJ, Itoh H, Hori S, Aikawa N, Okada Y. Neutrophil-derived matrix metalloproteinase 9 triggers acute aortic dissection. Circulation. 2012;126(25):3070–80. doi:10.1161/CIRCULATIONAHA.112.097097. PubMed.
15. Kurobe H, Hirata Y, Matsuoka Y, Sugasawa N, Higashida M, Nakayama T, Maxfield MW, Yoshida Y, Shimabukuro M, Kitagawa T, Sata M. Protective effects of selective mineralocorticoid receptor antagonist against aortic aneurysm progression in a novel murine model. J Surg Res. 2013;185(1):455–62. doi:10.1016/j.jss.2013.05.002. PubMed.
16. Kurobe H, Matsuoka Y, Hirata Y, Sugasawa N, Maxfield MW, Sata M, Kitagawa T. Azelnidipine suppresses the progression of aortic aneurysm in wild mice model through anti-inflammatory effects. J Thorac Cardiovasc Surg. 2013;146(6):1501–8. doi:10.1016/j.jtcvs.2013.02.073. PubMed.
17. Takayanagi T, Crawford KJ, Kobayashi T, Obama T, Tsuji T, Elliott KJ, Hashimoto T, Rizzo V, Eguchi S. Caveolin 1 is critical for abdominal aortic aneurysm formation induced by angiotensin II and inhibition of lysyl oxidase. Clinical science. 2014;126(11):785–94. doi: 10.1042/CS20130660. PubMed PMID: 24329494; PMCID: 4019733.

18. Obama T, Tsuji T, Kobayashi T, Fukuda Y, Takayanagi T, Taro Y, Kawai T, Forrester SJ, Elliott KJ, Choi E, Daugherty A, Rizzo V, Eguchi S. Epidermal growth factor receptor inhibitor protects against abdominal aortic aneurysm in a mouse model. Clin Sci. 2015;128 (9):559–65. doi:10.1042/CS20140696. PubMed.
19. Anzai A, Shimoda M, Endo J, Kohno T, Katsumata Y, Matsuhashi T, Yamamoto T, Ito K, Yan X, Shirakawa K, Shimizu-Hirota R, Yamada Y, Ueha S, Shinmura K, Okada Y, Fukuda K, Sano M. Adventitial CXCL1/G-CSF expression in response to acute aortic dissection triggers local neutrophil recruitment and activation leading to aortic rupture. Circ Res. 2015;116(4):612–23. doi:10.1161/CIRCRESAHA.116.304918. PubMed.
20. Daugherty A, Manning MW, Cassis LA. Angiotensin II promotes atherosclerotic lesions and aneurysms in apolipoprotein E-deficient mice. J Clin Invest. 2000;105(11):1605–12. PubMed.
21. Daugherty A, Cassis L. Chronic angiotensin II infusion promotes atherogenesis in low density lipoprotein receptor −/− mice. Ann N Y Acad Sci. 1999;892:108–18. Epub 2000/06/08. PubMed.
22. Ikonomidis JS, Gibson WC, Gardner J, Sweterlitsch S, Thompson RP, Mukherjee R, Spinale FG. A murine model of thoracic aortic aneurysms. J Surg Res. 2003;115(1):157–63. Epub 2003/10/24. doi: S0022480403001938 [pii]. PubMed.
23. Guo DC, Papke CL, He R, Milewicz DM. Pathogenesis of thoracic and abdominal aortic aneurysms. Ann N Y Acad Sci. 2006;1085:339–52. PubMed.
24. Saraff K, Babamusta F, Cassis LA, Daugherty A. Aortic dissection precedes formation of aneurysms and atherosclerosis in angiotensin II-infused, apolipoprotein E-deficient mice. Arterioscler Thromb Vasc Biol. 2003;23(9):1621–6. PubMed.
25. Majesky MW. Developmental basis of vascular smooth muscle diversity. Arterioscler Thromb Vasc Biol. 2007;27(6):1248–58. PubMed.

Part VI
Intracranial Aneurysm Models

Chapter 12
Technical Aspects of Mouse Intracranial Aneurysm Model

Yoshiteru Tada, Masaaki Korai, and Tomoki Hashimoto

Abstract Subarachnoid hemorrhage caused by the rupture of intracranial aneurysms results in catastrophic consequences with high morbidity and mortality. Mouse models of intracranial aneurysm help to improve our understanding of mechanisms for aneurysmal formation and rupture. Intracranial aneurysms can be induced by a combination of hypertension and a single injection of elastase into the cerebrospinal fluid in mice. In this model, subarachnoid hemorrhage due to aneurysmal rupture can be detected by a daily neurological examination. Our model will allow a better understanding of mechanisms of aneurysmal formation and rupture. Studies on the efficacy of pharmacological treatment on aneurysms are now conceivable to prevent aneurysmal rupture.

Keywords Intracranial aneurysm • Mouse • Hypertension

12.1 Introduction

Subarachnoid hemorrhage (SAH) due to the rupture of intracranial aneurysms carries a high mortality rate [1]. Endovascular or intracranial surgery (coiling or clipping) is performed to prevent their rupture. However, the morbidity and mortality associated with coiling and clipping of the aneurysms are not negligible. To establish pharmacological treatment for aneurysmal rupture, animal model of aneurysmal rupture is required.

Considering (1) the increasing detection rate of unruptured aneurysms, (2) the improved but still non-negligible adverse outcome rate associated with the coiling or clipping of unruptured aneurysm, (3) the high cost of these technically intensive

Y. Tada, M.D., Ph.D. • M. Korai, M.D.
Department of Anesthesia and Perioperative Care, University of California, 1001 Potrero Avenue, No. 3C-38, San Francisco, CA 94110, USA

Department of Neurosurgery, Institute of Biomedical Sciences, Tokushima University, Tokushima, Japan

T. Hashimoto, M.D. (✉)
Department of Anesthesia and Perioperative Care, University of California, 1001 Potrero Avenue, No. 3C-38, San Francisco, CA 94110, USA
e-mail: tomoki.hashimoto@ucsf.edu

M. Sata (ed.), *Mouse Models of Vascular Diseases*,
DOI 10.1007/978-4-431-55813-2_12

invasive therapies, and (4) the limited treatment options for patients with giant aneurysms, pharmacological techniques to stabilize aneurysms for the prevention of aneurysmal rupture may be an attractive alternative approach. Our proposal represents a unique effort to develop a strategy of pharmacological stabilization of intracranial aneurysms for the prevention of aneurysmal rupture.

Although many previous studies focused on the mechanisms of the formation of intracranial aneurysms, there is a paucity of studies that directly investigates the mechanisms of aneurysmal rupture or the pharmacological prevention of aneurysmal rupture. This paucity is primarily due to the lack of a suitable animal model in which aneurysmal rupture occurs spontaneously with a predictable time course and at a predictable rate. It has often been assumed that understanding the mechanisms of aneurysmal formation and growth provides insights into the mechanisms of aneurysmal rupture. This notion is based on an assumption that the processes of aneurysmal formation, growth, and rupture share the same or similar underlying mechanisms. However, there is no clear basis for such an assumption. Mechanisms of aneurysmal rupture may be fundamentally different from those of formation and growth.

We have developed a mouse model of intracranial aneurysm that recapitulates the key features of intracranial aneurysms, including spontaneous rupture [2–4]. A subarachnoid hemorrhage as a result of aneurysmal rupture causes neurological symptoms in this model [4]. Furthermore, the neurological symptoms associated with aneurysmal rupture can be easily detected with a simple neurological examination [4]. Our innovative animal model allows us to directly study the mechanisms of aneurysmal rupture. This model with or without modifications has been successfully used by multiple independent groups in mice and rats [3–11]. In this article, we described surgical techniques that are critical for the successful application of this model.

12.2 Description of the Model

Intracranial aneurysms were induced in 8- to 10-week-old male mice (C57BL/6J; Jackson Laboratory) and 10- to 12-week-old female mice. We combined systemic hypertension and a single injection of elastase in the cerebrospinal fluid at the right basal cistern to induce intracranial aneurysms.

12.3 Deoxycorticosterone Acetate (DOCA)-Salt Hypertension

To induce systemic hypertension, we used deoxycorticosterone acetate (DOCA)-salt hypertension. Mice underwent unilateral nephrectomy followed by an implantation of DOCA pellet 1 week later; 1 % NaCl drinking water was given on the same day as DOCA pellet implantation. To perform unilateral nephrectomy, anesthetized mouse is placed in the right lateral position. The mouse kidney is located retroperitoneally and approximately 1 cm caudal to the twelfth ribs. A short skin and abdominal muscle incisions are made. The left kidney is freed from the surrounding tissue and pulled out of the incision. The kidney should be isolated by dividing the adrenal gland with a sterile suture. The sterile suture is gently ligated around the renal vessels and ureter. The kidney is removed by incising as close as the ligature. The abdominal muscle and skin incisions are closed with suture. DOCA pellet should be placed on the opposite site to the nephrectomy site. The alternative way to induce hypertension is angiotensin II-induced hypertension as we previously described [2, 12].

12.4 Stereotaxic Injection of Elastase

The mouse is fixed in the stereotaxic frame with mouse adaptor (World Precision Instruments) to inject elastase (0–35 milliunits) into the cerebrospinal fluid at the right basal cistern using a 26-gauge needle (10 uL syringe Model 701 with 26 g 2-in. Hamilton Replacement needle Point style 3, Fisher Scientific) to disrupt elastic lamina. Mice received a single injection of elastase on the same day as DOCA implantation. Replacement of the tip of the needle was stereotaxically placed in the right basal cistern using the coordinates obtained from Mouse Brain Atlas (2.5 mm posterior to the bregma, 1.0 mm lateral to midline, and 5.0 mm ventral to the skull surface). Elastase (E7885, porcine pancreatic elastase, lyophilized powder, 20 mg, Sigma-Aldrich) was dissolved in PBS. 2.5 uL of the elastase solution was injected at 0.2uL/min. After stereotaxic injection of elastase, the needle was left in place for an additional 10 min to prevent the possible leakage of the elastase solution.

Although stereotaxic surgery is a well-established technique, a lot of training is required which is very time consuming to get high-accuracy position and stable fixation in mice. The mouse is anesthetized with an intraperitoneal injection of an appropriate dose of ketamine/xylazine cocktail. The mouse eyes should be protected with antibiotic cream. The mouse is mounted on a stereotaxic frame through the use of ear bars and a tooth bar. When you fix the mouse's head with ear bars, one of ear bars should be locked in place and then the ipsilateral auditory meatus should be put in. Then using the second ear bar, gently push the ear until a popping sound is heard, indicating insertion to the tympanic membrane. Keeping

the mouse's head in the same position and horizontally, open the mouth and then hook the tooth. This step is crucial to inject elastase into the cerebrospinal fluid. Unless accurate and stable position is achieved in the mouse, the tip of the needle is not optimally placed. When no further movement is possible, you can move on the next step. During the procedure the core temperature in mice should be maintained at 37 °C. The surgical procedures for the stereotaxic injection of elastase seem to cause significant perioperative stress to mice. Therefore, we inject 500 uL of saline intraperitoneally once a day for the first two postoperative days in mice.

The depth of the needle is another critical factor for the successful induction of aneurysm in this model. When the needle depth is too shallow, the injection of elastase into the brain parenchyma results in intracerebral hemorrhage similar to the collagenase-induced intracerebral hemorrhage. If the needle tip is too close to the surface of the brain, the injection of elastase into the cerebrospinal fluid can result in diffuse hemorrhage from the surface of the brain, even when the needle tip is inside the subarachnoid space. If the needle tip is too deep, the elastase goes into the subdural space. Place the tip of the needle to a depth of 5.2 mm from the surface of the skull and retract it back to a depth of 5.0 mm to penetrate the pia matter.

In our experience, we found that the stereotaxic coordinates need to be adjusted depending on the operator and the age of mice. Therefore, a series of test injections using dye (bromophenol blue, 2 mg/ml) or black ink was extremely important to ensure the correct placement of the needle tip at the right basal cistern. Each researcher should perform a series of test injections to adjust for the appropriated coordinates before starting the actual experiments. The spread of dye or black ink along the right half of the circle of Willis should be confirmed.

12.5 Evidences of Subarachnoid Hemorrhage

To detect aneurysmal rupture, two blinded observers performed daily neurological examination. Neurological signs were scored as follows: 0, normal function; 1, reduced eating or drinking activity demonstrated by the weight loss greater than 2 g of body weight (approximately 10 % weight loss) over 24 h; 2, flexion of torso and forelimb upon lifting of the whole animal by the tail; 3, circling to one side but normal posture at rest; 4, leaning to one side at rest; and 5, no spontaneous activity. Mice were euthanized when they developed neurological symptoms (score 1–5). All asymptomatic mice were sacrificed 21 or 28 days after aneurysm induction. To assess the intracranial aneurysms, the anesthetized mice are perfused with saline followed by perfusion with a bromophenol blue dye and gelatin mixture (20 %). After taking macroscopic pictures of the major vessel arteries, the brain tissues were fixed with 4 % paraformaldehyde for histological studies.

12.6 Time Course of the Occurrence of Subarachnoid Hemorrhage

In this model, 60–70 % of the mice had unruptured aneurysms at 7 days after aneurysm induction. The aneurysmal rupture started developing 7 days after aneurysm induction. 70–80 % of mice with aneurysm developed subarachnoid hemorrhage due to aneurysmal rupture. Therefore, aneurysm formation precedes aneurysmal rupture in this model. The time frame between Day 7 and mice Day 21–28 appears to represent a period during which preventive pharmacological therapies can be tested.

12.7 Overview of Elastase-Induced Intracranial Aneurysm in Hypertensive Mice

In this model, induced intracranial aneurysms are generally large and macroscopically apparent with a high incidence and short incubation period. Figure 12.1 shows representative intracranial aneurysms from this model. The aneurysms are easily distinguishable from the normal arteries without using histological assessment. In addition, the aneurysmal rupture occurred spontaneously with a high rate. Although mechanisms of aneurysmal rupture may be fundamentally different from those of formation and growth, we can study not only mechanisms of aneurysmal formation but also those of aneurysmal rupture using this model. Using this model, we demonstrated that aneurysmal formation was associated with matrix metalloproteinase (MMP) activation and macrophage [2, 3]. Doxycycline and minocycline prevented aneurysmal rupture possibly via their anti-inflammatory effects [4]. Normalization of blood pressure and the inhibition of the local renin-angiotensin system without reduction of blood pressure can prevent aneurysmal rupture [5]. Furthermore, the activation of estrogen receptor-β prevented aneurysmal formation and rupture in ovariectomized female mice [6, 13].

However, to induce intracranial aneurysms and aneurysmal rupture consistently, accurate stereotaxic procedure to inject elastase into the cerebrospinal fluid at the right basal cistern is critical [12]. This is one of the limitations of our model. Because exogenous elastase was used to induce aneurysms in our model, the early step of aneurysm formation that requires endogenous elastase may have been bypass.

In this model, the mechanisms of aneurysmal formation and rupture and the possible pharmacological therapy for the prevention of aneurysmal rupture can be studies for future studies that utilized various inhibitors, knockout mice, or transgenic mice.

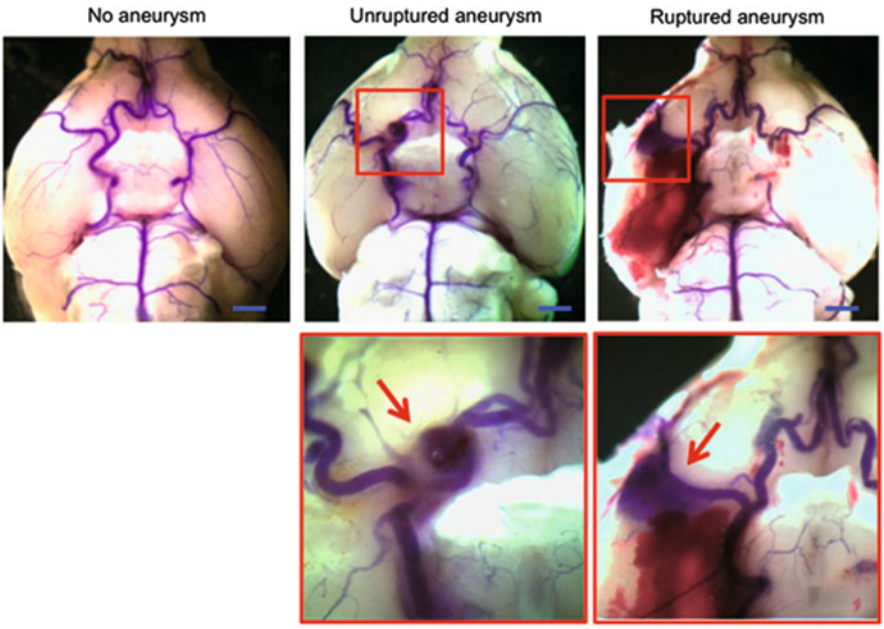

Fig. 12.1 Representative intracranial aneurysms in mice. *Left panel*: Normal cerebral artery. *Middle panel*: Unruptured aneurysm in the right anterior cerebral artery. *Right panel*: Ruptured aneurysm with subarachnoid hemorrhage in the right middle cerebral artery. Cerebral arteries were visualized by blue dyes dissolved in gelatin. *Arrows* indicate aneurysms. Bar = 2.5 mm (Reprinted by permission from Macmillan Publishers Ltd: Journal of Cerebral Blood Flow and Metabolism (Shimada et al. [7]), copyright 2015)

Sources of Funding This study was funded by National Institutes of Health (NIH) R01NS055876 (to T.H.), R01NS082280 (to T.H.).

There are no conflicts of interest.

Disclosures None.

References

1. Stegmayr B, Eriksson M, Asplund K. Declining mortality from subarachnoid hemorrhage: changes in incidence and case fatality from 1985 through 2000. Stroke. 2004;35:2059–63.
2. Nuki Y, Tsou TL, Kurihara C, Kanematsu M, Kanematsu Y, Hashimoto T. Elastase-induced intracranial aneurysms in hypertensive mice. Hypertension. 2009;54:1337–44.
3. Kanematsu Y, Kanematsu M, Kurihara C, Tada Y, Tsou TL, van Rooijen N, et al. Critical roles of macrophages in the formation of intracranial aneurysm. Stroke. 2011;42:173–8.
4. Makino H, Tada Y, Wada K, Liang EI, Chang M, Mobashery S, et al. Pharmacological stabilization of intracranial aneurysms in mice: a feasibility study. Stroke. 2012;43:2450–6.
5. Tada Y, Wada K, Shimada K, Makino H, Liang EI, Murakami S, et al. Roles of hypertension in the rupture of intracranial aneurysms. Stroke. 2014;45:579–86.

6. Tada Y, Wada K, Shimada K, Makino H, Liang EI, Murakami S, et al. Estrogen protects against intracranial aneurysm rupture in ovariectomized mice. Hypertension. 2014;63:1339–44.
7. Shimada K, Furukawa H, Wada K, Wei Y, Tada Y, Kuwabara A, et al. Angiotensin-(1–7) protects against the development of aneurysmal subarachnoid hemorrhage in mice. J Cereb Blood Flow Metab. 2015;35:1163.
8. Zhao J, Lin X, He C, Yang GY, Ling F. Study of cerebral aneurysms in a modified rat model: from real-time imaging to histological analysis. J Clin Neurosci. 2015;22:373–7.
9. Chu Y, Wilson K, Gu H, Wegman-Points L, Dooley SA, Pierce GL, et al. Myeloperoxidase is increased in human cerebral aneurysms and increases formation and rupture of cerebral aneurysms in mice. Stroke. 2015;46:1651.
10. Hosaka K, Downes DP, Nowicki KW, Hoh BL. Modified murine intracranial aneurysm model: aneurysm formation and rupture by elastase and hypertension. J Neurointerv Surg. 2014;6:474–9.
11. Starke RM, Chalouhi N, Jabbour PM, Tjoumakaris SI, Gonzalez LF, Rosenwasser RH, et al. Critical role of tnf-alpha in cerebral aneurysm formation and progression to rupture. J Neuroinflammation. 2014;11:77.
12. Tada Y, Kanematsu Y, Kanematsu M, Nuki Y, Liang EI, Wada K, et al. A mouse model of intracranial aneurysm: technical considerations. Acta Neurochir Suppl. 2011;111:31–5.
13. Tada Y, Makino H, Furukawa H, Shimada K, Wada K, Liang EI, et al. Roles of estrogen in the formation of intracranial aneurysms in ovariectomized female mice. Neurosurgery. 2014;75:690–5.

Chapter 13
Experimental Model of Cerebral Aneurysms in Ovariectomized Rats

Shinji Nagahiro and Keiko Kitazato

Abstract The mortality rate for subarachnoid hemorrhage from ruptured cerebral aneurysms (CAs) is approximately 50 %. Unruptured aneurysms are present in 2–5 % of adults; their reported annual rupture rate is about 0.5–1.0 %. The pathogenesis of CAs remains to be elucidated. However, there are limitations in CA research; human specimens usually consist of the aneurysmal fundus and do not reflect the pathology of the CA and there are no reliable, reproducible animal models of CAs.

To investigate the formation, structure change, and rupture of the aneurysmal wall we added oophorectomy to Hashimoto's rat model and established a highly reproducible CA model in rats. Because CAs often arise in postmenopausal women, the rats were subjected to estrogen deficiency, hemodynamic changes, and renal hypertension and fed a high-salt diet.

Here we describe our surgical procedures to induce CA in female rats and present a potential pharmacological treatment to attenuate aneurysm formation. Our rat model yields a better understanding of the pathological mechanisms underlying the formation of aneurysms and provides a means to assess the possibility of medicinal treatments.

Keywords Cerebral aneurysm • Rat • Hypertension • Hemodynamic change • Estrogen deficiency

13.1 Introduction

Cerebral aneurysms (CAs) arise in 2–5 % of adults. While the incidence of CAs has been reported to be high in Japan and Finland, it is low in India, Iran, the Middle East, and many parts of Africa. It is difficult to determine whether this is a geographic variation or attributable to differences in the diagnostic workup.

CAs tend to arise at branching sites of major arteries and at sites where arterial turns or curves impede the normal blood flow. Aneurysms arise frequently in

S. Nagahiro (✉) • K. Kitazato
Department of Neurosurgery, Institute of Biomedical Sciences, Tokushima University Graduate School, 3-18-15 Kuramoto-cho, Tokushima 770-8503, Japan
e-mail: sinji.nagahiro@gmail.com

M. Sata (ed.), *Mouse Models of Vascular Diseases*,
DOI 10.1007/978-4-431-55813-2_13

arteries of the anterior circulation. In large forensic clinical and autopsy series the sites of CAs were the internal carotid artery (ICA, 24–41 %), the anterior cerebral artery (ACA, 30–39 %), the middle cerebral artery (MCA, 20–33 %), and the vertebrobasilar artery (VBA, 4–12 %). The lowest morbidity and mortality rates were reported in patients with small anterior circulation aneurysms (0.8 % and 1.9 %, respectively) and highest in those with large posterior fossa aneurysms (9.6 % and 37.9 %, respectively).

CAs affect women more frequently than men. A retrospective study of cerebral angiograms showed that 67 % of patients harboring asymptomatic aneurysms were women [1]. In an autopsy study from Japan, the aneurysm rate was higher in women than men [2].

Some individuals with CAs suffer subarachnoid hemorrhage (SAH). While the incidence of SAH was stable in males of different ages, it was increased in women aged 40–69 years and there was a peak in women aged 50–59 years [3]. In more than 80 % of patients primary SAH is attributable to rupture of an intracranial aneurysm. The consequences of SAH due to the rupture of intracranial aneurysms are catastrophic. The mortality rate is high; 15 % of affected individuals died before hospitalization and 36 % died within 48 h of onset, 43 % of these in the first week and the other 57 % died within 6 months. Furthermore, half of the survivors suffered severe morbidity such as physical or psychosocial deficits 1 year after SAH.

Preventing the formation and progression of CAs therefore represents the best practical measure for avoiding the grim sequelae of SAH. Recent improvements in the management of patients with aneurysmal SAH resulted in a slight decrease in the mortality rate. While endovascular- or intracranial surgery (coiling or clipping) is performed to prevent SAH, these procedures may have deleterious effects. The successful treatment of CAs requires a good understanding of their pathogenesis and of the role various risk factors play in their formation, progression, and rupture.

Important questions remain, i.e., what are the factors involved in the formation of CAs, is it associated with congenital or acquired factors, what is the arterial layer critical to the formation of intracranial aneurysms, and how is the structure of the aneurysm formed, changed, and ruptured? However, there are limitations in CA research; human specimens usually consist of the aneurysmal fundus and do not reflect the pathology of the CA and there are no reliable, reproducible animal models of CAs.

13.2 Importance of Experimental Models

The wide spread of endovascular treatment and the trend to operate unruptured CAs resulted in a decrease in human aneurysmal tissues needed for the study of various aspects of CAs. The availability of cadaveric aneurysmal tissues has also declined due to the spread of neuroimaging technologies that reduce the number of individuals with SAH available for postmortem studies. The amount of aneurysmal tissue

harvested after the clipping of CAs is usually small and consists of the aneurysmal fundus which fails to reflect the pathology of CAs.

Consequently, reliable animal models are needed to compensate for the shortage in human aneurysmal tissues and to study the pathogenesis and risk factors of, and new treatment options for, CAs. We developed a new animal model to identify the pathogenesis of CAs. Because CAs often arise in postmenopausal women we established a highly reproducible rat model of CA by adding oophorectomy to Hashimoto's model.

13.3 Production of Cerebral Aneurysms by Renal Hypertension and Unilateral Ligation of Common Carotid Artery to Elicit Hemodynamic Changes

13.3.1 The Hashimoto Model

The rat aneurysm model involves the induction of renal hypertension and unilateral occlusion of the common carotid artery (CCA) to elicit hemodynamic changes on one side of the circle of Willis. Renal hypertension was induced via the bilateral ligation of the posterior renal arteries and by feeding the rats 1 % saline as a drinking water. The underlying pathology and the distribution of these experimental aneurysms are similar to those seen in humans.

Some rats subjected by Hashimoto et al. [4, 5] to the creation of renal infarcts and an increase in the unilateral cerebral blood flow developed intracranial aneurysms after a few months (Fig. 13.1), suggesting arterial hypertension as one of the most important factors in the formation of these aneurysms.

In normotensive humans, factors such as lifting heavy objects, bending, and stress may result in a transient, recurrent blood pressure elevation that may injure arterial walls and result in the formation, enlargement, and even rupture of aneurysms. *In vitro* experiments of Austin et al. [6] showed that a high pulse rate and/or a sudden increase in the blood pressure can increase the turbulence of flow within saccular aneurysms. This pressure-jump phenomenon tends to result in sudden aneurysmal enlargement, bleb formation, or the rupture of saccular aneurysms. However, the reproducibility of their model was low (20–30 %) and, similar to humans, approximately 3 months were required for the development of aneurysms. In our experiments we chose to use this type of aneurysm model.

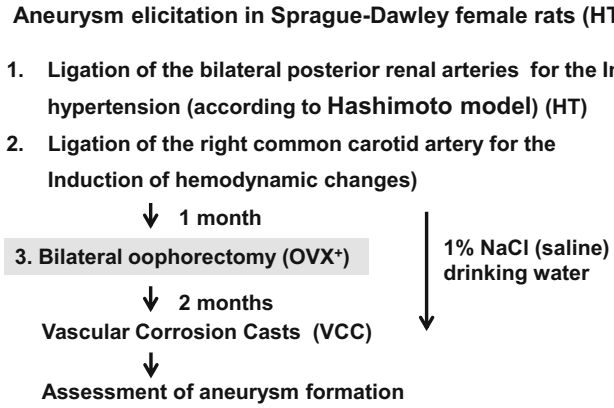

Fig. 13.1 Aneurysm elicitation in female Sprague Dawley rats by (*1*) Ligation of the bilateral posterior renal arteries for the induction of hypertension (according to the Hashimoto model) and (*2*) Ligation of the right common carotid artery for the induction of hemodynamic changes. The drinking water contained 1 % NaCl (saline). One month later the rats were subjected to bilateral oophorectomy (OVX). Aneurysm formation was assessed on vascular corrosion casts

13.3.2 Hashimoto's Model Plus Oophorectomy (Female Dominance in the Formation of CAs)

All experimental procedures and protocols were in accordance with the Japanese standards for the care and use of laboratory animals and were approved by the Care Committee of the University of Tokushima. Before any procedures, the rats were anesthetized by isofluorane (2–4 %) inhalation. Based on Hashimoto's model [4], we ligated the unilateral posterior renal artery to induce hypertension and the right common carotid artery to induce hemodynamic stress in 7-week-old female Sprague-Dawley rats. On the following day we ligated the contralateral posterior renal artery. The drinking water contained 1 % NaCl (Fig. 13.1).

We determined the blood pressure with the tail-cuff method and confirmed that it was significantly elevated 1 month after ligation of the bilateral posterior renal arteries. Then the animals underwent bilateral oophorectomy (OVX) to reduce their estrogen level. Two months later we also confirmed the elevation of blood pressure (Fig. 13.2). Then we sacrificed the rats to assess the formation of cerebral aneurysms on vascular corrosion casts and to confirm the decrease in the estrogen level of HT/OVX$^+$ rats (Fig. 13.2). Endothelial cells and the morphology of the inner lumen of the aneurysms were examined under a scanning electron microscope (SEM).

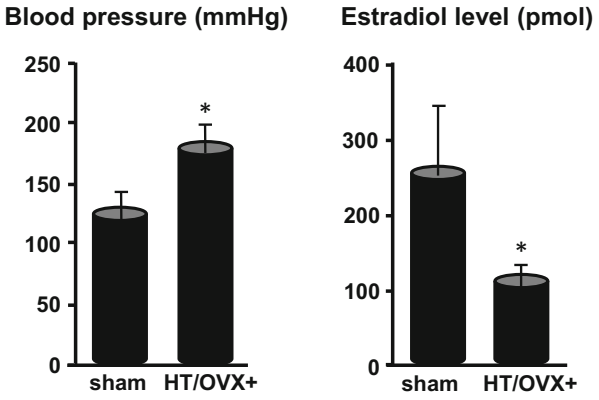

Fig. 13.2 Blood pressure and estradiol level in HT/OVX^{+} rats with experimentally produced renal hypertension and hemodynamic changes. *$p<0.05$ by the Student *t*-test

13.4 Assessment of the Cerebral Aneurysms

13.4.1 Vascular Corrosion Cast

Anesthetized rats were subjected to laparotomy/thoracotomy. The tip of a plastic cannula (19 G × 1¼″) inserted into the left ventricle was secured in the ascending aorta. After cutting the right atrium for drainage, the rats were perfused with 100 ml of heparinized (20 U/ml) phosphate-buffered saline using a perfusion pump (Fig. 13.3). The rate was 10 ml/min. We immediately prepared 10 ml of Batson's No. 17 plastic resin (Polysciences, Inc., PA, USA) in a 20-ml syringe according to the protocol provided by the manufacturer. Then we manually injected 10 ml of Batson's No. 17 plastic resin into the ascending aorta through the plastic cannula. After 24-h polymerization at room temperature the whole brain was removed and digested in 20 % KOH for 24–72 h to remove tissues surrounding vessels.

Vascular casting is a powerful tool for studying arterial vascular systems; it avoids shrinkage artifacts and maintains a three-dimensional geometry. Even under a conventional microscope we saw that the blood flow on the side opposite the carotid artery ligation was increased (Fig. 13.4). After 2–3 water rinses the vascular cast was dried in a desiccator containing silica gel and sputtered with gold.

The remaining vascular cast was mounted on an SEM stub using colloidal silver paste, sputter-coated with gold, and screened for the presence of aneurysmal changes under a Keyence VE-8800 (Osaka, Japan) SEM. The beam voltage was 3KV and the arterial bifurcations of major arteries were carefully examined. The corrosion cast sample of major arteries shown in Fig. 13.5 mirrors the intraluminal imprint seen under the SEM. Imprints of endothelial cell nuclei and endothelial cell borders are clearly visualized.

As many aneurysms formed at the bifurcation of the left anterior cerebral artery (ACA) and the olfactory artery (OA), we focused on this area (ACA-OA bifurcation) (Fig. 13.5). In normal rats endothelial cells are arranged and oriented in the direction of flow (Stage 0). We classified anomalous endothelial cell imprints into

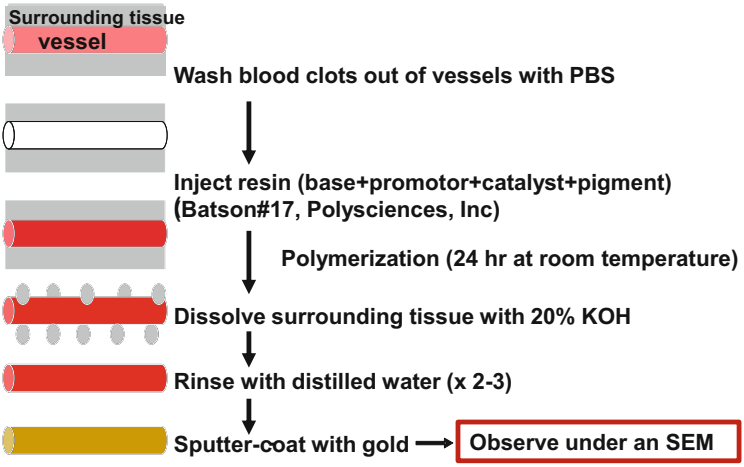

Fig. 13.3 Procedures for preparing vascular corrosion casts

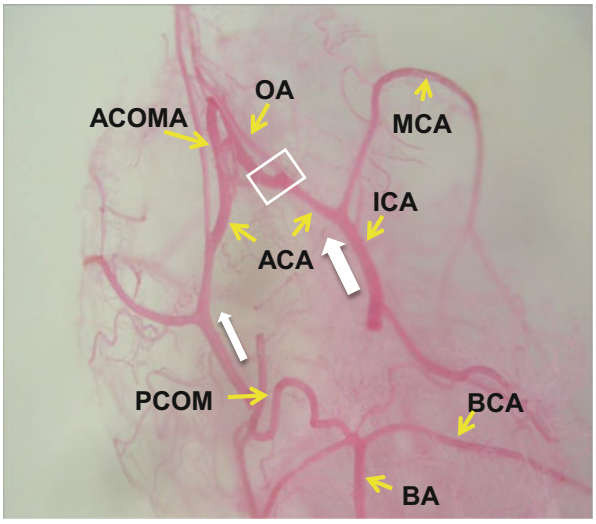

Fig. 13.4 Hemodynamic changes. The blood flow (*white arrow*) on the side opposite the carotid artery ligation (*left side*) was increased

3 stages. Stage I indicated that the imprints were irregular, Stage II that there was a slight elevation of the intimal pad apparently affecting the apex of the bifurcation rather than the apical intimal pad, the site of earlier changes. We posit that intra-aneurysmal pressure and blood flow patterns control the expansion of aneurysmal dilation toward the bifurcation apex. The aneurysmal dome exhibited irregularly-shaped endothelial imprints and there were areas devoid of endothelial cell markings (Stage III). The absence of endothelial cell imprints may be more pronounced

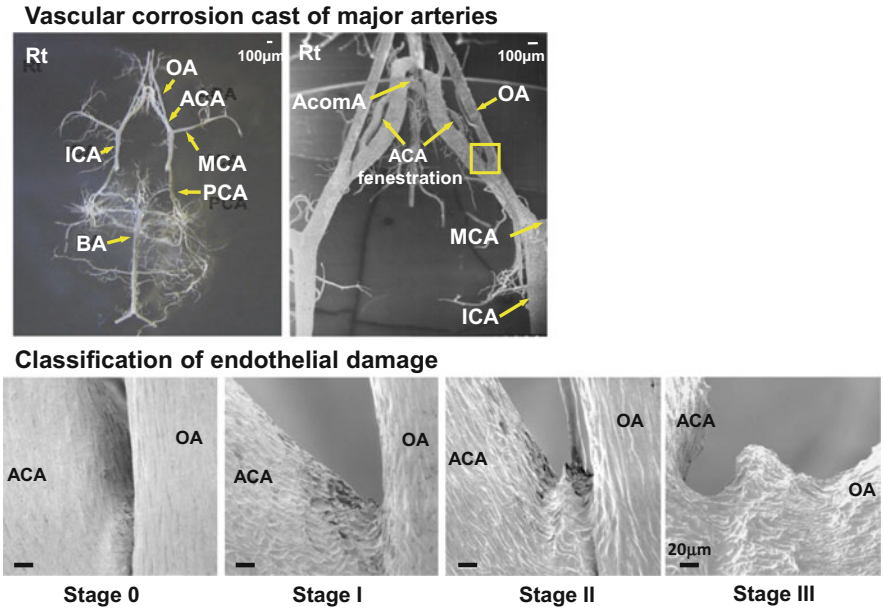

Fig. 13.5 Vascular corrosion casts of major arteries and classification of endothelial damage. Stage 0 = normal. Stage 1 = endothelial damage. Stage 2 = elevation of the intimal pad. Stage 3 = saccular aneurysm

in larger aneurysms and may be related to their increased incidence of rupture. We were able to differentiate early aneurysmal dilation (Stage II) from junctional dilation, considered by some as a pre-aneurysmal lesion. Junctional dilation was present in some rats and differed from aneurysmal dilation in that the area of dilation was covered by normal endothelium. Some of the junctional dilations were on the right-, i.e., the low shear-stress side. Based on these observations we suggest that true junctional dilations do not progress to Stage III (saccular aneurysms) without undergoing the changes described as Stage I–II.

Earlier studies to investigate the pathology of CAs in clinical and experimental settings relied on the appearance of arterial wall dilation, identified by either angiography or dissecting microscopy, for the diagnosis of aneurysmal changes [7]**.** Our technique yields material to study the ultrastructural and 3D morphology of large areas of the vascular tree.

Under SEM images, we found that the incidence of cerebral aneurysm formation was 3 times higher in hypertensive HT/OVX^{+} than HT/OVX^{-} rats (60 vs. 20 %). None of the control sham-operated rats developed aneurysms. Our aneurysm model was reliable and reproducible.

13.4.2 Immunohistochemical Findings

13.4.2.1 The Expression of Angiotensin II and the NADPH Oxidase Subunit

Compared to sham-operated rats, in HT/OVX^{+} rats there was obvious outward bulging of the arterial wall with disappearance of the internal elastic lamina. Note the strong immunoreactivity for angiotensin II (Ang II) antigen in the cerebral aneurysm (Fig. 13.6). In the cerebral aneurysmal wall and the parent artery adjacent to the lesion, there was immunoreactivity to a NADPH oxidase subunit, NOX4. Another subunit, p22phox was observed in the vascular intima and media of the cerebral aneurysm. These findings suggest that the renin-angiotensin system (RAS) was activated in association with hypertension and oxidative stress was increased in the aneurysmal wall (Fig. 13.6).

Immunohistochemical expression at the bifurcation of the anterior cerebral- and the olfactory artery in HT/OVX rats

	Ang II	Nox4	p22phox	ERα	ERβ	eNOS
normal	−	−	−	++	±	++
aneurysm	++	++	++	−	++	±

+ : positive
- : negative

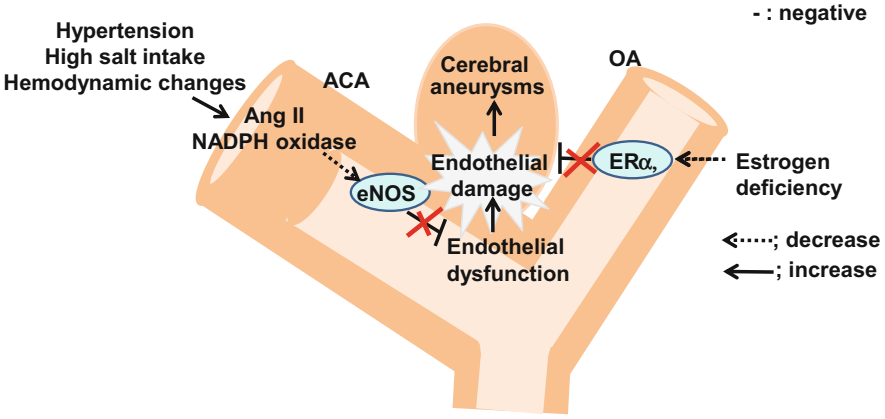

Fig. 13.6 Increased expression of angiotensin II (*Ang II*) and NADPH oxidase subunits (Nox4 and p22phox), decreased ERα and eNOS at the bifurcation of the anterior cerebral- and the olfactory artery in aneurysm model rats subjected to hypertension (*HT*), hemodynamic changes and oophorectomy (*OVX*$^{+}$)

13.4.2.2 The Expression of Estrogen Receptors (ERs)

Estrogen predominantly binds to ERα and exerts vasoprotective effects. Although ERβ has a low affinity for estrogen, like ERα it plays a vasoprotective role. In the aneurysmal wall of our HT/OVX$^+$ rats the expression of ERα was lower and the expression of ERβ was higher than those in sham-operated rats (Fig. 13.6), suggesting that under estrogen deficiency conditions ERβ may play a compensatory role.

13.4.2.3 eNOS Expression

In both sham and OVX$^+$/HT rats we observed PECAM 1-positive endothelial cells arrayed along the vascular lumen [7]. However, compared to sham-operated rats, the expression of eNOS was reduced in the aneurysmal wall and the parent artery of HT/OVX$^+$ rats (Fig. 13.6).

13.4.3 Analysis of the mRNA Level in the Aneurysmal Wall

Each intracranial artery in HT-, OVX$^+$-, and HT/OVX$^+$ rats was isolated and total RNA was extracted. Transcribed cDNA was subjected to quantitative real-time polymerase chain reaction assay (qRT-PCR). The mRNA level of eNOS was normalized with GAPDH mRNA as the internal standard. In HT-, OVX$^+$-, and HT/OVX$^+$ rats, the mRNA level of eNOS was significantly reduced [8]. This reduction was more marked in HT- than OVX$^+$ rats, suggesting a predominant vascular dysfunction due to hypertension. We confirmed this phenomenon using endothelial cells under the presence of angiotensin II and/or without 17-β estradiol in the in vitro study [8].

Taken together, these findings suggest that hypertension with hemodynamic change activates renin-angiotensin system (RAS), leading to the downregulation of eNOS and endothelial damage. On the other hand, estrogen deficiency decreases the expression of ERα, thereby decreasing antioxidative effects and increasing endothelial damage. These combined actions may facilitate the formation of CA (Fig. 13.6).

Furthermore, the upregulation of the mRNA level of inflammatory-related molecules including p-selectin, ICAM-1, VCAM-1, TNFα, and of RAS [9, 10] and the greater degree of extracellular matrix degradation in the aneurysmal wall of HT/OVX$^+$ rats are suggestive of a relationship between CAs and vascular degradation due to inflammation.

13.5 The Acquired Degenerative Changes

The apical intimal pad of arterial bifurcations where aneurysms arose is the site of greatest hemodynamic stress which is transmitted along the arterial wall. The incidence of aneurysms increases at sites where the cerebral arteries may be exposed to greater wear and tear as evidenced by anomalies in the circle of Willis, e.g., arterial fenestration, ICA agenesis, persistence of a primitive artery.

In our rat model, the formation of cerebral aneurysms is associated with endothelial damage and vascular degradation due to inflammatory-related molecules and is increased at ACA-OA bifurcation where the cerebral arteries may be exposed to greater wear and tear. Under the hypothesis that the opening of tight junctions due to the loss of the tight junction proteins occludin and zona occludens-1 (ZO-1) in damaged endothelium allows macrophage migration and leads to cerebral aneurysm formation, we examined tight junction proteins in our aneurysm model HT/OVX^{+} rats. We also examined the morphology of the vascular wall in the aneurysms and performed the immunohistochemical and qRT-PCR studies. In the very early stage before aneurysm formation, the expression of occludin and ZO-1 was reduced in injured endothelial cell junctions exhibiting gaps [10]. In the course of aneurysmal progression, the reduction in these proteins was correlated with macrophage migration. Furthermore, in HT/OVX^{+} rats we observed an increase in the degradation molecules matrix metalloproteinase-9, nicotinamide-adenine dinucleotide phosphate (NADPH) oxidase, and monocyte chemoattractant protein-1 [10]. At sites prone to the formation of aneurysms the reduction in tight junction proteins was associated with the expression of degradation molecules and the migration of macrophages. These observations suggest that the destruction of tight junctions facilitates macrophage migration, thereby accelerating the formation of cerebral aneurysms in rats (Fig. 13.7).

In clinical and experimental studies, degeneration and fragmentation of the internal elastic lamina was an important factor in the formation of CAs [7]. Damage of the internal elastic lamina may be attributable to hemodynamic changes or certain vascular wall pathologies. Remodeling of the extracellular matrix (ECM) was suggested to be implicated in the development of CAs [11].

A deficiency in type III collagen in the vessel walls of CAs was one of the very early reported findings [12]. Collagen and elastin embedded in proteoglycans and glycoproteins are the main components of the ECM in arterial vessels and determine their tensile strength. The total amount of collagen in the aneurysmal wall appears to be less than in normal arteries. Studies to identify the components of collagen and of the degradation molecules in the aneurysm wall are underway in our department.

The detection of elevated levels of local elastase activity in aneurysmal walls does not necessarily correspond with elevated plasma levels. There is support for the hypothesis that increased local proteolytic activity and vascular extracellular matrix remodeling play a role in the formation of cerebral aneurysms. In animal studies, vessels treated topically with elastase dilated and formed aneurysms.

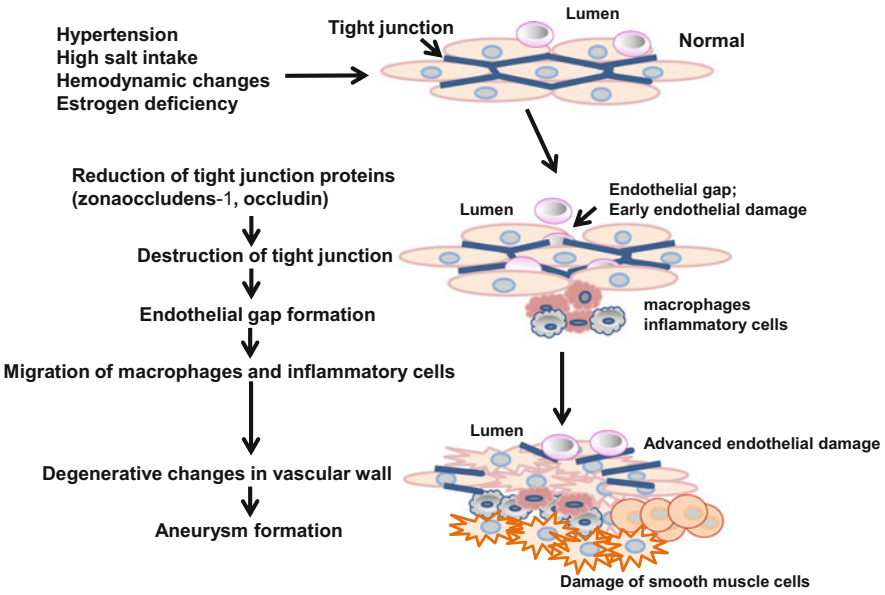

Fig. 13.7 Gap formation in the endothelial junction during early endothelial damage associated with a reduction in occludin and zona occludens-1 (*ZO-1*) in HT/OVX$^+$ rats. The gap formation facilitates migration of macrophages through gaps in the endothelial junction, thereby leading to degenerative changes in vascular wall and cerebral aneurysms

Another pathway to the remodeling of the ECM is apoptosis. Smooth muscle cells from arterial walls exhibited morphological apoptotic changes in the early stages of aneurysm development. However, the factors that lead to apoptotic changes in smooth muscle cells remain to be identified.

13.6 Medicinal Treatments

Using our highly reproducible aneurysm model, we examined the efficacy of several types of medicinal treatment to assess the potential of therapeutic alternatives other than coiling or clipping.

13.6.1 Hormone Replacement Therapy (HRT)

HT/OVX$^+$ rats were implanted 17-beta estradiol-releasing pellets (Innovative Research of America, Sarasota, FL, USA) under their dorsal skin for 2 months just after OVX. Eight weeks later, the CA changes were assessed using corrosion casts. The formation (Stage III) and progression (from Stage I to Stage II) of

aneurysmal changes were reduced by estradiol treatment (OVX^+/HT rats 86 %, OVX^+/HT/HRT rats 33 %, $p < 0.05$) [13].

13.6.2 Ang II Type I Receptor Blockade (ARB)

To further examine the effects of HT and estradiol deficiency on cerebral endothelial damage we used the ARB candesartan [7]. Estradiol deficiency had a somewhat greater effect on the formation of CAs than did HT alone. The growth of CAs (from Stage II to Stage III) was augmented by the combination of HT and estrogen deficiency. In contrast, treatment with ARB or HRT attenuated CA formation; treatment with HRT was slightly more efficacious than with ARB. Endothelial changes (Stage I) were observed in both ARB- and HRT rats. Endothelial damage was increased in OVX^+ rats, while HRT dramatically reduced it suggesting that estradiol deficiency may be associated with endothelial damage in the early phase of aneurysm formation [8]. HT facilitated the growth of cerebral aneurysms and ARB treatment inhibited aneurysmal progression.

13.6.3 Phosphodiesterase 4 (PDE4) Inhibitor

Vascular inflammation is associated with CAs. PDE4 is implicated in various inflammatory diseases due to cAMP degradation. PDE4 inhibitors suppress macrophage migration and the expression of endothelial leukocyte adhesion molecules and proinflammatory cytokines. To inhibit PDE4, rats were treated orally with ibudilast every day for 3 months [9]. Treatment with ibudilast had no effect on their systolic blood pressure. Immunohistochemically, activated PDE4 highly expressed in the aneurysmal wall was suppressed by ibudilast. The mRNA level of the leukocyte adhesion molecules, MMP-9 and TNF-α increased in the aneurysms was attenuated by ibudilast (Fig. 13.8). The blockade of PDE4 activation may contribute to the suppression of inflammation-related molecules, thereby inhibiting the formation of cerebral aneurysms.

13.6.4 Mineralocorticoid Receptor Antagonist

The mineralocorticoid receptor antagonist eplerenone prevents the formation of intracranial aneurysms and reduces the saline intake without affecting the blood pressure [14]. This was associated with a reduction in Ang II and the degradation molecules and resulted in the inhibition of macrophage migration and aneurysm formation. In vitro, occludin and ZO-1 were downregulated by Ang II and estrogen deficiency; their downregulation was reversed by eplerenone, the MMP inhibitor

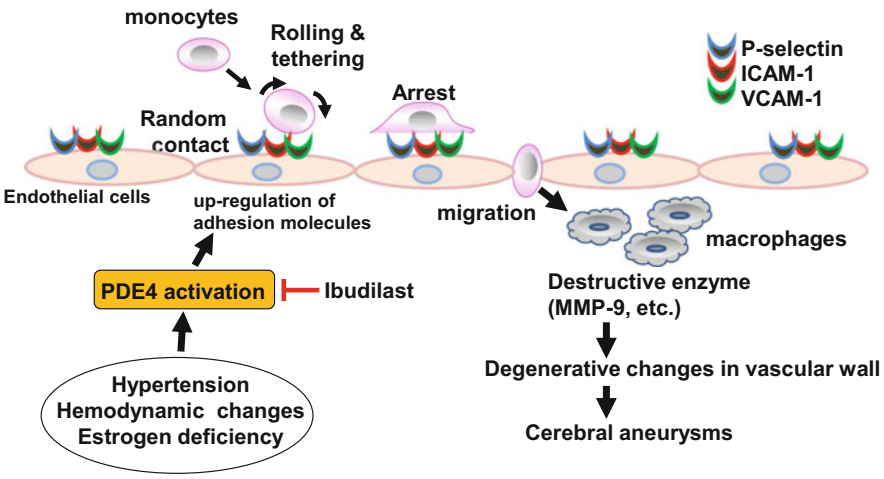

Fig. 13.8 Schematic role of PDE4 on the formation of cerebral aneurysm and the inhibition by ibudilast

SB3CT, and apocynin [14]**.** Among the drugs we tested, the inhibition rate of aneurysm formation by eplerenone was 85 %. Eplerenone most effectively prevented the formation of intracranial aneurysms (Table 13.1).

13.6.5 Statins

Statins may have beneficial effects on atherosclerosis and CAs [15]. Some studies also reported their efficacy in cerebral aneurysm models [16]. However, the detailed mechanisms underlying the benefits of statins remain unclear.

Using our model we first demonstrated that endothelial damage was present in 92 % of the HT/OVX^{+} rats within 6 weeks and the incidence of moderate protrusion (Stage II) and saccular aneurysms (Stage III) gradually increased with time (60 and 23 % at 12 weeks, 68 and 47 % at 24 weeks). Unexpectedly, statins exhibited bidirectional effects in our aneurysm model [17]. A high-dose hydrophilic statin and a lipophilic statin at any of the doses used induced aneurysmal rupture (Table 13.1). These detrimental effects were partly associated with the induction of apoptosis in the aneurysm wall. Based on our findings we urge the careful use of statins in patients with CAs, especially in postmenopausal women.

Table 13.1 Effects of various medicinal treatments in aneurysm model HT/OVX$^+$ rats

Drug	Dose	Inhibition	Mechanism(s)
17β estradiol	0.48 mg/60 day	67 %	Improvement of endothelial dysfunction
			Anti-oxidative
Candesartan	1 mg/kg	44 %	Improvement of endothelial dysfunction
			Anti-oxidative, anti-hypertensive
Ibudilast	60 mg/kg	47 %	Anti-inflammatory
Eplerenone	100 mg/kg	85 %	Anti-oxidative, Anti-inflammatory
Pravastatin	5 mg/kg	45 %	Improvement of endothelial dysfunction
	25, 50 mg/kg	Deleterious	Apoptosis
Simvastatin	5 mg/kg	Deleterious	Apoptosis
Olmesartan	0.3 mg/kg	54 %	Reduction in body Na^+

Candesartan and Olmesartan; angiotensin type I receptor antagonist, Ibudilast; inhibitor of phosphodiesterase 4, Eplerenone; mineralocorticoid receptor antagonist, Pravastatin; hydrophilic statin, Simvastatin; lipophilic statin

13.6.6 Na Diuretic ARB

In earlier studies we subjected our rats to bilateral renal ligation to induce hypertension (HT), gave them saline as their water, and then performed oophorectomy (HT/OVX$^+$ rats).

As the patients with unruptured CAs have not necessarily hypertension, we hypothesized that body sodium retention may be associated with the high incidence of CA formation in postmenopausal women without affecting blood pressure. To investigate the role of the combination of a high-salt diet (HSD) and OVX on the formation of cerebral aneurysms, we changed the order of these procedures in this study (Fig. 13.9). Female Sprague-Dawley rats aged 11 weeks were first subjected to OVX, then the ligation of the left CCA, and they were fed an 8 % high-salt diet on the same day. Two weeks later, we ligated the unilateral posterior renal artery. On the following day we ligated the contralateral posterior renal artery to induce hypertension (HSD/OVX$^+$/RL). After 3 weeks we recorded differences among sham rats fed a standard diet containing 0.3 % NaCl**,** sham rats fed an HSD (Oriental Yeast Co., Ltd., Japan) containing 8 % NaCl (HSD rats), and OVX$^+$ rats with or without RL that were fed an HSD (HSD/OVX$^+$ rats, HSD/OVX$^+$/RL rats). The incidence of unruptured aneurysms was higher in HSD/OVX$^+$ - and HSD/OVX$^+$/RL rats than in the HT/OVX$^+$ rats studied in our earlier investigation (average incidence 80–90 % vs. 60–70 %). The incidence of CAs was no significant difference between HSD/OVX$^+$- and HSD/OVX$^+$/RL rats [18]. Note the high incidence of CAs in HSD/OVX$^+$- and HSD/OVX$^+$/RL was associated with the increase in body Na^+/water ratio which means water-free sodium accumulation (Fig. 13.10). The increase in urinary Na^+/K^+ ratio was associated with the high-salt

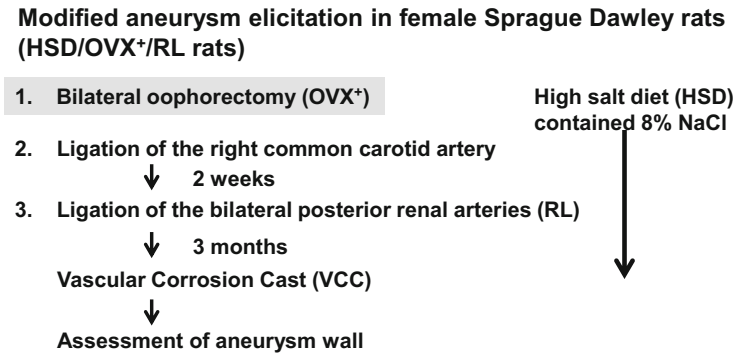

Fig. 13.9 Modified aneurysm elicitation in female Sprague Dawley rats by (*1*) Bilateral oophorectomy (OVX). (*2*) Ligation of the right common carotid artery for the induction of hemodynamic changes. The rats were fed an 8 % high salt diet (HSD). (*3*) Two weeks later the rats were subjected to ligation of the bilateral posterior renal arteries for the induction of hypertension as in Fig. 13.1

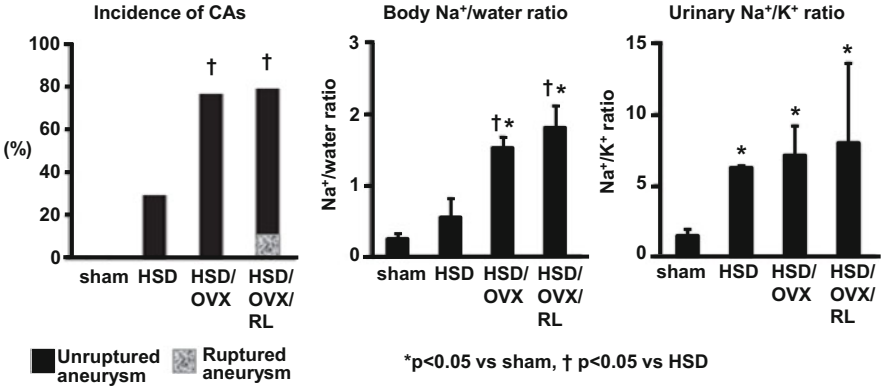

Fig. 13.10 Incidence of CAs, the body Na^+/K^+ ratio and urinary Na^+/K^+ ratio in rats fed a high-salt diet (*HSD*), and subjected to OVX (HSD/OVX) and/or renal hypertension induced by bilateral ligation of the posterior renal artery (HSD/OVX/RL)

intake. Interestingly, a few HSD/OVX^+/RL rats developed SAH at the anterior or posterior communicating artery. The ruptured sites in HSD/OVX^+/RL rats are similar to those in SAH patients. There was no ruptured aneurysm at ACA-OA bifurcation.

Treatment of HSD/OVX^+/RL rats with 0.3 mg/kg olmesartan without affecting their blood pressure significantly attenuated the incidence of cerebral aneurysms [18]. The vasoprotective effects of olmesartan were associated with an increase in the vascular Na^+ excretion pump, ATP1α2, and a decrease in the body sodium/water ratio. This alerts to the importance of therapeutic strategies that regulate water-free sodium accumulation to prevent aneurysm formation under the conditions of estrogen deficiency.

13.7 Conclusion and Perspective

Estrogen deficiency induces endothelial dysfunction and triggers endothelial damage. Additive hypertension enhances the generation of reactive oxygen species and inflammation, facilitating degradation of the vascular wall that leads to the formation of cerebral aneurysms at sites exposed to hemodynamic changes. Therapies targeting the endothelium and the management of hypertension may help to prevent CAs. Furthermore, the inhibition of inflammation and the regulation of water-free sodium accumulation may be an important therapeutic strategy to reduce the incidence of CAs. As the rate of SAH in our model was low, we are attempting to establish a reproducible model with a higher rate of SAH by applying further modifications to our present rat aneurysm model. Efforts are also underway to establish methods to identify vulnerable unruptured aneurysms and to prevent their rupture.

In summary, we demonstrated that estrogen deficiency combined with water-free sodium accumulation increased the susceptibility of rats to the formation of cerebral aneurysms and that hypertension enhances their progression. Our findings suggest that hormones and water-free sodium retention in addition to hypertension play a role in the pathogenesis of CAs. Our rat model is simple and highly reproducible with respect to aneurysm formation and of value in studies addressing the pathogenesis and progression of cerebral aneurysms. It can also be used to assess the efficacy of medical treatments.

References

1. Harada K, Fukuyama K, Shirouzu T, Ichinose M, Fujimura H, Kakumoto K, Yamanaga Y. Prevalence of unruptured intracranial aneurysms in healthy asymptomatic Japanese adults: differences in gender and age. Acta Neurochir (Wien). 2013;155:2037–43.
2. Iwamoto H, Kiyohara Y, Fujishima M, Kato I, Nakayama K, Sueishi K, Tsuneyoshi M. Prevalence of intracranial saccular aneurysms in a Japanese community based on a consecutive autopsy series during a 30-year observation period. The Hisayama study. Stroke. 1999;30:1390–5.
3. Hamdan A, Barnes J, Mitchell P. Subarachnoid hemorrhage and the female sex: analysis of risk factors, aneurysm characteristics, and outcomes. J Neurosurg. 2014;121:1367–73.
4. Hashimoto N, Handa H, Hazama F. Experimentally induced cerebral aneurysms in rats. Surg Neurol. 1978;10:3–8.
5. Handa H, Hashimoto N, Nagata I, Hazama F. Saccular cerebral aneurysms in rats: a newly developed animal model of the disease. Stroke. 1983;14:857–66.
6. Austin GM, Schievink W, Williams R. Controlled pressure-volume factors in the enlargement of intracranial aneurysms. Neurosurgery. 1989;24:722–30.
7. Morimoto M, Miyamoto S, Mizoguchi A, Kume N, Kita T, Hashimoto N. Mouse model of cerebral aneurysm: experimental induction by renal hypertension and local hemodynamic changes. Stroke. 2002;33:1911–5.
8. Tamura T, Jamous MA, Kitazato KT, Yagi K, Tada Y, Uno M, Nagahiro S. Endothelial damage due to impaired nitric oxide bioavailability triggers cerebral aneurysm formation in female rats. J Hypertens. 2009;27:1284–92.

9. Yagi K, Tada Y, Kitazato KT, Tamura T, Satomi J, Nagahiro S. Ibudilast inhibits cerebral aneurysms by down-regulating inflammation-related molecules in the vascular wall of rats. Neurosurgery. 2010;66:551–9.
10. Tada Y, Yagi K, Kitazato KT, Tamura T, Kinouchi T, Shimada K, Matsushita N, Nakajima N, Satomi J, Kageji T, Nagahiro S. Reduction of endothelial tight junction proteins is related to cerebral aneurysm formation in rats. J Hypertens. 2010;28:1883–91.
11. Penn DL, Witte SR, Komotar RJ, Sander Connolly E Jr. The role of vascular remodeling and inflammation in the pathogenesis of intracranial aneurysms. J Clin Neurosci. 2014;21:28–32.
12. Pope FM, Nicholls AC, Narcisi P, Bartlett J, Neil-Dwyer G, Doshi B. Some patients with cerebral aneurysms are deficient in type III collagen. Lancet. 1981;1:973–5.
13. Jamous MA, Nagahiro S, Kitazato KT, Tamura T, Kuwayama K, Satoh K. Role of estrogen deficiency in the formation and progression of cerebral aneurysms. Part II: experimental study of the effects of hormone replacement therapy in rats. J Neurosurg. 2005;103:1052–7.
14. Tada Y, Kitazato KT, Tamura T, Yagi K, Shimada K, Kinouchi T, Satomi J. Nagahiro S Role of mineralocorticoid receptor on experimental cerebral aneurysms in rats. Hypertension. 2009;54:552–7.
15. Stalenhoef AF. The benefit of statins in non-cardiac vascular surgery patients. J Vasc Surg. 2009;49:260–5.
16. Aoki T, Kataoka H, Ishibashi R, Nozaki K, Hashimoto N. Simvastatin suppresses the progression of experimentally induced cerebral aneurysms in rats. Stroke. 2008;39:1276–85.
17. Tada Y, Kitazato KT, Yagi K, Shimada K, Matsushita N, Kinouchi T, Kanematsu Y, Satomi J, Kageji T, Nagahiro S. Statins promote the growth of experimentally induced cerebral aneurysms in estrogen-deficient rats. Stroke. 2011;42:2286–93.
18. Matsushita N, Kitazato KT, Tada Y, Sumiyoshi M, Shimada K, Yagi K, Kanematsu Y, Satomi J, Nagahiro S. Increase in body Na+/water ratio is associated with cerebral aneurysm formation in oophorectomized rats. Hypertension. 2012;60:1309–15.

Part VII
Vascular Disease in Cerebral Arteries

Chapter 14
A Model of Stroke and Vascular Injury in the Brain

Munehisa Shimamura, Hironori Nakagami, Masataka Sata, Hitomi Kurinami, Kouji Wakayama, Hideki Mochizuki, and Ryuichi Morishita

Abstract Recent clinical trials have revealed high rates of delayed restenosis and hemorrhage in angioplasty and stenting in intracranial atherosclerotic diseases, but the causes of this are still unclear. These unfavorable results may be caused by unique properties of intracranial internal carotid arteries (IICAs) such as lack of an external elastic lamina and presence of surrounding cerebrospinal fluid. Clarification of the mechanism of remodeling after vascular injury to IICAs using injury models is needed, although several studies have clarified the pathophysiology and molecular mechanisms involved in the remodeling process after injury to extracranial arteries. In this section, a detailed protocol for an IICA injury (IICAI) model is summarized. We also review the intraluminal suture middle cerebral artery occlusion (MCAo) model in mice, which causes cerebral infarction in the area of the middle cerebral artery region, because the IICAI model is a modification of the intraluminal suture MCAo model.

M. Shimamura, M.D., Ph.D. (✉)
Division of Vascular Medicine and Epigenetics, Graduate School of Medicine, Department of Neurology, Osaka University, 2-2 Yamada-oka, Suita, Osaka 565-0871, Japan

Department of Neurology, Graduate School of Medicine, Osaka University, Osaka, Japan
e-mail: shimamuu@cgt.med.osaka-u.ac.jp

H. Nakagami • H. Kurinami
Division of Vascular Medicine and Epigenetics, Graduate School of Medicine, Department of Neurology, Osaka University, 2-2 Yamada-oka, Suita, Osaka 565-0871, Japan

M. Sata
Department of Cardiovascular Medicine, Institute of Health Biosciences, The University of Tokushima Graduate School, Tokushima, Japan

K. Wakayama
Department of Advanced Clinical Science and Therapeutics, Graduate School of Medicine, The University of Tokyo, Tokyo, Japan

H. Mochizuki
Department of Neurology, Graduate School of Medicine, Osaka University, Osaka, Japan

R. Morishita
Department of Clinical Gene Therapy, Graduate School of Medicine, Osaka University, Osaka, Japan

M. Sata (ed.), *Mouse Models of Vascular Diseases*,
DOI 10.1007/978-4-431-55813-2_14

Keywords Vascular injury • Intracranial arteries • Mouse model • Middle cerebral artery occlusion model

14.1 Introduction

More than 5–10 % of strokes or transient ischemic stroke (TIA) are caused by intracranial atherosclerotic diseases (ICAD) [1]. Because the risk factors for ICAD are hypertension, diabetes mellitus, hypercholesterolemia, and high Lp(a) [1–3], controlling these risk factors with medications is important for the prevention of ischemic stroke in ICAD. Warfarin and aspirin are also used for secondary prevention, but 2-year stroke rate of patients with ICAD is still 19.7 % [4]; therefore, percutaneous angioplasty and stenting (PTAS) was studied as a candidate therapeutic option for intracranial arterial stenosis in the brain. However, several major complications were found in patients treated using these techniques. The rate of delayed restenosis was 32.4 % using bare metal stent placement in the Stenting in Symptomatic Atherosclerotic Lesions of Vertebral and Intracranial Arteries trial [5]. A high incidence of restenosis was also observed in a meta-analysis, which analyzed previous reports on stenting for intracranial atherosclerosis [6]. Drug-eluting stents, such as Taxus and Cypher, are expected to overcome the restenosis, but their efficacy remains controversial. For example, one report demonstrated a restenosis rate of 5 % at 4 months after injury [7], whereas another showed a 38 % restenosis at 9 months after injury [8]. In addition, the results of the recent Stenting and Aggressive Medical Management for Preventing Recurrent Stroke in Intracranial Arterial Stenosis trial reported that a high rate of brain hemorrhage within 30 days of stenting is another important complication of ICAD [9].

Thus, these clinical data raise the need to clarify the mechanism behind the high rate of restenosis and hemorrhage in intracranial arteries and also explore therapies to prevent these problems. In extracranial arteries, such as femoral arteries and common carotid arteries, balloon-injury models and wire-injury models have been established to mimic the remolding process after PTA and PTAS and have been used to clarify its pathophysiology. Because of the intracranial arteries having a characteristic structure, specifically with regard to the paucity of elastic fibers in the media, the reduced adventitial tissue, the lack of an external elastic lamina [10, 11], and presence of surrounding cerebrospinal fluid, it is necessary to perform studies using an intracranial artery injury model.

The intracranial internal carotid artery injury (IICAI) model presented here [12] is a modification of the so-called suture model, which occludes the middle cerebral artery (MCA) transiently and causes a cerebral infarct in the cortex and caudate putamen (CP). The IICAI model is different from the MCA occlusion (MCAo) model in terms of larger size of suture, necessity of a scratch, and the limited strains of mice available.

In this review, we summarize the protocols for the MCAo and IICAI models.

14.2 Preparation

All experiments were approved by the Institutional Animal Care and Use Committee of Osaka University. They were conducted in accordance with the Osaka University Guidelines, which are based on the National Institutes of Health's *Guide for the Care and Use of Laboratory Animals* and the ARRIVE guidelines.

1. Animals

   MCAo model: male C57BL6/J mice (CLEA Japan Inc., Japan) aged 6–8 weeks are used. We have not tried the MCAo model in other strains, but many studies used other strains including C3H/HeN [13] and FVB mice [14].

   IICAI model: male FVB/N mice aged 6–8 weeks are used (CLEA Japan Inc., Japan). C57BL6/J mice are not suitable for the IICAI model because subarachnoid hemorrhage occurs immediately after scratching the intracranial artery in C57BL6/J mice.
2. Suture preparation

   MCAo model: A 6–0 monofilament suture (LOOK suture 916B, LOOK, USA) is cut into 15–20 mm long pieces. Round the tip (Fig. 14.1a) of the suture near a soldering iron (HE-20, Taiyo Electric Inc., Japan, (Fig. 14.1c)). Some sutures are not suitable for rounding because the quality of the material differs among products. The suture is marked 10 mm from the tip using white correction fluid (Fig. 14.1a).

   IICAI model: A 5–0 monofilament suture (Nesco suture GA05NA, Alfresa Corporation, Japan) is cut into 15–20 mm long pieces and coated with epoxide resin solution (#16323, Konishi, Japan) for a length of 6 mm and 300 μm in diameter from the tip (Fig. 14.1b). One way to make this suture is to first make a

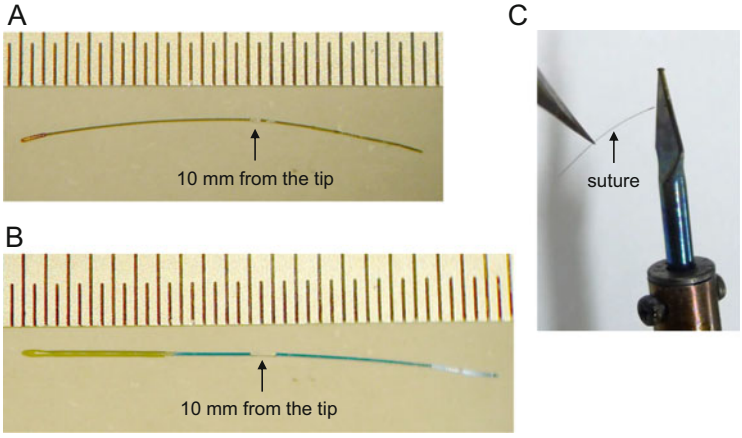

Fig. 14.1 Preparation of the intraluminal suture. (**a**) The intraluminal suture for the middle cerebral artery occlusion model. (**b**) The tip of the 6-monofilament was rounded using a soldering iron. (**c**) The intraluminal suture for the intracranial internal carotid artery injury model; the tip was coated with epoxide resin

hole in a piece of paper using a 29-G insulin syringe (ss-05 M2913, Terumo, Japan). After placing epoxide resin solution around the 5–0 monofilament, the suture is passed through the hole and marked 10 mm from the tip using white correction fluid.

14.3 Surgeries

The protocols for the MCAo and IICAI models are the same from step 3 to step 16.

3. Mice are anesthetized using isoflurane (4 %) in a chamber, and the fur on the head and the ventral neck region is shaved using a hair clipper (ER 803P, Panasonic, Japan). The level of isoflurane is then reduced to 1.7 %, and artificial tear ointment is applied to both eyes.
4. The mouse is placed in the abdominal position on a heating pad attached to a mouse Rotary Brain Anchor-block (MBB-100, Unique medical, Japan). A probe is inserted into the rectum, and the body temperature is maintained between 36.5 and 37.5 °C using a thermostat (ATC 402, Unique Medical).
5. After sterilization using 70 % ethanol, 0.5 % bupivacaine is injected subcutaneously along the prospective incision site. A midline incision is made on the head, and a fiber optic probe is glued on the right parietal bone 2-mm posterior and 4-mm lateral to the bregma (the right MCAo region) and connected to a laser Doppler flowmeter (Unique Medical).
6. The mouse is rotated and placed in the supine position. It is important that the neck is dorsiflexed sufficiently to obtain a large enough operative field. After sterilization using 70 % ethanol and the subcutaneous injection of 0.5 % bupivacaine, a midline incision is made on the neck under a stereomicroscope (Fig. 14.2a). A sufficient operative field is obtained using a retractor, which is remolded from a 26-G needle (Fig. 14.2a, asterisk).
7. The common carotid artery (CCA) is exposed carefully and is dissected free from the surrounding veins, nerves, and fascia (Fig. 14.2b).
8. A 6–0 silk suture is placed loosely around the CCA and then pulled in the caudal direction to show the external and internal carotid arteries (Fig. 14.2c).
9. The external carotid artery (ECA) and ICA are exposed carefully, and then dissected free from the surrounding veins, nerves, and fascia (Fig. 14.2d).
10. The distal portion of ECA is tied using a 6–0 silk suture (Fig. 14.2e) and then pulled rostrally (Fig. 14.2e asterisk).
11. The proximal portion of the ECA is tied loosely using a 6–0 silk suture (Fig. 14.2f), and the surgeon then ensures that no blood is flowing in the ECA.
12. A small incision is made in the portion between the distal and proximal sutures in the ECA using a 30-G needle (Dentronics, Japan) (Fig. 14.3a).
13. The prepared suture (step 2) is introduced into the ECA from the small incision (step 12). The tied suture in the proximal site of ECA (step 11) is loosened (Fig. 14.3b asterisk). The inserted suture is advanced to the bifurcation in the CCA and then moved slightly into the CCA (Fig. 14.3b).

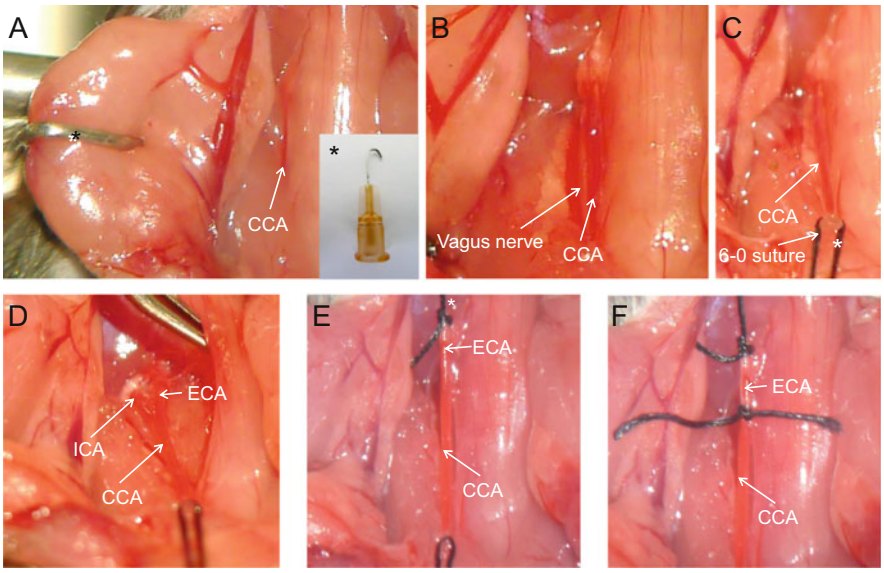

Fig. 14.2 Surgical procedures (protocols 6–11). (**a**) Protocol 6. The *asterisk* shows the retractor made from a 26-G needle. (**b**) Protocol 7. (**c**) Protocol 8. The *asterisk* shows the 6–0 silk suture around the CCA. (**d**) Protocol 9. (**e**) Protocol 10. The *asterisk* shows a 6–0 suture pulled in the direction of the rostrum. (**f**) Protocol 11. *CCA*, common carotid artery; *ECA*, external carotid artery; *ICA*, internal carotid artery

14. The suture tied to distal site of the ECA is pulled to the caudal (Fig. 14.3c asterisk) to change the direction of the inserted suture to ICA (Fig. 14.3c). The inserted suture is moved carefully to ensure that it does not enter the pterygo arteries until slight resistance is felt (Fig. 14.3d).
15. The suture tied to the distal site of the ECA, which is pulled to the caudal, is released (Fig. 14.3e #). The suture placed around the CCA is loosened to restore the blood flow (Fig. 14.3e asterisk).
16. The inserted suture is moved into the origin of the MCA until the CBF falls down (Figs. 14.4 and 14.5). Generally, 8–9 mm from the tip is sufficient to occlude the MCA.
17. A piece of PE-50 catheter is placed between the CCA and the suture around the CCA, and the suture is then tied to stop the flow in the CCA (Fig. 14.3f). Several drops of sterile saline are placed into the operative field to moisten the CCA, ICA, and ECA.

MCAo Model

18. Duration of ischemia is 40 min in our lab, but it should be adjusted to get sufficient infarct volume without causing high mortality. Typically, the CBF increases gradually 4–7 min after injury (# in Fig. 14.4a) and then drops

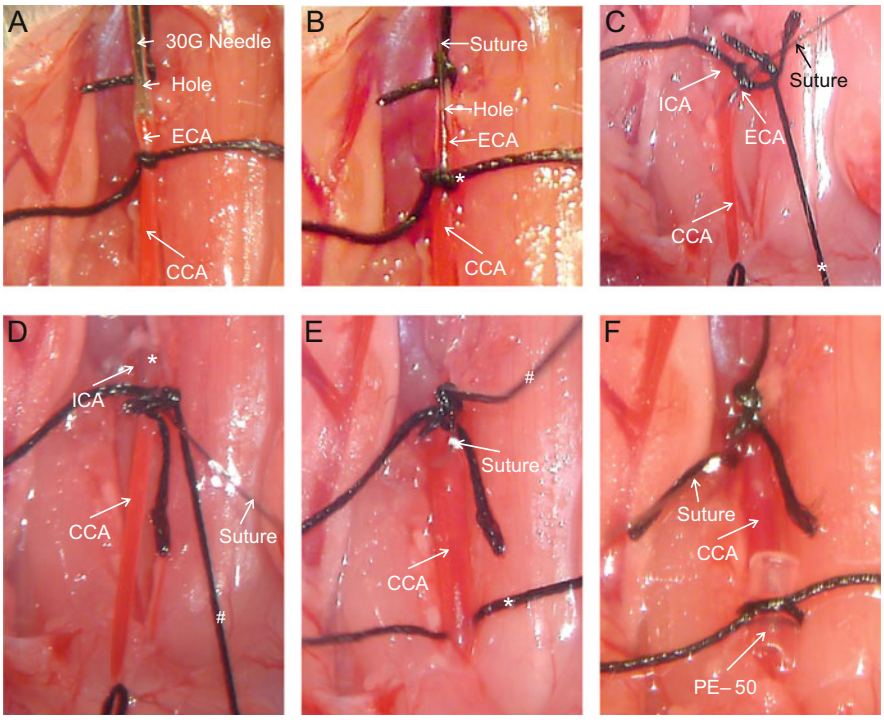

Fig. 14.3 Surgical procedures (protocols 12–14). (**a**) Protocol 12. (**b**) Protocol 13. The *asterisk* shows the loosened 6–0 suture in the proximal site of the ECA. (**c**) Protocol 14. (**d**) Protocol 14. The *asterisk* showed the tip of suture inserted into ICA. (**e**) Protocol 15. (**f**) Protocol 17. *CCA*, common carotid artery; *ECA*, external carotid artery; *ICA*, internal carotid artery

dramatically and recovers to the level of the CBF immediately after MCAo (# in Fig. 14.4a). This increase-drop-recovery wave occurs several times.

19. The suture is withdrawn carefully, and the 6–0 silk suture is tightened around the proximal site of the ECA. The CBF will recover slightly (Fig. 14.4a-19).
20. The level of isoflurane is reduced 1.4 % for 40 s.
21. The CCA is released from the PE-50 and the suture, and the CBF recovers gradually (Fig. 14.4a-20); the surgeon should then wait for at least 5 min to check the reperfusion. If the mean reduction in CBF in 40 min is <85 %, the mice should be excluded.
22. The incision is closed using a 4–0 silk suture with a simple interrupted pattern, and 0.25 % bupivacaine is administered at the incision site.
23. Recovery from anesthesia is monitored for 4 h, and tests for behavioral indications of infarction are performed. Typically the mice rotate to the right spontaneously or curl to left side when held by the tail.

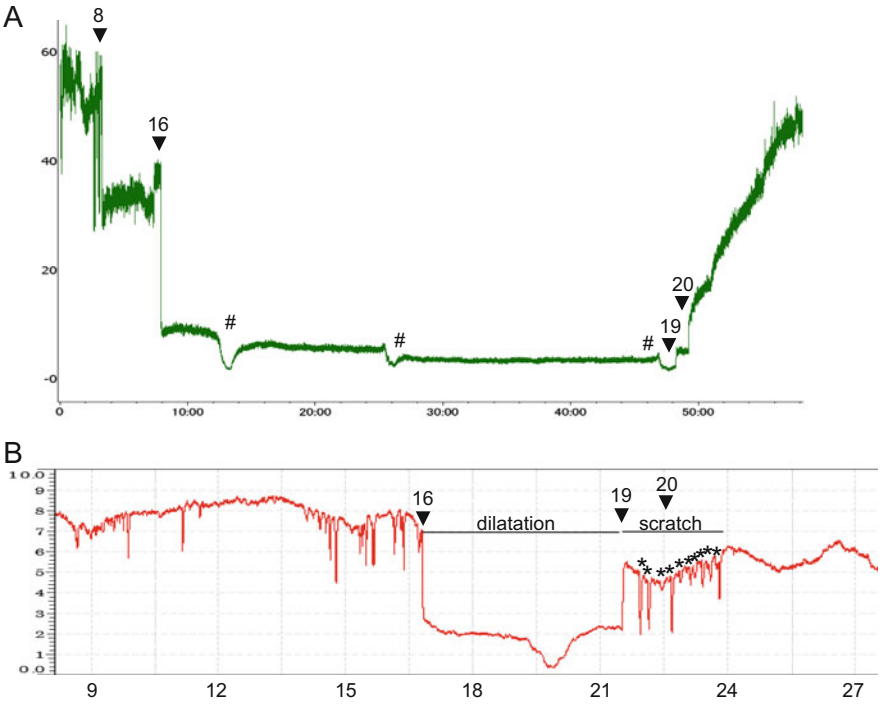

Fig. 14.4 Cerebral blood flow during surgery. (**a**) Middle cerebral artery occlusion model. (**b**) Intracranial internal carotid artery injury model. The *number* and *symbols* coincide with the protocol number mentioned in the main text (Fig. 14.4b was published previously [12])

IICAI Model (See the Schematic Diagram in Fig. 14.5a–c)

18. After waiting for 5 min, the suture is withdrawn carefully until the CBF recovers (Fig. 14.4b-19).
19. The suture is advanced again until the CBF is reduced; this is repeated 10 times to scratch the artery (Fig. 14.4b-20).
20. The inserted suture is withdrawn carefully. The 6–0 silk suture is tightened around the proximal site of the ECA.
21. The incision is closed using a 4–0 silk suture with a simple interrupted pattern, and 0.25 % bupivacaine is installed at the incision site.
22. Recovery from anesthesia is monitored for 1 h.

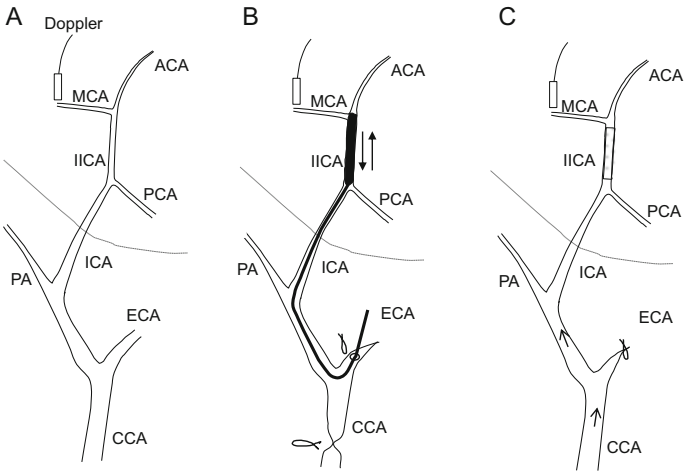

Fig. 14.5 Surgical procedures (protocols 15–17). (**a**) CBF is measured using laser Doppler in the right MCA area. (**b**) The intraluminal suture is advanced into the origin of the MCA. (**c**) The *dotted* area in the straight segment of the IICA will be damaged after IICAI. *Arrowhead*, the direction of blood flow. *ACA*, anterior cerebral artery; *CCA*, common carotid artery; *ECA*, external carotid artery; *IICAI*, intracranial internal carotid artery injury; *ICA*, internal carotid artery; *MCA*, middle cerebral artery; *PA*, pterygoid artery; *PCA*, posterior cerebral artery (Fig. 14.5 was published previously [12]). CBF was reduced compared with baseline (*arrowhead* in **b**). The suture is placed for 5 min, which dilates the artery. Slightly withdrawing the suture recovers CBF, and the suture is then advanced and withdrawn 10 times (*asterisks* in **b**)

14.4 Time Considerations

The MCAo model takes approximately 1 h from the start of surgery to reperfusion. The IICAI model requires around 40 min from the start of surgery to reperfusion.

14.5 Anticipated Results

14.5.1 MCAo Model

To check the infarct volume, the mice should be perfused with phosphate buffer followed by 4 % paraformaldehyde. The brain is removed carefully because an infarct brain is fragile. Postfixation is performed using 4 % paraformaldehyde for 12–24 h, and the brain is then immersed into 15 % sucrose for 1 day followed by 30 % sucrose for 2 days to cryoprotect the tissue. It is then embedded in a 1:2 mixture of 20 % sucrose and Tissue-Tek® OCT compound (Sakura FineTek,

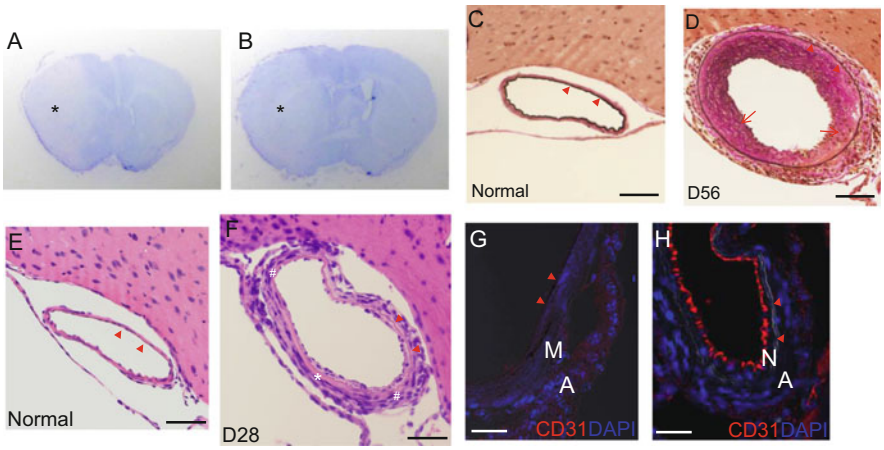

Fig. 14.6 Typical images of an infarcted brain and injured IICA. (**a** and **b**) Typical image of a cresyl violet-stained brain at +1.4 mm (**a**) or 0 mm (**b**) from the bregma 72 h after MCAo. The *white* areas (*asterisks*) show the infarcted areas. (**c** and **d**) Images of EVG staining in the normal IICA (**c**) or injured IICA on day 56 (**d**). *Red arrowhead*, internal elastic lamina; *red arrow*, neointimal hyperplasia. Bar = 50 μm. (**e** and **f**) Images of H&E staining in the normal IICA (**e**) or injured IICA on day 28 (**f**). Nuclei are not observed in the damaged media (*). On day 28, damaged media (*), mixed media, and adventitia (#) are observed. *Red arrowhead*, internal elastic lamina. Bar = 50 μm. (**g** and **h**) Immunohistochemistry for CD31. The endothelium is removed completely on day 1 (**g**). Re-endothelialization is almost complete on day 28 (**h**). *M* media, *a* adventitia, *N* neointimal; *red arrowhead*, internal elastic lamina. Bar = 25 μm (Fig. 14.6c–h was published previously [12]). *IICA* intracranial internal carotid artery, *MCAo* middle cerebral artery occlusion

Japan) and frozen in isopentan chilled in liquid nitrogen. The mixture containing 20 % sucrose prevents the section from curling. The tissue is cut into 12- to 30-μm thick sections using a cryostat, and the sections are stained with cresyl violet (031-04852, Wako, Japan). The infarct area presents as an unstained area in the cerebral cortex and caudate putamen (Fig. 14.6a, b). There are some variations in infarct volume even when the patterns of cerebral blood flow are similar [15]. Generally, the variation is greater in the caudal region, such as −1.4 mm from the bregma.

Alternatively, "TTC staining" could be used to visualize the infarct area. Here, fresh unfixed tissues are immersed in a 2 % solution of 2,3,5-triphenyltetrazolium chloride (TTC; Nakalai tesque) in normal saline at 37 °C for 15–30 min [16]. Alive tissues reveal red regions, but infarcted regions show white (unstained) in the cerebral cortex and caudate putamen [17]. Generally, TTC staining is quicker and makes it easier to distinguish the infarct area, but additional staining or immunohistochemistry cannot be performed.

14.5.2 IICAI Model

The brain fixed by perfusion with 4 % paraformaldehyde and depicted carefully to avoid damaging the circle of Willis. Postfixation is performed using 4 % paraformaldehyde for 24–48 h, and the brain is embedded in paraffin. For morphological analysis, cross-sections (6 μm) including the straight portion of IICAs are made (Fig. 14.5c).

For morphological analysis, EVG staining is suitable for observing the neointima because it shows the internal/external elastic lamina and the neointima is clearly distinguishable (Fig. 14.6c, d). H&E staining is suitable for assessing cellular infiltration and necrotic changes in the media (Fig. 14.6e, f). This staining reveals that the IICAs are dilated to double the size of a normal artery on day 1, without causing hemorrhage or disruption to the internal elastic lamina. Inflammatory cells start to accumulate outside the vessel wall on day 7. Neointimal hyperplasia begins to be observed from day 14 and continued to be grown up with increased thickness of adventitia, while the media was gradually extinct. The internal elastic lamina does not disappear throughout the remodeling process [12].

Immunohistochemistry for CD31 (anti-CD31 antibodies; 1:200, Spring Bioscience, Fremont, CA, USA) is helpful to check whether the endothelium was removed successfully after injury. The endothelium is removed 1 day after injury (Fig. 14.6g). In the IICAI model, re-endothelialization starts from day 7, and endothelial cells cover the vessel completely on day 28 (Fig. 14.6h). In addition, damage to the smooth muscle cells in the media can be assessed using immunohistochemistry for αSMA (1:1000, Sigma-Aldrich, St. Louis, MO, USA). αSMA-positive smooth muscle cells are lost completely on day 1 after injury (Fig. 14.7), partly due to apoptosis [18]. Unlike endothelial cells, αSMA-positive smooth muscle cells do not reemerge in the damaged media (Fig. 14.7c, d). However, αSMA-positive smooth muscle cells emerge in the neointima on day 28 (Fig. 14.7c). Immunohistochemistry for F4/80 (1:1000, Abcam, Cambridge, MA, UK) shows the unique pattern of activated macrophage infiltration in the intracranial arteries. Macrophages are observed mainly in the adventitia from day 7 and continue to be observed until day 56. F4/80-positive macrophages infiltrate into the media on day 14 but are absent on day 7 (Fig. 14.7e, f). Few F4/80-positive macrophages are observed in the neointima. We previously compared the remodeling processes in IICAs and extracranial arteries (femoral arteries) [12] and found that IICAs had a unique remodeling process. Briefly, the timing of neointimal formation is slower, SMCs are lost continuously in the media followed by extinction of the media itself, macrophages invade in the media on day 14, and the adventitia grows continuously until day 56. This unique process may be caused by differences in complexed wall share stress in the circle of Willis, cyclic circumferential strain due to the structural differences in the vessel walls, and easy macrophage invasion into the media due to the lack of an external elastic lamina [12].

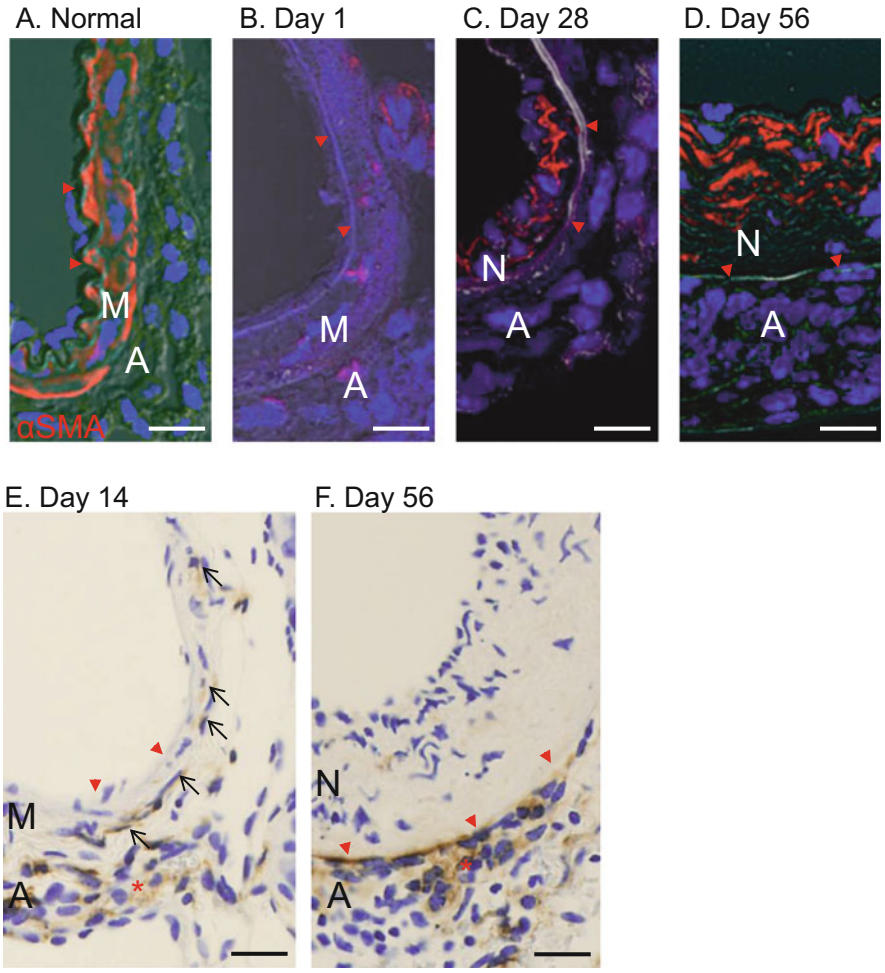

Fig. 14.7 αSMA-positive smooth muscle cells in media and F4/80 macrophages in injured IICAs. (**a**) Normal IICAs have αSMA-positive SMCs in the media. (**b**) They were lost on day 1 after injury (**b**). (**c** and **d**) These cells had not reemerged in the damaged media on days 28 and 56. However, αSMA-positive SMCs began to appear in the neointima (**c** and **d**). (**e** and **f**) F4/80-positive macrophages were observed mainly in the adventitia (*asterisk*). Some macrophages invaded into the media on day 14 (**e**, *arrow*). IICA, intracranial internal carotid artery; ICA, internal carotid artery; *M*, media; *A*, adventitia; *N*, neointimal; *red arrowhead*, internal elastic lamina; *arrows*, F4/80-positive cells in the media. Bar = 20 μm (Fig. 14.7a–f was taken from [12])

Neointimal formation in this model could be prevented by the intraperitoneal injection of rapamycin, similar to femoral arteries [19] where rapamycin (4 mg/kg/day in 0.33 % DMSO/0.2 % sodium carboxymethyl cellulose/0.25 % polysorbate-80) was started immediately after injury and continued once a day for 56 days without affecting re-endothelialization [12].

References

1. Jeng J-S, Tang S-C, Liu H-M. Epidemiology, diagnosis and management of intracranial atherosclerotic disease. Expert Rev Cardiovasc Ther. 2010;8:1423–32.
2. Schumacher HC, Meyers PM, Higashida RT, Derdeyn CP, Lavine SD, Nesbit GM, Sacks D, Rasmussen P, Wechsler LR. Reporting standards for angioplasty and stent-assisted angioplasty for intracranial atherosclerosis. J Vasc Interv Radiol. 2009;20:S451–73.
3. Arenillas JF, Molina CA, Chacón P, Rovira A, Montaner J, Coscojuela P, Sánchez E, Quintana M, Alvarez-Sabín J. High lipoprotein (a), diabetes, and the extent of symptomatic intracranial atherosclerosis. Neurology. 2004;63:27–32.
4. Chen S, Hanel RA. The final SAMMPRIS results: a review. World Neurosurg. 2014;82:5–6.
5. Stenting of Symptomatic Atherosclerotic Lesions in the Vertebral or Intracranial Arteries (SSYLVIA): study results. Stroke. 2004;35:1388–92.
6. Gröschel K, Schnaudigel S, Pilgram SM, Wasser K, Kastrup A. A systematic review on outcome after stenting for intracranial atherosclerosis. Stroke. 2009;40:e340–7.
7. Gupta R, Al-ali F, Thomas AJ, Horowitz MB, Barrow T, Vora NA, Uchino K, Hammer MD, Wechsler LR, Jovin G. Drug-Eluting Stent Placement in the Intracranial. Stroke. 2006. doi:10.1161/01.STR.0000242481.38262.7b.
8. Fields JD, Petersen BD, Lutsep HL, Nesbit GM, Liu KC, Dogan A, Lee DS, Clark WM, Barnwell SL. Drug eluting stents for symptomatic intracranial and vertebral artery stenosis. Interv Neuroradiol. 2011;17:241–7.
9. Chimowitz MI, Lynn MJ, Derdeyn CP, et al. Stenting versus aggressive medical therapy for intracranial arterial stenosis. N Engl J Med. 2011;365:993–1003.
10. Walmsley JG, Canham PB. Orientation of nuclei as indicators of smooth muscle cell alignment in the cerebral artery. Blood Vessels. 1979;16:43–51.
11. Lee RM. Morphology of cerebral arteries. Pharmacol Ther. 1995;66:149–73.
12. Shimamura M, Nakagami H, Sata M, et al. Unique remodeling processes after vascular injury in intracranial arteries: analysis using a novel mouse model. J Cereb Blood Flow Metab. 2013;33:1153–9.
13. Caso JR, Pradillo JM, Hurtado O, Lorenzo P, Moro MA, Lizasoain I. Toll-like receptor 4 is involved in brain damage and inflammation after experimental stroke. Circulation. 2007;115:1599–608.
14. Kim HA, Whittle SC, Lee S, Chu HX, Zhang SR, Wei Z, Arumugam TV, Vinh A, Drummond GR, Sobey CG. Brain immune cell composition and functional outcome after cerebral ischemia: comparison of two mouse strains. Front Cell Neurosci. 2014;8:365.
15. Shimamura M, Nakagami H, Osako MK, Kurinami H, Koriyama H, Zhengda P, Tomioka H, Tenma A, Wakayama K, Morishita R. OPG/RANKL/RANK axis is a critical inflammatory signaling system in ischemic brain in mice. Proc Natl Acad Sci U S A. 2014;111:8191–6.
16. Shimamura M, Sato N, Oshima K, Aoki M, Kurinami H, Waguri S, Uchiyama Y, Ogihara T, Kaneda Y, Morishita R. Novel therapeutic strategy to treat brain ischemia: overexpression of hepatocyte growth factor gene reduced ischemic injury without cerebral edema in rat model. Circulation. 2004;109:424–31.
17. Shimamura M, Taniyama Y, Katsuragi N, Koibuchi N, Kyutoku M, Sato N, Allahtavakoli M, Wakayama K, Nakagami H, Morishita R. Role of central nervous system periostin in cerebral ischemia. Stroke. 2012;43:1108–14.
18. Kurinami H, Sato N, Shinohara M, Takeuchi D, Takeda S, Shimamura M, Ogihara T, Morishita R. Prevention of amyloid beta-induced memory impairment by fluvastatin, associated with the decrease in amyloid beta accumulation and oxidative stress in amyloid beta injection mouse model. Int J Mol Med. 2008;21:531–7.
19. Shan J, Nguyen TB, Totary-Jain H, Dansky H, Marx SO, Marks AR. Leptin-enhanced neointimal hyperplasia is reduced by mTOR and PI3K inhibitors. Proc Natl Acad Sci U S A. 2008;105:19006–11.

Part VIII
Kawasaki Disease

Chapter 15
Analysis of Kawasaki Disease Using a Mouse Model, CAWS Vasculitis in DBA/2 Mice, Induced with a Water-Soluble Extracellular Polysaccharide Fraction Obtained from *Candida albicans*

Naoto Hirata and Naohito Ohno

Abstract It was reported previously that a *Candida albicans* water-soluble fraction (CAWS), including a mannoprotein and β-glucan complex, has strong potency in inducing fatal necrotizing arteritis in DBA/2 mice. In this article, histopathological changes and cardiac function in this system are reviewed. One mg/day CAWS was given to DBA/2 mice via peritoneal injection for 5 days. Aortitis was induced in the CAWS-treated DBA/2 mice, which died at an incidence of 100 % within a few weeks. Histological findings included stenosis in the left ventricular outflow tract (LVOT) and severe inflammatory changes of the aortic valve with fibrinoid necrosis. Cardiomegaly was observed and heart weight increased 1.62-fold ($P < 0.01$). Echocardiography revealed a severe reduction in contractility and dilatation of the cavity in the left ventricle (LV): LV fractional shortening (LVFS) decreased from 71 % to 38 % ($P < 0.01$), and the LV end-diastolic diameter (LVDd) increased from 2.21 to 3.26 mm ($P < 0.01$). The titer of BNP mRNA increased in the CAWS-treated group. Severe inflammatory changes resulting from CAWS brought about lethal LV dysfunction by aortic valve deformation with LVOT stenosis. This animal model is suggested to be extremely useful not only for analyzing KD but also for the development of therapeutic agents for various types of heart failure.

N. Hirata
Department of Pharmacy, Nagano Red Cross Hospital, 5-22-1 Wakasato, Nagano, Japan

Laboratory for Immunopharmacology of Microbial Products, School of Pharmacy, Tokyo University of Pharmacy and Life Sciences, 1432-1 Horinouchi, Hachioji, Tokyo 192-0392, Japan

N. Ohno (✉)
Laboratory for Immunopharmacology of Microbial Products, School of Pharmacy, Tokyo University of Pharmacy and Life Sciences, 1432-1 Horinouchi, Hachioji, Tokyo 192-0392, Japan
e-mail: ohnonao@toyaku.ac.jp

M. Sata (ed.), *Mouse Models of Vascular Diseases*,
DOI 10.1007/978-4-431-55813-2_15

Keywords *Candida albicans* • DBA/2 mice • Vasculitis • Kawasaki disease • Heart failure

15.1 Introduction

According to statistics from the World Health Organization (WHO) [1], among the world's leading causes of death were ischemic heart disease (12.8 %) and cerebrovascular disorder (10.8 %). Indeed, both diseases have firmly maintained their ranks as the top causes of death for many years, despite the development of treatments and preventive medicine. While cardiovascular diseases represent a threat to all mankind, enormous medical resources have been put into the treatment of these diseases, having a huge impact from the medical-economic viewpoint. In addition to research on the pathogenesis of these cardiovascular diseases, the development of treatment methods and novel drugs, as well as the investigation of treatment protocols, requires the accumulation of evidence through large-scale clinical studies. Furthermore, the establishment of excellent animal models is essential in basic studies and at preclinical stages.

In recent years, research results have shown that, in patients with reduced cardiac function after atherosclerosis or myocardial infarction, the activation and accumulation of inflammatory cells play important roles in the progression of lesions, which induce pathological structural changes, called remodeling of cardiovascular tissues, associated with persistent chronic inflammation [2]. During the onset and progression of atherosclerosis, damage to vascular endothelial cells, infiltration of activated macrophages into the vessel wall, and foam cell formation due to endocytosis of oxidized low-density-lipoprotein (LDL) cholesterol are observed [3]. Moreover, calcified lesions observed as a pathological feature of atherosclerosis are the final outcome of chronic inflammation, and clinically, inflammation markers such as high-sensitivity C-reactive protein (CRP) (hsCRP) have been suggested to be useful indices of atherosclerosis [4]. Furthermore, in patients with acute myocarditis, pericarditis, and vasculitis, the involvement of infection in the cardiovascular system and immune responses has been suggested. Many cases of vasculitis are intractable and of unknown pathogenesis. Among such cases, Kawasaki disease is representative and has been studied in Japan before the rest of the world, with notable advances [5].

Kawasaki disease was first reported in 1967 by Dr. Tomisaku Kawasaki, who then worked as a pediatrician at the Japanese Red Cross Medical Center. He analyzed and verified 50 of his patients and published an article reporting this condition, which was referred to as "acute febrile mucocutaneous syndrome with lymphoid involvement" [6]. This was followed by a succession of case reports mainly in Japan as well as in other Asian countries; subsequently, the name Kawasaki disease (KD) became established. This disease develops during childhood in most patients and is characterized by the formation of refractory inflammatory lesions in small+ and medium-sized arteries throughout the body. The

prognoses reported at the time of this report, which were compiled from 1967 to 1971, included 26 deaths out of 1857 cases, that is, a mortality rate of 1.4 %. At that time, the causes of death among those patients were unclear; however, from the fact that 30 % of the patients developed complications with coronary artery dilation and coronary aneurysms as sequelae after onset, it became clear that the presence or absence of coronary complications greatly affects the prognosis of KD [7]. In Japan, the number of patients with KD has been reported to be about 5000–6000 annually since the 1980s. The number of patients identified as having KD is increasing with improved diagnostic technologies, and more than 10,000 patients have been reported every year since 2004 [8].

The causes of KD are still unclear; thus, animal models of vasculitis syndromes, including KD, are useful for the development of methods of pathological analysis and treatments of vasculitis. In 1987, it was reported that the *Candida albicans*-derived substance (CADS) isolated from the feces of KD patients caused coronary arteritis that resembled KD in mice [9]. Following this report, collaborative research in our immunology laboratory found that the *C. albicans* water-soluble extracellular polysaccharide fraction [or *C. albicans* water-soluble fraction: (CAWS)] obtained from the culture supernatant of *C. albicans* had a strong vasculitis-inducing effect, as well as lethal activity, in highly sensitive mice such as DBA/2 mice [10, 11]. The administration of CAWS to DBA/2 mice causes the development of vasculitis in areas around the aortic valve and the coronary artery origin (CAWS vasculitis) [12]. Previous studies have shown that the main component of CAWS is the mannoprotein [13] and that when administered intravenously, CAWS exhibits acute lethal toxicity in mice, whereas intraperitoneal administration of CAWS causes severe vasculitis mainly in the aortic root and around the aortic valve as well as in the proximal portion of the coronary arteries. Moreover, these activities show significant variations between different mouse strains [10–14]. A murine model of CAWS vasculitis has been analyzed as an animal model that appropriately reflects the histopathology and pathological conditions of vasculitis syndromes, including KD. However, with regard to the powerful chronic lethal toxicity observed only in DBA/2 mice, many aspects remain unclear. It is possible that certain cardiovascular complications underlie the development of severe vascular lesions in DBA/2 mice; hence, this model potentially serves as a useful animal model for cardiovascular diseases as well as vasculitis. To this end, a detailed analysis of vascular lesion formation processes in DBA/2 mice and a thorough examination of the effects of vascular lesions on the biology of DBA/2 mice are required.

One of the representative examples of chronic and fatal conditions associated with cardiovascular lesions is chronic heart failure. Chronic heart failure is regarded as a condition that develops in later stages, as triggered by various cardiovascular abnormalities such as ischemic heart disease, valvular disease, cardiomyopathy, and pericarditis. Chronic heart failure is defined as “the pathological state of impaired pump function due to chronic myocardial contractile dysfunction, in which cardiac output is insufficient to meet blood volume for supplying oxygen requirement of important peripheral organs, and blood congestion in lung or

systemic veins disturbs vital activities for living of the patients" [15]. As chronic heart failure gradually progresses, as it transitions from the period of compensation to the period of decompensation, patients with chronic heart failure are repeatedly hospitalized and discharged owing to occasional acute exacerbation, with their cardiac function declining gradually.

There are various ways to classify heart failure depending on the causes, pathological conditions, stage, and subjective symptoms. The NYHA classification [16] proposed by the New York Heart Association (NYHA) has been used commonly in routine clinical settings owing to its convenience. The severity of heart failure is classified on the basis of subjective symptoms, including dyspnea on exertion, shortness of breath, decreased urine volume, edema in the limbs, hepatomegaly, and loss of appetite. In patients with heart failure, the development of these symptoms leads to decreased quality of life (QOL). In particular, at NYHA III or higher, the decrease in QOL is so significant that it interferes with the patient's daily life. In end-stage heart failure, patients generally show resistance to drug therapy, and owing to the heart burden induced by exacerbation of chronic kidney disease and respiratory failure, patients eventually develop resistance to diuretics administered in large amounts as well as to intravenous catecholamines that are given as the last resort. The prognosis of chronic heart failure is very poor, and patients with NYHA II heart failure or higher have prognoses as poor as or worse than those of advanced cancer patients, with a high frequency of sudden death due to fatal arrhythmia.

Drug therapy for chronic heart failure is mainly aimed at improving QOL and prognosis and includes vasodilator therapy with renin-angiotensin-aldosterone system inhibitors (ACE inhibitors, ARB), combined with diuretics, β receptor antagonists, and other drugs. The continued use of several drugs over the long term is required in almost all patients. The ACC/AHA Guidelines for the Management of Heart Failure [17], proposed by the relevant cardiovascular societies in the United States, emphasize preventive medicine according to the classification of heart failure stages, with a focus on heart failure risk factors such as hypertension, diabetes, and obesity. The guidelines recommend that, if even one risk factor is identified, the patient should be classified as Stage A and proactive medical and pharmaceutical interventions should be provided before onset, regardless of whether the patient presents with normal cardiac function or has no symptoms. The prognosis of patients with heart failure has steadily improved owing to the proper use of multidrug combination therapy and with advances in treatment technology. In this context, the role of pharmacists is considered very important for the management of heart failure in day-to-day clinical settings.

Currently, treatments for heart failure performed in clinical practice are based on drugs and treatment protocols recommended by the guidelines, the effects of which have been demonstrated on the basis of the vast amount of evidence accumulated through a number of prospective, large-scale clinical studies. The number of participants per study is in the hundreds or even tens of thousands, and improved QOL and extended life prognosis are considered as the most important outcomes. In Japan, attempts are also being actively made by pharmacists to establish evidence

by themselves. However, at the practical clinical level, there are obstacles for pharmacists alone to design and carry out a prospective clinical study as well as to analyze clinical data. Moreover, from the legal and basic medical knowledge perspectives, it is extremely difficult to continue a study without the cooperation of physicians. In this sense, good animal models of cardiovascular diseases play a very important role, serving as a bridge to fill the gap between preclinical basic research and clinical practice.

When applying the CAWS vasculitis model to research at the preclinical level, a basic study of the pathogenesis of vasculitis along with a detailed examination of cardiovascular complications is essential. Saijo et al. revealed that CAWS is a type of fungus-derived pathogen-associated molecular pattern (PAMP) and the mannoprotein, which is responsible for the core activities of CAWS, is recognized by dectin-2, an innate immune receptor [18]. However, the structure of the sugar chains constituting the mannoprotein, with which the main activities of CAWS are associated, is very complex, and since it has not been sufficiently analyzed, several analysis methods need to be combined in order to determine the sugar chain structure. Furthermore, since the progression of vascular lesions primarily occurs in the extracellular matrix structure, it is likely important structurally to compare sugar chains that constitute host connective tissues and sugar chains of CAWS and to analyze their structural similarities and interactions in sugar chain recognition in order to elucidate the mechanisms of vasculitis development. On the other hand, it has been shown that the sugar chain structure and biological activities of CAWS, such as vasculitis inducibility, vary significantly depending on the culturing conditions of *C. albicans*. *C. albicans* is a resident fungus in humans and causes infections. Therefore, important clues can be obtained from the growth conditions of *C. albicans,* which could lead to the development of vasculitis caused by the microorganism-derived components.

15.2 Histopathological Characteristics of CAWS Vasculitis in DBA/2 Mice

The acute toxicity, sensitivity to vasculitis induction, cytokine-inducing ability, and production of compounds, such as nitric oxide (NO), of CAWS largely differ among different mouse strains [10–14, 19]. CAWS administered intravenously is not lethally toxic in DBA/2 mice, but when administered intraperitoneally, these mice develop severe vasculitis, and 100 % die within a few weeks of follow-up observation [12]. Shinohara et al. and Uchiyama et al. reported [20, 21] that CAWS exhibits vasculitis-inducing activity following its continuous administration at 250 μg for 5 days, and exacerbation of vasculitis and shortening of survival were observed in a dose-dependent manner. During the observation period of about 10 weeks, the minimum dose of CAWS that resulted in the death of 100 % of mice was 4 mg administered continuously for 5 days. However, vasculitis was

observed at any dose; 100 % mortality can be observed over an extended period of observation, even at a low dose. Below, the process leading to the progression of vasculitis from the onset, the pathological features, and the characteristics of survival rate and lethal toxicity are described [22].

One week after CAWS administration, infiltration of inflammatory cells from the adventitial side into the medial elastic fibers is observed around the aortic valve from the sinus of Valsalva. The inflammatory tissue mainly consists of polymorphonuclear leukocytes, along with other cells including monocytes, histiocytes, and lymphoid cells. As inflammatory cells are also found near the intima, the presence of inflammation in the intima cannot be ruled out; however, there is no evidence suggesting the release of endothelial cells, that is, the formation of a thrombus.

In the second week, inflammatory changes from the adventitial/medial side toward the intimal side progress significantly, mainly in the aortic root including the aortic annulus, the origin of the coronary arteries, and the portion of sinus of Valsalva where branching to the coronary arteries occurs, and infiltration of inflammatory cells, mainly polynuclear leukocytes, along the elastic fibers is observed. At this point, inflammation of the intima has also occurred, although fewer polymorphonuclear leukocytes are involved than in the case of the adventitia, with more histiocyte-like cells. No obvious thrombi, the formation of which suggests the release of endothelial cells in the lumen of inflamed tissue, are observed.

At 3 weeks and thereafter, inflammatory lesions markedly expand over the entire circumference including the noncoronary arteriovenous sinus. In some parts, an abscess forms, as well as fibrinoid necrosis in the medial elastic fibers. The basic structure of the blood vessels, including the intima, medial elastic fibers, and adventitia, is destroyed, and significant vascular lesions form, to the extent that the aortic root exhibits advanced stenosis due to the marked thickening of the media, and the aortic valve tissue is severely deformed (Fig. 15.1).

The characteristics of inflammatory cells in CAWS vasculitis and how they affect the microstructure of the arteries were investigated in detail. Elastica van Gieson (EVG) staining revealed destroyed tunica media elastic lamina and inflammatory cells directly infiltrating into the extracellular matrix structure. Furthermore, 2 weeks after CAWS administration, infiltration of granulocyte cells through the elastic fibers was observed in vasculitis lesions. Inflammatory cells of various origins were observed, partly forming an abscess, and the infiltration of granulocytes abundantly containing granules within the cells, histiocytes filled with nuclei, and lymphoid cells was observed. These findings clearly showed that, in DBA/2 mice, CAWS vasculitis is characterized by marked infiltration and accumulation of various inflammatory cells, leading to the destruction of the basic three-layer structure of the arteries [22].

In addition to the name and definition of vasculitis according to the classification of Fauci et al., the Chapel Hill Consensus Conference (CHCC) proposed a vasculitis classification in 1994 [23]. According to the CHCC classification, in which vasculitis is classified on the basis of the size of vessels containing lesions, some forms of vasculitis show lesions in large vessels such as the aorta (giant cell arteritis or temporal arteritis, Takayasu's arteritis), whereas other forms show lesions in

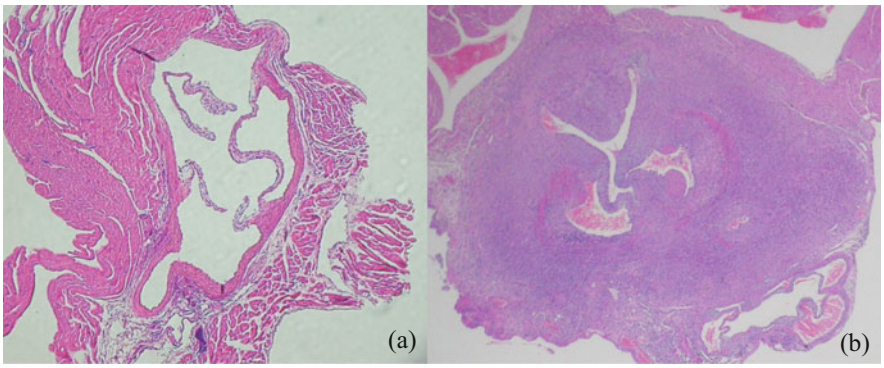

Fig. 15.1 Severe aortic valve stenosis of CAWS arteritis in DBA/2 mice
CAWS treatment DBA/2 mice were administered with CAWS via peritoneal injections for five consecutive days
(**a**) Untereated aortic valve of DBA/2 mouse, (**b**) The deformed aortic valve at fourth week after CAWS administration in DBA/2 mouse

small- to medium-sized arteries that branch into each organ or tissue (polyarteritis nodosa, KD, Wegener's granulomatosis, and Churg-Strauss syndrome). Other forms accompanying capillary inflammation include Henoch-Schonlein purpura and hypersensitivity vasculitis. Various clinical symptoms are presented depending on the site of the blood vessel affected. Almost 20 years has passed since the establishment of the classification, and with discussions regarding the handling of ANCA-related vasculitis among others, a new classification based on international clinical studies (DCVAS) [24] and a revised version of CHCC (CHCC 2012) have recently been proposed [25]. Regarding CAWS vasculitis observed in this study, inflammatory lesions found in all layers and over the entire circumference are observed in the aortic root as well as in the proximal portion of the coronary arteries. Thus, in terms of the site of lesion formation, CAWS vasculitis resembles KD. From the viewpoint of how inflammatory lesions develop over time, CAWS vasculitis shares more similarities with giant cell arteritis or Takayasu's arteritis, which develops from the adventitial side, as the accumulation of inflammatory cells toward the adventitial side is observed in the earliest stage, with almost no formation of thrombus (which strongly suggests desquamated endothelial cells and intimal damage). Histologically, however, CAWS vasculitis is classified as necrotizing vasculitis, since the basic vessel structure is destroyed 3 weeks after CAWS administration, and fibrinoid necrosis of the medial elastic fibers and intimal thickening are observed [26]. Inflammatory tissue is composed primarily of polynuclear leukocytes, and as inflammatory cells accumulate in the adventitia, migrate, and invade into the vasa vasorum, the infiltration progresses along the elastic fibers of the tunica media, possibly expanding inflammatory lesions [27, 28].

Although the localized nature of vascular lesions has not been fully elucidated, the involvement of anti-aortic antibodies (autoantibodies responsive to endothelial cells) in Takayasu's arteritis and immune complexes and antineutrophil

cytoplasmic antibodies (ANCAs) in vasculitis of the small- and medium-sized vascular system has been suggested [26]. Thus, it is possible that there is a dependence on the type of autoantigen. Moreover, given that the formation of vascular lesions, including atherosclerosis, often occurs in branched or curved areas of the arteries, physical stimuli in the vascular tissue, such as shear stress at branch points and sudden changes in wall pressure and blood flow, might be related to endothelial cell damage, with possible involvement in the localized nature of the lesions [29].

CAWS vasculitis represents an inflammatory response accompanied by significant enlargement of the spleen, and *in vitro* CAWS stimulation has been reported to increase inflammatory cytokine production markedly in splenocytes of DBA/2 mice [12]. The incidence and lethal toxicity of CAWS vasculitis, as well as its cytokine-inducing ability, greatly vary between different mouse strains [10–14, 19]. Associations between some forms of vasculitis and HLA alleles in humans have been suggested [30], but how the H-2 allele is associated with vasculitis in mice has not been examined fully. Moreover, DBA/2 mice are known to develop epicardial calcification frequently, which has been reported to be attributable to their abnormal nutritional status [31]. Since evidence of calcification is interpreted as the final outcome of inflammatory responses, the possibility cannot be ruled out that DBA/2 mice are susceptible to chronic inflammation of the vascular system.

In an animal model of KD-like vasculitis, vasculitis that resembles KD [32] can be caused by not only fungus-derived substances such as CAWS and CADS but also bacterium-derived substances such as *Lactobacillus casei* cell wall extracts (LCWE/LCCWE). In recent years, many reports have suggested the involvement of microbial infection and microbial antigens as a cause of vasculitis. These include the involvement of viruses such as human immunodeficiency virus, parvovirus B19, cytomegalovirus, and varicella-zoster virus and the involvement of infections by bacteria such as *Staphylococcus aureus* [33]. With the development of research on innate immunity, immunoactivating substances derived from microorganisms are now collectively referred to as PAMPs [34]. PAMPs are recognized by the innate immune system and control the differentiation of T cells through the activation of dendritic cells [35]. Many immunostimulants generally possess the characteristics of PAMPs, and although immunostimulants cause fewer side effects, various effects of PAMPs that stimulate immune responses could result in adverse events. It is worth noting that the murine model of CAWS vasculitis provides data suggesting this possibility.

Apo-E KO mice have been used widely as an animal model of atherosclerotic lesions. In Apo-E KO mice, arterial lesions are reported mainly to represent vascular endothelial cell damage due to abnormal lipid metabolism [36]. CAWS vasculitis initially develops from the adventitial side, and intimal thickening is not observed until the later stages of the inflammatory response. In Apo-E KO mice, however, the involvement of the medial elastic fibers and adventitia is hardly observed during the initial stage. From this perspective, the process of lesion formation greatly differs.

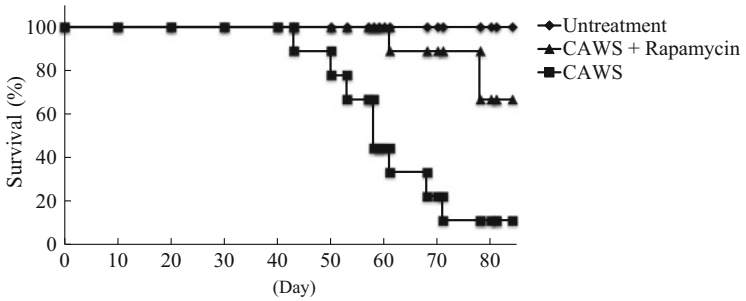

Fig. 15.2 Kaplan-Meier analysis of CAWS arteritis and efficacy of the therapeutic agent (rapamycin) in DBA/2 mice
CAWS-treated DBA/2 mice were administered with CAWS via peritoneal injections for five consecutive days. DBA/2 mice at 4 or 5 weeks of age were maintained in specific pathogen free (SPF) conditions and observed every day. Rapamycin (anti-inflammatory agent) was co-administered with CAWS

In the present model, vasculitis was induced in 100 % of the DBA/2 mice administered CAWS, and inflammatory responses were elicited in the initial stage following CAWS administration, which were so intense as to cause significant vascular lesions in a short period of time. CAWS vasculitis was not only limited to lesions in the aorta, but was also accompanied by advanced lesions of coronary artery origin, as well as in the aortic valve. The progression of CAWS vasculitis almost plateaus in about 4 weeks after administration, but in DBA/2 mice, lethal toxicity was observed from around 5 to 6 weeks. Furthermore, about 100 % died during the follow-up observation of a few weeks (Fig. 15.2). This trend is more significant in this strain than in other strains of high-CAWS-sensitivity mice, including C57Bl/6 and BALB/c mice. The cause of mortality in DBA/2 mice is difficult to explain solely on the basis of severe vasculitis, and since it takes several weeks of observation following the complete development of vasculitis until death, it is highly likely that sudden death was caused by the induction of fatal ventricular arrhythmia due to damage to the cardiac conduction system by remodeling, or complications with cardiac dysfunction due to aortic stenosis and regurgitation, or ischemic heart disease in DBA/2 mice with CAWS vasculitis. Furthermore, given that patients with acute heart failure or end-stage heart failure present with moist skin and cool extremities due to peripheral circulatory failure, as well as loss of appetite, it is possible that symptoms such as poor coat condition and weight loss, which appears to be due to decreased appetite, in DBA/2 mice might have resulted from heart disease complications. Taking these findings together, clarification of pathological conditions and cause of death in DBA/2 mice will require detailed studies, particularly one that focuses on the heart.

More detailed analysis of the pathological conditions of the present model will not only lead to the elucidation of vascular lesion formation mechanisms but also increase the utility of this strain as an excellent animal model to examine methods for treating cardiovascular diseases in preclinical stages.

15.3 Analysis of DBA/2 Mice as an Animal Model of CAWS Vasculitis with Left Ventricular Dysfunction

As described above, the murine model of CAWS vasculitis has contributed to the advancement of research as an animal model of KD. Despite this background, in humans, not all KD cases follow a simple clinical course of vasculitis alone, and some develop sequelae and complications such as coronary artery dilation and aneurysms, occasionally leading to death [6, 7]. Severe CAWS vasculitis is also induced in C57Bl/6 mice and BALB/c mice, but these other high-CAWS-sensitivity mice do not exhibit such severe lethal toxicity compared with DBA/2 mice [19]. Moreover, as mentioned above, the progression of CAWS vasculitis plateaus at 3–4 weeks after CAWS administration, whereas the lethal toxicity in DBA/2 mice was found appear after an observation period of several weeks. Taking these findings together, the lethal toxicity of CAWS vasculitis may not be primarily attributable to vasculitis itself. Rather, it is highly likely that valvular disease and ischemic heart disease occur in association with inflammatory changes in the aortic root, the opening of the coronary arteries, and around the aortic valve and the development of secondary cardiac dysfunction and complications during the interval period after the development of vasculitis leads to death. In this article, the complications of CAWS vasculitis in DBA/2 mice are considered, and the mechanisms underlying the severe lethal toxicity are discussed. In DBA/2 mice, we observed cardiomegaly as well as marked splenomegaly as organ changes following CAWS administration. In particular, cardiomegaly suggested cardiac complications associated with aortitis and coronary arteritis. Accordingly, in this article, we focus on structural and functional changes in the heart. In the first section, with regard to the lesions around the aorta, aortic valve, and myocardial tissue, we analyze morphological changes in inflammatory lesions and at the same time evaluate quantitatively the extent of cardiomegaly. In addition, we anatomically and histopathologically analyze CAWS vasculitis, with particular focus on the internal structure of the membrane tissue of the heart valve. Furthermore, in the second section, we analyze cardiac function *in vivo* by echocardiography, together with a comparative examination of B-type natriuretic peptide (BNP) expression, which is a useful diagnostic and prognostic marker of heart failure widely applied in clinical practice, between the group administered CAWS (hereafter, the CAWS group) and the control group [37].

As described above, aortic valve cusp thickening and significant deformation of the valve structure were observed in the CAWS group. In CAWS vasculitis, lesions did not simply manifest as vascular abnormality; rather, lesions also showed signs of potential severe morphological changes in the membrane tissue of the valve, mainly the aortic valve. In DBA/2 mice with CAWS vasculitis, we observed not only marked splenomegaly but also a significant heart weight increase with marked macroscopic cardiomegaly. In previous pathological analyses of tissue specimens, observations were performed using short-axis slices only; thus, it was difficult to obtain a full understanding of cardiovascular tissue. Accordingly, we prepared

long-axis slices for histopathological analysis and comparison. Long-axis slices were prepared to be able to observe the aortic valve and ventricle simultaneously from the aorta through the apex. The observation of HE-stained long-axis heart tissue slices revealed that inflammatory lesions were not confined to the area around the aortic valve and the sinus of Valsalva, but also infiltrated into the interventricular septum directly below the aortic valve, as well as the myocardial tissue of part of the left and right ventricles. Furthermore, it was also revealed that, owing to the infiltration and accumulation of inflammatory cells (particularly valve cusp thickening from the left ventricle to the aortic valve and inflammatory lesions directly under the annulus of the aortic valve), severe stenosis developed, which morphologically extended from the left ventricular outflow tract (LVOT) to the opening of the aortic valve; this is a new finding. Moreover, the observation at the myocardial cell level revealed that the cross-sectional area of left ventricular myocardial cells increased by 1.14-fold in the CAWS group compared with that in the control group, and concentric hypertrophy was observed [37].

In the body, cardiovascular tissue exhibits circulatory dynamics with its lumen filled up with blood. Thus, histopathological analysis after the animal has been sacrificed does not allow for the evaluation of cardiac function, such as hemodynamics, or anatomical morphological changes in cardiovascular tissue *in vivo*. It is essential to observe the cardiovascular structure in the living organism and evaluate cardiac function in order to determine the causes of death in DBA/2 mice. In particular, in order to evaluate *in vivo* cardiac function immediately before their death, minimally invasive evaluation methods are needed. Ultrasound cardiography (UCG) is less invasive to the body, and as it enables real-time observation of organ morphology and function, it is essential in heart disease examination in clinical settings and has been used widely [38]. In a typical UCG examination, heart morphology (the form and movement of left ventricle, left atrium, aorta, mitral valve, and aortic valve) is observed with a probe placed on the chest wall. The most common type of heart tomographic image is a B-mode image. On the basis of this image, an M-mode echo image is obtained, which yields a one-dimensional view of the selected structure moving over time. Measurements of blood flow are possible by Doppler echocardiography. The main cardiac parameters obtained by UCG include the following: aortic diameter (AoD), left atrial dimension (LAD), left ventricular diameter (LVD) (LVDd = left ventricular end-diastolic diameter; LVDs = left ventricular end-systolic diameter), interventricular septal thickness (IVS) (IVSd = interventricular septal thickness at end diastole; IVSs = interventricular septal thickness at end systole), left ventricular posterior wall thickness (LVPW) (LVPWd = left ventricular posterior wall thickness at end diastole, LVPWs = left ventricular posterior wall thickness at end systole), left ventricular fractional shortening (LVFS) (%) ((LVDd − LVDs) / LVDd × 100), left ventricular ejection fraction (LVEF): estimated by several calculation methods), and inferior vena cava (IVC). Changes in cardiac function following CAWS administration were closely observed; in particular, cardiac function during the 6th to 7th weeks (i.e., immediately before death) was evaluated in detail by UCG. At the time of UCG evaluation, 10 mice each were prepared for the CAWS

group and the control group; however, two of the CAWS mice died before examination, leaving eight available for the subsequent examination. However, two of the eight mice in the CAWS group died during UCG examination due to severe bradycardia leading to cardiac arrest. It was not possible to evaluate the cardiac function of these two mice immediately before their death; in these cases, the presence of severe heart disease was suggested [37]. The UCG of the six mice of the CAWS group, for which examination was feasible, revealed a diffuse, severe reduction of contractility in the left ventricle compared with the control group (Fig. 15.3). The segmental akinesia in the wall of left ventricle was not found. It was suggested that the influence of the ischemia did not cause infarction in CAWS arteritis. In the CAWS group, no clear changes in cardiac function were demonstrated for some time after the onset of vasculitis. However, after the development of vasculitis, the aortic valve outflow velocity tended to be higher than that in the control group, suggesting an increase in pressure load (pressure gap) due to the narrowing of the LVOT and aortic valve (Fig. 15.4). Above all, at the end stage, a significant increase in LVDd and a significant decrease in LVFS were observed, along with the thinning of the myocardial wall. It was revealed that DBA/2 mice

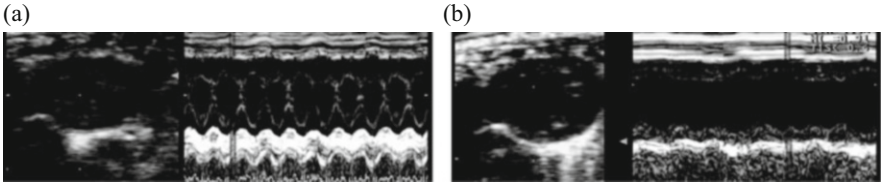

Fig. 15.3 Comparison of the cardiac function measured by echocardiography in untreated and CAWS treatment DBA/2 mice
CAWS treatment DBA/2 mice developed left ventricular dilution and dysfunction between 6 and 7 week after CAWS administration. (**a**) Untreated DBA/2 mouse, (**b**) The sixth week after CAWS administration
Left ventricular fractional shortening (LVFS) decreased from 71 % to 38 % ($P < 0.01$), and dilation of the left ventricular diastolic dimension (LVDd) was observed from 2.21 to 3.26 mm ($P < 0.01$) (**b**) $n = 10$ (untreated) and $n = 6$ (CAWS treatment)

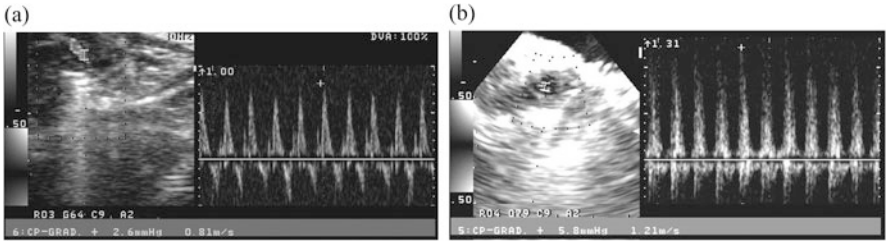

Fig. 15.4 Aortic valve and LVOT stenosis measured by echocardiography
The bloodstream increase (about 1.5 times) and pressure increase (more than two times) were found in the CAWS-treated DBA/2 mouse. (**a**) Untreated DBA/2 mouse, (**b**) The sixth week after CAWS administration

with CAWS vasculitis develop eccentric hypertrophy associated with aortic regurgitation (AR), which is accompanied by significant left ventricular dilation and reduced left ventricular contractility immediately before death.

15.4 Assessment of Cardiac Function in DBA/2 Mice After the Onset of CAWS Vasculitis with B-Type Natriuretic Peptide (BNP)

Brain or B-type natriuretic peptide (BNP) and N-terminal (NT) proBNP are biomarkers of heart failure widely used in clinical settings in Japan [39]. BNP was named after the fact that it was originally discovered from porcine brain tissue in 1998 [40]. BNP and atrial natriuretic peptide (ANP), which had been identified before BNP [41], were both found to be secreted from myocardial cells in proportion to the severity of heart failure [42, 43]. Later, in 1990, C-type natriuretic peptide (CNP) was also identified [44]. Thus, among the members of the natriuretic peptide family, BNP is often referred to as the "B-type" natriuretic peptide. Most studies on the natriuretic peptide family have been conducted in Japan, from their discovery to application. Along with ANP, BNP has been considered as a myocardial stress marker [45], with its precursor proBNP produced in response to increased cardiac load in myocardial cells, which is then converted by a protease into active BNP (half-life, about 20 min) and inactive NT-proBNP (half-life, 60–120 min) [39]. In mice, there have been studies in which blood ANP concentration and systolic blood pressure were compared among different mouse strains. These showed no significant differences in blood ANP concentration between inbred strains of wild-type mice [46, 47], leading to the conclusion that it is a useful indicator of cardiac function. Measurements of BNP and NT-proBNP could thus serve as prognostic indicators of acute and chronic heart failure, with high evidence according to clinical practice guidelines [48]. The onset of heart failure leads to other well-known pathological conditions of impaired diastolic performance and reduced systolic performance. However, differential diagnosis of these two conditions cannot be made on the basis of BNP level. Combining BNP with physiological tests such as UCG, however, can lead to a more accurate diagnosis [49]. Murine BNP cDNA has been identified by Ogawa et al. [50], but anti-mouse BNP antibodies are not commercially available at present as a reagent. This made it difficult for us to measure BNP at the protein level. Accordingly, in this section, induction of BNP by CAWS administration was observed at the mRNA level by the reverse transcription PCR method using RNA primers, as previously reported [51]. In the CAWS group, a significant increase in BNP mRNA expression level was observed 6 weeks after CAWS administration (Fig. 15.5).

In this article, with regard to a sharp decrease in survival rate observed in the chronic phase of CAWS vasculitis in DBA/2 mice, we analyze mainly the effect of inflammatory lesions on the internal structure of the heart and cardiac function, with

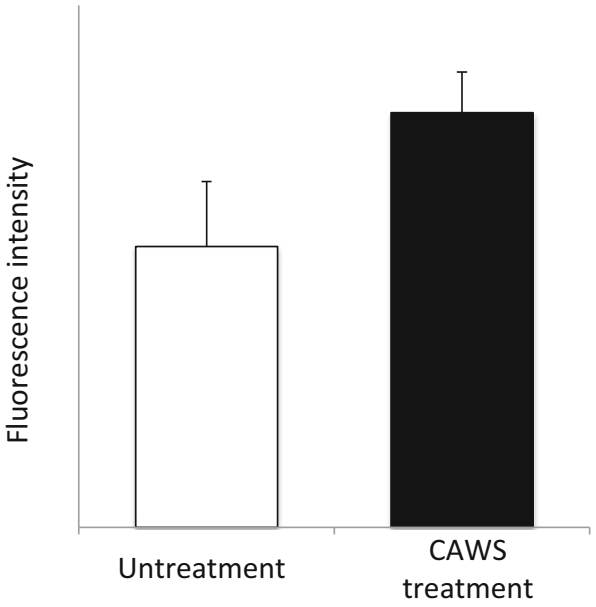

Fig. 15.5 mRNA expression of murine BNP in CAWS arteritis
The cDNA levels of murine BNP were examined by RT-PCR after 6 weeks CAWS administration

the aim of elucidating pathological conditions that may potentially lead to death [22, 37]. Valvular disease is a sequela of rheumatoid fever caused by group A hemolytic streptococcus infection and a representative inflammatory disease that could cause myocardial damage or cardiac dysfunction. This is believed to be due to an immunological cross-reaction between bacterium-derived component and autoantigen, which leads to the progression of valve tissue destruction [52]. Other acute diseases include viral myocarditis [53] and progressive destruction of the cardiac internal structure associated with acute pericarditis or infectious endocarditis. In these conditions, infections or inflammatory lesions greatly damage the internal structure and function of the heart and significantly affect patient prognosis [54]. In DBA/2 mice, although CAWS vasculitis is also accompanied by severe stenosis of coronary artery origin, previous studies showed no extensive infarct involving the left ventricle, scarred fibrous tissue, which is usually observed after myocardial infarction, inflammatory cell infiltration into inflamed myocardial tissue, or a valvular disease other than aortic valve disease. In addition, since ischemic heart disease by itself does not cause concentric hypertrophy with an increased myocardial cross-sectional area as a complication, CAWS vasculitis and accompanying left ventricular dysfunction might not have developed with ischemic heart disease as the direct underlying cause. In the present model, the major factor associated with concentric hypertrophy, which was observed in histopathological images, likely involves the narrowing of the LVOT directly under the aortic valve and the thickening and deformation of the aortic valve. These are developed as complications due to the progression of vascular lesions, which leads to the formation of inflammatory tissue around the aortic valve.

After CAWS administration, the overexpression of BNP mRNA, a cardiac stress marker, was observed in the myocardial cells of DBA/2 mice. It is assumed that this was caused by the narrowing of the LVOT, which caused pressure load particularly on the left ventricle, thereby inducing BNP in myocardial cells in the left ventricle. BNP belongs to the natriuretic peptide family, and it has been shown to exert its effects via the guanylate cyclase (GC) receptors NPR-A (GC-A) and NRP-B (GC-B) as well as NPR-C, which shows no GC activity. GC-A and GC-B increase intracellular cyclic GMP (cGMP) concentrations, and physiological activities are then expressed [55]. NPR-C is assumed to be mainly involved in the inactivation and clearance of the natriuretic peptide family [56]. GC-A is widely distributed in vascular endothelial cells, smooth muscle cells, and stromal cells. Among these cells, GC-A is abundantly expressed in mesangial cells (i.e., endothelial cells of the glomerular capillary) and epithelial cells of renal tubules. ANP and BNP have a strong affinity to the GC-A receptor and exert a vasodilatory effect to increase the glomerular filtration rate and the diuretic effect based on the suppression of sodium reabsorption mainly in the renal inner medullary collecting duct. ANP has been utilized primarily in Japan and BNP primarily in Europe and the United States as diuretics as well as for clinical purposes such as to treat acute heart failure [57]. In CAWS vasculitis, lesions may cause an excessive load in myocardial cells of DBA/2 mice, and BNP may be induced as part of biological reactions.

Clinically, similar conditions include aortic valve stenosis (AS) and hypertrophic obstructive cardiomyopathy (HOCM) [58, 59]. AS is a condition in which the aortic valve is narrowed owing to the degeneration of the aortic valve and congenital bicuspid aortic valve, or rheumatoid or inflammatory changes, resulting in chronic left ventricular pressure load and concentric hypertrophy. In a study of pathological tissue specimens from AS patients of various ages, 48 % showed degenerative changes, 27 % a bicuspid valve, and 23 % inflammatory changes among patients aged $\geq$70 years. On the other hand, among patients aged $<$70 years, 50 % showed a bicuspid valve, 25 % inflammatory changes, and 18 % degenerative changes. These findings suggest that congenital bicuspid valve accounts for a high percentage among relatively young age groups and that with age, patients tend to be less likely to develop AS due to bicuspid valve or inflammation and more likely to develop AS due to degeneration [60]. In AS, the left ventricle is exposed to pressure overload in the early stage from onset, although patients remain asymptomatic for some time. During this period, left ventricular remodeling as a compensatory reaction proceeds, with remarkable concentric hypertrophy occurring secondary to this event. For a while, left ventricular function is maintained without any symptoms owing to this compensation; however, deterioration of left ventricular function progresses gradually. Symptoms appear eventually, as the compensatory mechanism alone can no longer maintain the blood supply to the entire body. Clinically, when angina, syncope, and heart failure present as the symptoms of severe AS, the prognosis is extremely poor, and radical surgery such as valve replacement must be performed as early as possible. The average life expectancies from the emergence of angina, syncope, and heart failure are reportedly 5 years, 3 years, and 2 years, respectively [61]. A sharp decrease in survival rate is observed

after the onset of symptoms. This tendency appears to be very similar to that of the survival rate of DBA/2 mice with CAWS vasculitis as an animal model. However, in the natural course of AS alone, conversion to eccentric hypertrophy rarely occurs after the onset of concentric hypertrophy. In the present model, we observed left ventricular dysfunction associated with eccentric hypertrophy at the end stage immediately before death, which suggests that volume load due to aortic regurgitation (AR) and myocardial ischemia caused by stenosis of coronary artery origin might be involved in subsequent left ventricular dilation and reduced left ventricular function.

HOCM is a disease of unknown cause, in which the thickened wall of the heart muscle in the ventricular septum causes severe stenosis or obstruction in the LVOT. If left untreated, this condition can lead to left ventricular depression due to large left ventricular end-systolic pressure differences (load) in the left ventricle. Reduced left ventricular function observed at the end stages of AS and severe HOCM is caused by an extremely large and sustained pressure load imposed on the left ventricle, which arises from severe stenosis of the opening of the aortic valve and LVOT. This mechanically disturbs blood flow from the left ventricle to a great extent. In general, 10.15 % of the patients with hypertrophic cardiomyopathy (HCM) undergo transition into the dilated phase of hypertrophic cardiomyopathy (dHCM), with a prominently enlarged left ventricular cavity and reduced systolic performance [59]. The prognosis of dHCM is poor, likely because of the thinning of the ventricular wall due to aortic valve disease and chronic ischemia induced by insufficient blood supply to the hypertrophied myocardium [62]. In the present model, coronary artery lesions were also observed, suggesting that it is highly likely that, in addition to an increased blood demand to the hypertrophied myocardium, coronary artery lesions further exacerbated myocardial ischemia.

The mechanism leading to reduced left ventricular function can be summarized as follows. First, severe vasculitis lesions induce aortic valve cusp thickening and narrowing of the opening of the aortic valve, and the infiltration of inflammatory cells causes LVOT stenosis. The narrowing of the aortic valve and LVOT causes excessive and sustained pressure load on the left ventricle, thereby inducing concentric myocardial hypertrophy. As a hypertrophied myocardium requires larger amounts of oxygen and nutrients than a normal myocardium, increased coronary artery blood flow is necessary; however, owing to coronary artery lesions associated with vasculitis, myocardial blood supply is insufficient, and eventually, the entire left ventricular myocardium becomes severely ischemic. Owing to aortic valve disease and ischemia, the hypertrophied myocardium undergoes transitions to dilated-phase eccentric left ventricular hypertrophy, which causes rapid deterioration of left ventricular function, leading to death caused by heart failure or sudden death due to fatal arrhythmias. Left ventricular dysfunction observed in this model is assumed to exhibit left-heart-failure-predominant symptoms. Typically, in left heart failure, weight gain and peripheral edema are rarely or not observed. Here, the weight loss of about 10 % noted during the temporal weight change monitoring is thus assumed to be partly explained by the decreased appetite associated with heart failure symptoms and inflammatory reactions.

In the treatment of chronic heart failure, prognosis improvement is the most important outcome in clinical practice. Animal models enable easy observation of survival rate and are expected to be very useful not only for the development of novel therapeutic agents but also for studies of treatment protocols. For now, only a few good animal models exist for cardiovascular diseases, particularly in regard to chronic heart failure. Commonly used murine models of myocardial damage include those involving surgical treatment or genetic manipulation as well as models of coxsackievirus B3-induced myocarditis and encephalomyocarditis virus (EMCV)-induced myocarditis. In particular, as EMCV-induced myocarditis forms myocardial lesions resembling dilated cardiomyopathy accompanied by cardiac dysfunction, it is used as a human heart failure or animal cardiomyopathy model [63–65]. However, it requires an immense amount of effort and skilled techniques to generate heart disease models that involve surgical treatment or genetic manipulations, so it is difficult to generate a large number of samples simultaneously in a short time that match a large-scale clinical study. In this article, we showed that the murine model of CAWS vasculitis can also be used as an animal model of cardiovascular diseases accompanied by reduced left ventricular function. Furthermore, such a model only requires the intraperitoneal administration of CAWS, which is a very simple procedure, to achieve simultaneous development of vasculitis in 100 % of a large number of animals. Taken together, this animal model is suggested to be extremely useful for the development of therapeutic agents for heart failure (Fig. 15.2).

References

1. World health organization (WHO) The 10 leading causes of death by broad income group 2008. http://www.who.int/mediacentre/factsheets/fs310/en/index.html#
2. Swirski FK, Nahrendorf M. Leukocyte behavior in atherosclerosis, myocardial infarction, and heart failure. Science. 2013;339:161–6.
3. Packard RR, Libby P. Inflammation in atherosclerosis: from vascular biology to biomarker discovery and risk prediction. Clin Chem. 2008;54:24–38.
4. Corrado E, Rizzo M, Coppola G, Fattouch K, Novo G, Marturana I, Ferrara F, Novo S. An update on the role of markers of inflammation in atherosclerosis. J Atheroscler Thromb. 2010;17:1–11.
5. Taubert KA, Shulman ST. Kawasaki disease. Am Fam Physician. 1999;59:3093–102.
6. Kawasaki T. Acute febrile mucocutaneous syndrome with lymphoid involvement with specific desquamation of the fingers and toes in children. Arerugi. 1967;16:178.222.
7. Galeotti C, Bayry J, Kone-Paut I, Kaveri SV. Kawasaki disease: aetiopathogenesis and therapeutic utility of intravenous immunoglobulin. Autoimmun Rev. 2010;9:441–8.
8. Uehara R, Belay ED. Epidemiology of Kawasaki disease in Asia, Europe, and the United States. J Epidemiol. 2012;22:79–85.
9. Murata H, Naoe S. Experimental *Candida*-induced arteritis in mice--relation to arteritis in Kawasaki disease. Prog Clin Biol Res. 1987;250:523.
10. Nagi-Miura N, Shingo Y, Adachi Y, Ishida-Okawara A, Oharaseki T, Takahashi K, Naoe S, Suzuki K, Ohno N. Induction of coronary arteritis with administration of CAWS (*Candida*

albicans water-soluble fraction) depending on mouse strains. Immunopharmacol Immunotoxicol. 2004;26:527–43.
11. Ohno N. Chemistry and biology of angiitis inducer, *Candida albicans* water-soluble mannoprotein-beta-glucan complex (CAWS). Microbiol Immunol. 2003;47:479–90.
12. Nagi-Miura N, Harada T, Shinohara H, Kurihara K, Adachi Y, Ishida-Okawara A, Oharaseki T, Takahashi K, Naoe S, Suzuki K, Ohno N. Lethal and severe coronary arteritis in DBA/2 mice induced by fungal pathogen, CAWS *Candida albicans* water-soluble fraction. Atherosclerosis. 2006;186:310–20.
13. Tada R, Nagi-Miura N, Adachi Y, Ohno N. *Candida albicans* derived fungal PAMPS, CAWS, water soluble mannoprotein-beta-glucan complex shows similar immunotoxicological activity with bacterial endotoxin from Escherichia coli O9. Biol Pharm Bull. 2006;29:240–6.
14. Ohno N. A murine model of vasculitis induced by fungal polysaccharide. Cardiovasc Hematol Agents Med Chem. 2008;6:44–52.
15. Guidelines for Treatment of Chronic Heart Failure (JCS 2010) http://www.j-circ.or.jp/guideline/pdf/JCS2010_matsuzaki_h.pdf
16. The Criteria Committee of the New York Heart Association. Nomenclature and criteria for diagnosis of diseases of the heart and great vessels. 9th ed. Boston: Little, Brown & Co; 1994.
17. Hunt SA, Abraham WT, Chin MH, Feldman AM, Francis GS, Ganiats TG, Jessup M, Konstam MA, Mancini DM, Michl K, Oates JA, Rahko PS, Silver MA, Stevenson LW, Yancy CW. 2009 focused update incorporated into the ACC/AHA, 2005 Guidelines for the Diagnosis and Management of Heart Failure in Adults: a report of the American College of Cardiology Foundation/American Heart Association Task Force on Practice Guidelines: developed in collaboration with the International Society for Heart and Lung Transplantation. Circulation. 2009;119:e391–479.
18. Saijo S, Ikeda S. Dectin-2 recognition of alpha-mannans and induction of Th17 cell differentiation is essential for host defense against *Candida albicans*. Immunity. 2010;32:681–91.
19. Miura NN, Komai M, Adachi Y, Osada N, Kameoka Y, Suzuki K. Ohno N.IL-10 is a negative regulatory factor of CAWS-vasculitis in CBA/J mice as assessed by comparison with Bruton's tyrosine kinase-deficient CBA/N mice. J Immunol. 2009;183(5):3417–24. doi:10.4049/jimmunol.0802484. Epub 2009 Aug 12.PMID: 19675170.
20. Shinohara H, Nagi-Miura N, Ishibashi K, Adachi Y, Ishida-Okawara A, Oharaseki T, Takahashi K, Naoe S, Suzuki K, Ohno N. Beta-mannosyl linkages negatively regulate anaphylaxis and vasculitis in mice, induced by CAWS, fungal PAMPS composed of mannoprotein-beta-glucan complex secreted by *Candida albicans*. Biol Pharm Bull. 2006;29:1854–61.
21. Uchiyama M, Ohno N, Miura NN, Adachi Y, Aizawa MW, Tamura H, Tanaka S, Yadomae T. Chemical and immunochemical characterization of limulus factor G-activating substance of *Candida* spp. FEMS Immunol Med Microbiol. 1999;24:411–20.
22. Hirata N, Ishibashi K, Ohta S, Hata S, Shinohara H, Kitamura M. Histopathological examination and analysis of mortality in DBA/2 mouse vasculitis induced with CAWS, a water-soluble extracellular polysaccharide fraction obtained from candida albicans. Yakugaku zasshi. 2006;126:643–50.
23. Jennette JC, Falk RJ, Andrassy K, Bacon PA, Churg J, Gross WL, Hagen EC, Hoffman GS, Hunder GG, Kallenberg CG, et al. Nomenclature of systemic vasculitides. Proposal of an international consensus conference. Arthritis Rheum. 1994;37:187–92.
24. Luqmani RA, Suppiah R, Grayson PC, Merkel PA, Watts R. Nomenclature and classification of vasculitis – update on the ACR/EULAR diagnosis and classification of vasculitis study (DCVAS). Clin Exp Immunol. 2011;164 Suppl 1:11–3.
25. Jennette JC, Falk RJ, Bacon PA, Basu N, Cid MC, Ferrario F, Flores-Suarez LF, Gross WL, Guillevin L, Hagen EC, Hoffman GS, Jayne DR, Kallenberg CG, Lamprecht P, Langford CA, Luqmani RA, Mahr AD, Matteson EL, Merkel PA, Ozen S, Pusey CD, Rasmussen N, Rees AJ, Scott DG, Specks U, Stone JH, Takahashi K, Watts RA. 2012 revised International Chapel Hill Consensus Conference Nomenclature of Vasculitides. Arthritis Rheum. 2013;65:1–11.

26. Danila MI, Bridges Jr SL. Update on pathogenic mechanisms of systemic necrotizing vasculitis. Curr Rheumatol Rep. 2008;10:430–5.
27. Skaria AM, Ruffieux P, Piletta P, Chavaz P, Saurat JH, Borradori L. Takayasu arteritis and cutaneous necrotizing vasculitis. Dermatology. 2000;200:139–43.
28. Takahashi K, Oharaseki T, Wakayama M, Yokouchi Y, Naoe S, Murata H. Histopathological features of murine systemic vasculitis caused by *Candida albicans* extract – an animal model of Kawasaki disease. Inflamm Res. 2004;53:72–7.
29. Ridger V, Krams R, Carpi A, Evans PC. Hemodynamic parameters regulating vascular inflammation and atherosclerosis: a brief update. Biomed Pharmacother. 2008;62:536–40.
30. Monach PA, Merkel PA. Genetics of vasculitis. Curr Opin Rheumatol. 2010;22:157–63.
31. Van Vleet JF, Ferrans VJ. Ultrastructural changes in inherited cardiac calcinosis of DBA/2 mice. Am J Vet Res. 1987;48:255–61.
32. Schulte DJ, Yilmaz A, Shimada K, Fishbein MC, Lowe EL, Chen S, Wong M, Doherty TM, Lehman T, Crother TR, Sorrentino R, Arditi M. Involvement of innate and adaptive immunity in a murine model of coronary arteritis mimicking Kawasaki disease. J Immunol. 2009;183:5311–8.
33. Lidar M, Lipschitz N, Langevitz P, Shoenfeld Y. The infectious etiology of vasculitis. Autoimmunity. 2009;42:432–8.
34. Underhill DM, Ozinsky A. Toll-like receptors: key mediators of microbe detection. Curr Opin Immunol. 2002;14:103–10.
35. Amati L, Pepe M, Passeri ME, Mastronardi ML, Jirillo E, Covelli V. Toll-like receptor signaling mechanisms involved in dendritic cell activation: potential therapeutic control of T cell polarization. Curr Pharm Des. 2006;12:4247–54.
36. Meir KS, Leitersdorf E. Atherosclerosis in the apolipoprotein-E-deficient mouse: a decade of progress. Arterioscler Thromb Vasc Biol. 2004;24:1006–14.
37. Hirata N, Ishibashi K, Usui T, Yoshioka J, Hata S, Adachi Y, Nagi-Miura N, Ohta S, Ohno N. A model of left ventricular dysfunction complicated by CAWS arteritis in DBA/2 mice. Int J Vasc Med. 2012; ID 570297, 9 pages.
38. Reeves ST, Glas KE, Eltzschig H, Mathew JP, Rubenson DS, Hartman GS, Shernan SK, American Society of Echocardiography, Society of Cardiovascular Anesthesiologists. Guidelines for performing a comprehensive epicardial echocardiography examination: recommendations of the American Society of Echocardiography and the Society of Cardiovascular Anesthesiologists. J Am Soc Echocardiogr. 2007;20:427–37.
39. Balion C, McKelvie R, Don-Wauchope AC, Santaguida PL, Oremus M, Keshavarz H, Hill SA, Booth RA, Ali U, Brown JA, Bustamam A, Sohel N, Raina P. B-type natriuretic peptide-guided therapy: a systematic review. Heart Fail Rev. 2014;19(4):553–64. doi:10.1007/s10741-014-9451-x. PMID: 25074674.
40. Sudoh T, Kangawa K, Minamino N, Matsuo H. A new natriuretic peptide in porcine brain. Nature. 1988;332:78–81.
41. Kangawa K, Matsuo H. Purification and complete amino acid sequence of alpha-human atrial natriuretic polypeptide (alpha-hANP). Biochem Biophys Res Commun. 1984;118:131–9.
42. Mukoyama M, Nakao K, Saito Y, Ogawa Y, Hosoda K, Suga S, Shirakami G, Jougasaki M, Imura H. Increased human brain natriuretic peptide in congestive heart failure. N Engl J Med. 1990;13(323):757–8.
43. Mukoyama M, Nakao K, Hosoda K, Suga S, Saito Y, Ogawa Y, Shirakami G, Jougasaki M, Obata K, Yasue H, et al. Brain natriuretic peptide as a novel cardiac hormone in humans. Evidence for an exquisite dual natriuretic peptide system, atrial natriuretic peptide and brain natriuretic peptide. J Clin Invest. 1991;87:1402–12.
44. Sudoh T, Minamino N, Kangawa K, Matsuo H. C-type natriuretic peptide (CNP): a new member of natriuretic peptide family identified in porcine brain. Biochem Biophys Res Commun. 1990;168:863–70.
45. Mair J. Biochemistry of B-type natriuretic peptide. where are we now? Clin Chem Lab Med. 2008;46:1507–14.

46. Schoensiegel F, Bekeredjian R, Schrewe A, Weichenhan D, Frey N, Katus HA, Ivandic BT. Atrial natriuretic peptide and osteopontin are useful markers of cardiac disorders in mice. Comp Med. 2007;57:546–53.
47. Mifune H, Nishi Y, Tajiri Y, Yabuki A. Different A-type natriuretic peptide level in five strains of mice. J Vet Med Sci. 2012;74:499–502.
48. McMurray JJ, Adamopoulos S, Anker SD, et al. ESC Committee for Practice Guidelines. ESC guidelines for the diagnosis and treatment of acute and chronic heart failure 2012: The Task Force for the Diagnosis and Treatment of Acute and Chronic Heart Failure 2012 of the European Society of Cardiology. Developed in collaboration with the Heart Failure Association (HFA) of the ESC. Eur J Heart Fail. 2012;14:803–69.
49. Beck-da-Silva L, Rohde LE, Goldraich L, Clausell N. Clinical findings, natriuretic peptides, and echocardiography: integrating tools to optimize heart failure management. Congest Heart Fail. 2007;13:158–63.
50. Ogawa Y, Itoh H, Tamura N, et al. Molecular cloning of the complementary DNA and gene that encode mouse brain natriuretic peptide and generation of transgenic mice that overexpress the brain natriuretic peptide gene. J Clin Invest. 1994;93:1911.1921.
51. LaPointe MC, Mendez M, Leung A, Tao Z, Yang XP. Inhibition of cyclooxygenase-2 improves cardiac function after myocardial infarction in the mouse. Am J Physiol. 2004;286:1416.1424.
52. Guilherme L, Kohler KF, Kalil J. Rheumatic heart disease: mediation by complex immune events. Adv Clin Chem. 2011;53:31–50.
53. Sagar S, Liu PP, Cooper Jr LT. Myocarditis. Lancet. 2012;379:738–47.
54. Htwe TH, Khardori NM. Cardiac emergencies: infective endocarditis, pericarditis, and myocarditis. Med Clin North Am. 2012;96:1149–69.
55. Woodard GE, Rosado JA. Natriuretic peptides in vascular physiology and pathology. Int Rev Cell Mol Biol. 2008;268:59–93.
56. Rose RA, Giles WR. Natriuretic peptide C receptor signalling in the heart and vasculature. J Physiol. 2008;15(586):353–66.
57. Gassanov N, Biesenbach E, Caglayan E, Nia A, Fuhr U, Er F. Natriuretic peptides in therapy for decompensated heart failure. Eur J Clin Pharmacol. 2012;68:223–30.
58. Guidelines for Surgical and Interventional Treatment of Valvular Heart Disease (JCS 2012) http://www.j-circ.or.jp/guideline/pdf/JCS2012_ookita_h.pdf
59. Guidelines for Diagnosis and Treatment of Patients with Hypertrophic Cardiomyopathy (JCS 2012) http://www.j-circ.or.jp/guideline/pdf/JCS2012_doi_h.pdf
60. Passik CS, Ackermann DM, Pluth JR, et al. Temporal changes in the causes of aortic stenosis: a surgical pathologic study of 646 cases. Mayo Clin Proc. 1987;62:119–23.
61. Ross Jr J, Braunwald E. Aortic stenosis. Circulation. 1968;38(1 Suppl):61–7.
62. Opie LH, Commerford PJ, Gersh BJ, Pfeffer MA. Controversies in ventricular remodelling. Lancet. 2006;367:356–67.
63. Scheuermann-Freestone M, Freestone NS, Langenickel T, Hohnel K, Dietz R, Willenbrock R. A new model of congestive heart failure in the mouse due to chronic volume overload. Eur J Heart Fail. 2001;3:535–43.
64. Bayat H, Swaney JS, Ander AN, Dalton N, Kennedy BP, Hammond HK, Roth DM. Progressive heart failure after myocardial infarction in mice. Basic Res Cardiol. 2002;97:206–13.
65. Doi K. Experimental encephalomyocarditis virus infection in small laboratory rodents. J Comp Pathol. 2011;144:25–40.